© Copyright 2023

Zheyi Han

MEMS-integrated Alvarez Metalenses and Large-area Meta-optics

Zheyi Han

A dissertation

submitted in partial fulfillment of the

requirements for the degree of

Doctor of Philosophy

University of Washington

2023

Reading Committee:

Karl F. Böhringer, Chair

Arka Majumdar

Lih Lin

Program Authorized to Offer Degree:

Electrical and Computer Engineering

University of Washington

Abstract

MEMS-integrated Alvarez Metalenses and Large-area Meta-optics

Zheyi Han

Chair of the Supervisory Committee:
Professor Karl F. Böhringer
Electrical and Computer Engineering

Meta-optics – ultrathin and subwavelength-patterned diffractive optics – are novel replacements for bulky freeform optical elements showing high potential with their greatly reduced volume and high compatibility with modern microfabrication processes. Miniature lenses with tunable focus are essential components for many modern applications involving compact optical systems. While several tunable lenses have been reported with various tuning mechanisms, they often face challenges in power consumption, tuning speed, fabrication cost, or production scalability. In the first part of this thesis, we have adapted the mechanism of an Alvarez lens – a varifocal composite lens in which lateral shifts of two optical elements with cubic phase surfaces give rise to a change in optical power – to construct a miniature, MEMS-actuated meta-optic Alvarez lens. The implementation based on electrostatic microelectromechanical systems (MEMS) generates fast and controllable actuation with low power consumption. The utilization

of meta-optics as the optical elements greatly reduces the device volume compared to systems using conventional freeform lenses. The entire MEMS Alvarez metalens is fully compatible with modern semiconductor fabrication technologies, granting it the potential to be mass-produced at a low unit cost. In our latest prototype operating at 1550 nm wavelength, a total uniaxial displacement of 19 μm is achieved in the Alvarez metalens with direct-current (DC) voltage application up to 40 V, modulating the focal position within a total tuning range of 3.1 mm, producing more than two orders of magnitude change in focal length and 200 diopters change in optical power. The MEMS Alvarez metalens has a robust design that can potentially generate a much larger tuning range without substantially increasing device volume or energy consumption, making it desirable for a wide range of imaging and display applications. With some crucial modifications in materials selection and fabrication process design, we also demonstrate the potential to adapt the same design principle to fabricate miniature tunable Alvarez metalenses for the visible spectrum. Rising interest in compact optics with large apertures calls for the development of large-area meta-optics. In the second part of the thesis, we explain the fabrication challenges and demonstrate the process development to manufacture large-area meta-optics, focusing on processes compatible with fast prototyping and affordable mass-production. As examples, we present several application cases of fabricated large-area meta-optics operating in the spectra from long-wave infrared to visible frequencies.

TABLE OF CONTENTS

List of Figures vi

List of Tables xviii

Chapter 1. Overview 24

Chapter 2. Introduction to tunable Metalenses 26

2.1 Conventional Designs for Miniature Tunable Lens 26

2.2 Alvarez Tunable Lenses 28

2.3 Micro-electro-mechanical Systems (MEMS) 29

2.4 MEMS for Precision Displacement 30

2.5 Meta-optics 32

2.6 Tunable Meta-optics 33

Chapter 3. Design Principles of MEMS-integrated Alvarez Metalenses 37

3.1 Alvarez Meta-optic System 37

3.1.1 Alvarez Cubic Surfaces 38

3.1.2 Alvarez Meta-optic Discretization 40

3.2 MEMS Tuning Platform 42

3.2.1 Comb Drives for Electrostatic Actuation 43

3.2.2 Mechanical Folded Flexure for Controlled Displacement 52

Chapter 4. Small-aperture Near-IR MEMS Alvarez Metalens 64

4.1 Design Parameters 64

4.1.1 Alvarez Metalens Parameters and Simulations ... 64
4.1.2 MEMS Actuation Platform Parameters and Calculations ... 70
4.2 Device Fabrication ... 71
4.2.1 Microfabrication Process Flow ... 71
4.2.2 Fabricated Devices ... 73
4.3 Experimental Setup ... 75
4.4 Results and Analysis ... 76
4.4.1 Raw Image Noise Reduction ... 77
4.4.2 Electrostatic Tuning of the MEMS-actuated Platform ... 78
4.4.3 Focal Tuning of the Small-aperture MEMS-actuated Alvarez Metalens ... 81
4.4.4 Experimental Data Error Analysis ... 86
4.4.5 Tilting of the Focal Axis with Asymmetric Actuation ... 87
4.4.6 Alvarez Metalens with Manual Tuning to Explore the Effect of Aperture Size ... 89
4.5 Discussions and Conclusion ... 93
Chapter 5. Large-aperture Near-IR MEMS Alvarez Metalens ... 95
5.1 Design Parameters ... 95
5.1.1 Alvarez Metalens Parameters ... 96
5.1.2 MEMS Actuation Platform Parameters ... 98
5.2 Device Fabrication ... 101
5.2.1 Microfabrication Process Flow ... 101
5.2.2 Meta-optics Protection during Vapor Hydrogen Fluoride Etching ... 104
5.2.3 Fabricated Devices ... 106
5.3 Experimental Setup ... 109

5.4 Results and Analysis 110
5.4.1 MEMS-actuated Tuning Platform 110
5.4.2 Actuation Power Consumption 114
5.4.3 Focal Tuning of the Large-aperture MEMS-actuated Alvarez Metalens 116
5.4.4 Experimental Data Error Analysis 121
5.4.5 Tilting of the Focal Axis with Asymmetric Actuation 123
5.5 Discussion and Conclusion 124
Chapter 6. Visible MEMS Alvarez Metalens 126
6.1 Design Parameters 126
6.1.1 Alvarez Metalens Parameters 127
6.1.2 MEMS Actuation Platform Parameters 128
6.2 Device Fabrication 128
6.2.1 Microfabrication Process Flow 129
6.2.2 Fabricated Devices 131
6.3 Experimental Setup 132
6.4 Results and Analysis 133
6.4.1 Image Channel Separation for MEMS Actuation and Focal Tuning 133
6.4.2 Meta-optic Membrane Bulging 134
6.4.3 Uniaxial Movement of the Released MEMS Platform 135
6.5 Outlook 136
Chapter 7. Fabrication Challenges for Large-area Meta-optics 138
7.1 Tool Choice and Exposure Time 139

7.1.1 Electron Beam Lithography ... 140
7.1.2 Stepper Lithography ... 140
7.1.3 Laser Direct-Write ... 142
7.1.4 Exposure Method Comparison ... 143
7.2 Optical Proximity Effects ... 145
7.2.1 Size Compensation ... 148
7.2.2 Shape Compensation ... 151
7.3 Defects from Lithography and Dry Etching ... 155
7.3.1 Lithography Defects Near Wafer Edge ... 155
7.3.2 Excessive Heating with the Use of a Carrier Wafer ... 157
7.3.3 Scatterer Sidewall Profiles ... 159
Chapter 8. Fabrication of Large-area Long-wave Infrared (LWIR) Meta-optics ... 164
8.1 Introduction ... 164
8.2 General Fabrication Flow for Single-sided LWIR Meta-optics ... 164
8.3 Infrared Imaging under Ambient Thermal Radiation ... 166
8.3.1 Device Parameters ... 166
8.3.2 Device Fabrication ... 167
8.3.3 Optical Performance ... 169
8.4 Foveated Thermal Computational Imaging ... 170
8.4.1 Meta-optic Parameters ... 171
8.4.2 Device Fabrication ... 172
8.4.3 Optical Performance ... 175
8.5 MTF-engineered Meta-optics ... 177

8.5.1 Meta-optic Parameters 177

8.5.2 Device Fabrication 181

8.5.3 Optical Performance 184

8.6 Double-sided MTF-engineered Meta-optics 187

8.6.1 Meta-optic Parameters 188

8.6.2 Device Fabrication 188

Chapter 9. Fabrication of Large-area Middle-wave Infrared (MWIR) Meta-optics 192

9.1 Dual Band Computational Infrared Spectroscopy via Large Aperture Meta-Optics.. 192

9.2 Meta-optic Parameters 192

9.3 Fabrication Flow 193

9.4 Optical Performance 195

Chapter 10. Fabrication of Large-area Visible Meta-optics 197

10.1 Large Aperture Meta-optic for Full-Color Camera 197

10.2 Meta-optic Parameters 198

10.3 Device Fabrication 199

10.4 Optical Performance 202

Chapter 11. Outlook 204

11.1 3D Imaging by an Alvarez Grid 204

11.2 3D Imaging by Alvarez Scanning Lens 204

11.3 Fabrication Improvement for Large-area Meta-optics 206

Bibliography 208

LIST OF FIGURES

Figure 2.1. A camera module (left) for a chip-on-the-tip endoscope with optical system tunable by a traveling field linear drive (right) [1]. 27

Figure 2.2. A liquid tunable lens unit (left) based on electrowetting and the schematic illustration of the interior design (right) [2]. 27

Figure 2.3. Schematic of an electrically tunable optical zoom system using three composite liquid crystal lenses [3]. 27

Figure 2.4. Schematic of a tunable lens designed with Alvarez principle, showing the physical arrangement (a) without and (b) with lateral displacement [7]................................ 28

Figure 2.5. Schematic showing a MEMS-driven tunable Alvarez lens [8]. 29

Figure 2.6. Example of MEMS structures for precision displacement for both translational and rotational movement, including (a) a cantilever scanning tip for atomic force microscope (AFM) [10], (b) a MEMS scanning mirror [11], (c, d) microscale ratcheting gears [12, 13], (e) a 3-axis gyroscope [14], and (f) a self-reconfiguring metamorphic nanoinjector [15]. 30

Figure 2.7. Microscope pictures of the exact constraint folded flexure when (top) undeflected and (bottom) deflected by 100 μm [17].. 31

Figure 2.8. Microscope pictures of the Watt's flexure when (left) undeflected and (right) deflected by 100 μm [17]... 32

Figure 2.9. Scanning electron micrograph of a fabricated meta-optic with a zoom-in view showing the gradient in pillar size [47].. 33

Figure 2.10. Tunable meta-optic fabricated with gold scatterers on a stretchable polydimethylsiloxane (PDMS) substrate [61]. 35

Figure 2.11. An illustration of the dielectric elastomer actuator (DEA) metalens design. (A) A schematic of the device combining a metalens and a DEA with five addressable electrodes for electrical tuning the strain field of the meta-optic. (B) Optical microscope images (20 μm scale bar) of the metalens at (i) 0 V, (ii) 2.5 kV applied at the center electrode and (iii)

2.75 kV applied at V1 and V3. (iv) to (vi) shows the corresponding 2D Fourier transforms [54]. 35
Figure 2.12. Meta-optic scanning mirror on a MEMS platform. (a) Integration of the reflective meta-optic lens onto the 2D MEMS platform. (b) Optical microscope image of a MEMS scanner with a meta-optic mirror integrated [62]. 36
Figure 2.13. Tunable meta-optic doublet. (b) An optical microscope image of a fabricated lens on a membrane. (c) Simplified fabrication process of the lens on the glass substrate. (d) An optical microscope image of the fabricated lens on the glass substrate. (e) Schematics of the bonding process. (f) A microscope image of the final device. (g) Scanning electron micrograph of the lens on the membrane, and (h) nano-posts that form the lens. Scale bars are 100 µm in b, d, f, and g, and 1 µm in h [56]. 36
Figure 3.1. A conceptual illustration of an Alvarez meta-optic lens system [64]. 38
Figure 3.2. An illustration of how the change in overlapping pattern affects the resultant focusing power in a meta-optic Alvarez lens system [47]. 39
Figure 3.3. Schematic of exemplary scattering elements. (Left) A cylindrical silicon nitride nanopost on a silicon dioxide substrate. (Right) A square array of nanoposts with varying diameters (top view). 40
Figure 3.4. An example of simulated transmission coefficients as a function of the duty cycle for the silicon nitride nanoposts on a silicon substrate. 41
Figure 3.5. Illustration of an example MEMS-actuated Alvarez metalens system. 42
Figure 3.6. A simplified illustration of a voltage-controlled comb-drive system. 43
Figure 3.7. Plot of electric potential inside a comb drive finger unit cell under a bias. ... 47
Figure 3.8. Plot of electrostatic force versus the applied voltage for a single comb finger, showing a quadratic dependence. 48
Figure 3.9. Force for a single comb finger at 20 V as a function of displacement from equilibrium at 0 V. A clear deviation from first order analysis is evident as the fingers draw closer to each other. The inserts show electric potentials in the medium of a unit comb finger cell. Picture credits to James Whitehead from the NOISE Lab. 50
Figure 3.10. Microscope image of a snap-in situation occurred in one electrostatic comb drive of a fabricated device. 51

Figure 3.11. A sketch of the folded flexure design, which is compliant for the desirable motion along the y-axis and stiff for the undesirable sideway disturbance along x-axis. A load is applied at center. Anchors are indicated by the solid boxes [68]. 53
Figure 3.12. A sketch comparison between the original folded-flexure design on the left and the exact constraint folded flexure using a 1:2 lever and an extra leaf-spring on the right [17]. 55
Figure 3.13. Plot of principal stress across the MEMS platform with a leftward distributed load along the left comb drive. Black frame shows the neutral position of structures. 58
Figure 3.14. Zoom-in plot of principal stress in the displaced MEMS flexure. Black frame shows the neutral position of structures. 58
Figure 3.15. An exemplary MEMS-actuated Alvarez metalens system with 2-fold actuator design. Fillets and dimples are introduced to prevent mechanical failure and increase device robustness. 59
Figure 3.16. Plot of displacement for the MEMS platform with a leftward distributed load along the left comb drive. 60
Figure 3.17. Lateral displacement of the meta-optic platform versus force in the lateral (desired) direction. 61
Figure 3.18. Sideway displacement of the meta-optic platform versus (unintended) sideway disturbance load. 62
Figure 3.19. The first six resonant modes and eigenfrequencies of the actuator at 3.38 kHz, 4.02 kHz, 4.72 kHz, 7.64 kHz, 14.0 kHz, and 23.6 kHz. 63
Figure 4.1. Schematic of meta-optic scatterers. (Left) A silicon nitride cylindrical nanopost with diameter d and thickness t on a silicon substrate. (Right) Top view of an exemplary meta-optic array of a fixed periodicity p and varying nanopost diameters. 65
Figure 4.2. Simulated transmission phase and amplitude profiles of silicon nitride nanoposts as functions of duty cycle (d/p) for a chosen post thickness of 2 μm and a fixed array periodicity of 1.3 μm. The phase is normalized to 2π. 65
Figure 4.3. The 200 μm × 200 μm regular (left) and inverse (middle) Alvarez meta-optics with complementary cubic phase profiles overlay to produce a summed quadratic phase (right). Phase values are normalized to 2π. 67

Figure 4.4. Ideal Alvarez focal tuning behavior as a function of lateral symmetric displacement d (giving a total center-to-center offset of $2d$) between the optical elements theorized with a negligible axial separation gap, an operating wavelength λ = 1550 nm and a cubic parameter $A = 2.5335 \times 10^{14}$ m^{-3} 67
Figure 4.5. Simulated change of focal location and profile when the two meta-optics are laterally displaced at Δd = –3.5 µm, 0 µm, and +3.5 µm. The full simulation is performed with actuated displacement with 0.5 µm steps. 68
Figure 4.6. Simulated focal tuning behavior when a small lateral displacement is introduced in addition to an initial center-to-center offset of 20 µm, assuming a 50 µm axial separation gap between the two meta-optics from fabrication. The focal position is calculated from the weighted centroid of high-intensity regions. 68
Figure 4.7. Fabrication flow of a small-aperture MEMS-actuated meta-optic Alvarez lens. 72
Figure 4.8. SEM image of (a) a MEMS-actuated platform carrying the movable meta-optic in an Alvarez metalens, with (b) and (c) being the zoomed-in SEM images portraying the electrostatic comb drive and the meta-optic nanoposts. (d, e) Optical images of the Alvarez meta-optics with complementary cubic phase profiles that are overlaid on top of each other in the assembled Alvarez metalens and in summation impart a quadratic phase change on the incident light. 74
Figure 4.9. optical image of the (left) regular and (right) inverse Alvarez meta-optics with complementary cubic phase profiles, fabricated with silicon nitride nanoposts on silicon substrates. An initial 20 µm center-to-center lateral shift has been introduced between the meta-optics. They overlay on top of each other in the assembled Alvarez metalens and in summation impart a quadratic phase change on the incident light. 75
Figure 4.10. Experimental setup for focal tuning analysis. 75
Figure 4.11. Noise due to camera artifacts removed by reference subtraction. (a) A raw image captured by the IR camera. (b) A bright reference taken with a free path. (c) A dark reference taken with the light path blocked. (d) The processed image with noise due to camera artifacts removed. 77
Figure 4.12. IR image showing both the device and focal planes of a singlet metalens on a MEMS-actuated platform. 79

Figure 4.13. Actuated focal displacement and applied voltage over time. The general trend of the actuated displacement follows the square of the applied voltage. 80

Figure 4.14. Average actuated displacement as a function of applied voltage-squared during both loading and unloading, showing a linear dependence. No hysteresis behavior is observed with voltage loading and unloading, verifying the reversibility of the actuation process. 80

Figure 4.15. IR camera screenshots at (a) the device plane and (b) the focus plane of an Alvarez metalens illuminated with a 1550 nm SLD source. 82

Figure 4.16. Actuated displacement as a function of applied voltage with (a) negative actuation corresponding to a decreasing offset and (b) positive actuation corresponding to an increasing offset. 83

Figure 4.17. The shift of focal intensity profiles along the optical axis with (a) decreasing and (b) increasing center-to-center offsets between the Alvarez meta-optics at various actuation voltages and displacements. 84

Figure 4.18. Tuning in focal location (a) as a function of applied voltage and (b) as a function of actuated displacement with focus size defined by various intensity thresholds, giving a focal tuning range 10 times larger than the actuated Alvarez displacement. The black dash-dotted lines are provided as guides to the eye. 86

Figure 4.19. Focal tuning by manually displacing the Alvarez meta-optics relative to each other, on the diverging side with an aperture size of (a) 200 µm, (b) 500 µm, and (c) 1 mm, and on the converging side with an aperture size of (d) 200 µm, (e) 500 µm, and (f) 1 mm, compared to the corresponding ideal Alvarez behaviors. The 'misalignment' values estimate the deviation of the fitted Alverez metalens tuning behavior from the ideal designed Alvarez tuning behavior. Manual tuning data acquisition by Shane Colburn and Luocheng Huang from the NOISE Lab. 90

Figure 5.1. The designed cubic phase profiles for the two complementary Alvarez meta-optics and the total quadratic phase profile when they overlay. The designed Alvarez meta-optics have an operating wavelength λ = 1550 nm, a built-in offset of 40 µm, and a cubic parameter $A = 1 \times 10^{13}\ \mathrm{m}^{-3}$. Colorbar indicates a 2π phase span in radian. 96

Figure 5.2. Design of the Alvarez meta-optic. (a) Schematic of the scatterer made of a cylindrical silicon nitride nanopost on a silicon substrate. (b) The simulated transmission coefficients for the nanoposts as a function of the duty cycle (diameter/periodicity)................. 97

Figure 5.3. Schematic of Alvarez meta-optics integrated with an electrostatic MEMS actuator. 99

Figure 5.4. Summarized device fabrication process flow... 102

Figure 5.5. SEM images of silicon nitride meta-optics (a) before and (b) after vapor hydrogen fluoride (vHF) etching. 104

Figure 5.6. Optical images of silicon nitride Alvarez meta-optics before and after vHF etching. (a) Uncoated meta-optic before vHF etching. (b) Uncoated meta-optic etched with a fast-etching vHF process. (c) Meta-optic coated with a thin layer of ALD alumina and etched with a fast-etching vHF process. (d) Meta-optic coated with a thin layer of ALD alumina and etched with a slow-etching vHF process. (e) Meta-optic coated with a thick layer of ALD alumina and etched with a fast-etching vHF process. (f) Meta-optic coated with a thick layer of ALD alumina and etched with a slow-etching vHF process. 105

Figure 5.7. Scanning electron microscopy (SEM) images of Alvarez meta-optic lens with actuator Design 1. (a) An Alvarez meta-optic integrated with a MEMS tuning platform. (b) Comb-drive details showing the part of the mobile flexure backbone and interdigitated finger array. (c) Close-up view of the silicon nitride nanoposts sitting on the central silicon platform.. 107

Figure 5.8. Scanning electron microscopy (SEM) images of Alvarez meta-optic lens with actuator Design 2 with shorter springs and wider fingers. (a) An Alvarez meta-optic integrated with a MEMS tuning platform. (b) Comb-drive details showing the part of the mobile flexure backbone and interdigitated finger array. (c) Close-up view of the silicon nitride nanoposts sitting on the central silicon platform....................................... 108

Figure 5.9. Assembly of the Alvarez meta-optic lens showing (a) the bottom chip 1 carrying 10 mobile meta-optics and (c) the overlaid top chip 2 carrying 10 static meta-optics facing down (right), bonded with (b) anisotropic conductive film (ACF) as both the spacer and the adhesive.. 108

Figure 5.10. Experimental characterization setup for Alvarez lens electrostatic actuation and focal profile acquisition. 109
Figure 5.11. Exemplary (a) device plane and focal plane of the Alvarez meta-optic lens actuated at 40 V towards the right... 110
Figure 5.12. Experimental characterization of the MEMS platform with Design 1. (a) Measured actuated displacement and actuating voltage of the MEMS platform follow the same quadratic trend closely, showing negligible hysteresis. (b) Actuated displacement for both directions follows the comb-drive quadratic characteristics closely. The light shade bands indicate the associated error bars. 111
Figure 5.13. Experimental characterization of the MEMS platform with Design 2. (a) Measured actuated displacement and actuating voltage of the MEMS platform follow the same quadratic trend closely, showing negligible hysteresis. (b) Actuated displacement for both directions follows the comb-drive quadratic characteristics closely. The light shade bands indicate the associated error bars. 113
Figure 5.14. Electrical measurements. (a) Measured current and (b) calculated power of electrostatic actuator. 115
Figure 5.15. Focal profiles of the MEMS Alvarez meta-optical lens with actuator Design 1 at various actuation voltages, captured along the optical axis (z-axis) at 5 µm increments across a 0.8 mm span around the main intensity lobes. Square plots on the right show the intensity distributions in the found focal planes. All intensities are normalized to the maximum intensity measured at each actuation voltage. Inset: normalized intensity distributions across the focal spots at various actuation voltages.......................... 117
Figure 5.16. Focal tuning measurements of the MEMS Alvarez meta-optical lens with actuator Design 1. (a) Actuated displacement and the corresponding focal length modulated by actuation voltage. Dashed lines show the fitting to the theoretical behaviors. (b) Tunable focal length as a function of actuated displacement closely follows the theoretical reciprocal Alvarez tuning behavior... 118
Figure 5.17. Focal profiles of the MEMS Alvarez meta-optical lens with actuator Design 2 at various actuation voltages, captured along the optical axis (z-axis) at 5 µm increments

across a 0.8 mm span around the main intensity lobes. All intensities are normalized to the maximum intensity measured at each actuation voltage.. 120

Figure 5.18. Focal tuning measurements of the MEMS Alvarez meta-optical lens with actuator Design 2. (a) Actuated displacement and the corresponding focal length modulated by actuation voltage. Dashed lines show the fitting to the theoretical behaviors. (b) Tunable focal length as a function of actuated displacement closely follows the theoretical reciprocal Alvarez tuning behavior.. 121

Figure 5.19. Image correction for camera artifacts. (a) Dark reference taken with no device in the optical pathway. (b) A raw example image taken at the focal plane. (c) The same example image with camera artifacts corrected using the dark reference............................ 123

Figure 6.1. Simulated transmission phase and amplitude profiles of silicon nitride nanoposts on a silicon dioxide substrate as functions of duty cycle (*D*/*p*) for a chosen post thickness of 1.5 μm and a fixed array periodicity of 1 μm. The phase is normalized to 2π............ 127

Figure 6.2. Fabrication process flow of the mobile Alvarez meta-optic on MEMS actuator, the static Alvarez meta-optic, and the final composite Alvarez metalens. 129

Figure 6.3. Optical images of (a) a silicon-nitride Alvarez meta-optic on an oxide membrane carried by a MEMS actuator before release and (b) a silicon-nitride Alvarez meta-optic on the fused silica substrate. 131

Figure 6.4. Scanning electron microscopy (SEM) images of Alvarez meta-optic lens operating in the visible spectrum. (a) A visible Alvarez meta-optic integrated with a MEMS tuning platform. (b) Comb-drive details showing the part of the mobile flexure backbone and interdigitated finger array. (c) Close-up view of the silicon nitride nanoposts sitting on the central silicon dioxide platform. 132

Figure 6.5. Experimental setup for Alvarez lens electrostatic actuation and focal profile acquisition in the visible spectrum.. 133

Figure 6.6. Image channel separation. (a) Captured raw image at the device plane. (b) Captured raw image at the focal plane. (c) Actuator image extracted from the green channel of (a) and enhanced to show details. (d) Focus image extracted from the red channel of (b). 134

Figure 6.7. Optical profilometry of the meta-optic membrane. (a) A 3D height map showing the central meta-optic membrane bulging out of the plane (red) after release. (b) A 1D height

plot across the center of the meta-optic membrane relative to the MEMS actuator flexure. 135
Figure 6.8. Manual push test of a released MEMS tuning platform carrying the mobile Alvarez meta-optic. (a) Neutral position. (b) Pushed to the left... 136
Figure 7.1. Optical proximity effect resulting in the pattern size and shape differences between the design layout (left) and the actually patterned scatterers (right)...................... 145
Figure 7.2. Illustration of (left) laser beam intensity spreading and (right) the resultant line shortening and corner rounding in laser direct-write lithography.......................... 147
Figure 7.3. Size deviation between a designed pattern (left) and the corresponding fabricated pattern (right) for a meta-optic exposed with laser direct-write lithography.......... 148
Figure 7.4. Top-view SEM image of fabricated silicon scatterer array for an LWIR meta-optic without size compensation. The smallest pillars shrink in size due to optical proximity and linearity effect, making them too thin to be stable after DRIE, hence eventually falling down.. 149
Figure 7.5. Fabricated scatterer sizes with original CAD designs (left) and compensated CAD designs (right) for laser direct-write lithography. The insets show portions of the pattern layouts.. 150
Figure 7.6. Comparisons between input layout designs (left columns) and SEM images of the laser direct-write output patterns (right columns) at concave (top row) and convex (bottom row) corners without any shape compensation... 152
Figure 7.7. Comparisons between input layout designs (left columns) and SEM images of the laser direct-write output patterns (right columns) at concave (top row) and convex (bottom row) corners with the shape compensation using square notches and serifs. 153
Figure 7.8. SEM images of meta-optic scatterer patterning outcomes by laser direct-write without serifs (left) and with serifs (right). 154
Figure 7.9. LWIR Meta-optics with various dimensions patterned on silicon substrates with different diameters. When the meta-optic diameter is too close to the substrate size (middle), lithographic defects arise near the wafer edge, transferring patterning imperfections to the scatterer layer after dry etch.. 156
Figure 7.10. SEM images of scatterer etch profiles with and without the carrier wafer. 158

Figure 7.11. SEM image of MWIR silicon nitride meta-optic scatterers on silicon substrate patterned with fluorine-based ICP etching. 160
Figure 7.12. SEM image of visible silicon nitride meta-optic scatterers on fused silica substrate patterned with fluorine-based ICP etching. 161
Figure 7.13. SEM image of LWIR silicon meta-optic scatterers on silicon substrate patterned with DRIE. The scalloping from the Bosch process is apparent. 162
Figure 8.1. General fabrication flow for silicon LWIR meta-optics............................. 166
Figure 8.2. Fabricated LWIR meta-optic. (Left) Photograph of four 1-inch meta-optics fabricated on a 4-inch wafer. (Right) optical image of a meta-optic pattern near the aperture center. 168
Figure 8.3. SEM images of the fabricated LWIR meta-optic. (a) Top view. (b) Oblique view. 169
Figure 8.4. “In the wild” imaging using the LWIR meta-optic. (a) A hot soldering iron is seen in front of a steel plate covered with black tape with an emissivity of 0.95. (b) A close-up image of the hot soldering iron on a metal holder. (c) A person is holding an ice pack (left) and a blowtorch (right). (d), (e) and (f) display the corresponding images captures by the LWIR meta-optic, respectively [91]. 170
Figure 8.5. Four designs of silicon-based LWIR meta-optics fabricated on 4-in wafers for foveating imaging. The diameter spans from 12.7 mm to 75 mm, while the single-optic focal length varies from 25 mm to 150 mm. The top two (with 25 mm and 75 mm diameters) are eventually selected as a pair to perform the imaging experiments. 174
Figure 8.6. Optical images of the foveated meta-optics showing the mapped convex phase profile (left) and zoomed-in view of the varying scatterers (right). 175
Figure 8.7. SEM images of the meta-optic scatterers for foveated imaging viewed from the top (left) and at an oblique angle (right). 175
Figure 8.8. Experimental setup of foveated imaging. (Image credit to Vishwanath Saragadam at Rice University) 176
Figure 8.9. Static imaging in the wild captures an outdoor rooftop scene (left), where the perifoveal meta-optic generates an image with a large field of view (left) while the foveal meta-optics generates an image with finer details [93]... 177

Figure 8.10. Categories of scatterer designs used to construct MTF-engineered meta-optics, showing both the target layout designs (top row) and the corresponding SEM images of the fabricated structures (bottom row) with optical proximity corrections. Hyperboloid metalens for reference only consists of square scatterers. 180
Figure 8.11. Fabricated MTF-engineered meta-optics and hyperboloid metalenses with 1-cm diameters. (Left) 12 meta-optics fabricated on a 4-inch wafer. (Right) Optical image around the center of a complex MTF-engineered meta-optic. 182
Figure 8.12. SEM images of "simple" MTF-engineered meta-optics fabricated solely with square-based scatterers viewed from the top (left) and at an oblique angle (right). 182
Figure 8.13. SEM images of "complex" MTF-engineered meta-optics fabricated with multiple scatterer designs, viewed from the top (left) and at an oblique angle (right). 183
Figure 8.14. Fabricated MTF-engineered meta-optics and hyperboloid metalenses with 2-cm diameters. (Left) 7 meta-optics on a 4-inch wafer. (Right) Zoomed-in SEM image near the center of a complex MTF-engineered meta-optics. 184
Figure 8.15. Deconvoluted infrared images from black-painted metal stencils set before a hotplate, captured via a hyperboloid metalens (left column), a "simple" MTF-engineered meta-optic (middle column), and a "complex" MTF-engineered meta-optic. (Image credits to Anna Wirth-Singh and Saswata Mukherjee) 185
Figure 8.16. Deconvoluted infrared images of "in the wild" scenes, captured via a commercial refractive lens, a hyperboloid metalens, a "simple" MTF-engineered meta-optic, and a "complex" MTF-engineered meta-optic. The top row captures a grey car parking under the sun, and the bottom row captures me sitting against the glass doors of an air-conditioned library. (Image post-processed by Anna Wirth-Singh) 187
Figure 8.17. Fabrication process flow of double-sided MTF-engineered meta-optics... 190
Figure 8.18. Photographs and SEM images of the fabricated double-sided MTF-engineered meta-optics. (Top row) Entry meta-optics. (Bottom row) Exit meta-optics. 191
Figure 9.1. Fabrication flow of the MWIR dual-helix meta-optic with stepper lithography. 194
Figure 9.2. The fabricated MWIR dual-helix meta-optic. (a) Photography of the chip carrying an MWIR dual-helix meta-optic with an aperture size of 5 mm. (b) Optical image of the meta-

optic spiral pattern near the center. (c) SEM image of the meta-optic scatterers near the center, taken at an oblique angle of 45° [94]. 195

Figure 9.3. Characterization of the dual-helix meta-optic. (d) Experimental point spread functions for various wavelengths in the 1560 nm calibration range, with the main intensity lobes indicated by red dashed circles. The rotation angle of the lobe orientation as a function of wavelength for the 1560 and 1310 nm ranges are plotted in (e) and (f), respectively [94]. 196

Figure 10.1. Fabrication flow of the visible EDOF meta-optic with laser direct-write.. 200

Figure 10.2. Phone photo of the visible EDOF meta-optics with a 1-cm diameter. 200

Figure 10.3. Optical images of the fabricated visible meta-optic with laser direct-write.201

Figure 10.4. SEM images of the fabricated meta-optic scatterers. Unexpected shell-like structures are also patterned surrounding the designed scatterer pillars. 202

Figure 10.5. Point spread function (left) and modulation transfer function (right) of the laser direct-write visible EDOF meta-optic. (Image credits to Johannes Fröch.) 203

Figure 10.6. Comparison between the ground truth (top row), imaging results with the laser direct-write meta-optic (middle row), and the imaging results from the meta-optic written with electron beam lithography (bottom row). (Credits to Johannes Fröch.) 203

LIST OF TABLES

Table 3.1. Exemplary comb drive geometries used for electrostatic simulations. 46
Table 3.2. Exemplary flexure geometries and parameters used for mechanical simulations. 56
Table 4.3. Small-aperture Alvarez metalens parameters. 66
Table 4.4. MEMS actuation platform design parameters for the small-aperture Alvarez metalens. 71
Table 5.5. Large-aperture Alvarez metalens parameters. 98
Table 5.6. Design parameters and performances of the large-aperture MEMS Alvarez meta-optic lens. 101
Table 6.7. Visible Alvarez metalens parameters. 127
Table 6.8. MEMS actuation platform design parameters for the large-aperture visible Alvarez metalens. 128
Table 7.9. Tool resolution and exposure time for a circular meta-optic with a diameter of 1 cm, using the tools available at the Washington Nanofabrication Facility........ 143
Table 8.10. LWIR meta-optic parameters for broadband thermal imaging........ 167
Table 8.11. LWIR meta-optic parameters for foveated thermal computational imaging.172
Table 8.12. LWIR meta-optic parameters for MTF-engineered meta-optics. 177
Table 8.13. LWIR meta-optic parameters for double-sided MTF-engineered meta-optics.188
Table 9.14. Design parameters for dual-helix MWIR meta-optic. 193
Table 10.15. Scatterer parameters for visible EDOF meta-optics. 198

ACKNOWLEDGEMENTS

I want to thank many people, family and friends, for accompanying and supporting me through many years of happiness and suffering in my Ph.D. life.

Thanks to my committee members, Prof. Karl F. Böhringer, Prof. Arka Majumdar, Prof. Lih Lin, and Prof. Peter Pauzauskie, who have been so kind and supportive, making the journey of graduate school so much more inspiring and delightful. Very special thanks to my faculty advisor, Prof. Böhringer, who has advised me not only on academic pursuit but also on living a life (which seems to be the harder task). He is a fantastic advisor who has given me ultimate freedom in research while always being there if I need support. He has been bearing most of my frustration and tears for all these years, but he is always so gentle and calm, with a silent promise that everything will be fine. He has played a crucial role in preserving my sanity during this crazy swirl of Ph.D. pursuit. His partner, Hoai, is a great lady with much wisdom and delight, always sending me support in many aspects. Special thanks to my co-advisor, Prof. Majumdar, who has semi-adopted me into his group and greatly expanded my academic family with many wonderful and lively siblings. Support from fellows is another critical factor in a successful Ph.D., and the siblings from the Majumdar group are always happy to lend me a hand. Prof. Majumdar himself is very enthusiastic and energetic, inspiring me to work harder and explore more. Prof. Böhringer and Prof. Majumdar have very different personalities and academic styles, but together, I believe they are the best advisor duo I could ever get.

The works I have done during my Ph.D. were supported by TunOptix Inc. and the University of Washington. Part of this work was conducted at the Washington Nanofabrication Facility (WNF) / Molecular Analysis Facility (MAF), a National Nanotechnology Coordinated Infrastructure (NNCI) site at the University of Washington, which is supported in part by funds from the National Science Foundation (awards NNCI-1542101 and NNCI-2025489), the National Institutes of Health, the Molecular Engineering & Sciences Institute, the Clean Energy Institute, the Washington Research Foundation, the M. J. Murdock Charitable Trust, Altatech, ClassOne Technology, GCE Market, Google, and SPTS.

The Washington Nanofabrication Facility (WNF) is practically my second home here, not only because of the fabrication-heavy nature of my projects but also because of all the wonderful people I have met here. There have been devices breaking, tools malfunctioning, and a fair amount of stress and frustration in the cleanroom. However, there has never been a day that I did not look forward to getting gowned up in the “bunny suit” and jumping into my work. There have been multiple occasions when my advisor has “threatened” to revoke my cleanroom access so that I can get other stuff done. Sorry about that, Prof. Böhringer. WNF is just such a great place to work, and this is a bit addictive.

Ph.D. research can be stressful, and I tend to get pushy when frustrated. However, the cleanroom staff is always patient, professional, and open to discussion. The former director, Michael Khbeis, has taken me to exhibitions to interact with other professionals in the semiconductor industry. The current director, Maria Huffman, has managed the lab with her upright attitude and welcoming personality. The former lithography engineer, Duane Irish, who I tailed a lot when I first started with the cleanroom, has taught me about furnaces, stepper lithography, direct-write lithography, and many more chemical processing knowledge. Jean

Nielsen, our current lithography engineer, has always been so kind and diligent, so helpful, and often willing to fulfill my demanding requests out of her way. Her experience and knowledge in lithography have inspired me to explore new materials and improve my fabrication process flow for so many projects. Darick Baker has taught me about plasma deposition and ellipsometry. He is a great teacher for the microfabrication courses, which I both took and assisted in teaching with him. The former engineer, Andrew Lingley, is my other teacher in the general cleanroom environment. Fred Newman has taught me about the fascinating process of atomic layer deposition. Sarice Jones has been the solid support for backend processing and general maintenance. Shane Patrick has supervised lab operations and ensured everyone performs safe research in a shared facility. Mark Brunson and Cameron Toskey have supported me in general microscopy and profilometry. Mark Morgan and Grace Tong are the awesome etching engineers in charge of many critical tools, and I might have bothered them too much. They are a joyful team working hard with creativity. The former electron beam lithography (EBL) engineer, Richard Bojko, has taught me about scanning electron microscopy (SEM) and given me a master's project on the resistance enhancement of EBL resist. The current EBL engineer, Brant Hempel, is very knowledgeable about general lithography and has given me much advice on troubleshooting. The former facilities engineer, Albert Bailey, has provided me with much valuable knowledge on the fundamentals of tools and processes. The former project manager, Jason Tauscher, has been an excellent resource for communication and connected me with the University of California-Santa Barbara cleanroom when I needed additional support for my projects. We have amazing supporting staff outside the cleanroom environment as well. Konrad Schroder gets everything internet-related in order and has helped me recover important data several times. Sharon Li, Renske Dyedov, and Makeda Beck manage the logistics outside the cleanroom so efficiently that we can all work inside

without much worry. They are lovely people to chat with when met in the corridors. I have used the Molecular Analysis Facility (MAF) for device inspection and chemical analysis. Scott Braswell from MAF has taught me about their SEM and energy-dispersive X-ray spectroscopy (EDS). He is very experienced, knowledgeable, and always ready to help.

My projects involve MEMS, microfabrication, and meta-optics, but I have been relatively new to advanced optics. Many device testing experiments have become possible because of the help of many fellows from our neighboring photonic groups, especially the Nano Optoelectronic Integrated System Engineering (NOISE) Lab led by Prof. Majumdar. All of my thesis projects collaborate with them in one way or the other. Shane Colburn has taught me a lot about meta-optics and designed the Alvarez meta-optics used in my integrated tunable lenses. He and Luocheng Huang have helped me in supporting data acquisition. David Rosser and Yueyang Chen have taught me to use their customized stage and process for device assembly. Shane Colburn, James Whitehead, Abhi Saxena, Johannes Froch, and many more have taught and helped me set up the experiment in their optics lab. Without them, none of the results would be possible. As part of my side projects, I have enjoyed working with Saswata Mukherjee and Anna Wirth-Singh, participating in outdoor imaging experiments, and being amused by how much the devices I fabricated can perform. With all of them and many others, I have learned so much more during my years here.

It is almost impossible to complete a Ph.D. on one's own, and I am grateful that so many family and friends have accomplished this incredible achievement with me.

DEDICATION

To my amazing parents, who preferred the white-collar jobs in finance or government for their daughter but have nevertheless provided me with the best science education they can offer, encouraging me to pursue a master's and eventually a doctoral degree in engineering.

And Happy Birthday, Dad!

Chapter 1. OVERVIEW

Optical systems have been the crucial components for a wide range of modern applications, from miniature tunable lenses for integrated photonic devices and biomedical instruments, to large-scale wide-angle optics for surveillance and automobile monitoring. Many such devices have highly constrained size and weight, among which the dimension and volume of the optics contribute a significant part. As potential replacements, we introduce diffractive meta-optics to miniaturize bulky freeform refractive optics with significantly reduced volume. Meta-optics are two-dimensional, quasi-periodic arrays of subwavelength scatterers designed to control the phase, amplitude, and polarization of electromagnetic waves. They can mimic the novel optical functionalities of complex geometric curvatures on a flat, lightweight, microns-thick surface, and utilize well-established semiconductor microfabrication technologies for inexpensive, high-volume production and ready integration with electronic control.

This thesis is organized into two main sections based on two distinctive application categories of meta-optics that I have worked with during my pursuit of a doctoral degree.

The first part of this thesis (Chapter 1 to Chapter 6) will present my main thesis project on the design, fabrication and experimentation of miniature tunable lenses built with Alvarez cubic surfaces, marrying the modern technologies of micro-electrical mechanical systems (MEMS) and ultrathin dielectric meta-optics. Devices for near-IR and visible operation spectrum with different aperture sizes and tuning ranges are demonstrated, with discussions of their corresponding fabrication challenges and performance.

The second part of this thesis (Chapter 7 to Chapter 10) talks about fabrication challenges involved with making large-area meta-optics for long-wavelength all the way down to visible spectra. This part spans across several side projects I have participated in and been in charge of

the process development and device fabrication, hence the contents presented in this part of thesis focuses on the challenges and solutions encountered during the fabrication of large-area meta-optics without involving conventional electro-beam lithography.

Chapter 2. INTRODUCTION TO TUNABLE METALENSES

Miniature focus-tunable lenses are essential for many modern applications involving compact optical systems, such as augmented and virtual reality, microscopy, spectroscopy, sensing, and photonic integrated circuits. In many devices and instruments, the size and weight of the optics are highly constrained, while at the same time, low energy consumption and high controllability are often preferred attributes. Such requirements have posed new challenges for conventional tuning mechanisms of refractive and reflective optics, and hence calling for novel replacements such as diffractive meta-optics with high versatility.

2.1 CONVENTIONAL DESIGNS FOR MINIATURE TUNABLE LENS

There are three general approaches to design and implement miniature tunable lenses. The conventional way to change focus is by physically moving the lens along the optical axis – Figure 2.1 gives a camera fabricated with such a mechanism [1] – but the support and actuation structures often render such systems too bulky for compact devices. The approach of liquid tunable lenses contains chambers filled with liquid optical materials, whose optical power can be tuned by modulating either the shape of the flexible chamber or the index distribution of the liquid. Figure 2.2 shows a liquid tunable lens utilizing the electrowetting behavior of a conducting liquid [2]. However, such lenses tend to suffer from instability arising from the external environment and complexity in packaging due to the presence of liquids. Liquid crystal tunable lenses modulate focus by changing the liquid crystal's orientation induced by an applied electric field. Such technology is used in the tunable zoom system shown in Figure 2.3 [3]. However, such systems often have poor imaging performance due to the use of polarizers, which reduce incident

illumination and limit resolution. Solutions to create tunable lenses at microscale with low cost, low power but high speed and high efficiency are essential.

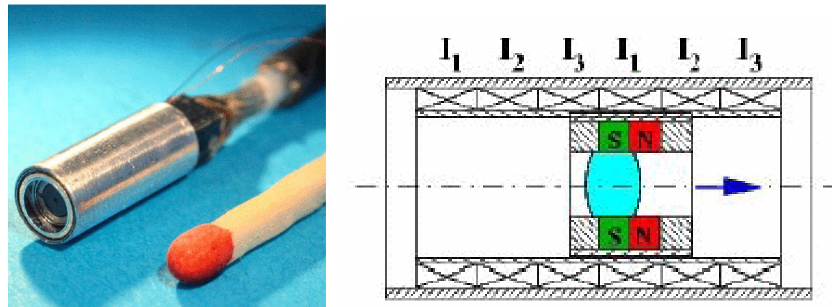

Figure 2.1. A camera module (left) for a chip-on-the-tip endoscope with optical system tunable by a traveling field linear drive (right) [1].

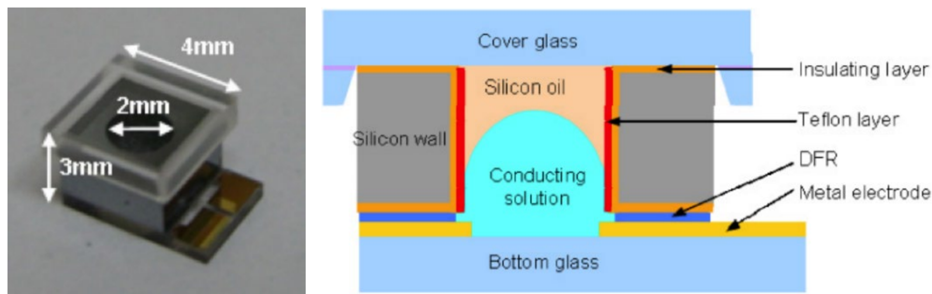

Figure 2.2. A liquid tunable lens unit (left) based on electrowetting and the schematic illustration of the interior design (right) [2].

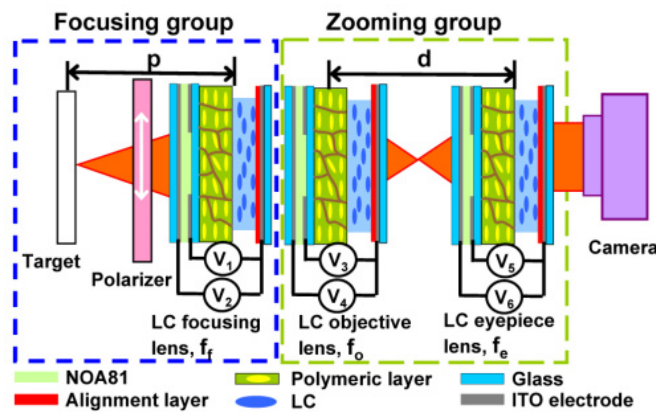

Figure 2.3. Schematic of an electrically tunable optical zoom system using three composite liquid crystal lenses [3].

2.2 ALVAREZ TUNABLE LENSES

A unique approach for creating a miniature lens system with tunable optical power is based on Alvarez lenses [4-6], a type of lens with varifocal capability, first developed by Alvarez and Lohmann independently in the 1960s. A typical Alvarez lens contains a pair of optical elements with complementary cubic surface profiles. Optical power modulation is achieved by the relative lateral displacement between the two optical elements in the direction perpendicular to the optical axis. In this way, the focal length change is inversely proportional to the lateral displacement, and the focal length can be tuned in both directions.

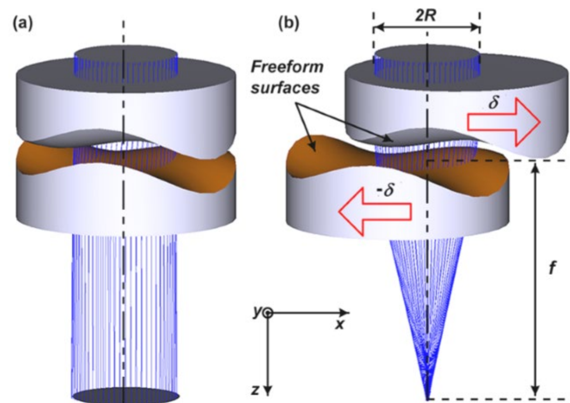

Figure 2.4. Schematic of a tunable lens designed with Alvarez principle, showing the physical arrangement (a) without and (b) with lateral displacement [7].

Previously some researchers integrated a pair of miniature, freeform optics with cubic surface profiles with a MEMS actuator to electrostatically displace the optical elements laterally for focus tuning within a compact package [8, 9]. In these works, however, the lens elements and the MEMS structure were manufactured separately and then manually assembled, requiring additional time and cost. Moreover, the conventional refractive optics used in these Alvarez systems require complex 3D geometries to produce the desired cubic surfaces for optimal performance and

mounting for assembly requirements. This often requires complicated fabrication and at the same time can be a substantial obstacle to further miniaturization.

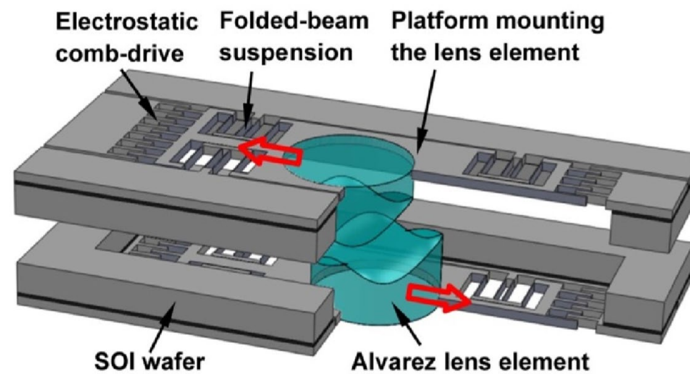

Figure 2.5. Schematic showing a MEMS-driven tunable Alvarez lens [8].

2.3 MICRO-ELECTRO-MECHANICAL SYSTEMS (MEMS)

The MEMS family covers a very large variety of micromachines and microsystems, which convert one form of energy into another by interacting with the surroundings, such as electrical-to-thermal and mechanical-to-electrical. Often, the devices converting a physical input to a signal output for measurement are called sensors, while the device creating a physical effect in response to a signal input are named actuators. Together, they can be described as transducers.

The MEMS devices are widely used for sensing, actuation, computation, and communication. The family of MEMS started blooming following the integrated circuits (IC) industry and has been expanding quickly with the recent technological development in related fields. MEMS devices can be further categorized into many subgroups based on the operational principle and resultant functionalities, such as optical, acoustic, magnetic, thermal, chemical, biological, and microfluidic systems. With their small size, compact designs, and efficient operation, MEMS are popular components for many fields, such as AR/VR headsets, automobiles, fiber-optic communications, environmental monitoring, and biomedical devices. Figure 2.6 shows the scanning electron

microscopic (SEM) images of several MEMS devices for sensing and actuation applications in a wide range of fields.

The manufacturing of MEMS devices utilizes the well-developed semiconductor nanofabrication of the IC industry, which enables mass production with low marginal cost and high integration compatibility with other electronic systems.

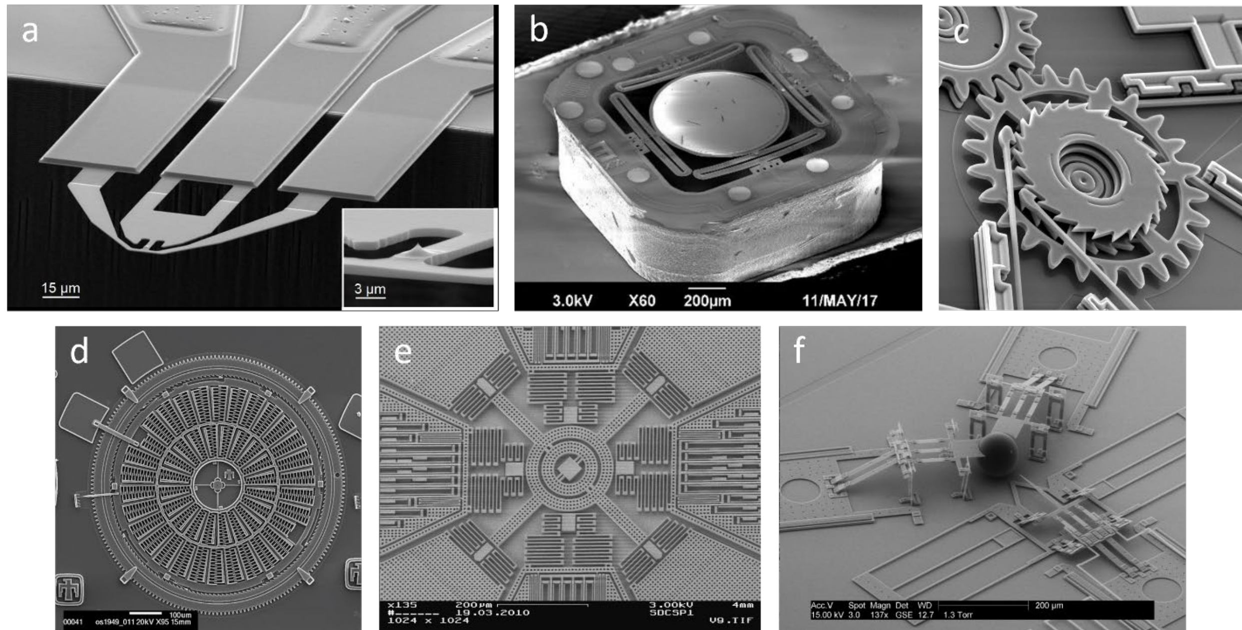

Figure 2.6. Example of MEMS structures for precision displacement for both translational and rotational movement, including (a) a cantilever scanning tip for atomic force microscope (AFM) [10], (b) a MEMS scanning mirror [11], (c, d) microscale ratcheting gears [12, 13], (e) a 3-axis gyroscope [14], and (f) a self-reconfiguring metamorphic nanoinjector [15].

2.4 MEMS FOR PRECISION DISPLACEMENT

Many sensor and actuator microsystems with precision displacement require a high level of control. The proper operation of the devices is greatly dependent on the predictable and reproducible behaviors enabled by carefully designed mechanics. To achieve such qualities, engineers often need to devise mechanical structures which are exactly constrained, free of

backlash, lightweight, and with a high stiffness ratio between the restricted and desirable movement directions [16].

Many precision displacement systems are designed with electrostatic comb drives and various kinds of folded flexures to generate an efficient mechanical motion with high controllability and reproducibility. As two examples, Figure 2.7 and Figure 2.8 show the exact constrained folded flexure and Watt's flexures in operation.

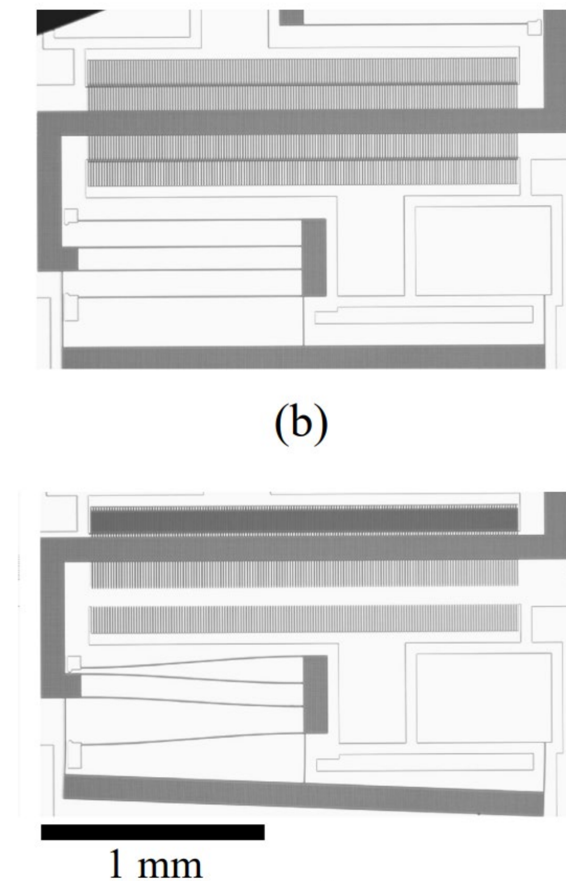

Figure 2.7. Microscope pictures of the exact constraint folded flexure when (top) undeflected and (bottom) deflected by 100 μm [17].

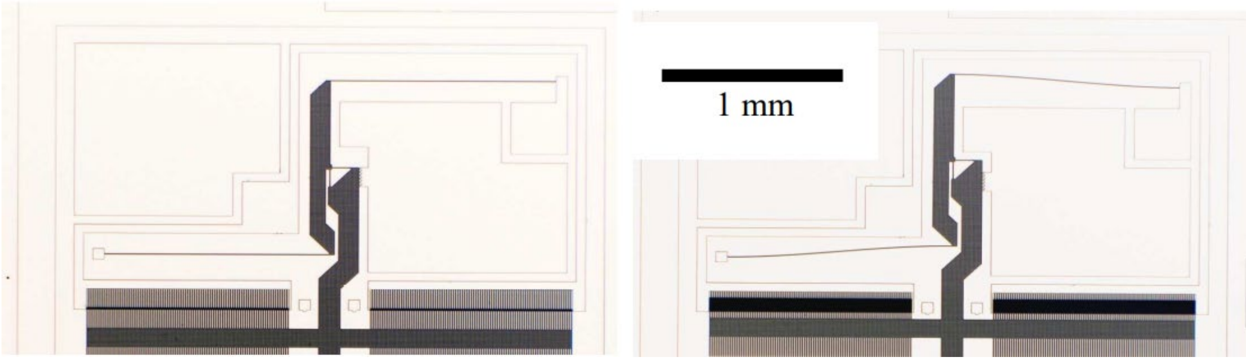

Figure 2.8. Microscope pictures of the Watt's flexure when (left) undeflected and (right) deflected by 100 μm [17].

2.5 META-OPTICS

As potential replacements for bulky freeform optics, meta-optics are two-dimensional, quasi-periodic arrays of subwavelength scatterers designed to arbitrarily control electromagnetic waves' phase, amplitude, and polarization [18] by imparting an abrupt, spatially varying phase profile on the incident light [19]. With meta-optics, complex and bulky geometric lens curvatures can be converted into a discretized spatial phase profile on a flat, wavelength-scale thin surface [20-24]. They present great potential to miniaturize bulky freeform optics with significantly reduced volume. Meta-optics can utilize well-established semiconductor microfabrication technologies for inexpensive, high-volume production and ready integration with electronic control. Their ability to produce the novel functionalities of freeform optics on a planar platform [25] has motivated the designs of meta-optical elements with a wide range of functionalities such as lenses [26-32], reflectors [33-35], vortex beam generators [36-39], holographic masks [40-42], blazed gratings [43, 44] and polarization optics [45, 46].

Figure 2.9 shows a typical meta-optic fabricated with silicon nitride scatterers on a fused silica substrate. The surface phase profile is constructed with a square-lattice array of cylindrical nanoposts with the same height but varying diameters.

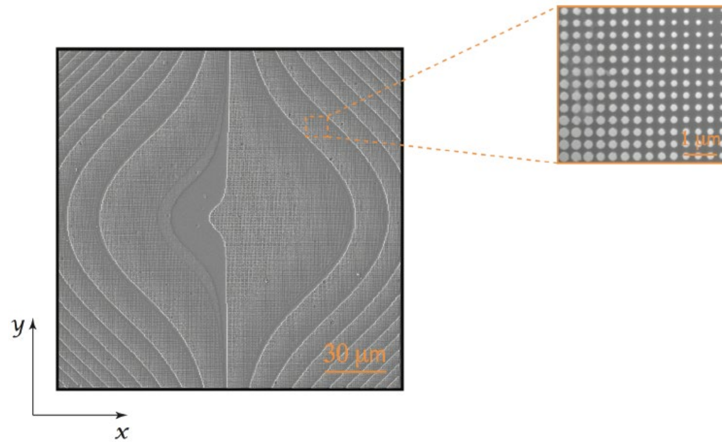

Figure 2.9. Scanning electron micrograph of a fabricated meta-optic with a zoom-in view showing the gradient in pillar size [47].

2.6 TUNABLE META-OPTICS

Recent advances in the design and fabrication of meta-optics have facilitated the active control and manipulation of light with tunable meta-optics. The application of external stimuli, including electrical [48], mechanical [49, 50], thermal [51], optical [52], and magnetic [53] control, can dynamically alter the structure and characteristics of the meta-optics and modulate their interaction with electromagnetic waves.

There have been multiple works attempting to modulate the optical power of meta-optics with various mechanisms. As illustrated in Figure 2.10, Ee et al. designed and fabricated a mechanically reconfigurable meta-optic on a stretchable membrane for the visible frequency range, with the deformation induced by four clamps individually mounted on translation stages [49]. The design by She et al. in Figure 2.11 combined meta-optics with a dielectric elastomer actuator to create an electrically tunable focal length by electrostatically compressing the elastomer in the direction of

its thickness leading to a lateral expansion in both the elastomer and the carried meta-optic; however, due to the limitations in the elastomer viscoelasticity, charge transfer, and dissipation time in electrodes, the response time of their design is capped at 33 ms [54]. Roy et al. designed a microscale tunable mirror by placing a reflective meta-optic lens on top of a 2D electrically actuated scanner platform [55], as shown in Figure 2.12. The angular rotation of the mirror plate scans the focal position of the meta-optic lens by several degrees in a three-dimensional space. The manual assembly required to integrate the individual micro-mirror and the external MEMS platform inevitably increases the overall fabrication time, rendering the device less desirable for mass production. Arbabi et al. fabricated and demonstrated a tunable meta-optic doublet lens realized by vertical MEMS actuation, as shown in Figure 2.13. Their system comprised both converging and diverging meta-optic lenses assembled on top of each other, giving a tunable focal distance controlled by the separation electrostatically varied between the two lenses [56]. While this method can provide a change in focal length inversely proportional to the vertical displacement, the fabrication entails an initial separation between lenses to reserve space for the designed actuation, which limits the overall tuning range if a thin device is desired. Additionally, the parallel plate actuator in their design can only increase the focal length from the initial value by decreasing the optics separation rather than tuning in both directions.

Owing to their exceptional capabilities in precise actuation and sensing within a confined space, there has been a rising interest in incorporating MEMS techniques to induce structural reconfiguration of the meta-optics and tune their optical properties in real-time. Such MEMS-actuated reconfigurations can either change the geometry and pitch of the scatterers in meta-optics by mechanical deformation [57, 58] or adjust the relative positions of the whole meta-optic in a composite unit to modulate the overall optical properties [55, 59, 60]. Despite significant progress,

the extent of the focal length modulation in a low-power MEMS-tunable metalens remains small (< 100 μm) when applying low to moderate tuning voltages. The main challenge to increase the tuning range while maintaining sufficient numerical aperture comes from the need to mechanically displace a large aperture meta-optic by a substantial amount, which makes the design and fabrication of MEMS structures difficult.

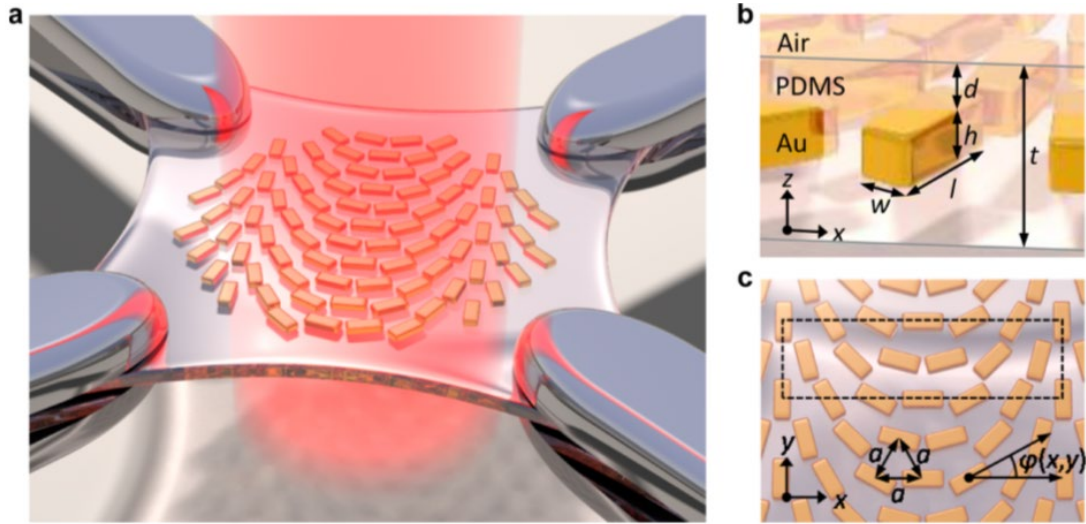

Figure 2.10. Tunable meta-optic fabricated with gold scatterers on a stretchable polydimethylsiloxane (PDMS) substrate [61].

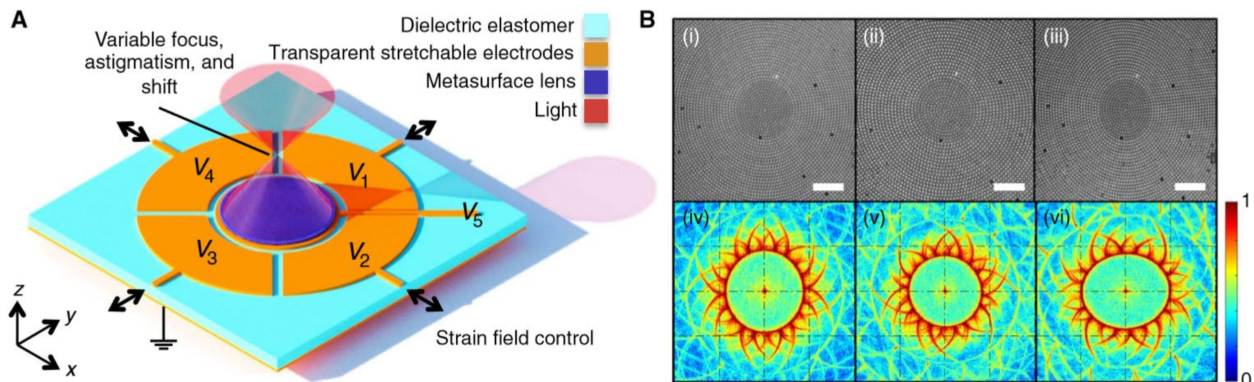

Figure 2.11. An illustration of the dielectric elastomer actuator (DEA) metalens design. (A) A schematic of the device combining a metalens and a DEA with five addressable electrodes for electrical tuning the strain field of the meta-optic. (B) Optical microscope images (20 μm scale bar) of the metalens at (i) 0 V, (ii) 2.5 kV applied at the center electrode and (iii) 2.75 kV applied at V1 and V3. (iv) to (vi) shows the corresponding 2D Fourier transforms [54].

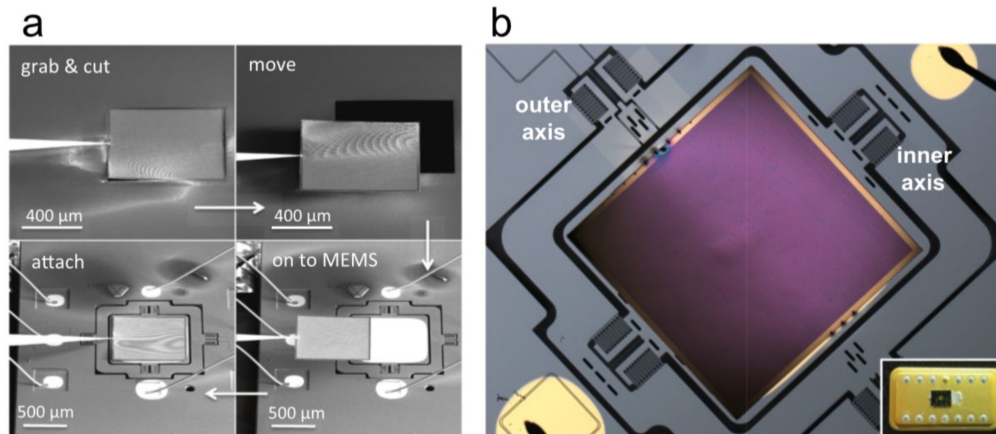

Figure 2.12. Meta-optic scanning mirror on a MEMS platform. (a) Integration of the reflective meta-optic lens onto the 2D MEMS platform. (b) Optical microscope image of a MEMS scanner with a meta-optic mirror integrated [62].

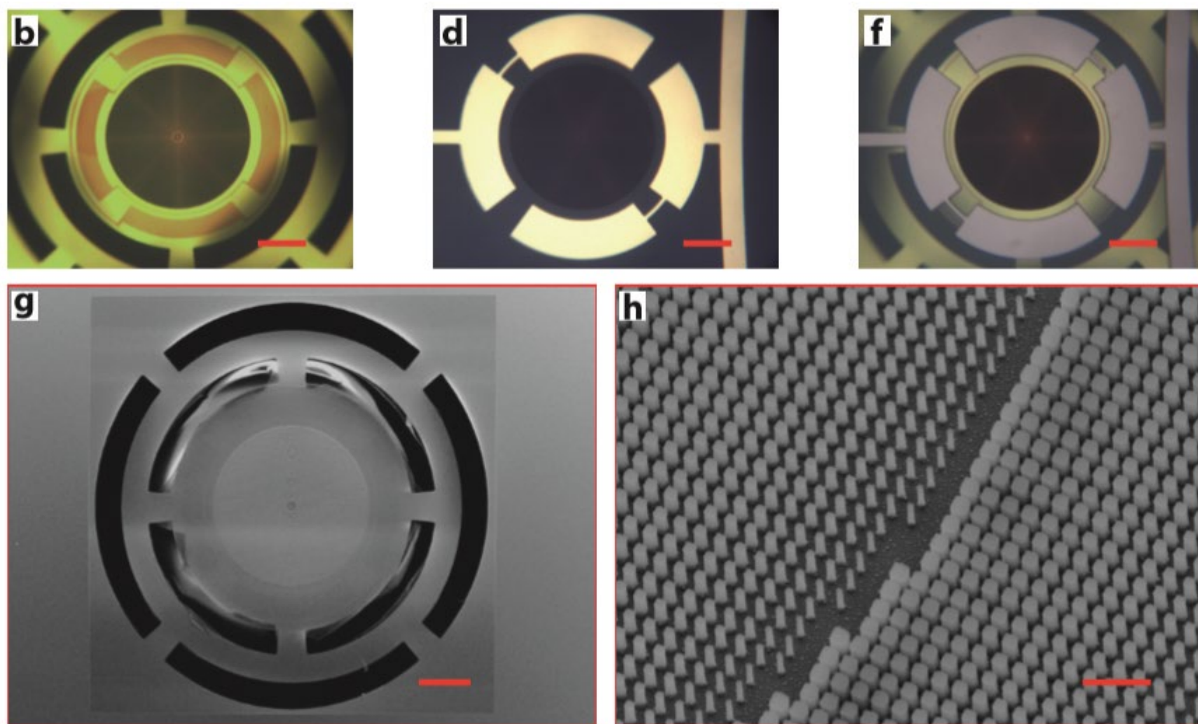

Figure 2.13. Tunable meta-optic doublet. (b) An optical microscope image of a fabricated lens on a membrane. (c) Simplified fabrication process of the lens on the glass substrate. (d) An optical microscope image of the fabricated lens on the glass substrate. (e) Schematics of the bonding process. (f) A microscope image of the final device. (g) Scanning electron micrograph of the lens on the membrane, and (h) nano-posts that form the lens. Scale bars are 100 µm in b, d, f, and g, and 1 µm in h [56].

Chapter 3. DESIGN PRINCIPLES OF MEMS-INTEGRATED ALVAREZ METALENSES

A possible solution to create a miniature, focus-tunable optical system compatible with large-scale microfabrication is to convert the 3D Alvarez optical elements into a pair of 2D meta-optics with complementary cubic surface profiles, which can be integrated with a micro-scale MEMS-actuated structure to introduce lateral displacement for optical modulation. Meta-optic Alvarez lenses have shown great potential for substantial focal length control with small relative lateral shifts. Recent works have demonstrated an Alvarez metalens inducing 2.5 mm focal tuning range in visible wavelengths over a 100 μm actuation range with a 150 μm wide square aperture [25] and another inducing a 6.62 cm focal tuning range in the infrared (IR) spectrum over a 2.75 mm actuation range with a 1 cm wide square aperture [63]. Currently, however, the displacement has been performed using optomechanical stages actuated manually, while a compact and electrically controllable solution has not been demonstrated.

We propose a family of miniature tunable lenses integrating Alvarez meta-optics and MEMS tuning platforms. The design of MEMS-integrated Alvarez meta-optics involves two main parts. First, we map the two complementary cubic surfaces onto the quasi-periodic arrays of flat meta-optics. Second, we design electrostatic actuators to induce the required lateral displacement to modulate the optical power of the assembled Alvarez lens.

3.1 Alvarez Meta-optic System

We map the two complementary Alvarez cubic phase profiles with diffractive meta-optics to realize the Alvarez tuning system with greatly reduced volume and improved compatibility with MEMS integration. Just like in the conventional system, when the two complementary Alvarez

meta-optics are placed in a stack and displaced laterally relative to each other as illustrated in Figure 3.1 [64], the summed phase profile of the overlapping meta-optics will vary corresponding to the change in the overlapped area of the two surfaces, producing a lens with different focusing power as demonstrated in Figure 3.2, hence producing the Alvarez tunable lens system.

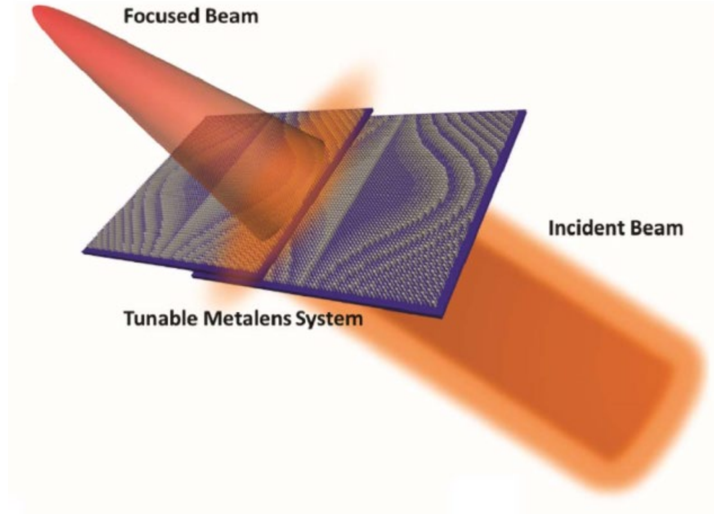

Figure 3.1. A conceptual illustration of an Alvarez meta-optic lens system [64].

3.1.1 *Alvarez Cubic Surfaces*

The design of an Alvarez varifocal lens system starts with defining the pair of complementary cubic surface profiles for the designed operating wavelength (1550 nm for mid-IR operation in Chapter 4 and 5, 623 nm for visible operation in Chapter 6). The regular and inverse cubic surfaces have the phase distributions

$$\varphi_{reg}(x, y) = -\varphi_{inv}(x, y) = A\left(\frac{1}{3}x^3 + xy^2\right) \qquad (3.1)$$

where (x, y) represents the in-plane coordinates. The constant A denotes the cubic phase strength determining the rate of phase variation with the units of inverse cubic length [25, 63]. The value of A is chosen based on the desirable aperture size and focal length range.

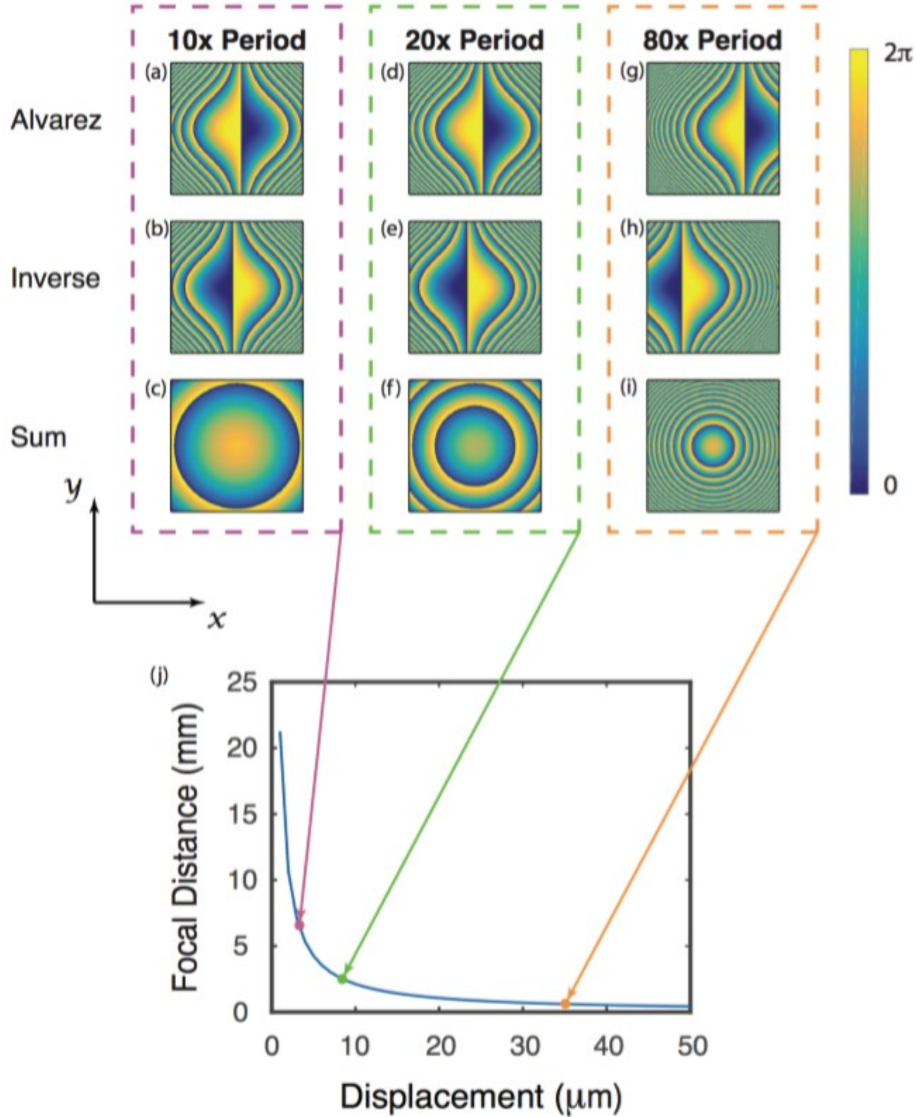

Figure 3.2. An illustration of how the change in overlapping pattern affects the resultant focusing power in a meta-optic Alvarez lens system [47].

As illustrated in Figure 3.2, when overlapped with a nonzero center-to-center offset, the two cubic surfaces in conjunction impart a quadratic total phase profile on an incident wavefront, with the form

$$\varphi_{Alvarez}(x,y) = \varphi_{reg}(x+d,y) + \varphi_{inv}(x-d,y) = 2Ad(x^2+y^2) + \frac{2}{3}Ad^3 \qquad (3.2)$$

whose focal length is tunable by laterally displacing the two surfaces in the opposite direction by an offset of d each (giving a total center-to-center offset of $2d$). With the constant d^3 term being

inconsequential, the quadratic term of the total Alvarez phase profile can be related to that of a standard quadratic lens, giving the reciprocal relation between the tunable focal length f and symmetric lateral displacement d as

$$f(d) = \frac{\pi}{2\lambda A d} \quad (3.3)$$

We note that, with the analytical expression of the Alvarez lens, we can readily scale the lens design to any arbitrary aperture and focus-tuning range by adjusting the parameters.

3.1.2 *Alvarez Meta-optic Discretization*

Once the complementary surface profile distributions are determined, we need to convert them into discretized arrays of physical scattering elements with finite dimensions.

We chose cylindrical nanoposts fabricated using silicon nitride scattering elements on a chosen substrate (silicon for near-IR operation in Chapter 4 and 5, silicon dioxide for visible operation in Chapter 6). Silicon nitride is a common material for semiconductor fabrication with high CMOS compatibility and low absorption losses in both near-IR and visible spectrum [65]. Figure 3.3 shows an exemplary schematic of such a silicon nitride nanoposts array with varying post diameters to map the desirable Alvarez surface profiles.

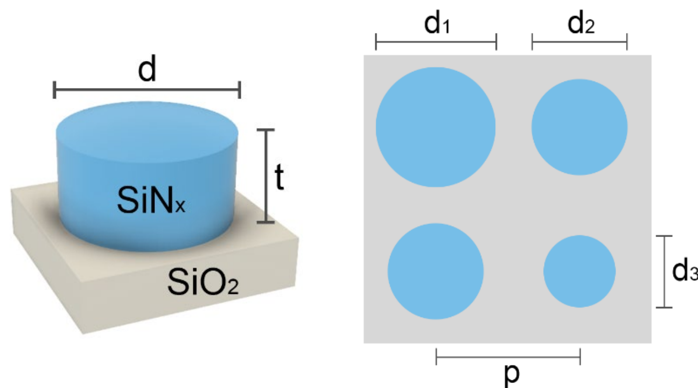

Figure 3.3. Schematic of exemplary scattering elements. (Left) A cylindrical silicon nitride nanopost on a silicon dioxide substrate. (Right) A square array of nanoposts with varying diameters (top view).

Via rigorous coupled-wave analysis (RCWA) [66], the transmission coefficients and phase shifts of the nanoposts for a fixed lattice constant and a chosen post height for specific operation scenarios (see Chapter 4-6 for details) are simulated as a function of the grating duty cycle, defined as the ratio between the post diameter and pitch. The calculated phases span from 0 to 2π while maintaining near-unity transmission amplitudes. Figure 3.4 is an example of such simulated transmission coefficients involving silicon nitride nanoposts on a silicon substrate. The phase profile is then quantized into a fixed number of linear steps of duty cycle, giving the corresponding discretized sub-wavelength cylindrical post diameters. Such dimensions are achievable with high-throughput stepper lithography [63], and we map them to the square array to construct the cubic phase profiles on the Alvarez meta-optics. The full list of selected duty cycles and the corresponding nanopost diameters are listed in the parameter tables in Chapter 4-6 corresponding to each project. We introduce an initial center-to-center offset between two meta-optics to ensure a finite focal length at the neutral state without any voltage bias. The focal length is then further tuned by introducing an additional displacement to this built-in offset via MEMS actuation.

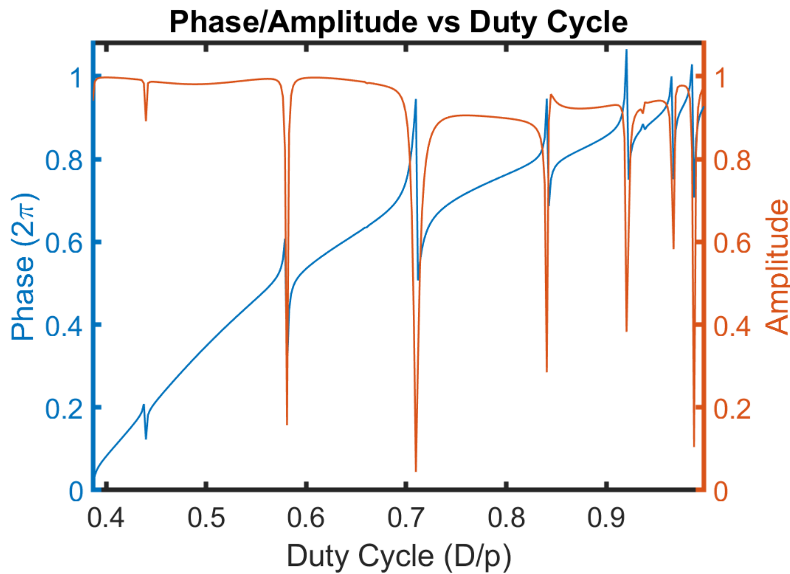

Figure 3.4. An example of simulated transmission coefficients as a function of the duty cycle for the silicon nitride nanoposts on a silicon substrate.

3.2 MEMS Tuning Platform

A conventional Alvarez lens utilizes the symmetric displacement of the two complementary cubic phase optics in opposite directions to modulate the center-to-center offset for focal tuning. Here in our adapted configuration, to enhance the robustness in prototype fabrication and device operation, we chose to alter the conventional mechanism to actively displace only one meta-optic relative to its static complement, producing a net change in the center-to-center offset between the two cubic surfaces. As a side effect, a lateral shift of the optical axis, albeit a small one, is also induced during focal length modulation.

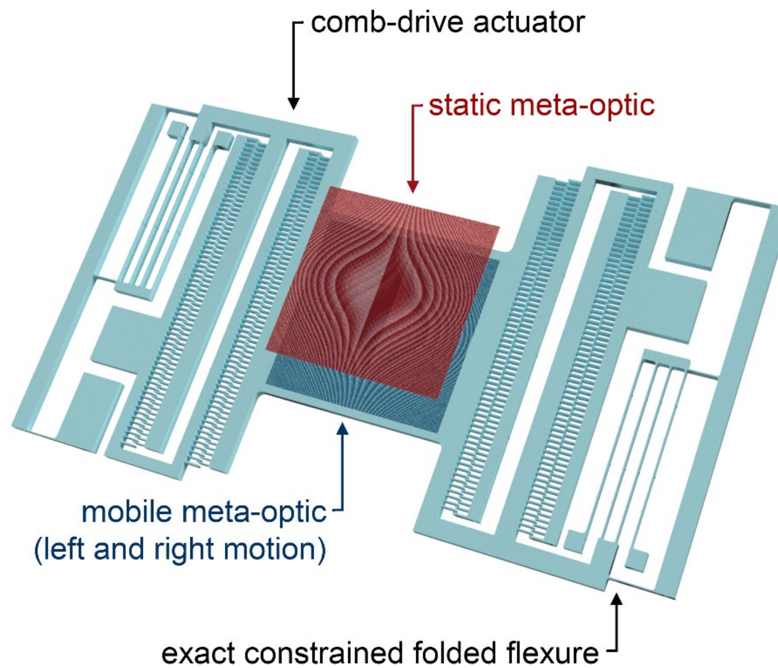

Figure 3.5. Illustration of an example MEMS-actuated Alvarez metalens system.

A miniature MEMS electrostatic actuator has been implemented to laterally displace one of the complementary Alvarez meta-optics relative to the other with high precision and speed as shown in Figure 3.5. The actuator design for the moving meta-optic is based on conventional linear comb drives [67] and exact constraint folded flexures [17] to introduce the electrostatic driving force and to generate the mechanical restoring force, respectively. The meta-optic sits on a central

platform with comb drives on opposite sides to control the displacement in both positive and negative directions along the actuation axis. The symmetric design enhances the mechanical stability and doubles the range of actuation without doubling the maximum voltage required.

3.2.1 *Comb Drives for Electrostatic Actuation*

Electrostatic comb drives can induce efficient, controllable displacement at low power with their high voltage-force conversion efficiencies realized by increased edge coupling length with the interdigitated fingers [67]. Hence, they are often popular candidates for microscale devices designed for sensing and micropositioning. In our Alvarez metalenses, we employ comb-drive actuators to electrostatically control the lateral displacement of the mobile meta-optic for optical power modulation.

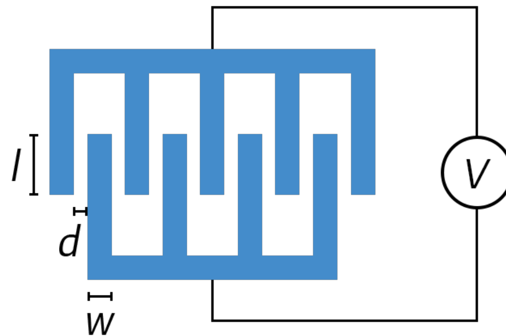

Figure 3.6. A simplified illustration of a voltage-controlled comb-drive system.

As illustrated in Figure 3.6, the typical design of a comb drive actuator consists of two comb structures with interdigitated fingers, of which one is fixed while the other is connected to a compliant suspension. A voltage applied across the two comb structures will lead to a deflection of the movable comb drawn by the electrostatic forces created in the capacitors between the fingers with different potentials.

Since the electrostatic forces are created by capacitive interactions without any physical contact between the two combs, there is no DC current flowing in the device, realizing low power

actuation. The design of using an array of small fingers instead of one single large parallel plate capacitor significantly increases the area for capacitive interaction and hence the resultant electrostatic force with a given applied voltage.

Moreover, the linear comb design allows controlled motion over a larger displacement range compared to the parallel plate capacitor. The substrate and the mobile comb are usually grounded to prevent the development of electrostatic pull-down forces acting on structures in suspension, and only the stationary comb is at a non-zero potential to generate an electrostatic driving force between the combs.

3.2.1.1 Electrostatic Driving Force

When the mobile comb displacement due to the electrostatic forces is relatively small and the separation between the backbone of one comb to the fingertips of the other comb remains relatively large, the electrostatic forces arise predominantly from the parallel plate capacitors formed between the interdigitated fingers. With the assumption that the fringing field effect is negligible, the total capacitance between the interdigitated fingers in each comb drive can be estimated as

$$C_{total} = 2N\frac{\varepsilon l h}{d_{sep}} \tag{3.4}$$

where N is the number of finger pairs, ε is the permittivity of the medium (air in this case) between the fingers which have interdigitating length l, height h, and separation d_{sep}. With a voltage V applied across the comb drive, the corresponding electrostatic force driving the lateral motion is quadratically dependent on the applied voltage as

$$F_{el}(V) = \frac{dW(V)}{dl} = \frac{d}{dl}\left(\frac{1}{2}C_{total}V^2\right) = \frac{N\varepsilon h V^2}{d_{sep}} \tag{3.5}$$

Given the movable comb, carrying the meta-optic platform, is connected to some mechanical flexure with a spring constant k_{sp}, then at equilibrium, the lateral displacement of the movable comb is

$$x(V) = \frac{F_{el}(V)}{k_{sp}} = \frac{N\varepsilon h V^2}{k_{sp} d_{sep}} \tag{3.6}$$

Note that the actuated displacement is linearly proportional to the electrostatic force, making comb drives better candidates for large displacements than parallel plate capacitors. Since the physical dimensions and material properties do not change after fabrication, with proper device calibration, the exact actuated displacement can be predicted by Eq. (3.6) at any given actuation voltage. Such controllability makes comb-drive actuators very attractive structures for applications involving micropositioning.

3.2.1.2 Electrostatic Simulation Setup

To understand the generic electrostatic behaviors of our MEMS actuator, we utilize COMSOL Multiphysics® Electrostatics finite element analysis to investigate the electrical characteristics of the comb drive elements with a set of exemplary geometries as listed in Table 3.1. The exact values of the actual device presented in Chapters 4-6 are influenced by both the detailed design requirements and actual fabrication accuracy.

The simulation of individual comb drive fingers is performed using periodic boundary condition. This method has significantly reduced the computational requirements while sacrificing little simulation accuracy, as fingers near the ends of the comb arrays only have a small contribution to the entire comb arrays of 250 fingers or more. In the simulation setup, the fingers are assumed to be perfectly rigid and aligned exactly in between opposing fingers. Fillets are used to approximate the fabricated geometries using the proposed techniques. The doped silicon

actuator layer is assumed to be a perfect electrical conductor. This is done by assigning all faces of each finger to their respective terminal boundary condition while excluding the domain volume from the simulation.

Table 3.1. Exemplary comb drive geometries used for electrostatic simulations.

Finger width (in-plane)	2 μm
Finger thickness (out-of-plane)	5 μm
Finger length (in-plane)	15 μm
Finger pitch	8 μm
Finger gap (axis of motion)	displacement + 10 μm
Applied voltage	20 V

3.2.1.3 Electric Potential Profile Simulation

Figure 3.7 shows the electric potential around a single unit of electrostatic comb drive finger set. The right (red) side consists of a movable finger with an applied voltage of 20 V. The left (blue) side consists of the side surfaces of two stationary grounded fingers. As shown in the figure, most of the electric potential variation occurs close to the tip of the finger as well as between the side surfaces of the interleaved fingers at different potentials, which creates the electrostatic force for actuation.

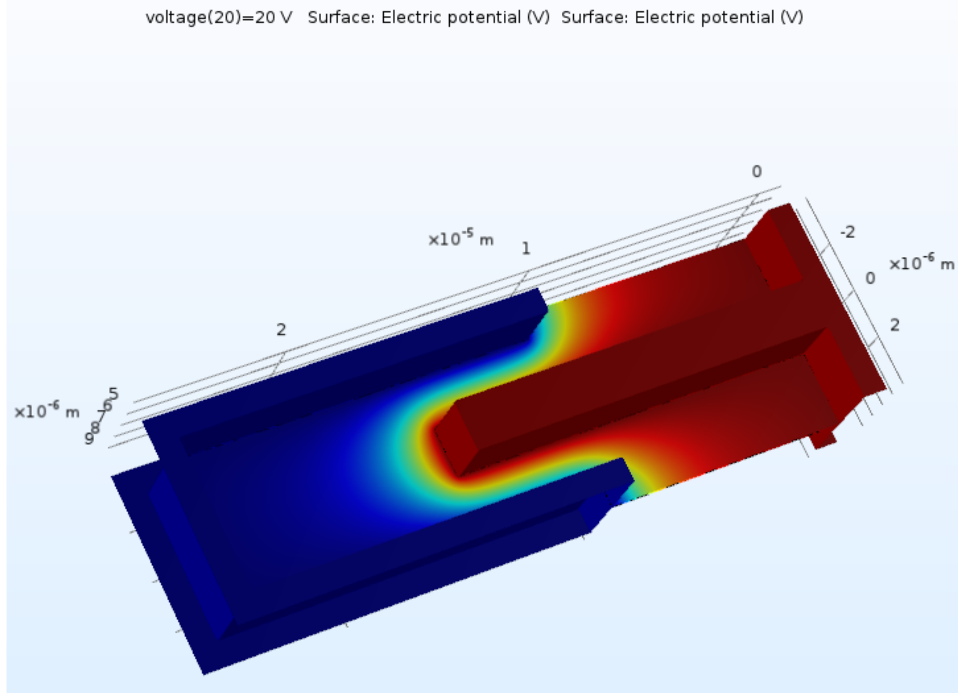

Figure 3.7. Plot of electric potential inside a comb drive finger unit cell under a bias.

3.2.1.4 Electrostatic Force versus Voltage Simulation

For a fixed geometry and displacement – here the displacement is assumed to be small to intermediate so that the effect of the tip-to-backbone capacitors are negligible – the voltage across the comb drive is swept to study the electrostatic force response of a single finger unit (as shown in Figure 3.7) to the applied voltage. The result, as illustrated in Figure 3.8, shows a quadratic dependence of the generated electrostatic force on the voltage applied across the combs, which aligns with the expectation expressed by Eq. (3.5).

Note that the simulation shows that the electrostatic force created by one comb finger unit at 20 V is approximately 11 nN, then with 125 units in one comb drive, the total force created (assuming negligible effect of fringing fields) will be 1.38 μN, which is very similar to the analytically calculated value 1.33 μN based on Eq. (3.5).

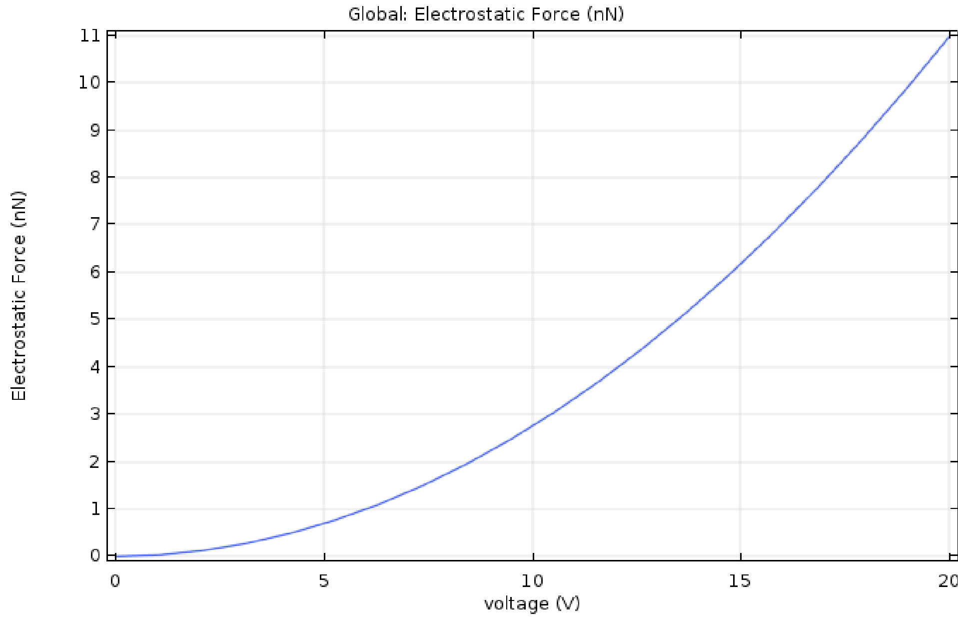

Figure 3.8. Plot of electrostatic force versus the applied voltage for a single comb finger, showing a quadratic dependence.

3.2.1.5 Electrostatic Force versus Displacement Simulation

In order to understand how the electrostatic forces are generated in one comb affected by the finger displacement, a comb finger unit as plotted in Figure 3.7 is swept with range of 14 µm displacement between the opposite combs (from 4 µm further part to 10 µm towards each other), with positive values indicating the two combs are drawing closer to each other relative to the neutral position (10 µm displacement is when the two combs are in direct physical contact).

Eq. (3.4) shows that the capacitance value increases inversely to the parallel plate separation d_{sep}, which for the tip-to-backbone capacitors is the gap between the tip of a comb and the backbone of the other. Whenever there is an electrostatic force deforming the physical structures of the actuator, the structures will always produce a mechanical restoring spring force as the response trying to balance the electrostatic force. The physical structure of the actuator can be considered with a spring constant k_{sp}, which is discussed further in Section 3.2.2. By Hooke's

law, the restoring force has a linear dependence on the displacement or deformation x, with the spring constant as the constant coefficient:

$$F_s = k_{sp}x \tag{3.7}$$

As shown in the left and middle cases of Figure 3.9, at small to intermediate values of displacement (with relatively large tip-to-backbone separation between the combs), the simulation results agree with the simple approximation of Eq. (3.5) that the electrostatic forces generated between the fingers are nearly independent of the change in relative displacement. In this range, the generated electrostatic forces can be balanced by the restoring forces imparted by the physical structures and the comb-drive actuators can operate under equilibrium.

However, at large inward displacements above 7 μm (small tip-to-backbone separations below 3 μm), the values of tip-to-backbone capacitance increases rapidly according to Eq. (3.4) because of the inverse relationship between the capacitance and tip-to-backbone gap. As a result, the electrostatic forces generated between the tip-to-backbone region quickly dominates over the electrostatic forces generated by the two sideway capacitors with a more than linear increasing rate, as illustrated by the right case of Figure 3.9.

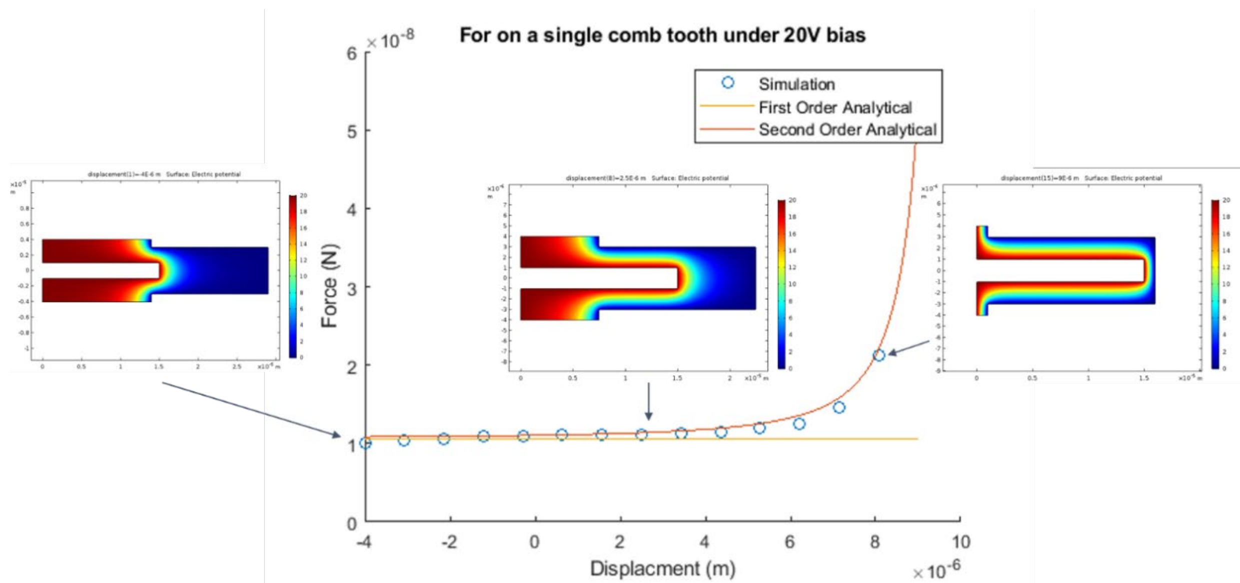

Figure 3.9. Force for a single comb finger at 20 V as a function of displacement from equilibrium at 0 V. A clear deviation from first order analysis is evident as the fingers draw closer to each other. The inserts show electric potentials in the medium of a unit comb finger cell. Picture credits to James Whitehead from the NOISE Lab.

3.2.1.6 Electrostatic Pull-in Failure

As discussed in the precious section, at large tip-to-backbone separation (small inward displacement), the electrostatic forces are relatively independent of the displacement value. However, at small tip-to-backbone separation (large inward displacement), the tip-to-backbone capacitances increase quickly with an inverse relation to the separation value and quickly dominates the source of electrostatic forces.

Meanwhile, the mechanical restoring force generated only increases linearly as a response to the displacement. Therefore, at larger displacement values with non-linear electrostatic force increase, the pull-in force generated in the comb drive will quickly surpass the restoring spring force of the mechanical structures, leading to a sudden snap-in of the combs and hence device failure. This possibility must be carefully investigated when designing a comb drive for any chosen

range of actuation, to ensure stable device operation in which the restoring force of the deformed structures are always sufficient to balance the electrostatic forces generated.

For example, in the simulated case, with an initial separation of 10 µm between the stationary and movable combs at neutral position, the maximum stable inward actuation range for each electrostatic comb drive is approximately 7 µm – beyond which the restoring spring force in the deformed mechanical structures will be no longer able to balance the electrostatic force and the two comb finger arrays will snap into each other immediately.

Figure 3.10 shows a zoom-in microscope image of a fabricated comb drive under a snap-in situation. The comb drive experienced an unstable lateral displacement towards left, in which the comb arrays were so close that the restoring spring force in the mechanical structure could no longer balance the increasing electrostatic force between the tips of one comb finger array to the backbone of the other finger array, and they immediately snapped into each other laterally and remain in contact even when the potential difference applied between them was removed.

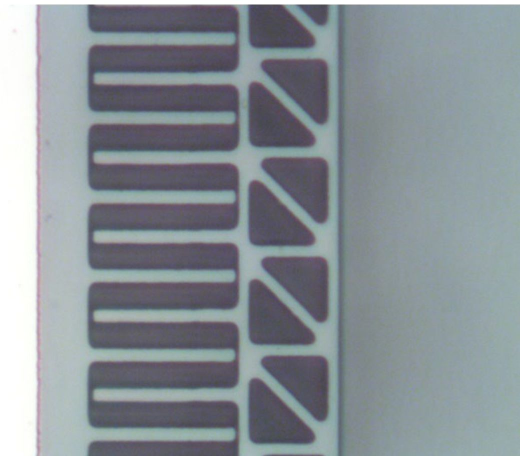

Figure 3.10. Microscope image of a snap-in situation occurred in one electrostatic comb drive of a fabricated device.

Therefore, in the actual device, the separation between the interleaved fingers should always be designed with enough space for stable electrostatic actuation of the target range of motion,

during which the electrostatic force will never exceed the restoring spring force generated by the actuated displacement or deformation of the mechanical structure, and the displaced comb can always be restored to the neutral position by spring force once the applied voltage is removed. Otherwise, additional mechanical stoppers can also be introduced in the flexure design to limit the travel range of the combs and hence prevent them from snapping into each other under high voltage.

3.2.2 *Mechanical Folded Flexure for Controlled Displacement*

For unidirectional actuation, a suspension platform, which is mechanically compliant along the direction of the desired movement while stiff in any other orthogonal directions, is required to allow the intended actuated motion while minimizing misalignment due to other random motions.

3.2.2.1 Folded Flexure

In the case of electrostatic actuation with comb drives, any motion or rotation in undesired directions are even more catastrophic as once the comb drive fingers are disturbed sideways or rotationally out of their stable modes of operation, they will readily snap into each other due to unbalanced electrostatic force. To reduce the development of extensional sideway forces at large displacements, a folded flexure design (Figure 3.11) developed by Legtenberg et al. [68] has been implemented as the foundation of the mechanical compliant structures.

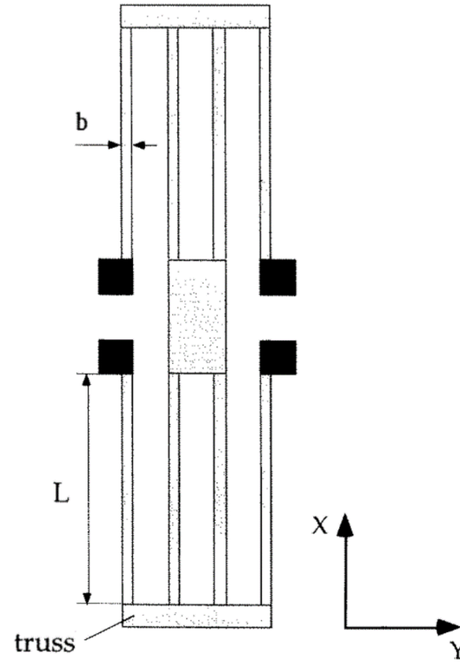

Figure 3.11. A sketch of the folded flexure design, which is compliant for the desirable motion along the y-axis and stiff for the undesirable sideway disturbance along x-axis. A load is applied at center. Anchors are indicated by the solid boxes [68].

For a folded flexure structure with Young's modulus E, length L, width b and thickness h, assuming rigid trusses, the spring constants in the axial/sideways (k_x) and lateral (k_y) directions can be calculated as [69]

$$k_x = \frac{2Ebh}{L} \tag{3.8}$$

$$k_y = \frac{2Ebh^3}{L^3} \tag{3.9}$$

The stiffness ratio of the structure, which is defined as the ratio between the sideway stiffness k_x and lateral stiffness k_y, is then

$$\frac{k_x}{k_y} = \left(\frac{L}{b}\right)^2 \tag{3.10}$$

With proper choices of L and b, the folded flexure design with a high stiffness ratio can strongly reduce the development of sideways deflections and ensure a larger range of linear movement of the central platform in the designed lateral direction.

3.2.2.2 Leaf-spring Lever for Sideway Motion Control

However, when at relatively large linear deflections, a significant decrease in stiffness along the sideway direction has been observed in the folded flexure by Brouwer et al. [17]. At large displacement in the lateral actuation direction, the bending and deformation of the folded flexure leads to mechanical instability in the sideway direction. The sideway stiffness is now significantly smaller than that described in Eq. (3.8) as the individual spring beams with length L are no longer straight rigid beams designed to resist sideway deformation. Brouwer et al. have observed a decrease of several orders in the sideway stiffness at large lateral actuation displacement. Such significant reduction in sideway stiffness can cause sideway snap-in leading to limited actuation range and poor device performance.

Therefore, they have proposed the exact constraint folded flexure (Figure 3.12) as an improvement to the original design of folded flexure. By attaching a 1:2 lever and extra leaf-spring to the folded flexure, they limited the movement of the intermediate body in response to the movement of the shuttle, reducing the coupled effect between the flexure lateral motion along the y-direction and the change in sideway stiffness along the x-direction. By limiting the resultant sideway deformation of the spring beams, such decoupling effect is crucial when a large lateral displacement value is actuated along the y-direction, preserving sideway stiffness and hence preventing sideway motion along the x-direction or rotation which would otherwise hinder the desirable uniaxial operation.

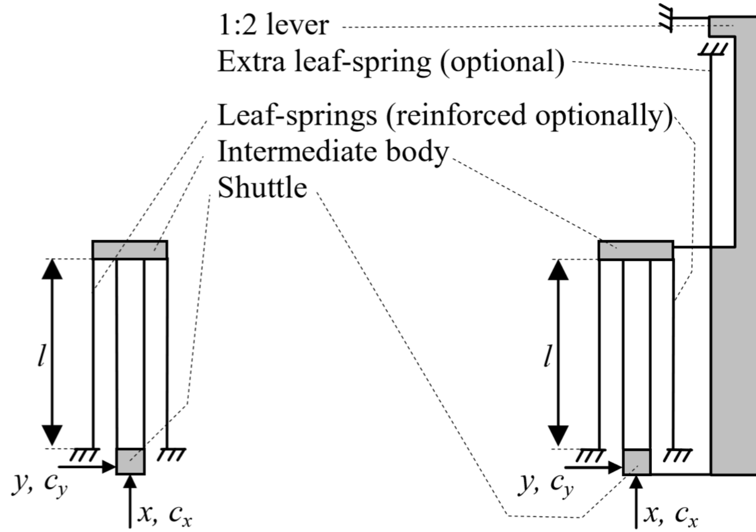

Figure 3.12. A sketch comparison between the original folded-flexure design on the left and the exact constraint folded flexure using a 1:2 lever and an extra leaf-spring on the right [17].

3.2.2.3 Two-fold Actuator Design

To generate the restoring mechanical force for our MEMS tuning platform, we design a modified version of the exact constrained folded flexures [17] utilizing their sideways stiffness stability at relatively large displacement. As shown in the earlier schematic of Figure 3.5, our actuation platform features a 2-fold rotationally symmetric design of both the electrostatic actuators and the exact constraint folded flexures, to enable uniaxial actuation in both positive and negative directions.

By Hooke's law, the displacement is linearly proportional to the spring force in the flexure with a spring constant k_{sp}. At equilibrium, the electrostatic driving force generated by the comb-drive actuators balances with the restoring spring force arisen in the compliant structures. Combining Hooke's law and Eq. (3.5), the actuated lateral displacement Δd is quadratically dependent on the applied voltage following the relation

$$\Delta d = \frac{F_{el}(V)}{k_{sp}} = \frac{N\varepsilon h V^2}{k_{sp} d_{sep}} \tag{3.11}$$

Such direct dependence of the displacement on the driving voltage provides for high reproducibility and controllability in any calibrated system. Because of the electrostatic actuation mechanism, no current flows in the device when applied with direct-current (DC) voltages, enabling very low-power consumption at no more than several nanowatts.

3.2.2.4 Mechanical Simulation Setup

COMSOL Multiphysics® Solid Mechanics finite element analysis was used to simulate the deformation of the 3D structure under applied forces. In the simulation model, there are 125 pairs of fingers and hence 250 sideways parallel-plate capacitors in one comb drive of the design. A distributed load was applied to the comb fingers to mimic electrostatic driving forces for lateral actuation. We purposely apply a fixed load of 9.9 µN, which is larger than the estimated electrostatic force of 1.38 µN in Section 3.2.1.4, to exaggerate the mechanical response for easy inspection. Anchors were modeled using a fixed boundary constraint. A stationary study and an eigenfrequency study were performed to determine deformation, stress, and possible resonance frequencies of the actuator.

Table 3.2. Exemplary flexure geometries and parameters used for mechanical simulations.

Parameter	Value
Spring length	500 µm
Spring width	4 µm
Spring thickness	6 µm
Finger pairs per comb	125
Silicon <100> Young's modulus	130 GPa

Table 3.2 lists the exemplary geometries and parameters used for the COMSOL simulation of mechanical responses. As the proposed actuator also contains the side levers and other subtle structures which will contribute some changes to the overall device stiffness, the analytical calculation for the exact actuator spring constant is tiresome while simulations can do the job

instead. Here, as a simplified analytical estimation, we temporarily assume that the mechanical contribution of other structures is negligible, and the actuator stiffness is mainly determined by the two folded flexures, then the actuator spring constant in the sideway (undesirable) direction can be calculated as

$$k_x = \frac{2\cdot(130\ GPa)\cdot(4\ \mu m)\cdot(6\ \mu m)}{500\ \mu m} = 12480\ N/m \tag{3.12}$$

The device spring constant in the lateral (desirable) direction is then

$$k_y = \frac{2\cdot(130\ GPa)\cdot(6\ \mu m)\cdot(4\ \mu m)^3}{(500\ \mu m)^3} = 0.799\ N/m \tag{3.13}$$

Obviously, the designed actuator based on folded flexures is flexible in the lateral direction of actuation while very stiff in the sideway direction, giving a very high stiffness ratio of

$$\frac{k_x}{k_y} = \left(\frac{500\ \mu m}{4\ \mu m}\right)^2 = 15625 \tag{3.14}$$

Even with some variation in the actual designs for different projects, we expect to have stiffness ratios on the same order, which is crucial to produce controlled uniaxial actuation for optical modulation in an Alvarez lens system.

3.2.2.5 Stress Distribution Simulation

In the stationary study, the stress distribution over the actuator is simulated with a fixed load of 9.9 μN applied on the actuator towards the left, mimicking electrostatic forces attracting the central platform towards the left.

Figure 3.13 and Figure 3.14 plot the distribution of simulated principal stress across the actuated MEMS platform. Local high stress indicates high probabilities of failure or fracture. Other than the bending springs, high stresses also occur at the joints between flexible spring beams and rigid flexures or anchors, indicating vulnerable points. This issue is even more concerning if such devices are designed for potentially high-frequency operations, during which the cyclic stress

application will induce continuous wear at these high-stress spots which will gradually lead to eventual mechanical failure, shortening device lifetime.

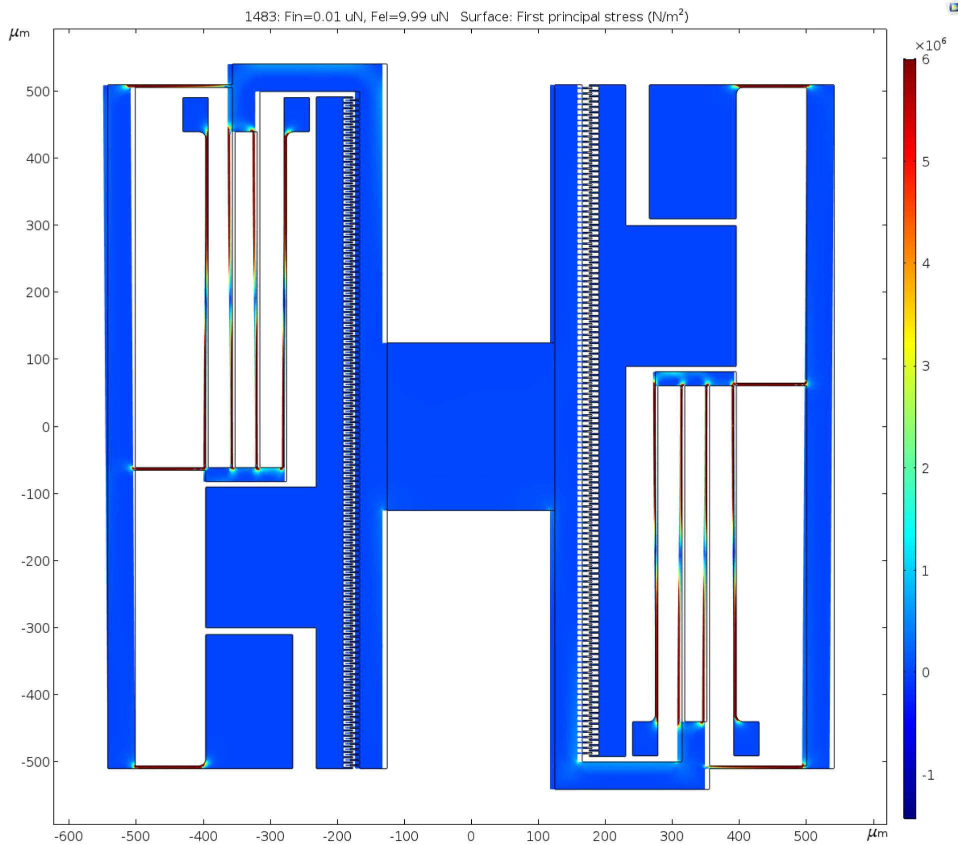

Figure 3.13. Plot of principal stress across the MEMS platform with a leftward distributed load along the left comb drive. Black frame shows the neutral position of structures.

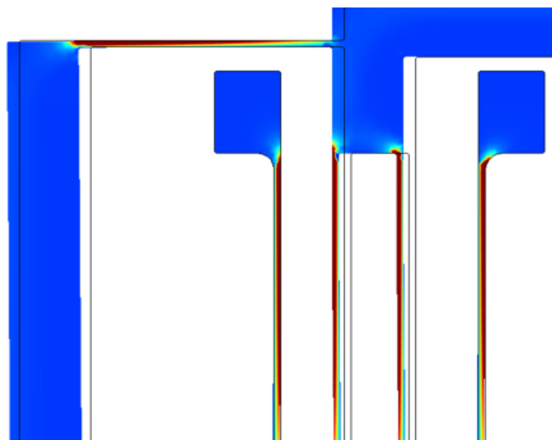

Figure 3.14. Zoom-in plot of principal stress in the displaced MEMS flexure. Black frame shows the neutral position of structures.

Therefore, in the updated MEMS actuator platform design as shown in the circular insets of Figure 3.15, we introduce fillets (rounding of corners) at mechanical hot spots such as corners to reduce, redistribute and partially relieve stress created during actuation and prolong device lifetime especially for many-cycle operations. We also introduce horizontal dimples (small protrusions) sparsely placed along the backbones and long springs in the folded flexures to prevent structural sticking if accidentally running into contact during large-displacement operation.

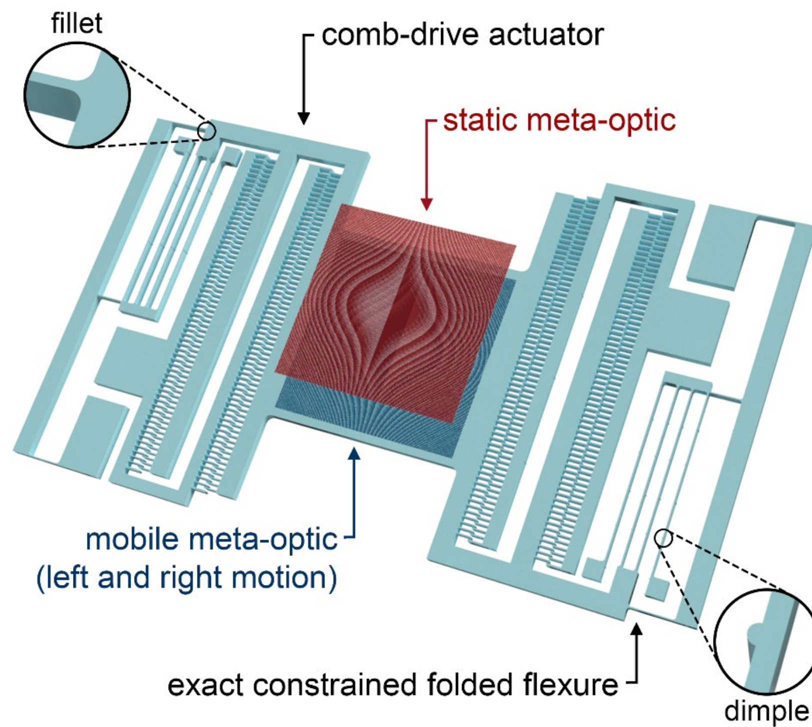

Figure 3.15. An exemplary MEMS-actuated Alvarez metalens system with 2-fold actuator design. Fillets and dimples are introduced to prevent mechanical failure and increase device robustness.

3.2.2.6 Displacement Field Simulation

Using the same model, the overall displacement field of the actuator platform was simulated with a distributed leftward force of 9.99 μN applied on the movable comb on the left side of the central platform, mimicking the electrostatic force created between the left set of comb drive under an

applied voltage, as shown in Figure 3.16. The lateral displacement for the central meta-optic is generated by the thin and long flexure springs deforming under the distributed force acting between comb fingers on the left side.

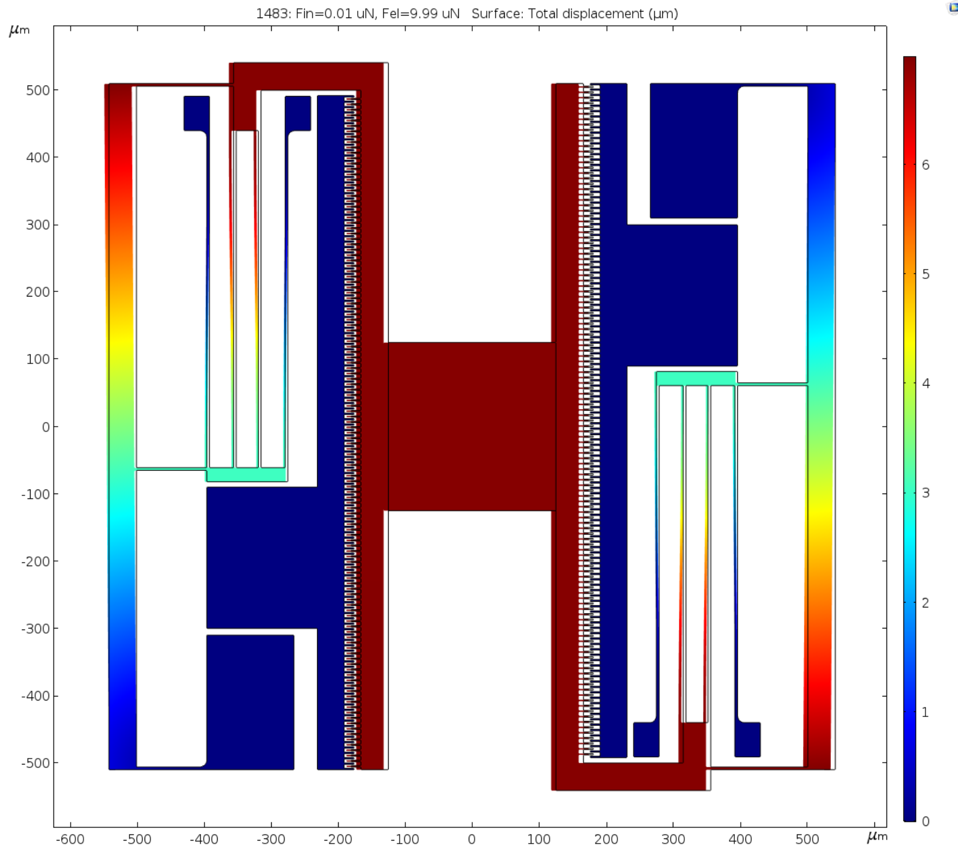

Figure 3.16. Plot of displacement for the MEMS platform with a leftward distributed load along the left comb drive.

3.2.2.7 Lateral (Desired) Displacement versus Applied Force

The displacement of the central meta-optic platform as a function of applied force is evaluated with a distributed load sweep from 0.01 N to 9.99 µN applied leftwards mimicking the electrostatic force created between the comb fingers. Figure 3.17 plots the simulated result, which indicates a linear relationship between the platform displacement and the electrostatic force on the comb drive, as predicted by Eq. (3.6).

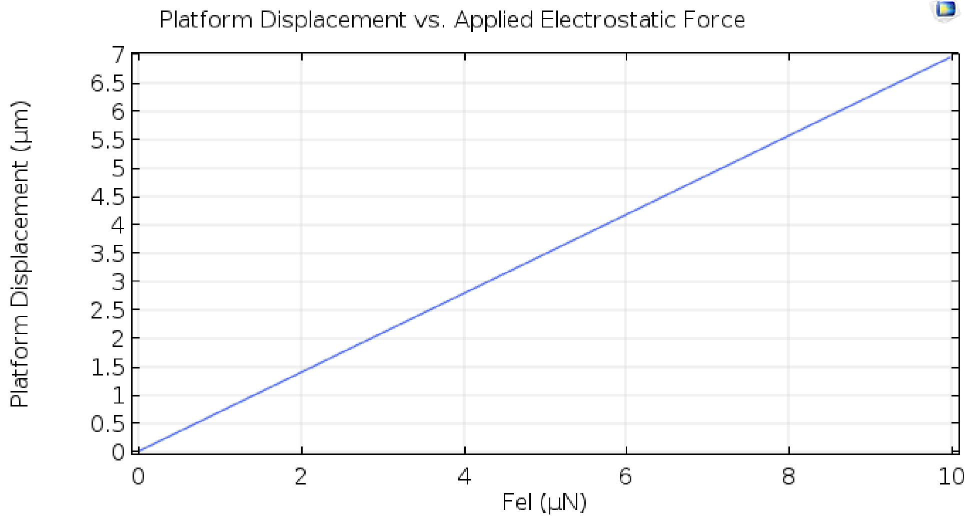

Figure 3.17. Lateral displacement of the meta-optic platform versus force in the lateral (desired) direction.

From the slope of the displacement-force plot of Figure 3.17, we can extract the actuator's effective lateral stiffness along the desired direction of motion, giving a value of 1.43 N/m. Note that this lateral spring constant is about 1.8 times of the analytical value calculated (0.799 N/m) in Eq. (3.13). However, as mentioned in Section 3.2.1.4, since the exact analytical calculation for the entire actuator is complicated, only the combined spring constant of the two folded flexures is calculated as a simplified estimation. Other mechanical structures in the device contribute to some additional stiffness and the simulation result has verified that assumption. Nevertheless, the simulated result and analytical calculation for actuator stiffness are still sufficiently close, proving that we have an actuator design operating as desired.

3.2.2.8 Sideway (Undesired) Displacement versus Applied Force

With a force sweep of the same magnitudes (0.01 – 9.99 μN) applied on the central platform orthogonally to the principal axis of motion, the corresponding displacement-force graph is plotted in Figure 3.18, giving a sideways stiffness greater than 10^{11} N/m, which is 11 orders larger than

the lateral stiffness found above. Note this simulated stiffness is higher than the analytical estimation in Eq. (3.12) due to the contribution of other mechanical structures such as the side levers, which we have ignored in calculation due to analytical complexity. Such a big difference in stiffness values between the lateral and sideway directions ensures that the actuator is compliant along the lateral direction for the desired motion while mechanically resistant to any undesired force or acceleration along the orthogonal directions.

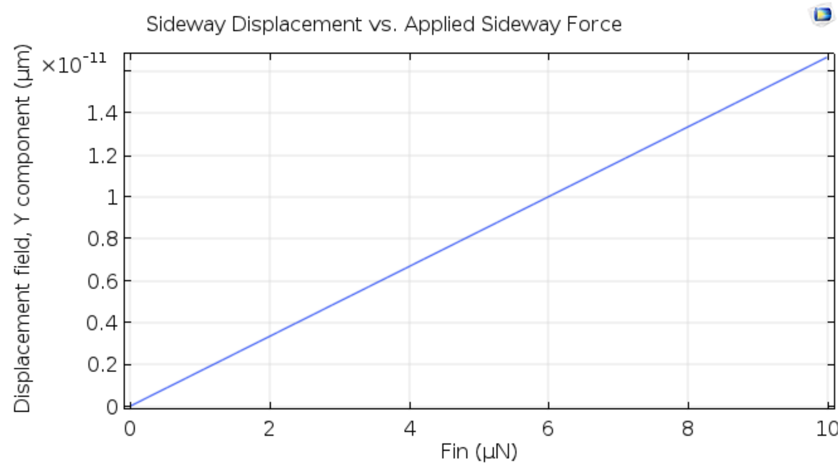

Figure 3.18. Sideway displacement of the meta-optic platform versus (unintended) sideway disturbance load.

3.2.2.9 Eigenfrequency Simulation

Electrostatic actuators utilizing silicon comb drives have been employed in applications operating at relatively high frequencies around a few kHz [68, 70] for their mechanical robustness and fast response to electrical signals. The proposed Alvarez meta-optic lens has similar potentials to be operated at least kHz frequencies for scanning applications.

With an eigenfrequency study using COMSOL Multiphysics® Solid Mechanics finite element analysis using the same geometries listed in Table 3.2, the first six resonant modes and frequencies were identified to determine the appropriate driving frequency ranges and modes for the proposed

actuator design. These six resonances occur at 3.38 kHz, 4.02 kHz, 4.72 kHz, 7.64 kHz, 14.0 kHz, and 23.6 kHz, with the corresponding resonant modes as illustrated in Figure 3.19. The simulation predicts a mechanical resonance at 3.38 kHz for the proposed MEMS platform for Alvarez metalens, showing potential for high-speed high-precision varifocal tuning in sensing and display applications.

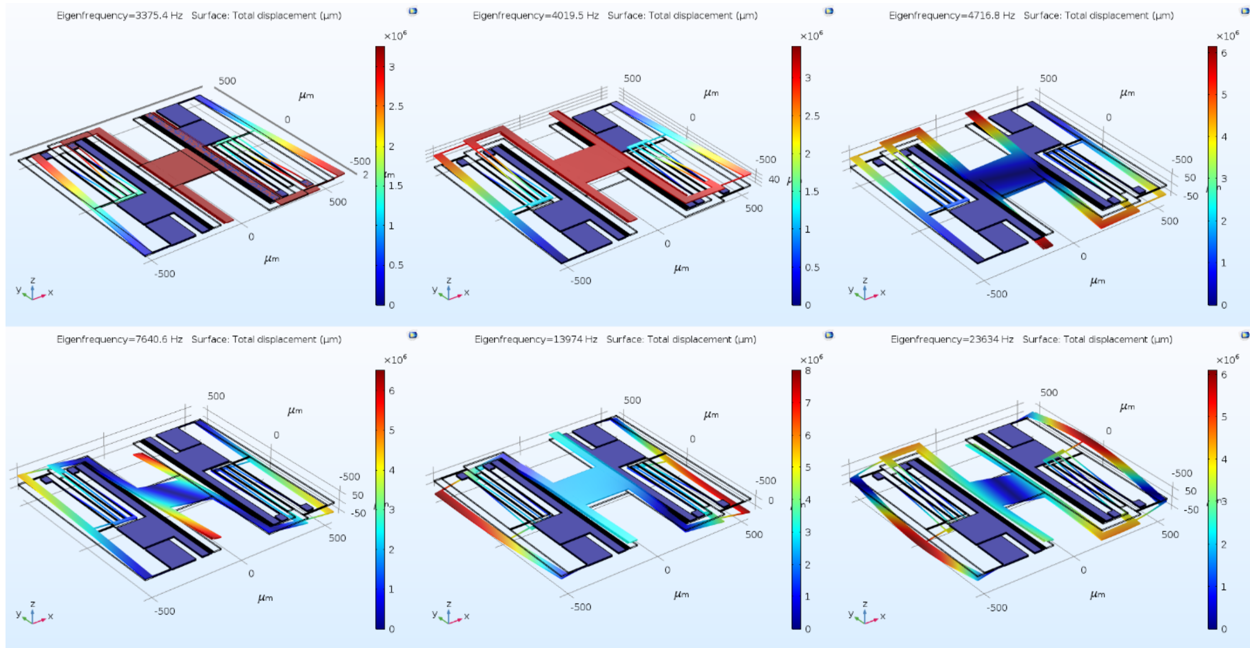

Figure 3.19. The first six resonant modes and eigenfrequencies of the actuator at 3.38 kHz, 4.02 kHz, 4.72 kHz, 7.64 kHz, 14.0 kHz, and 23.6 kHz.

Chapter 4. SMALL-APERTURE NEAR-IR MEMS ALVAREZ METALENS

In this work, we present a silicon nitride meta-optic-based Alvarez lens actuated by an electrostatic MEMS platform, capable of producing focal length modulation 10 times larger than the actuated displacement. The meta-optics are fabricated with high-throughput stepper lithography and the entire structure is fully compatible with well-developed semiconductor nanofabrication technologies, providing high reliability, low cost, and the potential for production scalability. To prove the concept, we start with an Alvarez metalens design with a small square aperture of 200 μm width. The electrostatic actuation performance of the MEMS tuning platform is verified utilizing a meta-optic singlet lens.

4.1 Design Parameters

The design of MEMS-integrated Alvarez meta-optics starts with mapping the two complementary cubic surfaces with diffractive meta-optics, and then followed with the configuring electrostatic actuators for focal modulation.

4.1.1 *Alvarez Metalens Parameters and Simulations*

Silicon nitride nanoposts have been used as the fundamental scattering elements for their low absorption losses in both infrared and visible wavelengths due to their wide bandgap while exhibiting similar performance to other material platforms [65]. Figure 4.1 illustrates the fundamental scatter elements consisting of cylindrical silicon nitride nanoposts on lightly doped silicon substrates, arranged in a square array. As shown in Figure 4.2, the transmission coefficients of the nanoposts for a fixed lattice constant of 1.3 μm and a post thickness of 2 μm on a silicon substrate was simulated as a function of grating duty cycle using rigorous coupled-wave analysis

(RCWA) [66]. The calculated phase spans from 0 to 2π while maintaining near unity amplitude. The phase profile was then quantized into six linear steps from 0 to 2π, giving the corresponding six cylindrical post diameters achievable with stepper lithography to construct the Alvarez cubic phase profiles for the two complementary meta-optic optical elements presented in this work.

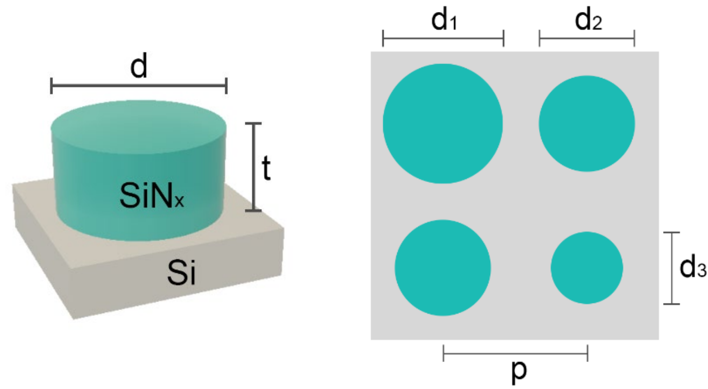

Figure 4.1. Schematic of meta-optic scatterers. (Left) A silicon nitride cylindrical nanopost with diameter *d* and thickness *t* on a silicon substrate. (Right) Top view of an exemplary meta-optic array of a fixed periodicity *p* and varying nanopost diameters.

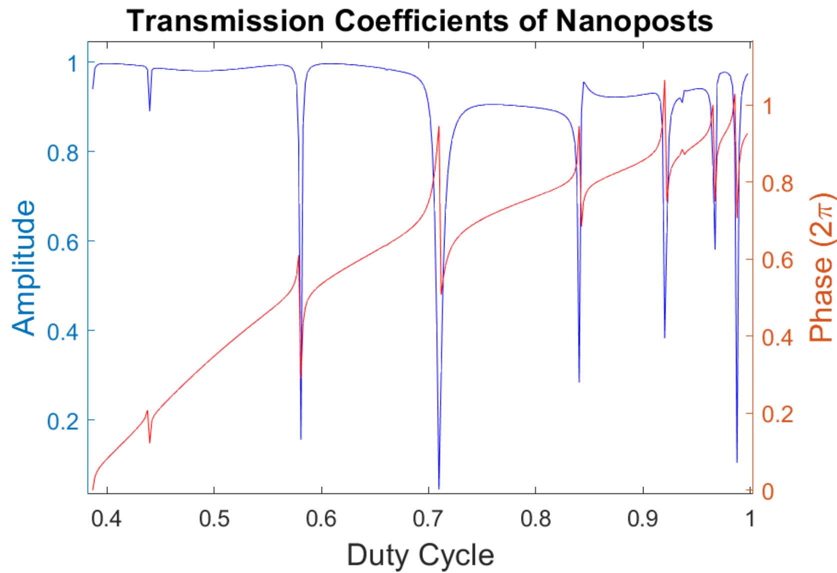

Figure 4.2. Simulated transmission phase and amplitude profiles of silicon nitride nanoposts as functions of duty cycle (*d/p*) for a chosen post thickness of 2 μm and a fixed array periodicity of 1.3 μm. The phase is normalized to 2π.

Table 4.3. Small-aperture Alvarez metalens parameters.

Square Array		
Aperture Size	200 µm × 200 µm	
Lattice Constant	1.3 µm	
Post Height	2 µm	
Individual Elements	Duty Cycle	Diameter (µm)
Nanopost 1	0.3948	513.3
Nanopost 2	0.4316	561.1
Nanopost 3	0.4991	648.8
Nanopost 4	0.5932	771.1
Nanopost 5	0.7404	962.5
Nanopost 6	0.9019	1172

We have designed and fabricated the Alvarez lens device to be integrated with the MEMS platform for the IR spectrum consisting of two separate Alvarez meta-optics with an aperture of $200\ \mu\text{m}$. Table 4.3 lists the design parameters for the small-aperture Alvarez meta-optics. When positioned with their surfaces parallel and aligned along the optical axis, the two Alvarez meta-optics in conjunction form a singlet metalens imparting a quadratic phase profile onto the incident wavefront as shown in Figure 4.3. The phase profiles of the regular and inverse meta-optics of the Alvarez pair have the expressions described by Eq. (3.1) and form a quadratic overall phase following Eq. (3.2) with a cubic phase strength $A = 2.5335 \times 10^{14}\ m^{-3}$.

A zero summed phase corresponding to a flat lens will be produced if the centers of the two Alvarez phase patterns are exactly aligned. For the specific Alvarez lens fabrication and experiments presented in this work, to accommodate data collection over our achievable actuation range with the current actuator designs, an initial offset of $d = 10$ µm has been introduced to the two meta-optics respectively in opposite directions, hence giving a total of 20 µm initial center-to-center lateral offset between the Alvarez phase masks as captured in Figure 4.3.

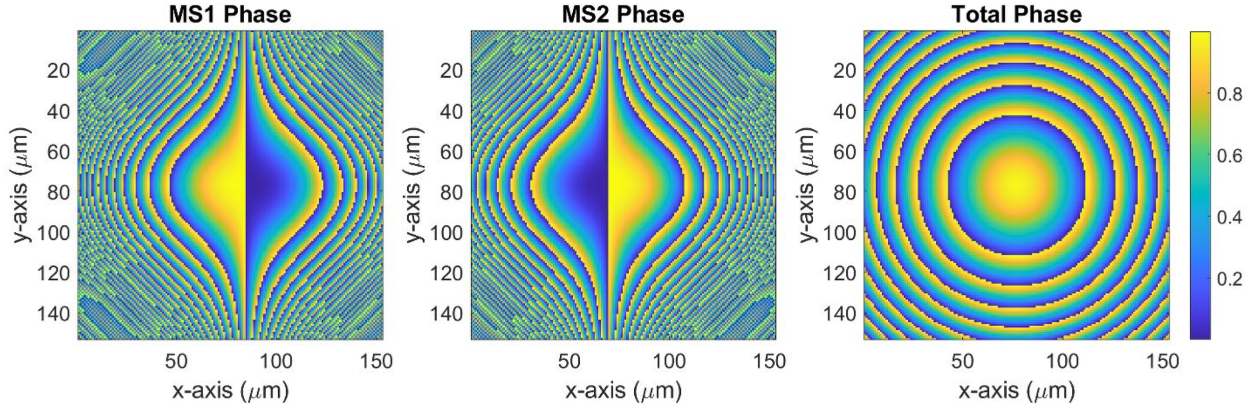

Figure 4.3. The 200 μm × 200 μm regular (left) and inverse (middle) Alvarez meta-optics with complementary cubic phase profiles overlay to produce a summed quadratic phase (right). Phase values are normalized to 2π.

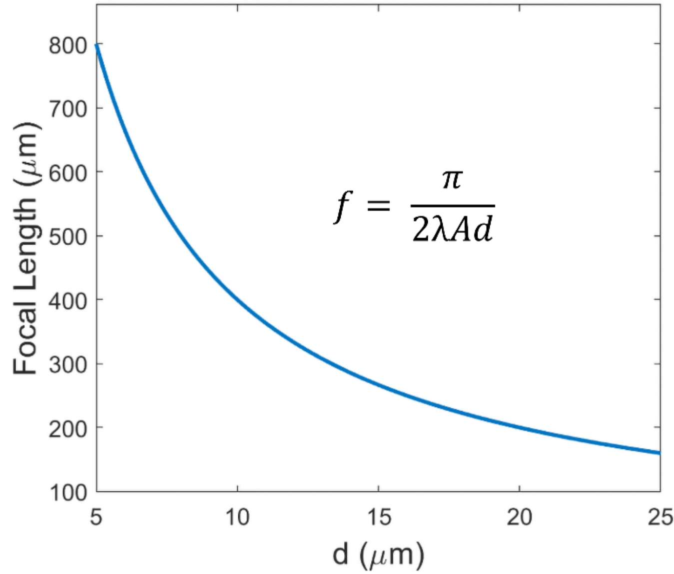

Figure 4.4. Ideal Alvarez focal tuning behavior as a function of lateral symmetric displacement d (giving a total center-to-center offset of $2d$) between the optical elements theorized with a negligible axial separation gap, an operating wavelength λ = 1550 nm and a cubic parameter $A = 2.5335 \times 10^{14}$ m^{-3}.

Figure 4.4 illustrates the ideal tuning behavior of the Alvarez lens assuming no axial separation exists between the two complementary phase masks [63], showing a nonlinear dependence of the focal position on the lateral offset. A larger center-to-center lateral offset

between the Alvarez phase masks gives rise to a more rapidly varying phase profile, corresponding to a lens with a shorter focal length [25].

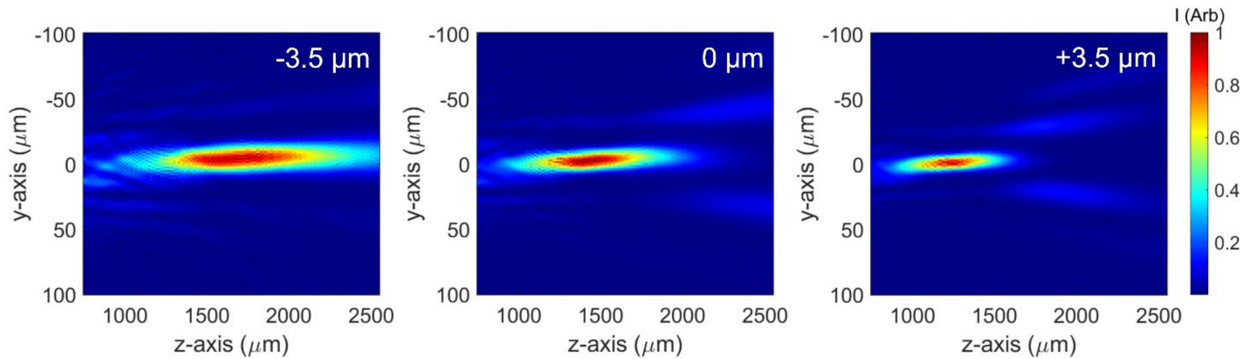

Figure 4.5. Simulated change of focal location and profile when the two meta-optics are laterally displaced at $\Delta d = -3.5$ μm, 0 μm, and +3.5 μm. The full simulation is performed with actuated displacement with 0.5 μm steps.

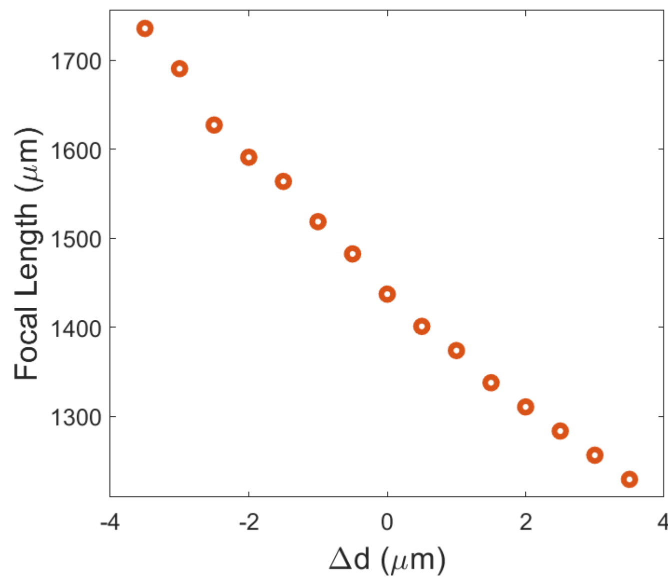

Figure 4.6. Simulated focal tuning behavior when a small lateral displacement is introduced in addition to an initial center-to-center offset of 20 μm, assuming a 50 μm axial separation gap between the two meta-optics from fabrication. The focal position is calculated from the weighted centroid of high-intensity regions.

To simulate the behavior of the designed meta-optic Alvarez lens under a more realistic situation, we introduce a 50-μm axial gap between two meta-optics from the proposed bonding

process and discretize the lateral displacement into small microscale steps as expected with the typical operation of the electrostatic actuator. Figure 4.5 and Figure 4.6 plot the simulated results of actuated displacement and the corresponding focal length modulation. Note that in our MEMS-actuated Alvarez metalens, in order to increase device robustness, only one meta-optic phase mask is actuated relative to the other, instead of both phase masks being actuated simultaneously in opposite directions as in a conventional Alvarez lens. Hence the actuated displacement Δd presented in Figure 4.5 and Figure 4.6 adds to the total center-to-center offset between the two meta-optic phase plates, accompanied by a small translational shift of the optical axis during tuning. The 50 μm axial separation gives rise to diffraction in the space between two meta-optics, leading to distortion and shifting of the focal spot along the optical axis, as illustrated in Figure 4.5. Specifically, the separation between two meta-optics deviates the summed effects of the Alvarez elements from a simple phase addition. Instead of focusing onto a single point as expected by a singlet lens, the light incident on the Alvarez stack creates multiple closely spaced intensity maxima, forming an elongated and aberrated intensity cluster along the optical axis (Figure 4.5). We denote the focal length by the centroid of the high-intensity clusters and plot the location of the centroid as a function of the displacement in Figure 4.6. The simulation reveals close-to-linear tuning of the focal length with sub-micron displacement steps.

The meta-optic singlet lens employed for simple motion tracking to verify the performance of the MEMS tuning platform in Section 4.4.1 was designed with a similar procedure, using the same nanoposts with chosen diameters mapping a quadratic phase profile for a converging singlet lens instead.

4.1.2 *MEMS Actuation Platform Parameters and Calculations*

Table 4.4 lists the design parameters for the MEMS electrostatic platform supporting the 200 μm tunable Alvarez metalens.

For all our actuators in this project, we can analytically estimate the actuator stiffness following the process described in Section 3.2.2. The actuator flexures have spring beams with length $L = 500$ μm, width $b = 4$ μm and height $h = 5$ or 6 μm. The actuation occurs in the (100) silicon plane with a Young's modulus $E = 130$ GPa [71]. Using Eq. (3.9), we can calculate the lateral stiffness in the actuation direction as

$$k_y = \frac{2\cdot(130\ GPa)\cdot(5\ or\ 6\ \mu m)\cdot(4\ \mu m)^3}{(500\ \mu m)^3} = 0.666\ or\ 0.799\ N/m \qquad (4.15)$$

The effect of the additional 1:2 lever is difficult to calculate analytically but is expected to slightly increase the value of stiffness. As shown in Section 3.2.2.9, we performed an eigenfrequency analysis on our fundamental MEMS actuator design using COMSOL Multiphysics, which predicted a mechanical resonance at 3.4 kHz, showing potential for high-speed high-precision varifocal tuning in sensing and display applications.

Table 4.4. MEMS actuation platform design parameters for the small-aperture Alvarez metalens.

Comb Fingers	Width (μm)	2
	Length (μm)	15
	Height (μm)	5 or 6
	Gap (μm)	2
Folded Springs	Width (μm)	4
	Length (μm)	500
	Height (μm)	5 or 6
	Lateral Stiffness (N/m)	0.666 or 0.799
	Natural Frequency (Hz)	3400
Focal Tuning	Voltage (V)	–20 to +20
	Displacement (μm)	6.3
	Focal Length (μm)	68

4.2 DEVICE FABRICATION

The two complementary Alvarez meta-optics were fabricated in two parts first – one actuatable meta-optic half-plate carried by an electrostatic MEMS platform and one stationary meta-optic half-plate on a silicon substrate – then aligned and bonded together to establish the Alvarez system. A schematic of the fabrication flow can be found in Figure 4.7.

4.2.1 *Microfabrication Process Flow*

The first Alvarez meta-optic was fabricated on a silicon-on-insulator (SOI) wafer with a silicon device layer of 5-6 μm and a buried-oxide (BOX) layer of 2-4 μm. On top of the device layer, 2 μm of silicon nitride was deposited by plasma-enhanced chemical vapor deposition (PECVD). The first meta-optic was patterned into the silicon nitride with stepper lithography and inductively coupled plasma (ICP) etching. The MEMS electrostatic actuator carrying the meta-optic was patterned into the silicon device layer and etched by deep reactive ion etching (DRIE). Electrical

contact pads for voltage application and chip-level alignment marks were created at the designated locations by electron beam evaporation and lift-off of a gold/nickel/chromium (100 nm/100 nm/10 nm) stack. DRIE holes were etched from the backside of the wafer to remove the silicon substrate under the central meta-optic platform, aiding the final hydrogen fluoride (HF) vapor etch to release the MEMS actuator.

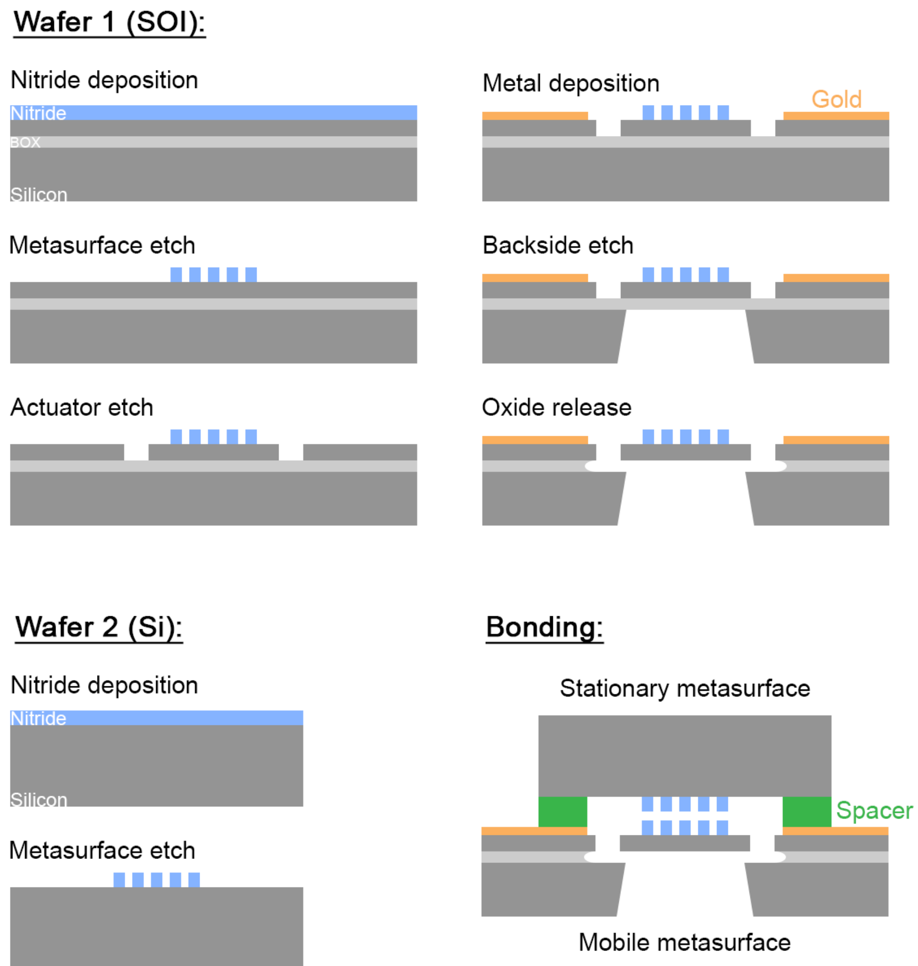

Figure 4.7. Fabrication flow of a small-aperture MEMS-actuated meta-optic Alvarez lens.

The second Alvarez meta-optic was fabricated on a double-side polished (DSP) silicon wafer. A 2 µm layer of PECVD silicon nitride was deposited and patterned with the second meta-optic

using stepper lithography and ICP etching. Chip-level alignment marks were etched through the silicon substrate with DRIE.

Wafers carrying the two meta-optics respectively were diced into individual chips. The chips with mobile meta-optics were released with vapor HF etch. Then a chip with the actuator carrying the first mobile meta-optic was placed in parallel and aligned face-to-face with a chip carrying the second stationary meta-optic on a custom-built piezo positioning stage, using 50 µm thick Kapton tape pieces to create a gap between the chips as electrical insulation and to prevent accidental scratching between the meta-optics. Once aligned the chips were bonded by applying ultraviolet (UV) sensitive resin along the stack edges to complete the assembly of the MEMS meta-optic Alvarez lens. In the potential mass production of such Alvarez metalenses, the alignment and bonding of the meta-optic pairs would be done on the wafer level by a commercial wafer bonding system with a deposited spacer layer before dicing into individual device chips.

4.2.2 *Fabricated Devices*

Figure 4.8 shows the scanning electron microscope (SEM) and optical images of a fabricated MEMS actuator carrying the mobile meta-optic of the Alvarez pair, which is then aligned and bonded on top of the complementary meta-optic fabricated on a stationary substrate. As shown in Figure 4.8a, the actuator design used here has two sets of comb drives and folded flexures on the opposite sides of the platform to double the actuation range under signals applied alternatively on both sides of the actuator and to prevent rotational displacement during the movement. Figure 4.8b shows a zoomed-in SEM image of a comb drive. The suspended left comb is attached to the central platform for displacement while the stationary right comb is anchored to the substrate. One of the silicon nitride Alvarez meta-optics is carried by the central platform attached to the suspended combs of each set of comb drive while the other is fabricated on a stationary silicon substrate.

Figure 4.8c shows the details of one meta-optic composed of a 2D array of cylindrical silicon nitride nanoposts, generating the desired phase profile for the Alvarez optics. Figure 4.9 shows optical images of the pair of Alvarez meta-optics with complementary surface profiles, fabricated with silicon nitride nanoposts arrays on silicon substrates. The two chips carrying the meta-optics are overlaid on top of each other in the bonded lens system. Together they impart a quadratic total phase on the incoming wavefront. The optical power modulation is controlled by further lateral displacement between the two meta-optics following a reciprocal relation.

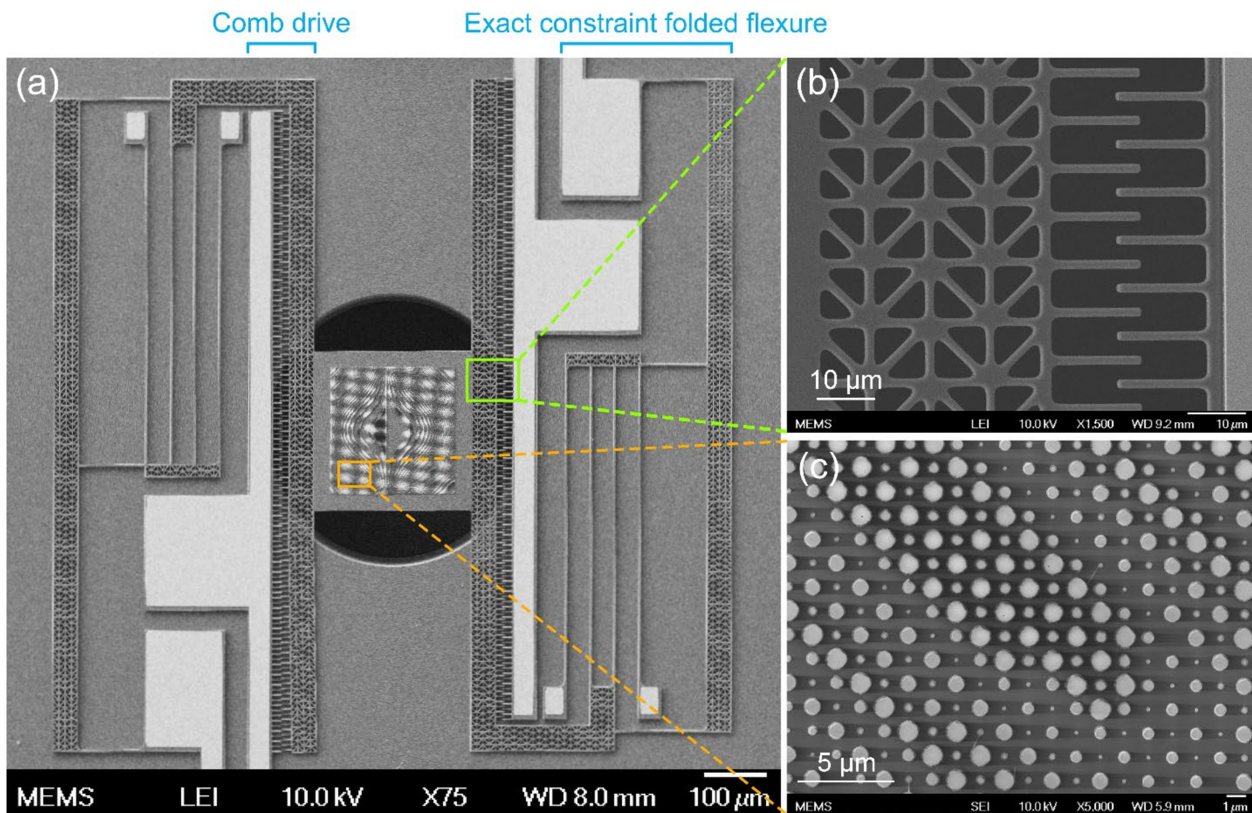

Figure 4.8. SEM image of (a) a MEMS-actuated platform carrying the movable meta-optic in an Alvarez metalens, with (b) and (c) being the zoomed-in SEM images portraying the electrostatic comb drive and the meta-optic nanoposts. (d, e) Optical images of the Alvarez meta-optics with complementary cubic phase profiles that are overlaid on top of each other in the assembled Alvarez metalens and in summation impart a quadratic phase change on the incident light.

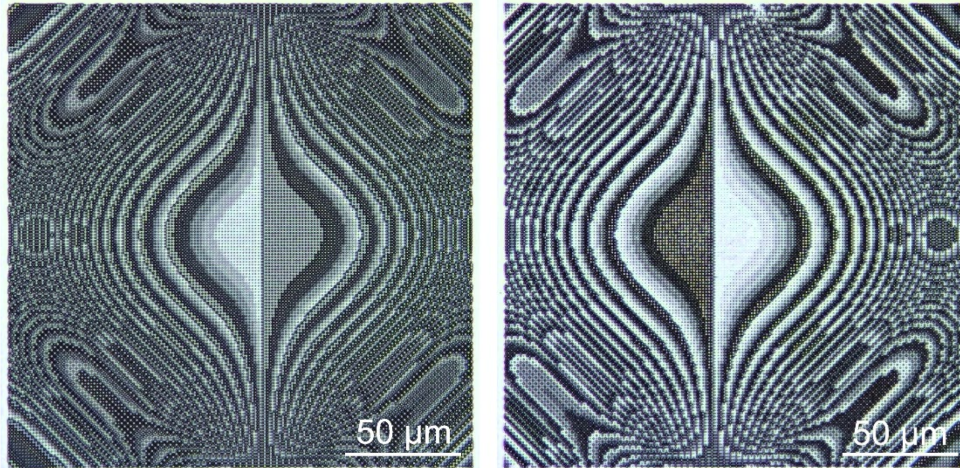

Figure 4.9. optical image of the (left) regular and (right) inverse Alvarez meta-optics with complementary cubic phase profiles, fabricated with silicon nitride nanoposts on silicon substrates. An initial 20 μm center-to-center lateral shift has been introduced between the meta-optics. They overlay on top of each other in the assembled Alvarez metalens and in summation impart a quadratic phase change on the incident light.

4.3 EXPERIMENTAL SETUP

Both tuning experiments of the MEMS meta-optic singlet lens and the MEMS meta-optic Alvarez lens used the same fundamental setup as shown in Figure 4.10.

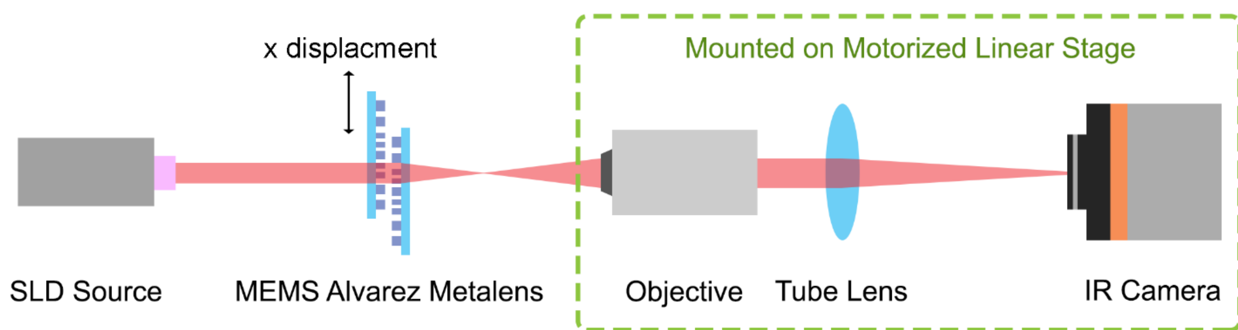

Figure 4.10. Experimental setup for focal tuning analysis.

The actuator chip was attached to a glass microscope slide using transparent UV resin. The glass slide was then mounted vertically onto a 3-axis translation stage manually moved by micro-positioners for the initial alignment of the metalens to the rest of the setup. A source meter

(Keithley 2450) grounded the chip substrates and applied the required voltages across the comb drives of the test devices for electrostatic actuation via probing to the respective contact pads. A superluminescent laser diode (SLD) source of 1550 nm (Thorlabs S5FC1005P) was aligned with the optical axis of the metalens, illuminating it from one side. The incident light interacted with the meta-optic lens and formed a focus along the optical axis. The light spreading from the focus was then collected and converted to parallel rays by the infinity-corrected objective (Mitutoyo M Plan Apo 20x Objective, NA = 0.42, f = 20 mm) on the other side of the meta-optic lens, which was then converged by a tube lens to be captured by the IR camera (Xenics Bobcat) exporting the live image to a control computer, which stored the data as sequential screenshots or video clips.

The objective, tube lens, and the IR camera were mounted at fixed distances on a motorized linear stage (Newport ILS100CC), which was controlled by a motion controller (Newport ESP301) to change the distance between the optics and the meta-optic lens by steps as small as 1 μm. A non-zero voltage applied across the comb drive of the MEMS actuator laterally displaced the mobile meta-optic, leading to focal tuning along the optical axis. The linear motorized stage was then used to scan along the optical axis to investigate the focal position as a function of the applied voltage.

4.4 Results and Analysis

We acquire the images and videos capturing the operating Alvarez meta-optic lens, perform basic noise reduction to remove camera artifacts, and then analyze the MEMS actuation and focal tuning behavior of the device.

4.4.1 *Raw Image Noise Reduction*

Due to the intrinsic non-uniformity of the IR camera, the captured raw images contained vertical stripes as shown in Figure 4.11a. To remove the stripe patterns in the images, a bright reference (Figure 4.11b) was taken when the incident light directly illuminated the camera detector and a dark reference (Figure 4.11c) was taken when the incident light from the SLD source was completely blocked. The existence of static vertical stripes in the light and dark references identify them as systematic noise.

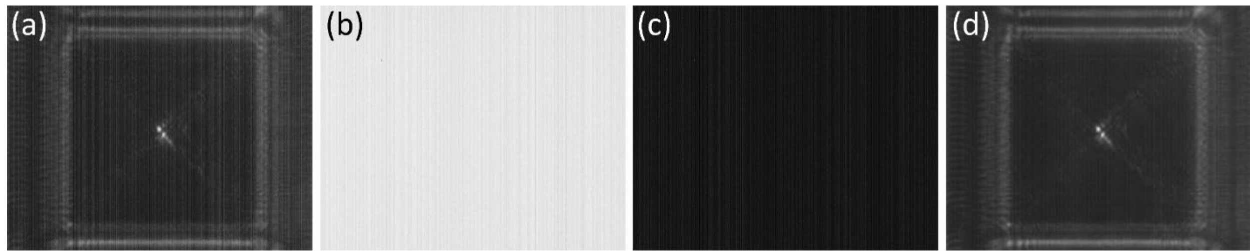

Figure 4.11. Noise due to camera artifacts removed by reference subtraction. (a) A raw image captured by the IR camera. (b) A bright reference taken with a free path. (c) A dark reference taken with the light path blocked. (d) The processed image with noise due to camera artifacts removed.

With the pixel intensities expressed in the double numeric data type (0 = black and 1 = white), the systematic noise subtraction is conducted pixel-wise to produce Figure 4.11d following the algorithm:

$$I_{processed} = I_{raw} + \left(1 - I_{bright}\right) - I_{dark} \tag{4.16}$$

This process also removed most image defects due to bad camera pixels.

4.4.2 *Electrostatic Tuning of the MEMS-actuated Platform*

Prior to testing the meta-optic Alvarez lens, we fabricated a separate structure with a singlet converging meta-optic lens with a diameter of 200 μm on the central platform of the MEMS actuator to aid motion tracking by examining the movement of the focal spot (Figure 4.12). The meta-optic design followed the usual procedure [65] which is outlined in Section 3.1. The left and right sides of the platform were attached to two sets of comb drives respectively. The prototype actuator was fabricated with 2 comb drive sets per side (with 125 finger pairs in each) and a device layer thickness of 6 μm. With the MEMS actuator chip mounted on a glass stage, a superluminescent diode (SLD) source of 1550 nm illuminated the meta-optic lens from the back. The resulting focal spot was monitored by an IR camera in front as an indication of the lens location (the experimental setup is described in Section 4.3). Since the focal spot was located approximately 200 µm in front of the meta-optic, for demonstration of the relative lateral position of the meta-optic and the focal spot, Figure 4.12 is an image overlay of the device surface plane and the focal plane. A DC voltage ramping from 0 V to 18 V and then back to 0 V with a step size of 500 mV was applied to the right comb drive sets of the actuator to electrostatically pull the central platform. The maximum testing voltage was chosen based on the actuator dimensions to avoid electrostatic pull-in between the combs. The increasing voltage pulled the meta-optic and the focal spot towards the right. By turning down the voltage, the focal spot relaxed back to its neutral position equilibrated by the spring force in the flexures. Figure 4.13 plots both the displacement of the focal spot and the applied voltage as time elapses, showing a clear positive correlation between the actuated displacement and the actuation voltage. The IR camera resolution (approximately 0.9 pixels per micron) limits the number of pixels available for focal spot tracking, giving rise to the distinctive steps in the actuated displacement analysis shown in both Figure 4.13 and Figure 4.14.

The symmetric displacement during voltage ramp-up and ramp-down in Figure 4.13 shows the absence of hysteresis and the reversibility of the platform actuation. The linear fit of the focal displacement (averaged over all captured video frames at each applied voltage) as a function of the voltage-squared (Figure 4.14) further confirms that the actuated displacement is quadratically dependent on the voltage applied. The stiffness of the platform actuator can be calculated from the slope in Figure 4.14 according to Eq. (3.11), giving a spring constant of 0.713 N/m for this electrostatic actuator, which is 11% smaller than the analytically calculated value presented earlier, giving a softer device than predicted, probably due to fabrication discrepancies resulting in thinner structures. While we observe a displacement of 3.1 μm under a voltage application of 18 V, if a voltage is applied to the left rather than the right side of the actuator, the meta-optic can be displaced in the opposite direction, doubling the range of physical motion.

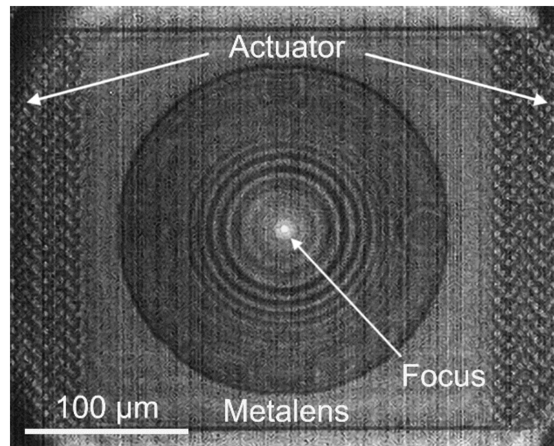

Figure 4.12. IR image showing both the device and focal planes of a singlet metalens on a MEMS-actuated platform.

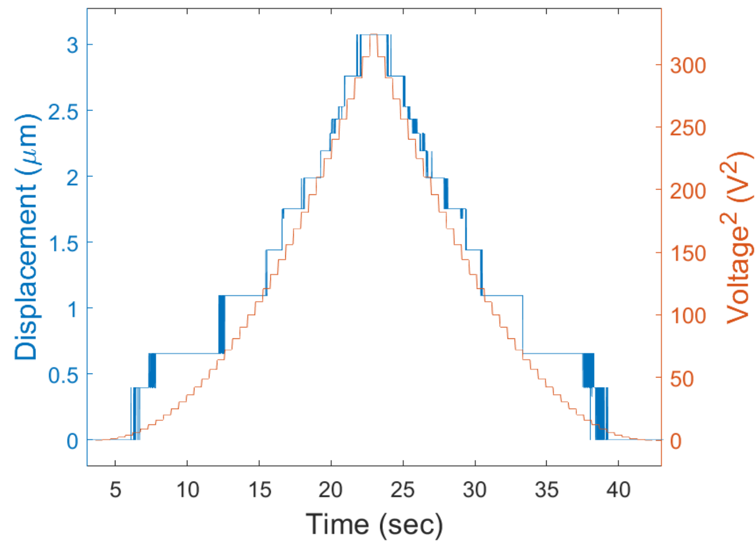

Figure 4.13. Actuated focal displacement and applied voltage over time. The general trend of the actuated displacement follows the square of the applied voltage.

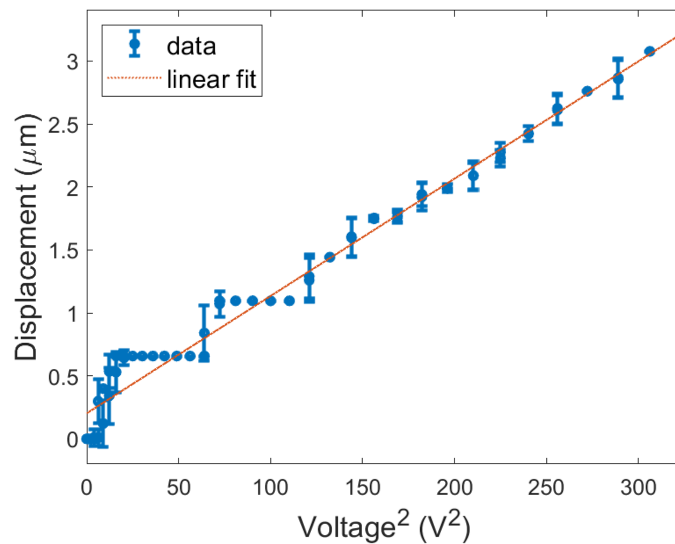

Figure 4.14. Average actuated displacement as a function of applied voltage-squared during both loading and unloading, showing a linear dependence. No hysteresis behavior is observed with voltage loading and unloading, verifying the reversibility of the actuation process.

4.4.3 *Focal Tuning of the Small-aperture MEMS-actuated Alvarez Metalens*

A full meta-optic Alvarez lens was fabricated with the process flow described in Section 4.2, with one Alvarez meta-optic on the actuator membrane while the other on a stationary surface. The electrostatic actuator used for the Alvarez lens had 2 comb drive sets per actuation side with a device layer thickness of 5 µm. The focal tuning of the meta-optic Alvarez lens was measured with the Alvarez chip mounted on a translation stage and illuminated with a 1550 nm SLD source. A voltage between 0 and 20 V was applied to the comb drive to actuate the central meta-optic platform, changing the lateral offset between two Alvarez meta-optics. The maximum testing voltage was chosen based on the actuator dimensions to avoid electrostatic pull-in between the combs. At any point in time, we actuated the comb drives only on one side: the right-side actuation increased the lateral offset, whereas the left side actuation decreased the lateral offset. Note that we always applied a positive DC voltage in this experiment but denoted the case of decreasing offset (controlled by choosing which set of comb drive to actuate) between two meta-optics by negative voltage and displacement notations. Hence, with a negative voltage, we observe a longer focal length. Similarly, positive voltage and displacement correspond to an increasing lateral offset and a shorter focal length. An IR camera was aligned with the Alvarez lens and the source to monitor the focal tuning behavior. The distance between the Alvarez metalens and the IR camera was controlled by a motorized linear translation stage to scan across the intensity profiles along the optical axis in microscale fine steps and locate the focal plane tuned by the input voltage. Detailed information on the setup is included in Section 4.3.

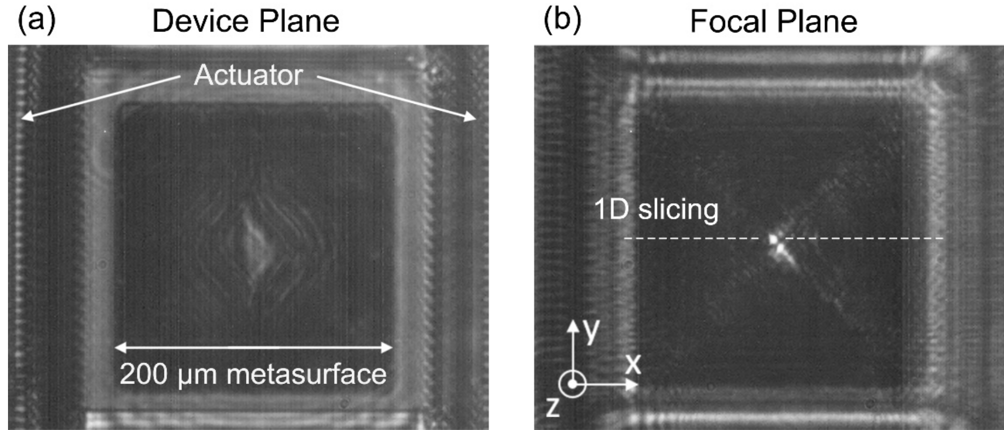

Figure 4.15. IR camera screenshots at (a) the device plane and (b) the focus plane of an Alvarez metalens illuminated with a 1550 nm SLD source.

Figure 4.18a is a camera screenshot showing the two Alvarez meta-optics overlaying on top of each other. The bottom meta-optic sits on a stationary surface while the top meta-optic is carried by a MEMS actuator. The comb drives employed to electrostatically displace the top meta-optic laterally in opposite directions are partially captured at the edges of the image. By adjusting the distance between the IR camera and the Alvarez lens, a bright focused spot as shown in Figure 4.18b was found approximately 200 μm away from the Alvarez lens. We attribute this discrepancy between theory and experimental results on the focal tuning range of the Alvarez lens to the small aperture and the 50 μm axial separation between the meta-optics. The side peak shown beside the central focal spot in Figure 4.18b emerged due to the gap and misalignment between the Alvarez meta-optics which led to the incomplete cancellation of the cubic phase terms in the conjugate system. To test the effect of the aperture size, we measured the focus tuning of several Alvarez lenses with various aperture sizes without MEMS actuation. In these lenses, the lateral separation was actuated manually, and we found a higher tolerance to misalignment and hence a better match between the theory and the experiment as the aperture size increased (see Section 4.4.6). In the experiment of the MEMS-actuated Alvarez metalens, at every applied voltage, the intensity profile

along the optical axis was captured over a 100 μm range around the brightest spot with an increment of 1 μm. We processed the captured images to reduce systematic noise. Baseline references at no illumination and full illumination were taken to remove anomalies due to camera artifacts by comparison and subtraction (see Section 4.4.1).

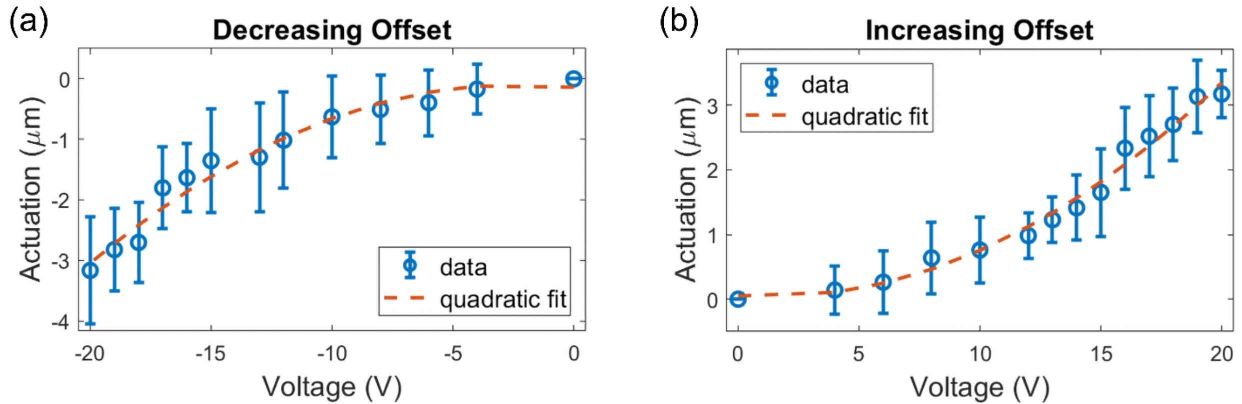

Figure 4.16. Actuated displacement as a function of applied voltage with (a) negative actuation corresponding to a decreasing offset and (b) positive actuation corresponding to an increasing offset.

With the aid of the camera screenshots capturing the actuator as shown in Figure 4.15a, the actuated displacement at an applied voltage was determined from the change in the lateral position of the actuated platform relative to its neutral position using edge detection. Figure 4.16 plot the actuated displacement of the top meta-optic at various applied voltages, and as shown by Eq. (3.11), the displacement electrostatically actuated with the comb drives is quadratically dependent on the actuation voltage and hence can be well controlled for a calibrated system. The total stiffness of the folded flexures in the Alvarez system can be calculated from the quadratic fit of the displacement-voltage plots, giving 0.590 N/m when actuated towards the negative direction and 0.586 N/m towards the positive, verifying the symmetry of the mechanical design. The actual stiffness values are 12% smaller than the predicted values presented earlier, which we ascribe to

fabrication discrepancies resulting in reasonable deviations in both electrostatic and restoring forces.

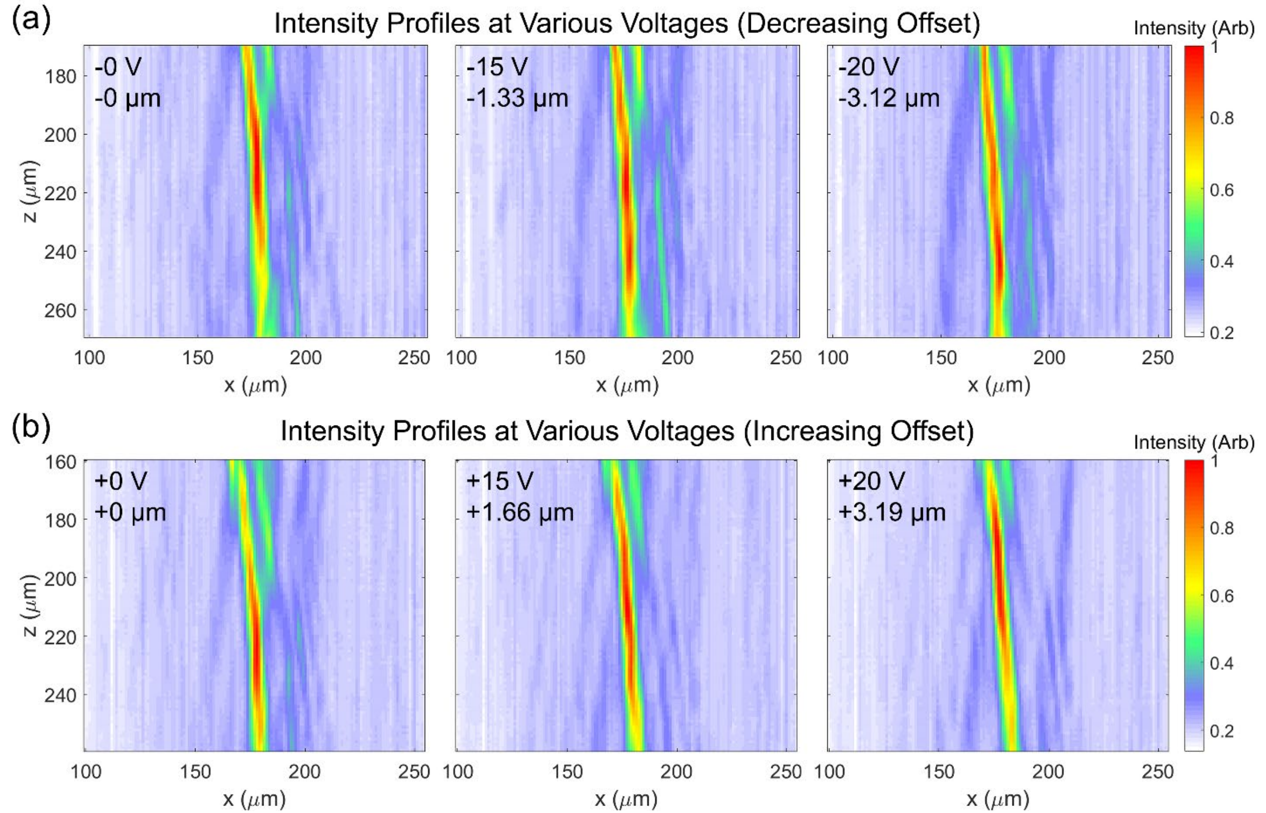

Figure 4.17. The shift of focal intensity profiles along the optical axis with (a) decreasing and (b) increasing center-to-center offsets between the Alvarez meta-optics at various actuation voltages and displacements.

For each set of scanned data with the same actuation voltage, a 1D slice of intensities was taken from each screenshot at the same location across the central bright spot, as indicated in Figure 4.18b. All the 1D slices were then combined into a 2D intensity plot over the scanning distance along the optical axis, as shown in Figure 4.17. The slight tilting of the focal axes shown here was the result of displacing only one meta-optic in the Alvarez optics pair, which introduced an additional linear term into the system's phase function, effectively acting as a beam deflector (details in Section 4.4.5). In the combined plots, a soft Gaussian filter was applied to reduce the

residual stripe-patterned nonuniformity due to camera artifacts. Then the intensities were normalized and a threshold was taken to identify and isolate the region of high intensities. The focal position along the optical axis was calculated by locating the weighted centroid of the pixels above the defined intensity threshold to minimize the effect of background noise. Such absolute positions of the focal spots are estimations due to the difficulty in the visual determination of the zero plane at the device surface. In order to better visualize the focal tuning behavior, the net change in focal position was instead plotted as a function of actuation voltage in Figure 4.18a, using the corresponding neutral focal position without voltage application as the reference. Such a focal-voltage relation is then translated to a function of actuated displacement in Figure 4.18b using the displacement-voltage data pairs presented in Figure 4.16. The focal locations plotted in Figure 4.18 are identified by the weighted centroids of high-intensity clusters above various threshold choices. A higher threshold percentile gives rise to a smaller isolated region of high-intensity pixels for focal search – 0.1% corresponds to a bright area of 18 μm^2 while 0.5% corresponds to a bright area of 90 μm^2. As shown in Figure 4.18h, the Alvarez metalens has produced a tunable focal length range of 68 μm with a total actuated displacement of 6.3 μm, generating a focal length tuning range that is over 10 times larger than the actuated displacement. With the neutral focal length of 216 μm, this focal tuning range corresponds to 1460 diopters change in optical power. At sub-micron displacement steps realized with electrostatic actuation, transition states have been observed in the focal tuning curves due to axial separation between the meta-optics from the bonding spacer. With a larger focus spot defined with a lower threshold percentile, a smoother tuning behavior can be produced with a slightly smaller range of tuning due to the asymmetric intensity distribution along the optical axis.

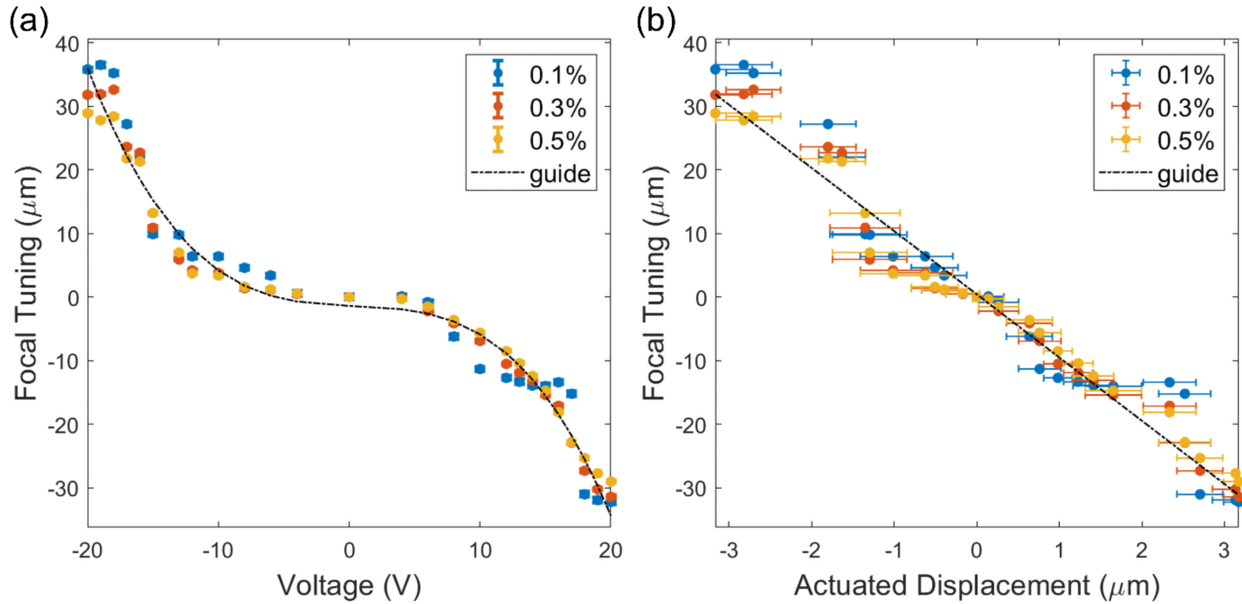

Figure 4.18. Tuning in focal location (a) as a function of applied voltage and (b) as a function of actuated displacement with focus size defined by various intensity thresholds, giving a focal tuning range 10 times larger than the actuated Alvarez displacement. The black dash-dotted lines are provided as guides to the eye.

4.4.4 *Experimental Data Error Analysis*

The actuated displacement for the meta-optic singlet lens was calculated as the averaged focal location shift at each applied voltage. Based on the frame rate of the source video for focal tracking and the defined linear ramping of applied voltage, the focal shift was analyzed from 33 frames for each voltage step. The error bar of each averaged displacement was calculated from the standard deviation of the 33 focal shifts within the same voltage step.

The actuated displacement at each applied voltage for the meta-optic Alvarez lens was calculated as the average of all net platform displacements from valid edge detection at various locations in the corresponding screenshot. Its associated error was calculated from the standard deviation of displacements detected at multiple edges at each applied voltage.

The focal position along the optical axis at each applied voltage was found as the location of the weighted centroid of the high-intensity pixel regions above the defined thresholds, with the normalized intensity values as the weights. The corresponding associated analytical uncertainty σ was calculated using error propagation as the reciprocal square root of the sum of all the individual weights (normalized intensities) w_i involved, mathematically expressed as [72]

$$\sigma = \frac{1}{\sqrt{\sum w_i}} \tag{4.17}$$

With the chosen intensity threshold percentiles of 0.1%, 0.3%, and 0.5%, the calculated uncertainties are all below 0.5 µm, hence it may be difficult to notice in the focal tuning plots. On one hand, a larger intensity threshold percentile value defines a more dispersed focal spot, which includes more pixels in the weighted centroid calculation. As described in the above equation, the increase in the size of the information pool for calculation leads to an increased sum of weights, and hence a smaller uncertainty. However, on the other hand, the definition of focal spot confines its footprint so the area of high-intensity pixels included for the calculation cannot be increased indefinitely. In applications, the area of the focal spot may need to be carefully defined case by case according to the operation requirements.

4.4.5 *Tilting of the Focal Axis with Asymmetric Actuation*

A typical Alvarez lens should have the two cubic phase elements laterally actuated by the same distance simultaneously in the opposite directions. As described in the main text, to increase the robustness of our prototype Alvarez metalenses, only one of the complementary meta-optics was fabricated on the MEMS-actuated platform to introduce the relative displacement between the pair. Such asymmetric actuation introduced a longitudinal shift of the focal plane along the optical axis and a lateral shift of the focal spot along the actuation direction [63]. To demonstrate this effect

mathematically, we can derive the system's phase function with one of the cubic phase plates being laterally actuated by a displacement d along the x-direction while the other stays stationary. d_0 denotes the initial center offset we introduced to each meta-optic in opposite directions to aid experimentation. Using the cubic phase expressions in Eq. (5) of the main text, the system's phase function can be shown as

$$\begin{aligned} \varphi_{Alvarez}(x,y) &= \varphi_{reg}(x+d_0+d,y)+\varphi_{inv}(x-d_0,y) \\ &= A\left[\frac{1}{3}(x+d_0+d)^3+(x+d_0+d)y^2\right]-A\left[\frac{1}{3}(x-d_0)^3+(x-d_0)y^2\right] \\ &= (2d_0+d)(x^2+y^2)+Ad(2d_0+d)x+A\left(\frac{2}{3}{d_0}^3+{d_0}^2d+d_0d^2+\frac{1}{3}d^3\right) \end{aligned} \tag{4.18}$$

where the constant A denotes the cubic phase strength.

Neglecting the constant phase terms, we can rewrite the system's phase function as

$$\varphi(x,y) = A(2d_0+d)(x^2+y^2)+Ad(2d_0+d)x \tag{4.19}$$

We now interpret the phase function as a superposition of two different components, with the first term equivalent to a quadratic lens with a focal length at an operating wavelength λ given by

$$f(d) = \frac{\pi}{\lambda A(2d_0+d)} \tag{4.20}$$

The second term of the system's phase represents a linear phase ramp in x for a beam deflector with a deflection angle given by the generalized law of refraction [20]:

$$n_t \sin\theta_t - n_i \sin\theta_i = \frac{\lambda_0}{2\pi}\frac{d\Phi}{dx} \tag{4.21}$$

where n_i and n_t are the local indices of refraction, θ_i and θ_t are the angles of incidence and transmission, λ_0 is the vacuum wavelength and Φ is the abrupt phase shift at the interface.

Assuming operation in vacuum ($n_i = n_t = 1$) and normal incidence ($\theta_i = 0$), we can substitute the second term of our phase function for the abrupt phase shift at interface, i.e., $\Phi = Ad(2d_0+d)x$, and solve for θ_t

$$\theta_t = \sin^{-1}\left[\frac{\lambda_0 A d(2d_0+d)}{2\pi}\right] \tag{4.22}$$

which represents the deflection angle of the focal axis.

For example, in our fabricated device with an operating wavelength $\lambda_0 = 1550\ nm$, a cubic parameter $A = 2.5335 \times 10^{14}\ m^{-3}$, a built-in center-to-center offset $2d_0 = 20\ \mu m$, and a maximum actuated displacement along one direction $d = 3.17\ \mu m$, the estimated tilting of the focal axis can be calculated as

$$\theta_t = \sin^{-1}\left[\frac{(1550\ nm)(2.5335\times10^{14}\ m^{-3})(3.17\ \mu m)(20\ \mu m+3.17\ \mu m)}{2\pi}\right] = 0.263° \tag{4.23}$$

which is expected to be small in magnitude for an ideal device. The optical axis tilting in Figure 4.17 is slightly larger than 1°, most likely due to fabrication variations and imperfect assembly.

4.4.6 *Alvarez Metalens with Manual Tuning to Explore the Effect of Aperture Size*

We measured the performance of Alvarez meta-optic lenses via manual tuning to investigate the causes of the observed deviation in measured focal tuning behavior of the MEMS Alvarez metalens from the designed Alvarez behavior under ideal conditions. These devices consisted of Alvarez metalenses fabricated with the same meta-optic designs for the 200 µm aperture (as reported in the main text) and additional Alvarez metalens with increased aperture sizes of 500 µm and 1 mm but without the MEMS actuator structures. Two complementary Alvarez meta-optics were mounted on two 3-axis translational stages in a setup similar to what is shown in Figure 4.10. The meta-optics were then manually brought against each other as closely as possible without scratching, aligned and then actuated laterally for equal displacement in opposite directions to generate focal tuning. Due to the accuracy limitation of manual actuation, larger ranges of displacement were introduced, leading to larger focal tuning ranges than the MEMS Alvarez metalens reported in Section 4.4.3. In the manual experiments, the tuning behaviors on both the

diverging and converging sides of the Alvarez lens were investigated, as shown in Figure 4.19, by introducing center-to-center offsets between the meta-optics in the opposite directions.

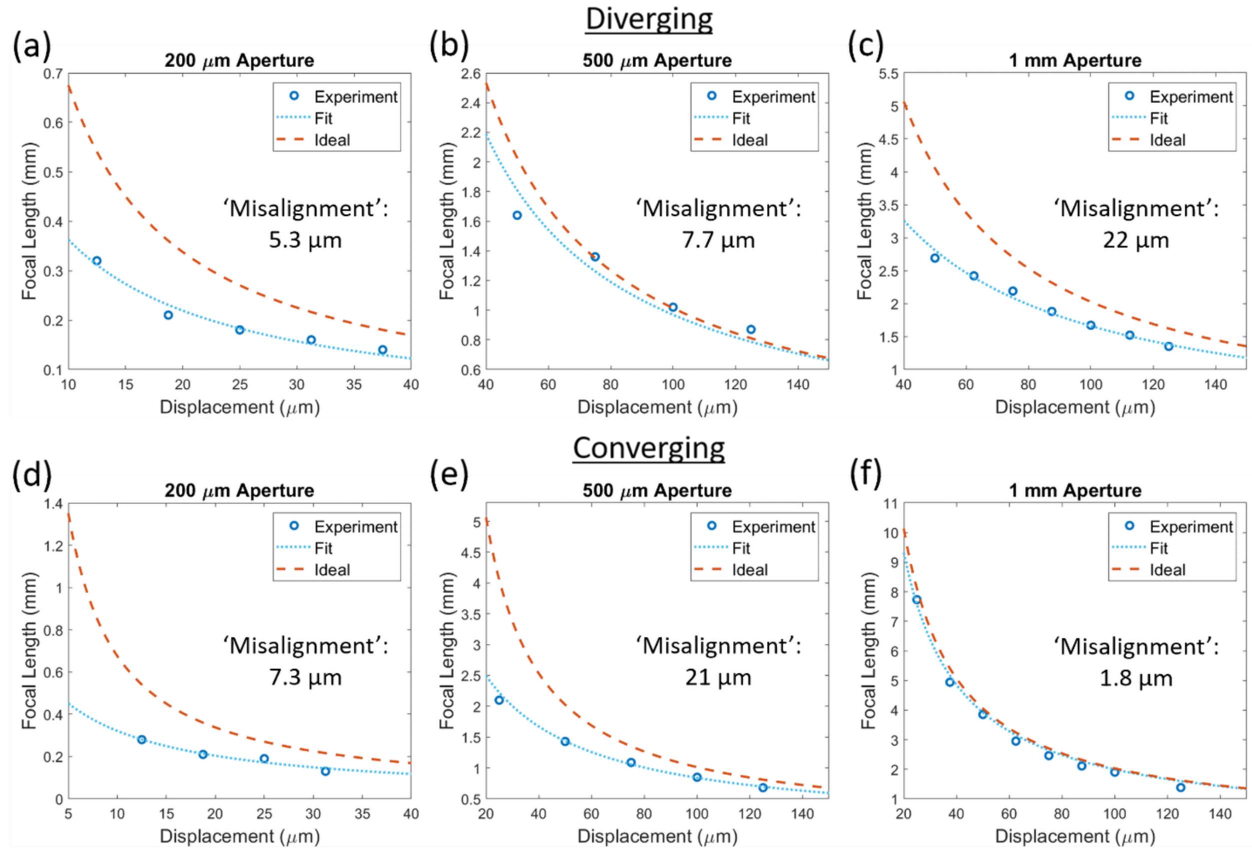

Figure 4.19. Focal tuning by manually displacing the Alvarez meta-optics relative to each other, on the diverging side with an aperture size of (a) 200 μm, (b) 500 μm, and (c) 1 mm, and on the converging side with an aperture size of (d) 200 μm, (e) 500 μm, and (f) 1 mm, compared to the corresponding ideal Alvarez behaviors. The 'misalignment' values estimate the deviation of the fitted Alverez metalens tuning behavior from the ideal designed Alvarez tuning behavior. Manual tuning data acquisition by Shane Colburn and Luocheng Huang from the NOISE Lab.

We measured the performance of Alvarez meta-optic lenses via manual tuning to investigate the causes of the observed deviation in measured focal tuning behavior of the MEMS Alvarez metalens from the designed Alvarez behavior under ideal conditions. These devices consisted of Alvarez metalenses fabricated with the same meta-optic designs for the 200 μm aperture (as reported in the main text) and additional Alvarez metalens with increased aperture sizes of 500 μm

and 1 mm but without the MEMS actuator structures. Two complementary Alvarez meta-optics were mounted on two 3-axis translational stages as shown in the setup (Figure 4.10). The meta-optics were then manually brought against each other with a negligible axial separation gap, aligned and then actuated laterally for equal displacement in opposite directions to generate focal tuning. Due to the accuracy limitation of manual actuation, larger ranges of displacement were introduced, leading to larger focal tuning ranges than the MEMS Alvarez metalens reported in the main text. In the manual experiments, the tuning behaviors on both the diverging and converging sides of the Alvarez lens were investigated, as shown in Figure 4.19, by introducing center-to-center offsets between the meta-optics in the opposite directions.

Figure 4.19 shows the recorded shifts in focal position along the optical axis as a function of manually actuated lateral center-to-center displacements between the meta-optics. In each set we plot the experimental data, a fitted curve accounting for lateral misalignment, and also the corresponding ideal behavior of the Alvarez lenses designed with a negligible separation gap, which is governed by the Alvarez lens equation [63]

$$f(d) = \frac{\pi}{2\lambda A d} \tag{4.24}$$

where f denotes the focal length, λ the operating wavelength, A the design cubic parameter, and d the displacement translated by the complementary meta-optics in the opposite directions giving a total center-to-center offset of $2d$.

The manually tuned focal lengths of the 200 μm metalens at small displacements are similar to the corresponding focal lengths electrostatically tuned in the MEMS-actuated Alvarez metalens with an initial center-to-center offset of 20 μm (details in the Section 4.1.1), showing that the MEMS integration process has limited effect on the tuning behavior deviation and therefore

probably not the main cause. Meanwhile, all the manually tuned focal positions with various aperture sizes have exhibited smaller values than the corresponding ideal predictions.

While fitting the measured data to the Alvarez tuning curve, a 'misalignment' value Δd was calculated as an estimation of the misalignment introduced during manual assembly of the Alvarez metalens, assuming only translational misalignment along the actuation direction, hence causing the deviation of the fitted experimental Alvarez curve from the ideal Alvarez curve following the relation

$$f(d) = \frac{\pi}{2\lambda A(d+\Delta d)} \tag{4.25}$$

The discrepancies in the 'misalignment' values for the same Alvarez lens (for diverging and the converging configuration, see Figure 4.19) indicate that there could be misalignment in directions other than translational. Nevertheless, these 'misalignment' values can act as crude quantitative estimates of the extent of total misalignment between the meta-optics and can be used for preliminary behavior analysis across different aperture sizes.

During the design of Alvarez meta-optics, we chose various cubic parameters (values of A) for each aperture size to achieve desirable tuning behaviors – typically a smaller cubic value for a larger aperture – which is also likely to affect the device tolerance on misalignment.

Meanwhile, Figure 4.19a and Figure 4.19b show that an Alvarez metalens with a larger aperture generally has a higher tolerance to misalignment and can still perform much better (closer to the ideal scenario) than one with a smaller aperture and a smaller misalignment. However, the comparison between Figure 4.19b and Figure 4.19c also shows that such increased tolerance due to larger aperture still has its limit, especially when the misalignment in the optical element is significantly worse. In conclusion, the quantitative comparison between the fit and ideal curves

shows that the deviation between the experiment and theory increases as the aperture size of meta-optics decreases, probably with lower tolerance to misalignment overall.

4.5 Discussions and Conclusion

We have designed, fabricated, and characterized a MEMS-actuated meta-optic lens with a tunable focus modulated based on the Alvarez tuning principle. With voltage application below 20 V, actuated displacement of up to 6.3 μm has given rise to focal length modulation over a range of 68 μm, corresponding to more than 10 times scaling between the actuation input and focal tuning output. The MEMS electrostatic actuation using linear comb drives provides high controllability for its quadratic relation between the actuated displacement and actuation voltage. Replacing bulky freeform optics with flat, wavelength-scale thick meta-optics together with the MEMS-driven Alvarez structure will allow the ultimate miniaturization of optical devices with tunable focal length, making them more mechanically and thermally robust, with advantages such as fast tuning, compact size, simple packaging, and low energy consumption.

Such MEMS-actuated Alvarez metalenses with a tunable focus in IR or visible frequencies will have great potential in 3D imaging and depth-sensing applications such as realizing mixed reality displays [73-75] and ultra-compact endoscopes [76, 77]. Additionally, by using a pair of quartic meta-optics and computational imaging, the color information can be incorporated in a similar tunable geometry [78]. Their full compatibility with well-established semiconductor microfabrication technologies allows them to be mass-produced with high reproducibility.

Although in the work reported here we have mainly focused on a MEMS-actuated Alvarez metalens with a 200 μm square aperture, Alvarez metalenses with larger apertures have been demonstrated with manual actuation [25, 63] and the Alvarez tuning principle is capable of continuously producing further focal tuning with an increasing lateral displacement between the

two optical elements while maintaining high tuning efficiency. With the successful demonstration of the current MEMS Alvarez metalens, a larger lateral actuation can be achieved by reconfiguring the electrostatic MEMS actuator design or adjusting the actuation voltage below the pull-in threshold. The focusing behavior is significantly affected by the axial separation between the two Alvarez meta-optics created during bonding. Uneven resin curing in this process can also lead to wedge errors which will shift or distort the focal spot. To mitigate this, a thinner spacer layer deposited with high uniformity is desirable and a larger area of Alvarez meta-optics can be implemented to increase the aperture size.

While this work has demonstrated a MEMS-actuated meta-optic Alvarez lens operating in the IR spectrum, others have reported a meta-optic-based Alvarez lens operating for visible wavelengths when manually displaced on a fine translation stage [25]. While our current Alvarez meta-optics are fabricated with silicon nitride nanoposts on a silicon membrane or substrate, the silicon underneath the Alvarez meta-optics can be replaced with silicon oxide or quartz to create a clear optical path for the visible wavelength operation.

Chapter 5. LARGE-APERTURE NEAR-IR MEMS ALVAREZ METALENS

Here, we demonstrate a MEMS-tunable, 0.5-mm aperture infrared (IR) meta-optical lens exploiting the Alvarez principle. The reported focal length tuning range is 3.1 mm, approximately 40 times more than that of previous works [79, 80]. Aperture size and tuning range increases are facilitated by new models for the Alvarez meta-optics, redesign of the mechanical structures to support larger aperture and focal tuning range, and a novel bonding process to ensure better alignment between two meta-optics and negligible axial gap between meta-optics. We demonstrate how the MEMS Alvarez lens's mechanical properties, actuation range, natural frequency, and tuning sensitivity can be readily modified by adjusting the comb-drive design parameters with minimal to no change in the device footprint. Additionally, the comb-drive actuators allow changing aperture size easily without drastically altering the actuator's operating mechanism or footprint. Such conveniences provide significant design flexibility either to accommodate particular application requirements or to improve focal tuning efficiency. The entire fabrication process is CMOS compatible using common semiconductor materials without involving electron-beam lithography, suitable for potential high-volume, low-cost mass production.

5.1 Design Parameters

The design of MEMS-integrated Alvarez meta-optics involves two main parts. First, we map the two complementary cubic surfaces onto the quasi-periodic arrays of flat meta-optics. Second, we design electrostatic actuators to induce the required lateral displacement to modulate the optical power of the assembled Alvarez lens.

5.1.1 *Alvarez Metalens Parameters*

We have designed a pair of square Alvarez meta-optics with an aperture size of 0.5 mm. They host complementary cubic surface profiles for a designed operating wavelength of 1550 nm. The regular and inverse surfaces have the phase distributions described in Eq. (3.1).

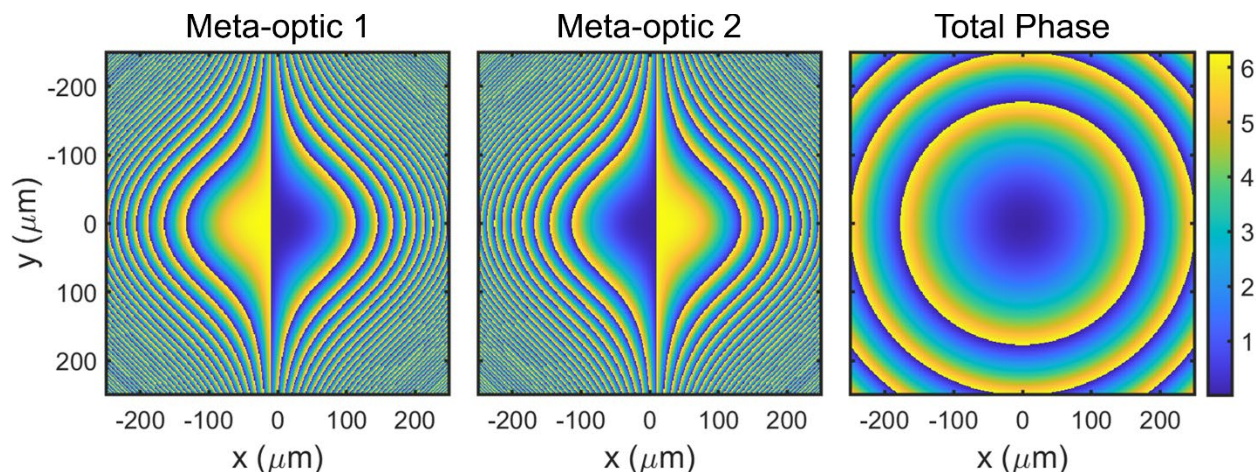

Figure 5.1. The designed cubic phase profiles for the two complementary Alvarez meta-optics and the total quadratic phase profile when they overlay. The designed Alvarez meta-optics have an operating wavelength λ = 1550 nm, a built-in offset of 40 μm, and a cubic parameter A = 1×10^{13} m^{-3}. Colorbar indicates a 2π phase span in radian.

As illustrated in Figure 5.1, when overlapped with a nonzero center-to-center offset, the two Alvarez cubic surfaces in conjunction impart a quadratic total phase profile on an incident wavefront, with the form described by Eq. (3.2), whose focal length is tunable with laterally displacing the two surfaces in the opposite direction by an offset of d each (giving a total center-to-center offset of $2d$). With the constant d^3 term being inconsequential, the quadratic term of the total Alvarez phase profile can be related to that of a standard quadratic lens, giving the reciprocal relation between the tunable focal length f and symmetric lateral displacement d as Eq. (3.3). We note that, with the analytical expression of the Alvarez lens, we can readily scale the lens design to any arbitrary aperture and focus-tuning range by adjusting the parameters.

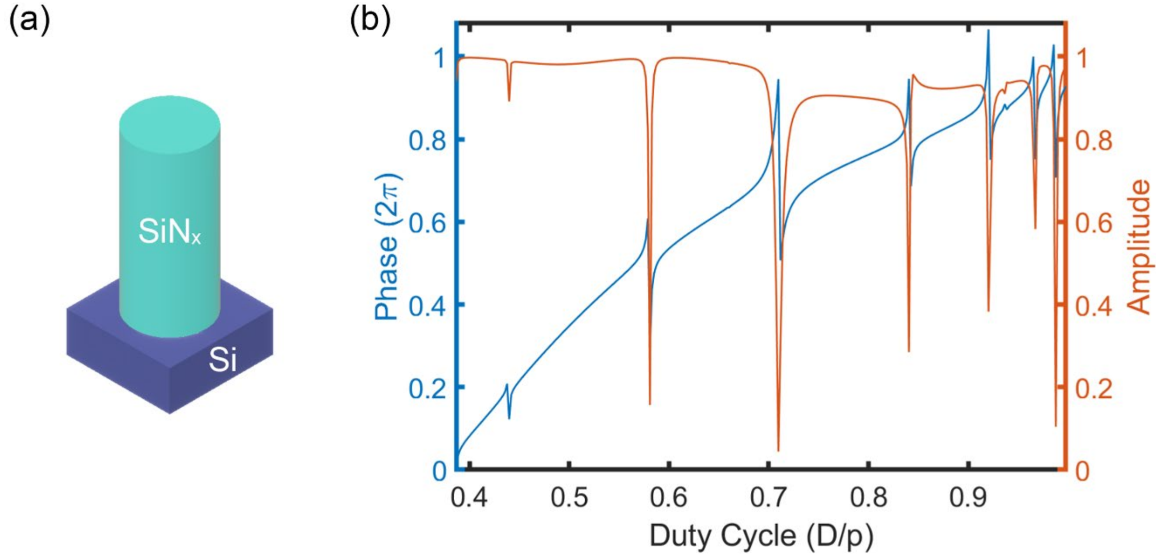

Figure 5.2. Design of the Alvarez meta-optic. (a) Schematic of the scatterer made of a cylindrical silicon nitride nanopost on a silicon substrate. (b) The simulated transmission coefficients for the nanoposts as a function of the duty cycle (diameter/periodicity).

We chose cylindrical nanoposts fabricated using silicon nitride on a silicon substrate as the scattering elements, as shown in Figure 5.2a. Via rigorous coupled-wave analysis (RCWA), the transmission coefficients and phase shifts of the nanoposts for a fixed lattice constant of 1.3 μm and a post height of 2 μm are simulated as a function of the grating duty cycle, defined as the ratio between the post diameter and pitch. The calculated phase spans from 0 to 2π while maintaining near-unity transmission amplitude, as shown in Figure 5.2b. The phase profile is then quantized into six linear steps of duty cycle, giving the corresponding six cylindrical post diameters between 513 nm and 1172 nm. Such dimensions are achievable with high-throughput stepper lithography [63], and we map them to the square array to construct the cubic phase profiles on the Alvarez meta-optics. We introduce an initial 40 μm center-to-center offset between two meta-optics. The focal length is then further tuned by introducing an additional displacement to this built-in offset via MEMS actuation.

Table 5.5 lists the design dimensions for the two complementary Alvarez meta-optics, including the square array layouts and the individual nanoposts used to map the cubic surface profiles. The six linear steps of nanopost duty cycles and their corresponding diameters are selected from the simulated transmitted coefficients (presented in Figure 1 of the main paper) to produce a near-unity amplitude and a phase range from 0 to 2π.

Table 5.5. Large-aperture Alvarez metalens parameters.

Square Array		
Aperture Size	500 μm × 500 μm	
Lattice Constant	1.3 μm	
Post Height	2 μm	
Individual Elements	Duty Cycle	Diameter (μm)
Nanopost 1	0.3948	513.3
Nanopost 2	0.4316	561.1
Nanopost 3	0.4991	648.8
Nanopost 4	0.5932	771.1
Nanopost 5	0.7404	962.5
Nanopost 6	0.9019	1172

5.1.2 *MEMS Actuation Platform Parameters*

The conventional configuration of the Alvarez lens displaces two complementary cubic optics symmetrically in opposite directions to modulate the center-to-center offset for focal tuning. Here, to ensure fabrication robustness, we chose to alter the conventional mechanism to actively displace only one meta-optic relative to its static complement, producing a net change in the center-to-center offset between the two cubic surfaces.

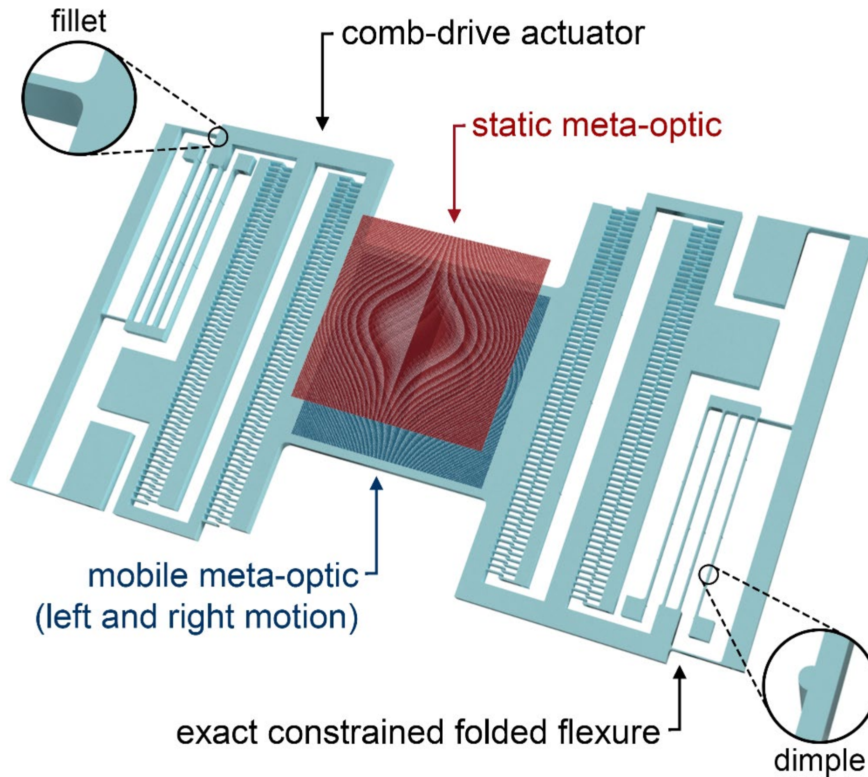

Figure 5.3. Schematic of Alvarez meta-optics integrated with an electrostatic MEMS actuator.

Comb-drive actuators exemplified in Figure 5.3 have high voltage-force conversion efficiencies realized by increased edge coupling length with the interdigitated fingers [67]. Hence, we employ them to electrostatically control the lateral displacement of the mobile meta-optic. The meta-optic sits on a central platform with comb drives on opposite sides to control the displacement in both positive and negative directions along the actuation axis. The symmetric design enhances the mechanical stability and doubles the range of actuation without doubling the maximum voltage required. The magnitude of electrostatic force F_{el} driving the lateral motion is quadratically dependent on the applied voltage as described by Eq. (3.5).

To generate the restoring mechanical force in the actuator, we design a modified version of the exact constrained folded flexures [17] for their sideways stiffness stability at relatively large displacement. As shown in the circular insets of Figure 5.3, we introduce fillets (rounding of

corners) at mechanical hot spots to reduce, redistribute and partially relieve stress created during actuation and prolong device lifetime especially for many-cycle operations. We also introduce horizontal dimples (small protrusions) sparsely placed along the backbones and long springs in the folded flexures to prevent structural sticking if accidentally running into contact during large-displacement operation.

By Hooke's law, the displacement is linearly proportional to the spring force in the flexure with a spring constant k_{sp}. Hence at the equilibrium between the electrostatic driving force and restoring spring force, the actuated lateral displacement Δd is quadratically dependent on the applied voltage following the relation described in Eq. (3.11). Such direct dependence of the displacement on the driving voltage provides for high reproducibility and controllability in any calibrated system. Because of the electrostatic actuation mechanism, no current flows in the device when applied with direct-current (DC) voltages, enabling very low-power consumption at no more than several nanowatts.

To examine how different dimension parameters affect the electro-mechanical performance of the actuator platform, we have fabricated and tested two designs with different spring lengths and finger arrays for comparison. Table 5.6 summarizes the dimensions and performances of the two designs.

Table 5.6. Design parameters and performances of the large-aperture MEMS Alvarez meta-optic lens.

		Design 1	Design 2
Comb Fingers	Width (μm)	2	3
	Length (μm)	40	40
	Height (μm)	11	11
	Gap (μm)	2	2
Folded Springs	Width (μm)	4	4
	Length (μm)	700	500
	Height (μm)	11	11
	Lateral Stiffness (N/m)	1.15	2.29
	Natural Frequency (Hz)	1300	1800
Focal Tuning	Voltage (V)	–10 to +40	–15 to +55
	Displacement (μm)	–1.2 to +18.1	–0.5 to +13.1
	Focal Length (mm)	5.8 to 2.7	6.0 to 3.0

5.2 DEVICE FABRICATION

We fabricate two complementary Alvarez meta-optics on two separate substrates before aligning and bonding them to form the final Alvarez lens.

5.2.1 *Microfabrication Process Flow*

Figure 5.4 summarizes the fabrication process flow. Compared to our previous demonstration [80], given that we are now integrating a significantly larger meta-optic on the MEMS platform and using modestly higher actuation voltages to induce larger displacements, to alleviate any out-of-plane sagging offset of the release optics due to imbalanced fringing fields, a thicker silicon layer of 11 μm is employed for the actuator. Similarly, to assist a more efficient and stable release process for the suspended flexures, we have carefully designed the release hole patterns to create a more even exposure for release reactions while still ensuring strong mechanical stability within

the flexures. Finally, we employ a flip-chip bonding process to reduce the vertical separation down to 10 μm and lateral misalignment to less than 3 μm between the two meta-optics.

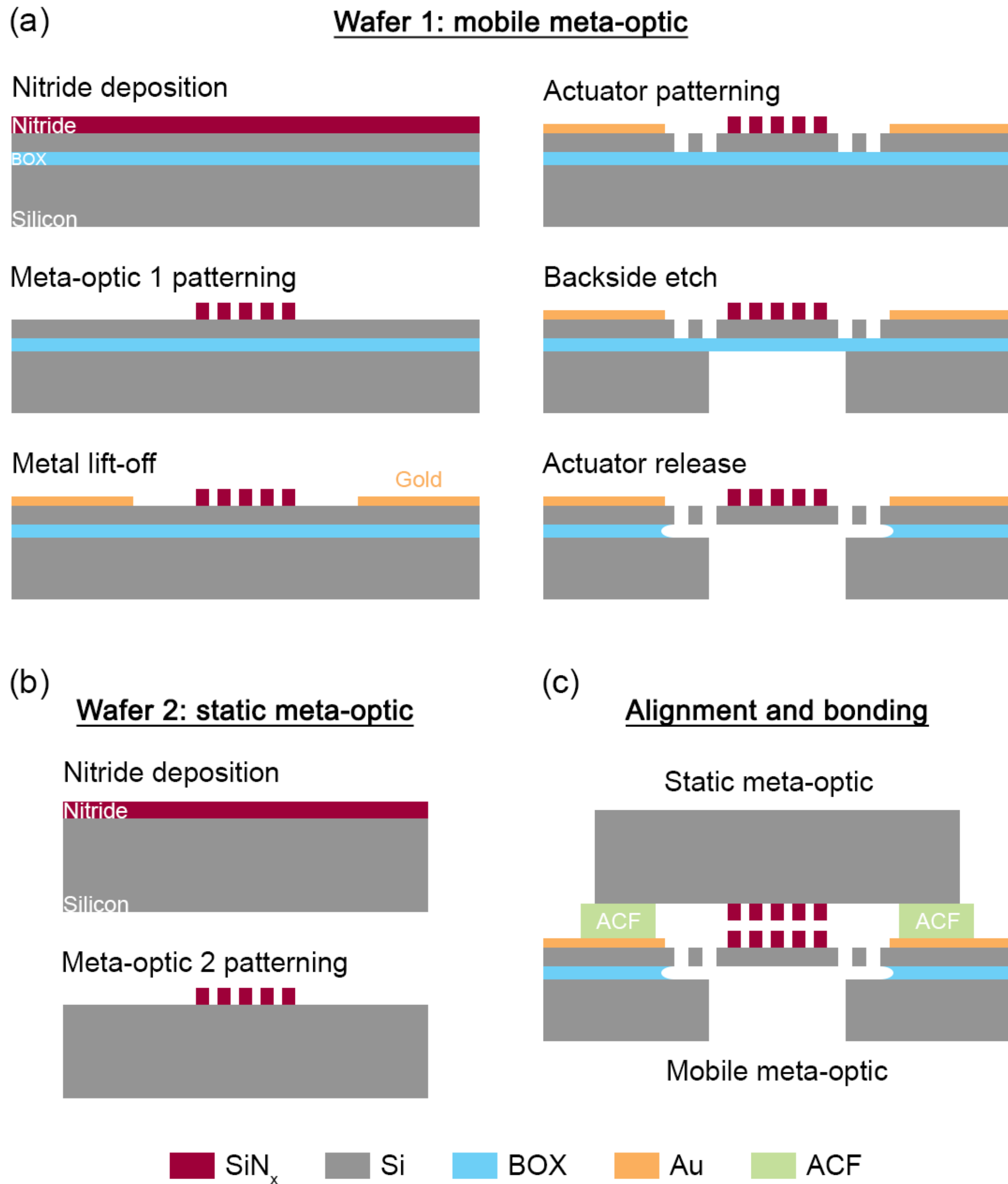

Figure 5.4. Summarized device fabrication process flow.

We fabricate the mobile meta-optic on a silicon-on-insulator (SOI) wafer with the electrostatic actuators, as shown in Figure 5.4a. A 2 μm thick silicon nitride layer is first deposited with plasma-

enhanced chemical vapor deposition (PECVD) on the SOI wafer. We employ i-line stepper lithography to pattern the meta-optic with high throughput. The meta-optic pattern is then transferred to the silicon nitride layer via fluorine-based inductively coupled plasma (ICP-F) etching utilizing an aluminum hard mask. A metal stack consisting of 10 nm thick chromium and 150 nm thick gold is evaporated and lifted off to form the contact lines and probing pads defined by direct-write lithography. The 11 μm thick silicon device layer is then patterned with the actuator design using direct-write lithography and etched with deep reactive-ion etching (DRIE). We use direct-write lithography for quick prototyping of various actuator designs. This step can be easily replaced by more efficient flash exposure processes such as stepper lithography for cost efficiency in potential high-throughput production. After the actuator fabrication, a backside DRIE step is performed to remove the 400 μm handle silicon under the central meta-optic plate to aid the later release process. The wafer is diced into individual chips containing multiple devices before being etched in vapor hydrogen fluoride (vHF) to remove the exposed buried oxide (BOX) and release the actuator with the mobile meta-optic.

We fabricate the static meta-optic on a 525 μm thick double-side polished silicon wafer, as shown in Figure 5.4b. Similarly, a 2 μm layer of PECVD silicon nitride is deposited, and the static meta-optic is patterned with stepper lithography followed by ICP-F etching into the thin film. The wafer is then diced into individual chips, each containing multiple meta-optics corresponding to their mobile counterparts.

The mobile meta-optic on the MEMS actuator and the static meta-optic are then assembled to create the complete Alvarez unit, as shown in Figure 5.4c. For an Alvarez lens, it is crucial to have a small gap between two optics [25]. To ensure that, the chip with mobile meta-optics and the one with static meta-optics are aligned and bonded on a flip-chip bonder, using pieces of an anisotropic

conductive film (ACF) both as the spacer and the adhesive layer to create a significantly smaller axial gap with high controllability. This commercial ACF contains polymer particles in a thermoplastic adhesive matrix. The spherical particles have radii around 10 μm. After applying heat and pressure, the adhesive spacer flows to a thickness measured to be approximately 10 μm and cross-links, securing the two chips in an aligned stack with a minimal gap sufficient to prevent meta-optic scratching during operation.

5.2.2 *Meta-optics Protection during Vapor Hydrogen Fluoride Etching*

After the first batch of devices, we realize that our silicon nitride deposited by PECVD has a relatively high susceptivity to chemical attack by vapor hydrogen fluoride during the last fabrication stage of MEMS release. As shown in the comparison in the SEM images of Figure 5.5, the silicon nitride meta-optic is severely etched by the hydrogen fluoride, and the loss of scatterer definition inevitably affects the device performance. Macroscopically, the HF-attacked silicon nitride meta-optic turns reddish brown, as shown by the difference between Figure 5.6a and b.

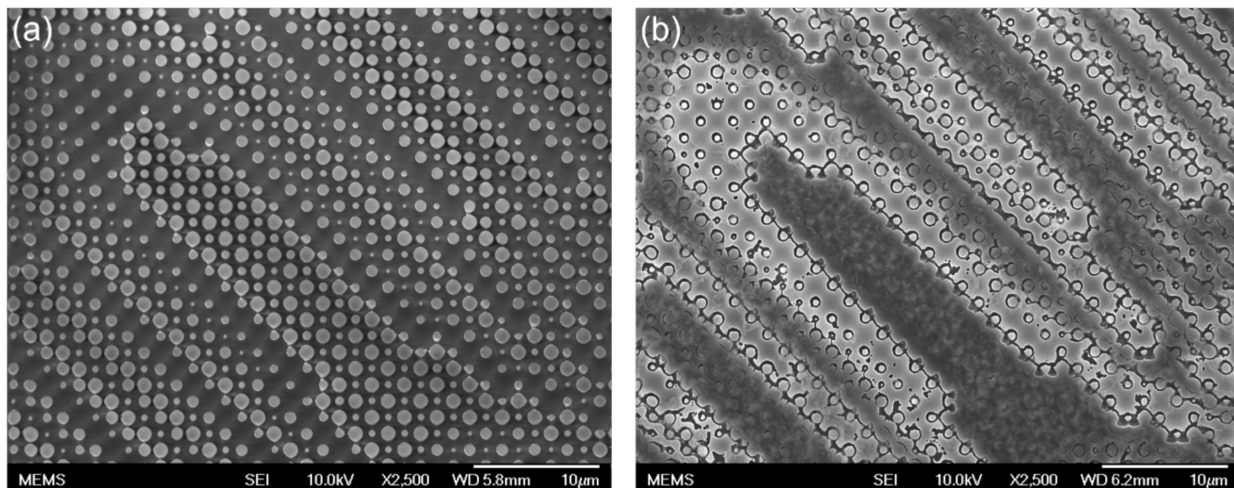

Figure 5.5. SEM images of silicon nitride meta-optics (a) before and (b) after vapor hydrogen fluoride (vHF) etching.

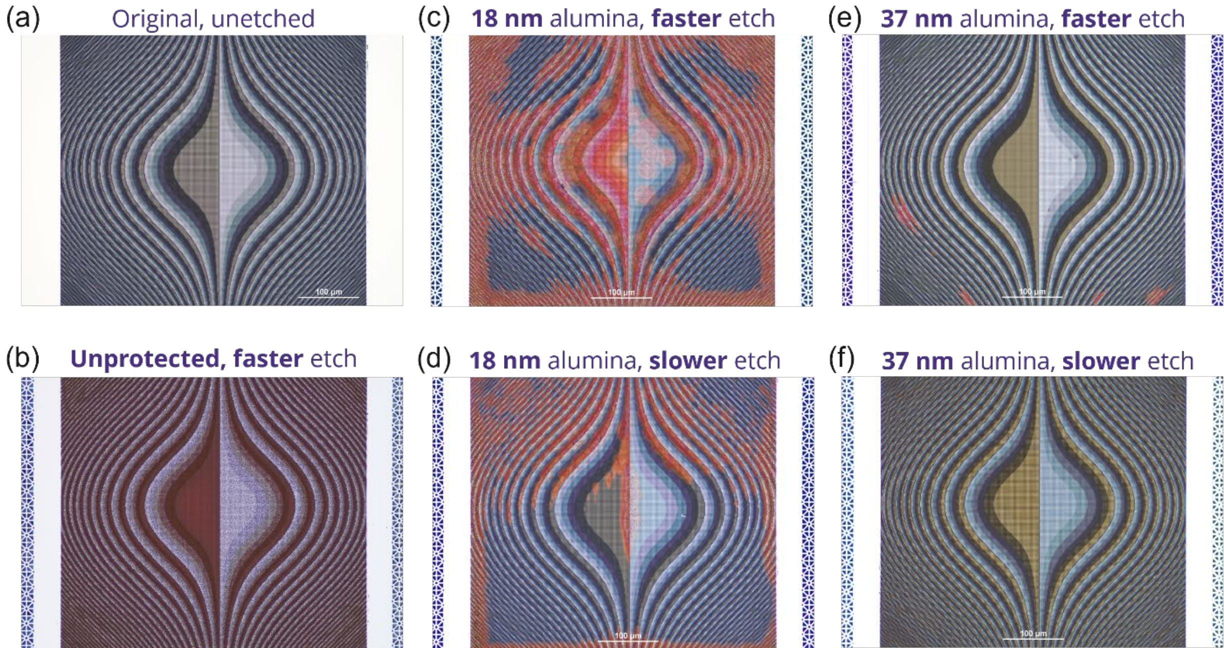

Figure 5.6. Optical images of silicon nitride Alvarez meta-optics before and after vHF etching. (a) Uncoated meta-optic before vHF etching. (b) Uncoated meta-optic etched with a fast-etching vHF process. (c) Meta-optic coated with a thin layer of ALD alumina and etched with a fast-etching vHF process. (d) Meta-optic coated with a thin layer of ALD alumina and etched with a slow-etching vHF process. (e) Meta-optic coated with a thick layer of ALD alumina and etched with a fast-etching vHF process. (f) Meta-optic coated with a thick layer of ALD alumina and etched with a slow-etching vHF process.

As a measure to protect the silicon nitride meta-optics from being damaged by vapor hydrogen fluoride during release, we explore the potential of slowing down chemical attack by two primary means – the introduction of an alumina protection coating and changing the etch rate of the vHF process. We employ atomic layer deposition (ALD) to create an alumina coating covering the silicon nitride meta-optics and use ellipsometer to verify the deposited thickness with high precision.

We first deposit an alumina layer of 18 nm and etch the device with the same original vHF release process, which has a faster etch rate and a shorter etching time. As shown in Figure 5.6c, though the alumina-protected meta-optics is still attacked by vHF, the area of attack has decreased

compared to the unprotected case of Figure 5.6b. Then we switch the vHF release process to an alternative recipe with a slower etch rate but longer total etching time. With the same 18-nm thick alumina protection, we reach the result of Figure 5.6d showing a further reduced attack on the silicon nitride meta-optics.

We double the alumina deposition time and increase its thickness to 37 nm. The corresponding devices after both faster (Figure 5.6e) and slower vHF (Figure 5.6f) release etching processes have shown further improvement in meta-optic protection. The combination of the thicker 37 nm alumina protection and a slower vHF etching process produces the best outcome in Figure 5.6f where no visible chemical damage is observed after the full vHF release process.

To sum up, the result comparison between the rows (Figure 5.6c to d, e to f) indicates that increasing the alumina layer thickness has granted more protection for the silicon nitride meta-optics. At the same time, the result comparison across columns (Figure 5.6c to e, d to f) shows that employing a vHF process with a slower etch rate (even with a longer total etching time) has reduced the extent of chemical attack. Therefore, a good combination of introducing alumina protection and slowing down vHF etching can effectively prevent damage to the silicon nitride meta-optics during the MEMS release process and preserve device integrity.

5.2.3 *Fabricated Devices*

Figure 5.7a and Figure 5.8a show the two fabricated designs of mobile meta-optics on the central silicon platform of a comb-drive actuator before bonding with their static counterparts. Figure 5.7b and Figure 5.8b captures the interdigitated fingers that generate the electrostatic force driving the lateral displacement upon voltage application and part of the release holes designed to assist the vHF process in releasing the mobile half comb-drive for actuation. Figure 5.7c and Figure 5.8c

zoom into a portion of the meta-optic consisting of silicon nitride nanoposts with varying diameters arranged in a two-dimensional quasi-periodic array to construct one Alvarez meta-optic.

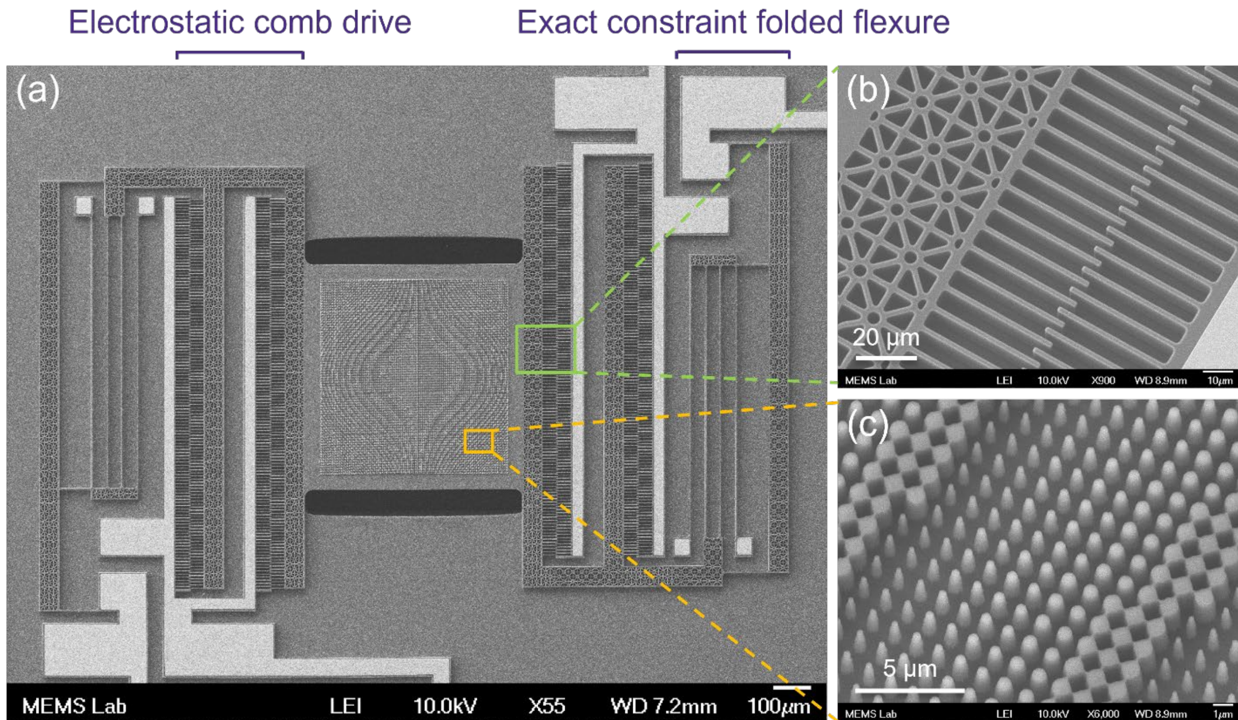

Figure 5.7. Scanning electron microscopy (SEM) images of Alvarez meta-optic lens with actuator Design 1. (a) An Alvarez meta-optic integrated with a MEMS tuning platform. (b) Comb-drive details showing the part of the mobile flexure backbone and interdigitated finger array. (c) Close-up view of the silicon nitride nanoposts sitting on the central silicon platform.

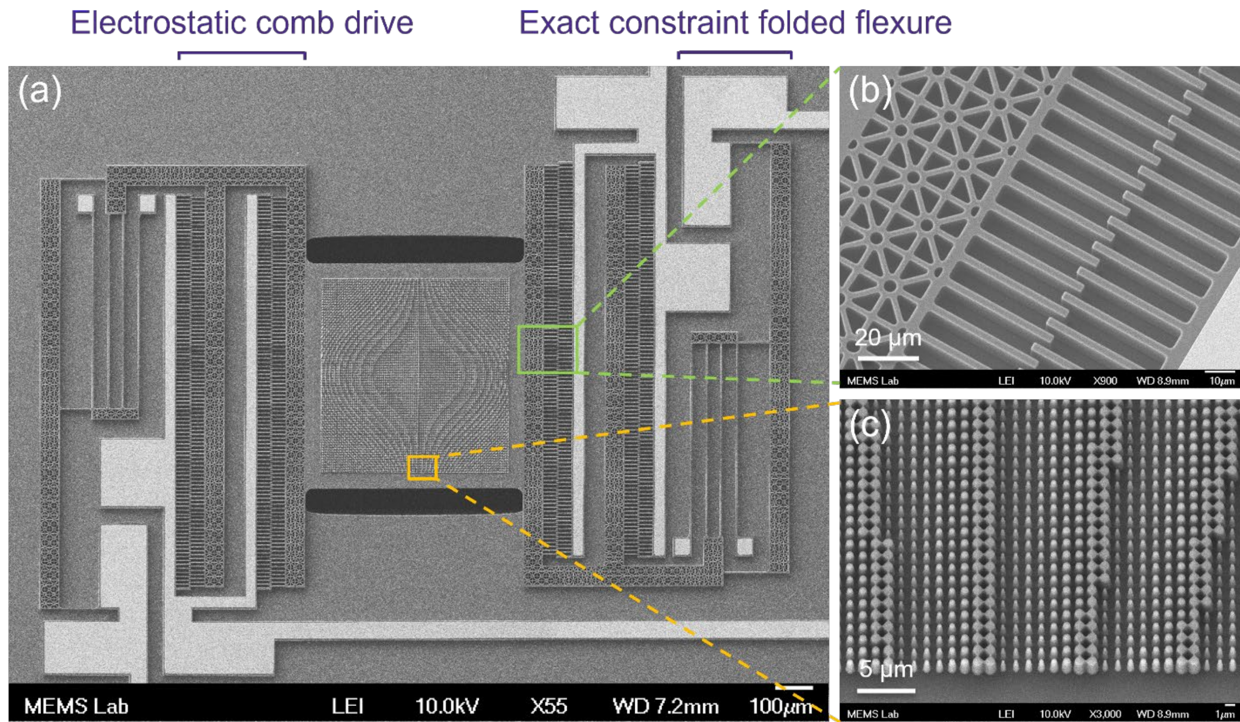

Figure 5.8. Scanning electron microscopy (SEM) images of Alvarez meta-optic lens with actuator Design 2 with shorter springs and wider fingers. (a) An Alvarez meta-optic integrated with a MEMS tuning platform. (b) Comb-drive details showing the part of the mobile flexure backbone and interdigitated finger array. (c) Close-up view of the silicon nitride nanoposts sitting on the central silicon platform.

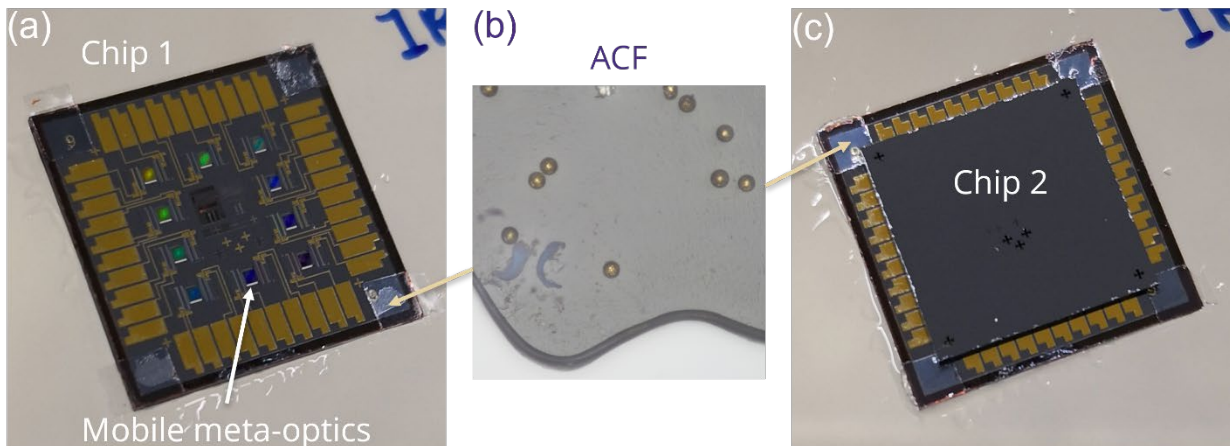

Figure 5.9. Assembly of the Alvarez meta-optic lens showing (a) the bottom chip 1 carrying 10 mobile meta-optics and (c) the overlaid top chip 2 carrying 10 static meta-optics facing down (right), bonded with (b) anisotropic conductive film (ACF) as both the spacer and the adhesive.

Figure 5.9 captures an SOI chip carrying 10 mobile meta-optics on electrostatic actuators, each having an overall device footprint of 2 mm × 1.2 mm. Figure 5.9f shows the final Alvarez stack when the second chip with 10 complementary stationary meta-optics is aligned and bonded face-down with its mobile counterpart. The exposed contact pads along the chip edges are used for electrical probing during the focal tuning tests. The measurements at the chip-to-chip alignment marks confirm that the translational misalignment does not exceed 3 µm in all directions, and the rotational misalignment is less than 0.03° between the two meta-optics.

5.3 Experimental Setup

Figure 5.10 illustrates the general experimental setup for all the MEMS actuation and focal tuning measurements. The chip stack containing Alvarez meta-optic lenses is affixed using transparent ultraviolet (UV) resin to a microscope slide, which is clamped vertically on a 3-axis micro-manipulator stage, perpendicular to the optical axis. We probe the Alvarez lens with a DC voltage to laterally actuate the mobile meta-optic relative to the static one. A 1550 nm superluminescent diode (SLD) source illuminates the Alvarez lens through a collimator. The incident light interacts with the meta-optic stack and converges to a focal spot along the optical axis on the other side. An IR microscope setup on a translation stage is used to measure the in-plane intensity profiles.

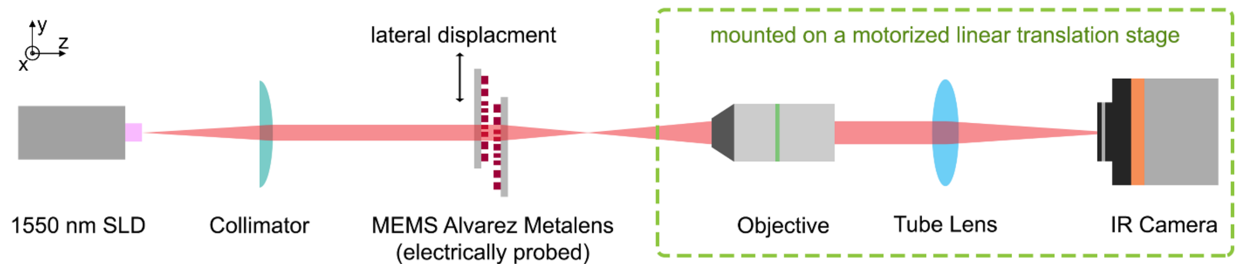

Figure 5.10. Experimental characterization setup for Alvarez lens electrostatic actuation and focal profile acquisition.

5.4 RESULTS AND ANALYSIS

After acquiring the images and videos capturing the operating Alvarez meta-optic lens as functions of the applied voltage, we analyze the MEMS actuation performance and track focal tuning behavior of the device.

5.4.1 *MEMS-actuated Tuning Platform*

Since the electrostatic actuators in our MEMS Alvarez lens consist of comb-drives on both left and right of the central plate, enabling actuation in both directions, we use sign conventions to differentiate the two sides. The positive voltage indicates the stimulus applied on the right comb drives. The corresponding positive displacement pulls the mobile meta-optic towards the right, increasing the center-to-center offset between the Alvarez meta-optic pair. In contrast, negative voltage and displacement values are attributed to the left, reducing the center-to-center offset. To evaluate the performance of electrostatic actuation, we apply a continuous linear voltage ramp from 0 V to 40 V and then back down to 0 V on both sides of the actuator respectively and monitor the lateral displacement at the focal plane via video recording.

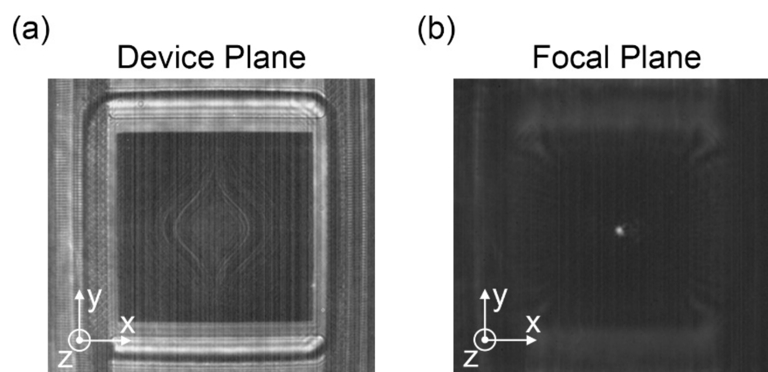

Figure 5.11. Exemplary (a) device plane and focal plane of the Alvarez meta-optic lens actuated at 40 V towards the right.

Figure 5.11a and Figure 5.11b show the representative screenshots displaying the device plane and the corresponding focal plane when the mobile meta-optic is pulled electrostatically towards the right at 40 V. We measure the lateral displacement of the mobile meta-optic at any instance in the video by analyzing the comb-drive motion using edge detection of the compliant flexures.

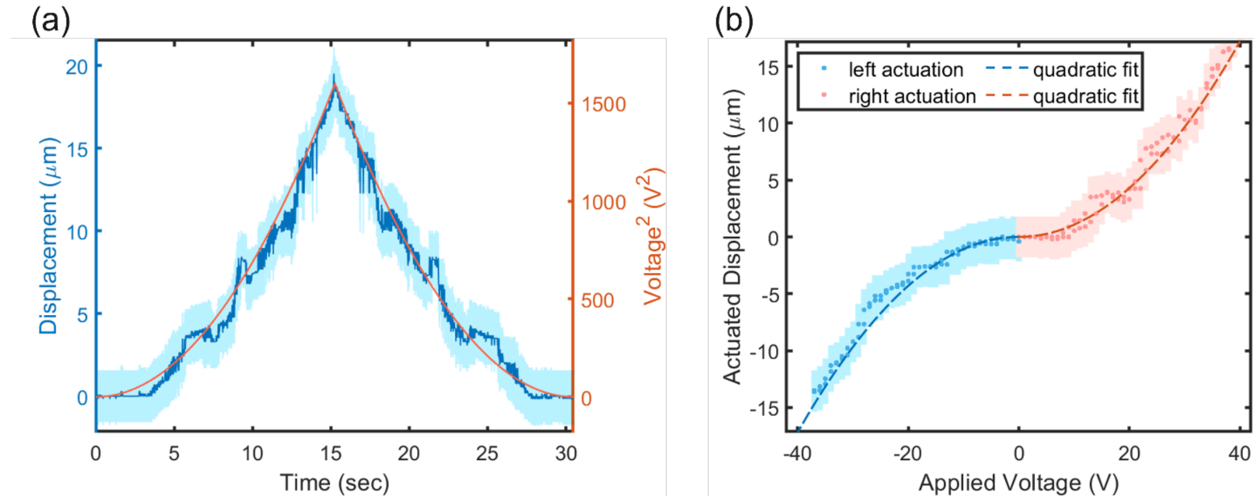

Figure 5.12. Experimental characterization of the MEMS platform with Design 1. (a) Measured actuated displacement and actuating voltage of the MEMS platform follow the same quadratic trend closely, showing negligible hysteresis. (b) Actuated displacement for both directions follows the comb-drive quadratic characteristics closely. The light shade bands indicate the associated error bars.

Figure 5.12a plots the displacement of the mobile meta-optic and the corresponding actuation voltage on the right-side comb drives during the ramping process. The displacement increases from 0 μm to 18 μm before it decreases as the applied voltage rises from 0 V to 40 V and then goes back down. The symmetric local kinks and noise in the displacement curve result from the camera resolution limit and the image intensity nonuniformity due to residual camera artifacts interfering with the edge detection process. The error bars reflect the uncertainty associated with edge detection and camera resolution limit (details described in Section 5.4.4.1). The actuated displacement follows closely with the square of the actuation voltage during both ramp-up and

ramp-down with negligible hysteresis, granting high controllability and reproducibility of the tuning process using such comb-drive actuators. Figure 5.12b plots the displacement versus actuation voltage for actuation on both left and right sides of the same MEMS Alvarez lens. All the data points lie close to the characteristic quadratic displacement-voltage dependency presented in Eq. (3.6), with some minor deviations between the two sides due to fabrication imperfections. The quadratic fitting gives a measured spring constant of 1.15 N/m, close to the analytical estimate of 1.07 N/m. The analytical estimates for the spring constants are based on the folded flexures [69], which effectively determine the compliance in the actuator. The minor discrepancies between the measured and analytical values can be attributed to fabrication imperfections and the addition of side levers for enhanced sideways stability [17]. Compared to the analytical stiffness of 32,700 N/m in the perpendicular direction, the stiffness ratio between the perpendicular and the actuating directions is as high as 28,500, producing guided uniaxial motion with high reliability.

The actuator performance of Design 2 with shorter springs and fewer interdigitated finger pairs is presented in Figure 5.13. Similar to Design 1, the actuated displacement in actuator Design 2 follows the voltage squared curve with negligible hysteresis as shown in Figure 5.13a. Figure 5.13b plots the actuation on both the device's left and right sides, and all the data points lie close to the theoretical quadratic fit between displacement and voltage. Calculation from the fit gives a measured lateral spring constant of 2.29 N/m (close to its analytical estimate of 2.93 N/m). With the analytical perpendicular stiffness being 45800 N/m, Design 2 is shown to have a stiffness ratio as high as 20000, promising guided uniaxial displacement.

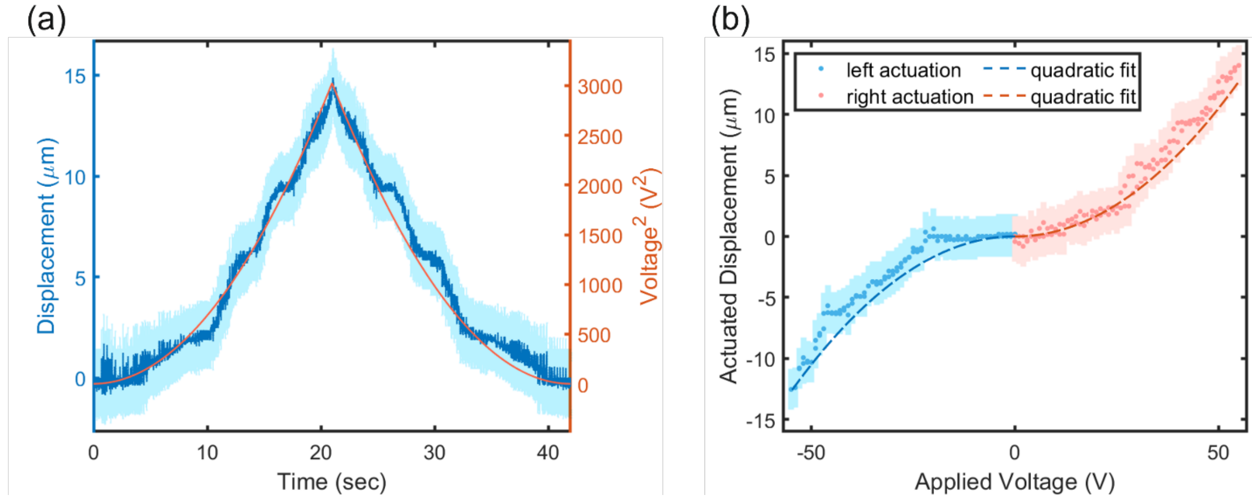

Figure 5.13. Experimental characterization of the MEMS platform with Design 2. (a) Measured actuated displacement and actuating voltage of the MEMS platform follow the same quadratic trend closely, showing negligible hysteresis. (b) Actuated displacement for both directions follows the comb-drive quadratic characteristics closely. The light shade bands indicate the associated error bars.

In both actuator designs, such high stiffness ratios between the perpendicular and lateral directions ensure high robustness during actuation, providing controlled uniaxial displacement essential for tuning Alvarez meta-optics. We note that the stiffness along the perpendicular direction could not be measured in the experiments due to minimal displacement along that direction, which confirms the high-stiffness-ratio design for highly controllable uniaxial actuation.

Both actuator designs have a total mass of mobile structures around m = 18 µg. With the measured spring constants of $k_{sp}^{(1)}$ = 1.15 N/m and $k_{sp}^{(2)}$ = 2.29 N/m, we can calculate the natural frequency of the actuators as

$$f_0 = \frac{1}{2\pi}\sqrt{\frac{k_{sp}}{m}} \tag{5.26}$$

giving the corresponding natural frequencies as $f_0^{(1)}$ = 1.3 kHz and $f_0^{(2)}$ = 1.8 kHz for the two designs, showing potential for kHz operation. The comparison shows that although the second

actuator design has a stiffer structure and requires slightly higher actuation voltage, its resonance will occur at a higher frequency, making the device more robust over a wider operating frequency range. Hence, the actuator designs can be flexibly modified within the same footprint to boost specific attributes to fulfill different application requirements.

5.4.2 *Actuation Power Consumption*

For the MEMS tunable Alvarez meta-optic lenses, we calculate the DC power consumption based on the measured current values and estimate the power consumption per switching based on the measured spring constants and design capacitor dimensions.

5.4.2.1 Static operation at DC voltage

While various DC actuation voltages are applied between 0 V and 40 V on the devices with actuator Design 1, the resultant currents are recorded as shown in Figure 5.14a, which are only several nano-amperes, agreeing with the theory of electrostatic actuation. The source of DC current is probably the leakage current through the substrate. As described in Section 5.4.1, negative voltage values indicate the application to the left comb-drives, while the positive voltage values indicate the application to the right comb-drives. The voltage application on the left side does not continue much further once the focal spot is too stretched and dim to evaluate accurately. The power consumption of the device is calculated as the product of voltage and current

$$P = V \times I = \frac{V^2}{R} \tag{5.27}$$

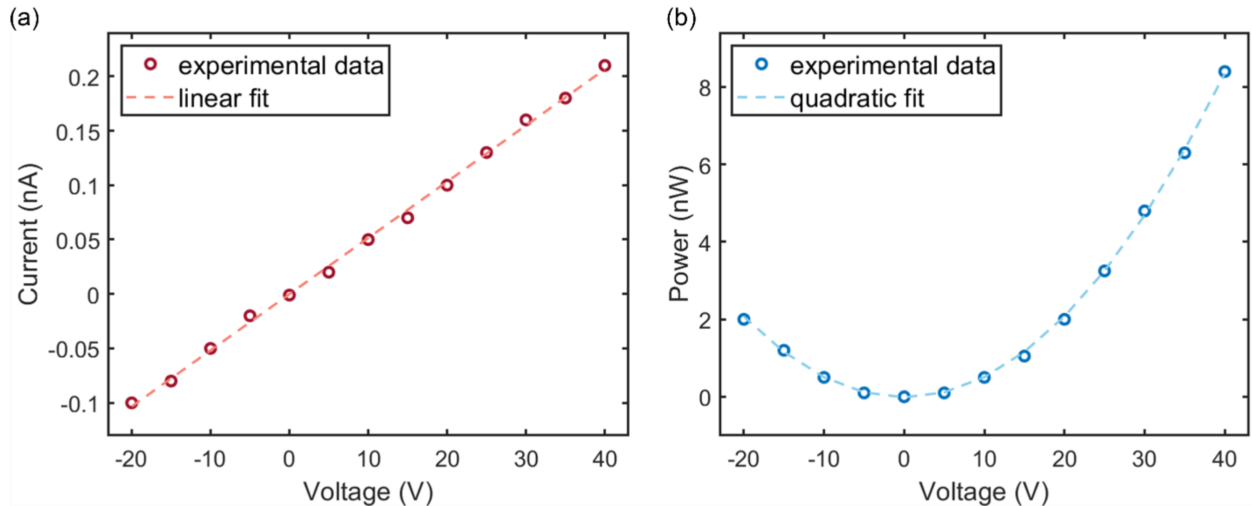

Figure 5.14. Electrical measurements. (a) Measured current and (b) calculated power of electrostatic actuator.

Figure 5.14b plots the power calculated as the product of measured current and actuation DC voltage. The calculated power closely follows the theoretical quadratic dependence on the applied voltage.

5.4.2.2 Energy consumed per switching

Besides the static power calculated in Section 5.4.2.1 for a device held at a constant voltage, we expect a small amount of power consumption whenever the voltage switches and the capacitive energy stored in the comb-drive is built up or released.

Taking Design 1 with dimensions summarized in Table 5.6 as an example, there are N = 252 finger pairs on each actuation side of the device, where finger height h = 11 μm and finger gap d_{sep} = 2 μm. The initial finger overlap is l_0 = 5 μm. For estimation, we will calculate the largest power consumption at the highest application voltage V = 40 V, which induces a maximum lateral actuation of Δd = 18.1 μm. With the dielectric medium being air, when the actuator is at its maximum displacement, the capacitance in the comb drive is

$$C = 2N\frac{\varepsilon(l_0+\Delta d)h}{d_{sep}} = 2\times 252\times\frac{(8.854\times10^{-12}\ F\cdot m^{-1})(5\ \mu m+18.1\ \mu m)(11\ \mu m)}{2\ \mu m} = 0.567\ pF \quad (5.28)$$

and the stored capacitive energy is

$$W = \frac{CV^2}{2} = \frac{(0.567\ pF)(40\ V)^2}{2} = 45.4\ nJ \quad (5.29)$$

Assuming the actuator is operating right below the natural resonance f_0 = 1300 Hz (see Section 5.4.1) before instability sets in, the maximum power consumption can be estimated from the energy required to charge the capacitor per period

$$P = \frac{W}{period} = \frac{45.4\ nJ}{1/1300\ Hz} = 0.590\ \mu W \quad (5.30)$$

realizing low power consumption when operating at kHz tuning frequencies.

For all the actuator operations under DC voltages, the current values detected are in nano-amperes, which are probably due to minor leakage current via the substrate. The resultant powers are no more than 10 nW, realizing very low power consumption with DC operation. We estimate the power consumption at higher operating frequencies by calculating the capacitive energy consumed per switching (i.e., per period) based on the measured properties and design dimensions. With a natural frequency of 1.3 kHz, the MEMS Alvarez lens presented in this paper is estimated to have a maximum switching power consumption below 1 μW, realizing low power consumption for kHz tuning.

5.4.3 *Focal Tuning of the Large-aperture MEMS-actuated Alvarez Metalens*

To tune the focal length, we apply a DC voltage across the comb drives on one side of the mobile meta-optic, displacing it laterally to modulate the center-to-center offset between the two Alvarez meta-optics. The lateral displacement of the mobile meta-optic is found by using edge detection in the device plane. Then the linear translation stage moves the IR microscope away from the device to find the region where the transmitted light focuses. The microscope scans along the optical axis

with increments of 5 µm to capture the intensity profiles within a total of 0.8 mm span around the main intensity lobe to search for the focal plane. We apply an actuation voltage up to 40 V to pull the mobile meta-optic towards the right – indicated by positive voltage and displacement values – before reaching the regime of pull-in instability. Then we apply an actuation voltage up to 10 V to pull it towards the left – indicated by negative voltage and displacement values. As the offset decreases, the focal length increases, eventually making the focal spot large and dim.

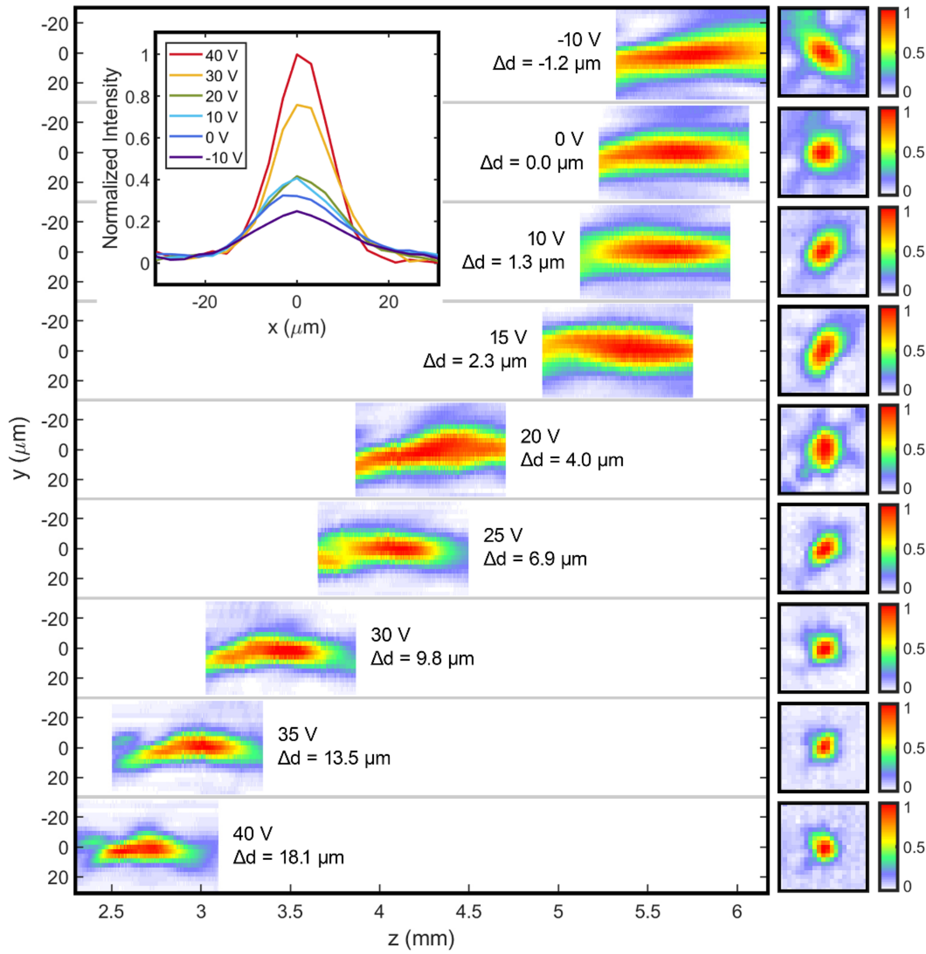

Figure 5.15. Focal profiles of the MEMS Alvarez meta-optical lens with actuator Design 1 at various actuation voltages, captured along the optical axis (z-axis) at 5 µm increments across a 0.8 mm span around the main intensity lobes. Square plots on the right show the intensity distributions in the found focal planes. All intensities are normalized to the maximum intensity measured at each actuation voltage. Inset: normalized intensity distributions across the focal spots at various actuation voltages.

Figure 5.15 displays the changes in focal profile and location along the optical axis (z-axis) at varying actuation voltage and actuated displacement, which modulate the center-to-center offset between the two Alvarez meta-optics. We define the focal length as the distance from the device (located at $z = 0$ mm plane) to the x-y plane, where we have the highest intensity spot. The square images at the right side of each row show the corresponding intensity distributions at the focal planes. We note that a higher actuation voltage induces a larger lateral displacement, which translates to a larger center-to-center offset between the two meta-optics, resulting in shorter focal length and higher effective numerical aperture. Hence, we obtain a sharper focal spot with higher actuation voltage, as shown in the inset of Figure 5.15. We also observe some aberrations in the focal spot shape, primarily coming from the slight misalignment between two meta-optics.

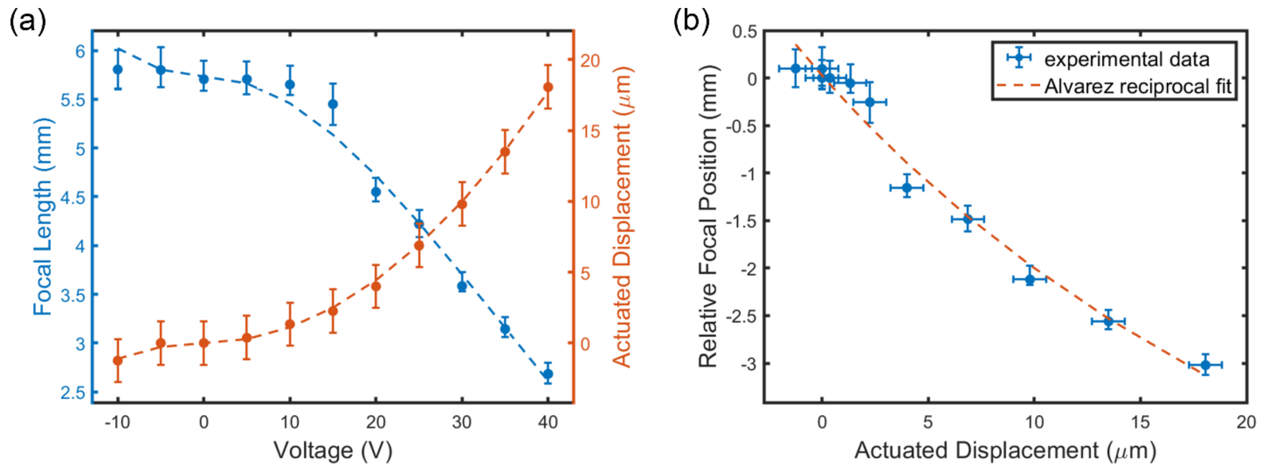

Figure 5.16. Focal tuning measurements of the MEMS Alvarez meta-optical lens with actuator Design 1. (a) Actuated displacement and the corresponding focal length modulated by actuation voltage. Dashed lines show the fitting to the theoretical behaviors. (b) Tunable focal length as a function of actuated displacement closely follows the theoretical reciprocal Alvarez tuning behavior.

Figure 5.16a plots the actuated displacement and the resultant focal length as functions of the applied voltage. As the applied voltage increases from –10 V to +40 V (sign indicating actuation directions only), the induced lateral displacement in the mobile meta-optic increases from –1.2 μm

to +18.1 μm, and their absolute values show a quadratic dependence on the voltages, agreeing with the theoretical behavior of comb-drive actuators. The lateral displacements add onto the built-in 40 μm center-to-center offset between the Alvarez meta-optics and modulate the focal length from 5.8 mm to 2.7 mm, producing a total focal tuning range of 3.1 mm and a change in optical power of 200 diopters. The dashed lines plot the fitting to the corresponding characteristic behaviors, with inflection occurring at 0 V. The displacement-voltage data closely follows the quadratic behavior described in Eq. (3.6), and the focal length-voltage data follows the relation predicted by the combination of Eq. (3.3) and Eq. (3.6). We note that the focal length shift at around 20 V is slightly off, which we attribute to experimental imperfections. The displacement error bars reflect the uncertainties associated with edge detection and camera resolution limit, while the focal length error bars reflect the uncertainties associated with camera artifact.

Figure 5.16b plots the focal length *f* versus the actuated displacement Δd, which follows the adapted theoretical Alvarez tuning behavior closely as

$$f(\Delta d) = \frac{\pi}{2\lambda A(d_0 + \Delta d)} \tag{5.31}$$

where d_0 = 40 μm is the initial center-to-center offset introduced in the designs of Alvarez meta-optics and λ = 1550 nm is the operating wavelength. The good fit between experiment and theory confirms the successful adaptation of a conventional Alvarez system to a miniature on-chip system via MEMS-integrated meta-optics. The experimental data give an actual value for the cubic phase strength *A* as $(5.42 \pm 1.08) \times 10^{12}$ m^{-3}, close to the designed value of 1.0×10^{13} m^{-3}.

The focal tuning performance of the Alvarez lens with the alternative actuator Design 2 is consistent and summarized in Figure 5.17 and Figure 5.18. With fewer finger pairs to produce electrostatic forces for actuation, both the actuated range of displacement and tuning range of focal length are slightly reduced. It produces a focal length tuning of 3.0 mm and an optical power

change of 166 diopters, realized by lateral displacements ranging from –0.5 µm to +13.1 µm induced by voltages between –15 V and +55 V, following the adapted theoretical Alvarez tuning behavior closely. With shorter springs and fewer fingers in Design 2, the compliant structures are stiffer in the alternative MEMS platform compared to Design 1, hence requiring a larger actuation voltage range for optical power modulation, whereas having a higher estimated resonant frequencies at 1.8 kHz.

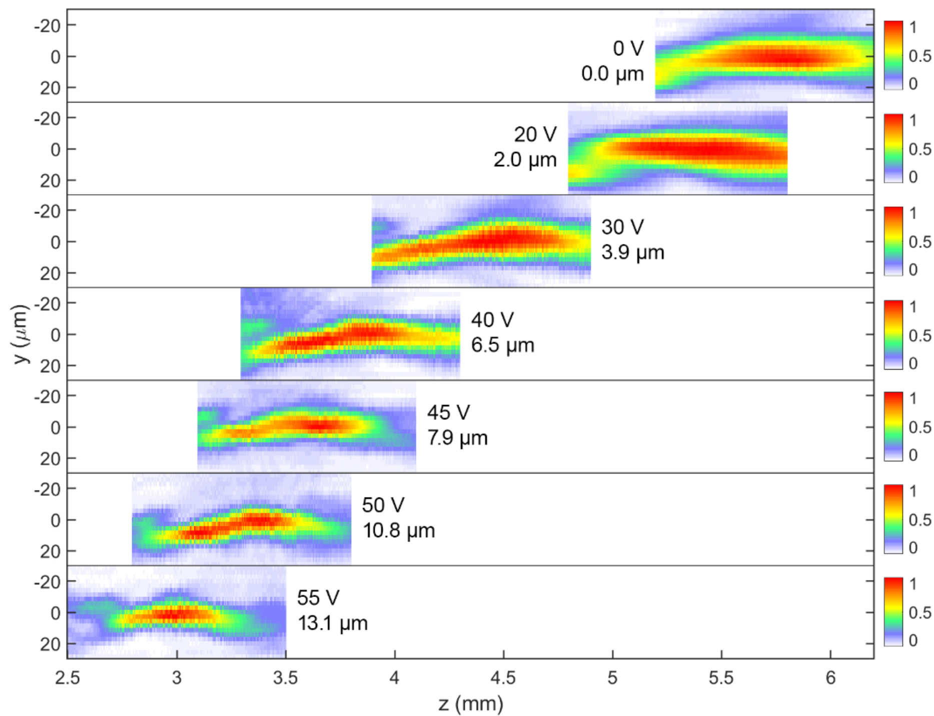

Figure 5.17. Focal profiles of the MEMS Alvarez meta-optical lens with actuator Design 2 at various actuation voltages, captured along the optical axis (z-axis) at 5 µm increments across a 0.8 mm span around the main intensity lobes. All intensities are normalized to the maximum intensity measured at each actuation voltage.

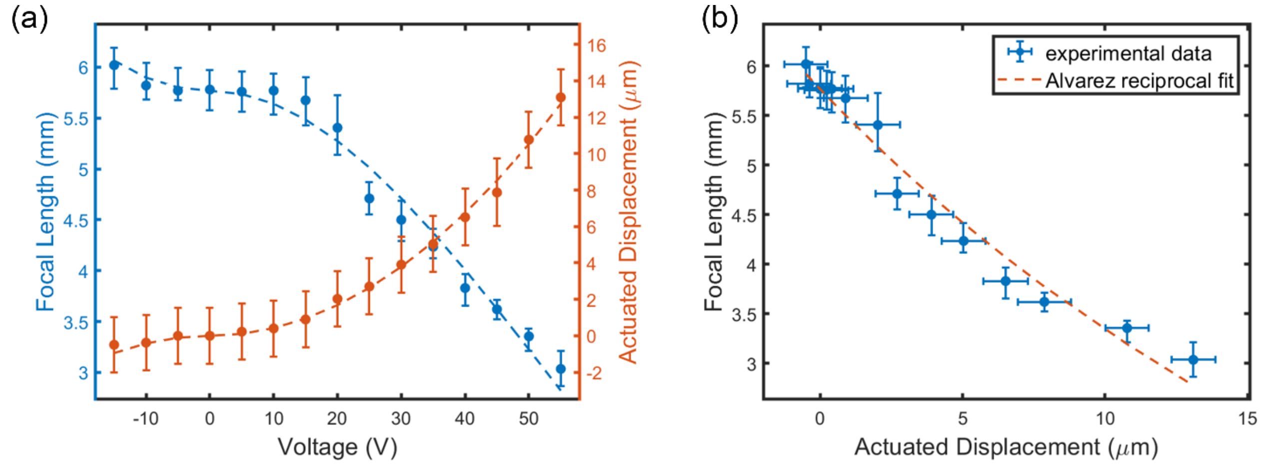

Figure 5.18. Focal tuning measurements of the MEMS Alvarez meta-optical lens with actuator Design 2. (a) Actuated displacement and the corresponding focal length modulated by actuation voltage. Dashed lines show the fitting to the theoretical behaviors. (b) Tunable focal length as a function of actuated displacement closely follows the theoretical reciprocal Alvarez tuning behavior.

5.4.4 *Experimental Data Error Analysis*

For the MEMS actuation data and Alvarez focal tuning data, we estimate the corresponding error based on the uncertainties of the analysis methods and the physical camera limitations.

5.4.4.1 Uncertainties in edge detection of MEMS platform actuation

The infrared camera captures the actuated displacement of the MEMS platform induced by various voltages. We perform edge detection of actuated features at multiple locations in each video frame to analyze local displacements. The algorithm automatically omits outliers and ambiguous readout due to camera defects or resolution limitations. Given the valid local displacements $x_1, x_2, \dots, x_N$ with a standard deviation σ_x, the overall device displacement is calculated as their mean

$$\bar{x} = \frac{\sum x_i}{N} \tag{5.32}$$

We estimate the associated uncertainty by the standard deviation of the mean $\sigma_{\bar{x}}$ [72], calculated as

$$\sigma_{\bar{x}} = \frac{\sigma_x}{\sqrt{N}} \tag{5.33}$$

Another source of uncertainty can come from the resolution limit of the camera, which limits the location reading accuracy to the distance corresponding to half of a pixel. Therefore, in the actuated displacement data presented in the main paper, the error bars have been calculated as the corresponding standard deviation of the mean from the edge detection results or the distance of a half camera pixel, whichever is larger.

5.4.4.2 Uncertainties in focal tracking of Alvarez tuning

The infrared camera we have used to monitor the Alvarez metalens has intrinsic artifacts and defects such as uneven stripes and dead pixels, as shown in Figure 5.19a. They are visible in raw device images captured by the camera, as shown in Figure 5.19b. In focal tracking, we analyze the in-plane distribution of intensities to identify the bright clusters near the center as the potential focal spot. All the potential focal spots found from images taken along the optical axis are then compared to search for the brightest spot as the focus and the corresponding image plane as the focal plane at the given actuation voltage. Therefore, it is crucial to remove the abnormalities in the images prior to focal tracking. Since the camera artifacts and defects are mostly static, we use an algorithm to extract their locations and intensity deviation relative to the background to correct the corresponding abnormalities in the raw device images. As shown in Figure 5.19c, although there is some faint stripe residue left, probably due to random intensity noise intervening with the correction process, the majority of the abnormalities have been removed, producing images ready for focal tracking.

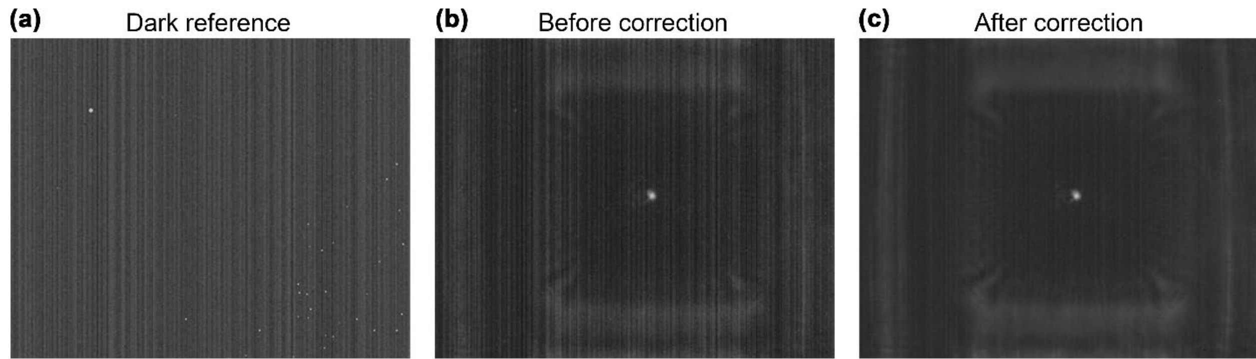

Figure 5.19. Image correction for camera artifacts. (a) Dark reference taken with no device in the optical pathway. (b) A raw example image taken at the focal plane. (c) The same example image with camera artifacts corrected using the dark reference.

However, just as the camera artifacts introduce local intensity offsets, the corresponding correction process will inevitably modify the captured pixel intensities at the potential focal spots, and the exact values of modification are affected by the artifact locations relative to the focal spots. Therefore, the most predominant uncertainty in focal tracking comes from the possible deviation in the search results caused by the spatially varying intensity abnormalities and the corresponding correction process. To estimate the range of uncertainties, we find the nominal focal plane first, which is defined as the *x-y* plane where the highest intensity spot resides. Then we offset the intensity value of every pixel in the focal spot by a sigma of the dark reference image used to perform the image correction, mimicking the extreme case of intensity deviation from the correction process. We search for the planes where the intensities of the potential focal spot decrease to the offset value, estimating the boundaries for uncertainties in focal plane tracking if the artifact removal process had locally over-corrected the local intensities around the focal spot.

5.4.5 *Tilting of the Focal Axis with Asymmetric Actuation*

To ensure device robustness, we only actuate one of the Alvarez meta-optic laterally relative to its static complement. This action deviates from the conventional symmetric actuation of Alvarez

lenses, and hence creates a slight tilting of the focal axis when the focal plane moves along the optical axis in response to the electrostatic actuation. The detailed analytical explanation of focal axis tilting as a function of actuated lateral displacement are described in Section 4.4.5.

Taking the results of our actuator Design 1 as an example, the built-in center-to-center offset of the two complementary meta-optics are $2d_0 = 40\ \mu m$ and the maximum actuated displacement adding to it is $d = 18.1\ \mu m$. Given the operating wavelength is $\lambda_0 = 1550\ nm$ and the cubic parameter $A = 1 \times 10^{13}\ m^{-3}$ (here we use the larger designed value rather than the smaller calculated value for the sake of over-estimation), the expected tiling of the focal axis can be calculated based on Eq. (4.22) as

$$\theta_t = \sin^{-1}\left[\frac{\lambda_0 A d(2d_0+d)}{2\pi}\right] = \sin^{-1}\left[\frac{(1550\ nm)(1\times10^{13}\ m^{-3})(18.1\ \mu m)(58.1\ \mu m)}{2\pi}\right] = 0.149° \quad (5.34)$$

which is very small. As shown in Figure 5.19, although intensity distribution profiles are slightly asymmetric for various voltages, they do not shift in plane (along *y*-axis) as they travel along the optical axis during optical powder modulation, showing negligible focal axis tilting.

5.5 Discussion and Conclusion

We demonstrated a miniature varifocal lens using MEMS-integrated meta-optics exploiting the concept of Alvarez lens. The efficient comb-drive actuation produces a maximum displacement range of 19 μm with input voltages below 40 V. The inverse-dependence of the focal length on the displacement in an Alvarez lens enables a focal tuning by 3.1 mm, more than an order of magnitude larger than the previous reports [79, 80]. Thanks to the electrostatic actuation, the consumed power is lower than 10 nW for DC operation and less than 1 μW for higher tuning frequencies into kHz. Additionally, the whole fabrication process is compatible with high-volume manufacturing, making such an integrated platform attractive for various applications requiring miniature tunable

free-space optics. One limitation of the demonstrated Alvarez lens will be its limited field of view, as the tuning expression is strictly valid only for normal incidence of light.

The complementary cubic surface profiles in the Alvarez system require accurate alignment to achieve optimal performance. While translational misalignment along the actuation direction can be compensated by electrostatic displacement, misalignment along the perpendicular or rotational direction is more challenging to correct in the assembled stack. Though small, the translational misalignment (< 3 μm) and rotational misalignment ($< 0.03°$) in our device still might have contributed to the non-spherical foci at some voltages, where the cubic surface terms fail to cancel each other altogether when overlapping. An alternative chip and bonding process with better accuracy together with a meta-optic design upgrade with higher misalignment tolerance may provide better results. Like other meta-optics, our varifocal lens suffers from chromatic aberration, limiting the operation to a narrow bandwidth around the design wavelength. Possible improvements can involve further engineering of the meta-optics, such as the quartic meta-optics, which have been recently employed to simultaneously achieve achromatic operation and varifocal control at visible wavelengths [81].

Chapter 6. VISIBLE MEMS ALVAREZ METALENS

Miniature varifocal lenses for the visible spectrum have attracted great interest in a wide range of applications, such as near-eye displays, compact endoscopes, spectrometers, and volumetric imaging microscopes. Many such devices have highly constrained sizes and weights. To replace the bulky conventional refractive optics, we employ ultra-thin diffractive meta-optics, which are quasi-periodic arrays of planar sub-wavelength structures that can mimic the optical functionalities of complex geometric curvatures on a flat, lightweight, microns-thick surface. We utilize the Alvarez principle to create the varifocal metalens, in which the optical power modulation is achieved by the microscale relative lateral displacement between the two optical elements with complementary cubic surface profiles. We employ an electrostatic micro-electro-mechanical system (MEMS) to induce the actuated displacement with high controllability and energy efficiency. We have previously demonstrated such an optics-MEMS integrated varifocal system for the near-infrared regime [1]. In this ongoing work, we aim to adapt the mechanism to the visible regime, which brings up new challenges for device integration, material compatibility, and fabrication process development.

6.1 DESIGN PARAMETERS

Similar to the near-IR tunable metalenses, the two main components of this visible tunable lens are the Alvarez meta-optic pair and the MEMS tuning platform to introduce the relative lateral displacement between the pair for optical power modulation.

6.1.1 *Alvarez Metalens Parameters*

Table 6.7 summaries the meta-optic parameters for the visible Alvarez cubic half-plates. The meta-optics are designed by Shane Colburn from the NOISE Lab. Compared to the near-IR devices presented earlier, both the periodicity and nanopost dimensions have been reduced to produce desirable optical performance in the visible spectrum.

Table 6.7. Visible Alvarez metalens parameters.

Square Array		
Aperture Size	500 μm × 500 μm	
Lattice Constant	1 μm	
Post Height	1.5 μm	
Individual Elements	**Duty Cycle**	**Diameter (μm)**
Nanopost 1	0.5083	508.3
Nanopost 2	0.5614	561.4
Nanopost 3	0.5864	586.4
Nanopost 4	0.6462	646.2
Nanopost 5	0.7409	740.9

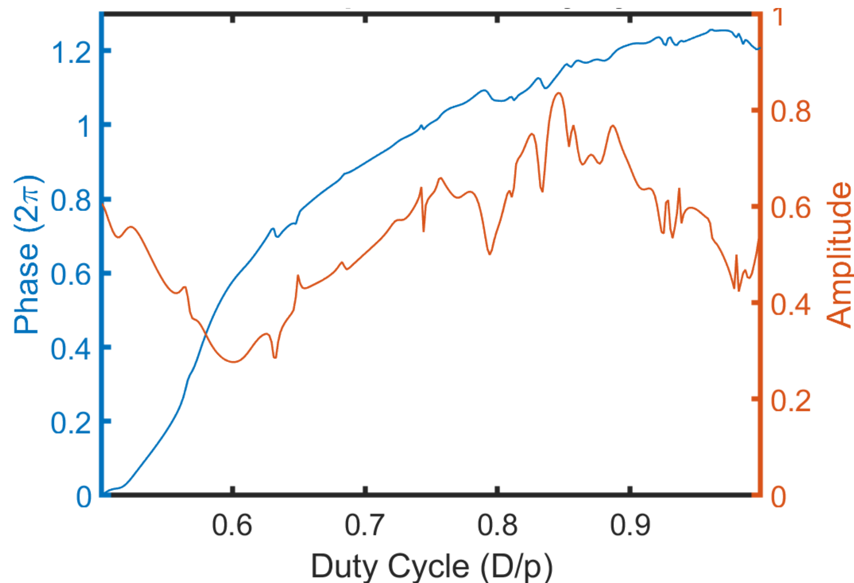

Figure 6.1. Simulated transmission phase and amplitude profiles of silicon nitride nanoposts on a silicon dioxide substrate as functions of duty cycle (*D*/*p*) for a chosen post thickness of 1.5 μm and a fixed array periodicity of 1 μm. The phase is normalized to 2π.

Figure 6.1 shows the simulated transmission coefficients for the visible Alvarez meta-optics. Note that the simulated phase span is less than the ideal 2π value and the simulated amplitude is lower than one. This is the result of sacrificing some of the pattern resolutions while switching the meta-optic patterning method from the conventional high precision but slow electron beam lithography to high throughput stepper lithography for its potential for fast prototyping and low-cost mass-production.

6.1.2 *MEMS Actuation Platform Parameters*

Table 6.8 summarizes the mechanical parameters for the MEMS actuation platform. Since we can adapt the previous MEMS design from the near-IR devices, the calculations produce similar predictions in the same order.

Table 6.8. MEMS actuation platform design parameters for the large-aperture visible Alvarez metalens.

Comb Fingers	Width (μm)	2
	Length (μm)	40
	Height (μm)	12
	Gap (μm)	2
Folded Springs	Width (μm)	4
	Length (μm)	500
	Height (μm)	12
	Lateral Stiffness (N/m)	3.19
	Natural Frequency (Hz)	2500

6.2 DEVICE FABRICATION

We fabricate the pair of silicon nitride Alvarez meta-optics on two separate wafers before aligning and bonding them to construct the composite Alvarez metalens. One meta-optic and the MEMS actuator are fabricated on a silicon-on-insulator wafer to induce lateral displacement for focal

tunability. The other meta-optic is fabricated on a fused silica wafer, which will remain static relative to its complement in the final metalens assembly. Figure 6.2 summarizes the fabrication process flow.

6.2.1 *Microfabrication Process Flow*

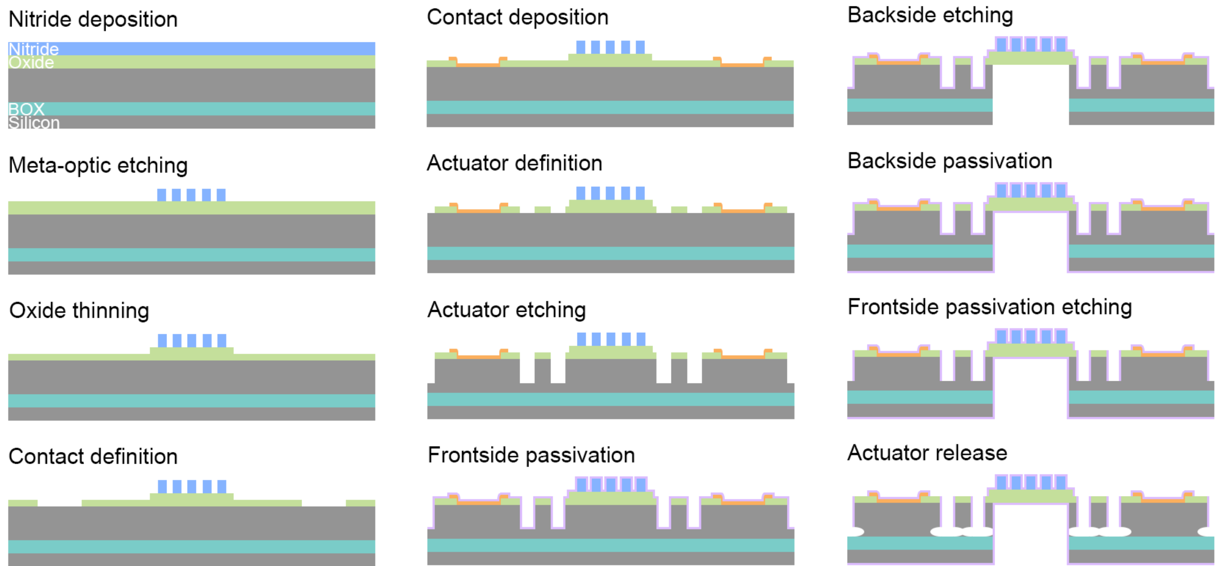

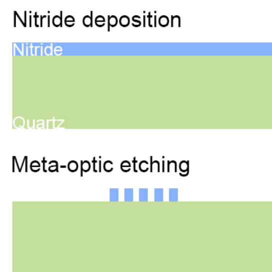

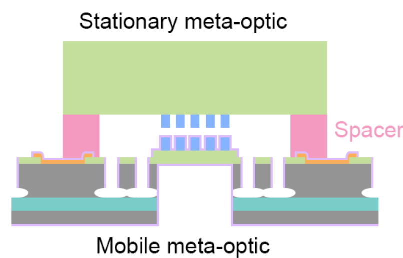

Figure 6.2. Fabrication process flow of the mobile Alvarez meta-optic on MEMS actuator, the static Alvarez meta-optic, and the final composite Alvarez metalens.

For the mobile meta-optic fabricated on the SOI wafer, we use plasma-enhanced chemical vapor deposition (PECVD) to deposit 6 μm of silicon dioxide for the base membrane and 1.5 μm of silicon nitride on top for the meta-optic scatterers. We employ the deep-ultraviolet (DUV)

stepper lithography and fluorine-based inductively coupled plasma (ICP-F) etching to pattern the silicon nitride meta-optic layer. We use direct-write lithography and ICP-F etching to define the area for electrical contacts. A metal stack of 10 nm chromium and 150 nm gold is deposited and lifted off to create the electrical connections for actuation. The MEMS actuator is patterned and etched partially into the 20-μm device silicon layer via direct-write lithography and deep reactive-ion etching (DRIE). We employ atomic layer deposition (ALD) to passivate the device surface with 80 nm of silicon dioxide. We use contact lithography and DRIE to pattern the backside of the wafer and remove the silicon and buried oxide below the meta-optic membrane to create a transparent optical path. We follow with another ALD passivation to protect the silicon from the backside. From the front side of the wafer, we use anisotropic reactive-ion etching (RIE) to open horizontal silicon surfaces at the bottom of the silicon MEMS actuator. After dicing the wafer into individual chips, we employ xenon difluoride (XeF_2) vapor etch to undercut the exposed device silicon and release the alumina-protected silicon MEMS actuator carrying the mobile meta-optic.

The static meta-optic is fabricated on a fused silica wafer. Like its mobile complement, a 1.5-μm PECVD silicon nitride is deposited and patterned via DUV stepper lithography and ICP-F etching, utilizing an aluminum hard mask. After stripping the metal, the wafer is diced into individual chips for assembly.

The chips carrying the mobile meta-optics and the static meta-optics are then aligned and bonded face-to-face utilizing a flip-chip bonder. We use anisotropic conductive film both as the spacer and the adhesive for the assembly to create an axial gap of 10 μm between the pair of complementary Alvarez meta-optics for free movement during focal tuning.

6.2.2 *Fabricated Devices*

Figure 6.3a shows the optical images of a fabricated visible Alvarez meta-optic carried by a MEMS tuning platform, and Figure 6.3b shows the complementary Alvarez meta-optic on a static fused silica substrate. Once the meta-optics on MEMS are released, their complement meta-optics will be aligned and bonded face-down on top of them to construct the complete Alvarez metalens.

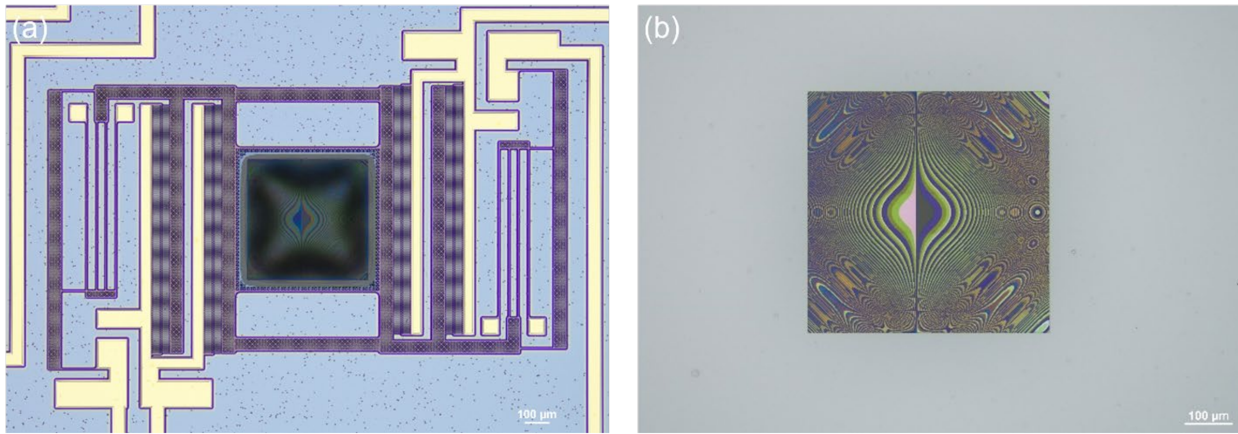

Figure 6.3. Optical images of (a) a silicon-nitride Alvarez meta-optic on an oxide membrane carried by a MEMS actuator before release and (b) a silicon-nitride Alvarez meta-optic on the fused silica substrate.

Figure 6.4a presents an SEM image of the mobile meta-optic on the MEMS tuning platform. Similar to the previous device designs for the near-IR spectrum, the electrostatic actuator here has a 2-fold symmetric design with driving comb drives and compliant folded flexures on both sides of the central platform, ensuring rotational stability and doubling the actuation range with the same applied voltage. The zoomed-in images in Figure 6.4b and Figure 6.4c show part of the comb drives and the silicon nitride meta-optics on the silicon dioxide membrane. The silicon dioxide passivation on the meta-optic protects the silicon nitride nanoposts from any chemical damage during the XeF_2 release process.

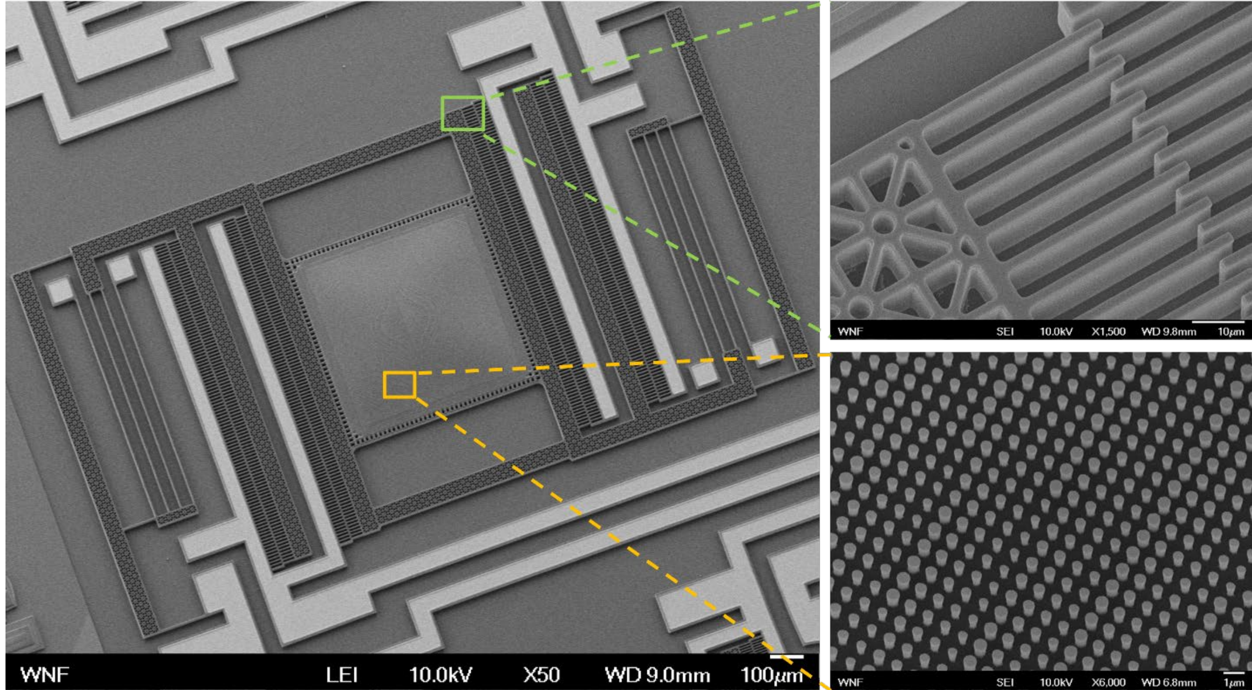

Figure 6.4. Scanning electron microscopy (SEM) images of Alvarez meta-optic lens operating in the visible spectrum. (a) A visible Alvarez meta-optic integrated with a MEMS tuning platform. (b) Comb-drive details showing the part of the mobile flexure backbone and interdigitated finger array. (c) Close-up view of the silicon nitride nanoposts sitting on the central silicon dioxide platform.

6.3 EXPERIMENTAL SETUP

Figure 6.5 illustrates the experimental setup for MEMS actuation and focal tuning measurements of the Alvarez meta-optic lens operating in the visible spectrum. We use a 633 nm red laser source through a collimator to illuminate the Alvarez meta-optic lens held vertically on a 3-axis micro-manipulator stage perpendicular to the optical axis. We probe the Alvarez lens with a DC voltage to laterally actuate the mobile meta-optic relative to its static complement. The incident red light interacts with the meta-optic stack and converges to the focal plane on the other side of the Alvarez lens. A 530 nm light-emitting diode (LED) source illuminates the actuator surface through a beam splitter for MEMS performance monitoring. An objective collects the light beams and converges

them onto a recording camera, connected to a control computer for image and video acquisition. The objective and the camera are installed on a linear translation stage, which can move and scan across the intensity profiles along the optical axis in small increment steps.

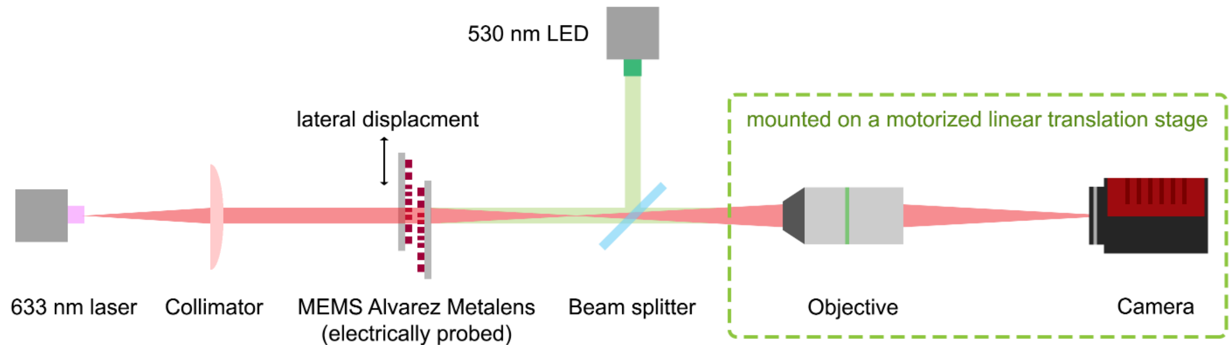

Figure 6.5. Experimental setup for Alvarez lens electrostatic actuation and focal profile acquisition in the visible spectrum.

6.4 Results and Analysis

This project is still ongoing, and we are at the stages of Alvarez meta-optic lens assembly and data acquisition. This thesis presents the preliminary results we have collected so far and provides an outlook on the next steps.

6.4.1 *Image Channel Separation for MEMS Actuation and Focal Tuning*

As described in the experimental setup of Section 6.3, we use a green LED source at 530 nm to monitor the MEMS actuation behavior, whereas we utilize a red laser at the designed wavelength of 633 nm to track the focal tunability of our Alvarez meta-optic lens. Both channels are captured simultaneously by the detector camera, which produces the multi-color images shown in Figure 6.6a and b. Figure 6.6a appears dimmer overall to prevent pixel saturation at the brightest locations. During post-processing, we can easily separate the green and red channels for electro-mechanical and optical analysis, respectively. On the one hand, we extract the green channel to have a

standalone reflected image of the actuator, as shown in Figure 6.6c. With simple brightness and contrast enhancements, we can recover many details to aid the motion tracking of the central meta-optic platform and analysis the electrostatic performance of the MEMS actuator. On the other hand, we extract the red channel to isolate the transmitted light through the Alvarez lens and track the intensity distribution in the focal plane. By translating the detector camera along the optical axis, we can obtain a 3D profile of the intensity distribution around the focal spot.

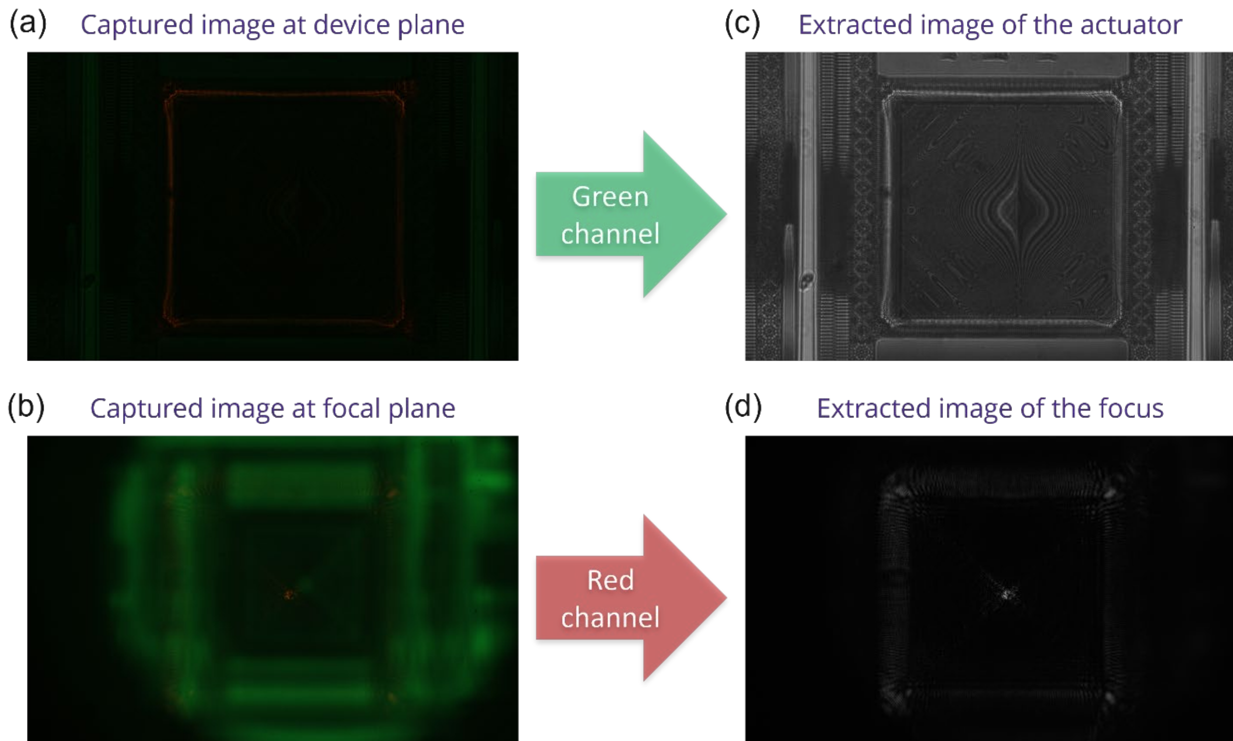

Figure 6.6. Image channel separation. (a) Captured raw image at the device plane. (b) Captured raw image at the focal plane. (c) Actuator image extracted from the green channel of (a) and enhanced to show details. (d) Focus image extracted from the red channel of (b).

6.4.2 *Meta-optic Membrane Bulging*

To create a transparent optical path, our mobile Alvarez meta-optic sits on a microns-thick layer of silicon dioxide membrane after the final device release. PECVD deposits the oxide layer at a temperature of 350 °C, which creates a considerable amount of stress inside the film due to the

thermal expansion coefficient mismatch between the deposited oxide and the device silicon layer underneath. When the device silicon layer is removed to create the transparent path, the thermal stress inside the oxide membrane causes it to bulge above the plane relative to the MEMS structure in the surroundings, as shown in the height map shown in Figure 6.7a. The membrane area bulges upwards, with its center at the highest point (higher structures indicated by redder colors). By plotting the height across a 1D slide through the membrane center, we obtain Figure 6.7b showing a maximum of 15 µm upward bulging of the meta-optic membrane relative to the silicon actuator structure connected to it. We need to take this out-of-plane deformation into account when we reserve the axial gap between the two complementary Alvarez meta-optics for bonding to prevent accidental scratching between the meta-optics during lateral actuation.

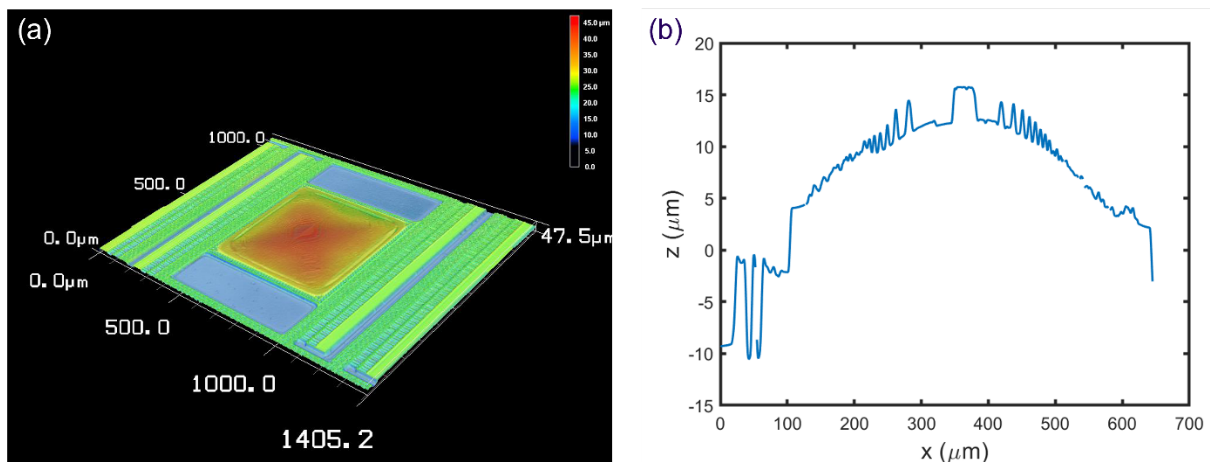

Figure 6.7. Optical profilometry of the meta-optic membrane. (a) A 3D height map showing the central meta-optic membrane bulging out of the plane (red) after release. (b) A 1D height plot across the center of the meta-optic membrane relative to the MEMS actuator flexure.

6.4.3 *Uniaxial Movement of the Released MEMS Platform*

After releasing the MEMS tuning platform carrying the mobile Alvarez meta-optic, we verify the uniaxial motion with a manual push test. The optical images in Figure 6.8 show the same device

at its neutral released position (Figure 6.8a) and when being pushed towards the left by an eyelash brush (Figure 6.8b). When displaced, the comb-drive pairs on the left side visibly move into each other, while the comb-drive pairs on the right side are drawn apart from each other. Once the force is removed, the actuator readily springs back to its neutral position. The uniaxial motion is evident in the lateral displacement of the comb fingers with undetectable sideway disturbance. This manual test verifies the high stiffness ratio between the orthogonal directions in the compliant flexures, ensuring uniaxial actuation with high stability.

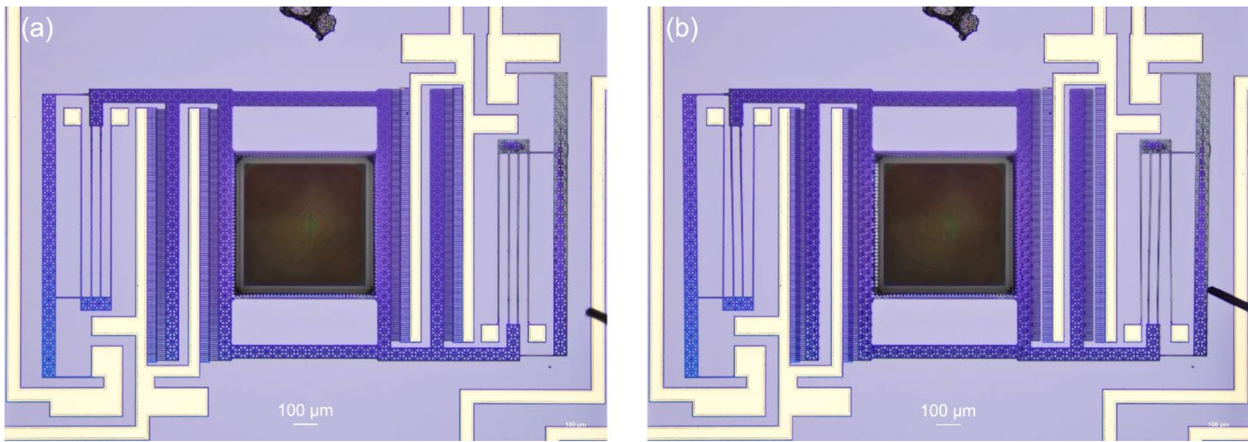

Figure 6.8. Manual push test of a released MEMS tuning platform carrying the mobile Alvarez meta-optic. (a) Neutral position. (b) Pushed to the left.

6.5 Outlook

Currently, we are investigating and improving the MEMS release step with XeF_2 etching for the mobile meta-optic on the MEMS tuning platform. After which, we plan to perform more extensive focal tuning experiments with lateral MEMS actuation in the device plane perpendicular to the optical axis. We will study the electro-mechanical behaviors of the electrostatic actuators and verify their controllability and reliability against the theoretical models. The intensity distribution around the focal spot will be collected with the experimental setup scanning along the optical axis. From the collected intensity data, we will evaluate the focal distribution, locate the focal planes,

and examine how the focal length varies with the applied actuation voltage. We hope to demonstrate and characterize such miniature focus-tunable lenses integrating MEMS actuation and Alvarez meta-optics designed for the visible range, which will have great potentials to be utilized in compact optical systems requiring imaging or sensing in the visible frequencies.

Chapter 7. FABRICATION CHALLENGES FOR LARGE-AREA META-OPTICS

Today's meta-optics are primarily fabricated with the conventional electron beam lithography (EBL) method, especially for meta-optics that operate with a wavelength below 1 μm [19, 82]. However, as a high-precision but expensive and slow fabrication technique, electron beam lithography is seldom compatible with low-cost, large-scale manufacturing schemes or iterative prototyping processes. More affordable alternatives of fabrication methods with fast speed and satisfactory resolution will benefit both research and commercialization.

There has been a rising interest in large-area meta-optics, which have large apertures (at least centimeters wide) while still being ultra-thin and lightweight. They can capture images with better quantity and also present the potential to be employed in a wider range of applications calling for large-area compact optics. However, most of the meta-optics fabricated with EBL have aperture sizes no more than a few millimeters due to slow exposure rate and high operation cost, which make fabricating large-area meta-optics with EBL an unreasonable task in most scenarios.

From Chapter 8 to Chapter 10, we present multiple projects which use non-EBL methods such as stepper lithography and laser direct-write available on site at the Washington Nanofabrication Facility to fabricate meta-optics for the long-wave infrared, mid-wave infrared, and visible spectra. Especially with direct laser writing, we can enable frequent iteration of prototyping and the capability to pattern extremely large meta-optics that is almost impractical for conventional EBL or stepper systems. We have fabricated meta-optics as large as 75 mm in diameter with direct-write, and this is still far away from the ultimate aperture limit achievable.

When we switch meta-optics fabrication form EBL to stepper or laser direct-write and expand their apertures, we are bound to face many challenges, such as patterning integrity and etch

complexities. We utilize and adapt patterning and etching correction methods initially developed for the IC industry to our large-area meta-optics, ensuring decent fabrication qualities while taking advantage of fast prototyping, high throughput, and large-area capability of non-EBL patterning methods. Note that although our fabrication tools are far away from the state-of-art, the evaluation and correction techniques are always applicable for other nanophotonics fabrication process development with simultaneous resolution and throughput requirements, especially when the patterning feature size is on the same order as the lithography resolution limit.

In this Chapter, I will go through some critical aspects of consideration when patterning large-area meta-optics with the equipment available at the Washington Nanofabrication Facility and the solutions or corrections I have implemented to improve the quality of patterning and etching with the developed processes for large-area meta-optics. I also give some examples of the meta-optics projects fabricated with such processes. The projects presented in Chapter 8 to Chapter 10 are collaborations among multiple research groups. Most of the meta-optics are designed by the NOISE Lab led by Prof. Arka Majumdar and their collaborators. My responsibility is to evaluate the feasibility of the optical designs in manufacturing, introduce appropriate corrections to ensure patterning integrity, and develop and execute the fabrication process to produce the physical meta-optics for device characterizations. Therefore, the emphasis of those chapters will be more on the process development and fabrication outcome. More thorough information on the optical designs and performance can be found in the quoted publications, respectively.

7.1 TOOL CHOICE AND EXPOSURE TIME

One main challenge of fabricating large-area meta-optics is the patterning time, especially for potential mass-production applications. Not only will the exposure time affect the turnaround time of research and development, but the cost of using the exposure tools will also contribute to the

final cost of individual devices if they make it to the production stage. Therefore, we need to choose the appropriate tool according to the required pattern resolution with a reasonable estimation of patterning time.

7.1.1 *Electron Beam Lithography*

The current typical process used for meta-optic patterning is electron beam lithography (EBL) for its capability of writing extremely fine patterns. The technique, in brief, consists of scanning a beam of electrons across a surface coated with an electron-sensitive resist film, depositing energies in the desired regions to write the designed pattern. The main advantage of EBL is its high patterning resolution, down to several nanometers, as well as its high flexibility for pattern design and prototyping. However, due to its small beam spot for high resolution and serial patterning nature, EBL is often orders of magnitude slower than typical optical lithography methods. At the same time, to ensure reliability and accuracy, the maintenance of an EBL system is very expensive and complicated, driving up the corresponding production cost of devices [83].

7.1.2 *Stepper Lithography*

A stepper, as the name indicates, involves a high-speed stage that steps the wafer relative to the fixed imaging optics and the pattern reticle (photomask for stepper systems), projecting the designed image from the reticle to the photoresist-coated wafer. In a typical highly automated stepper system, a wafer loaded into the tool is first oriented and aligned before transferring onto the exposure stage, correcting its position with respect to the ideal image field. Once the wafer is loaded onto the exposure stage, it is placed directly under the autofocus system, which will also detect any wafer flatness error and correct for wafer tilting. Once the wafer is properly positioned and brought into focus, a shutter in the illumination system opens and passes light through the

bladed portion of the reticle, imaging the corresponding area on the wafer with a reduction power N defined by the projection lens. Because of the reduction (if $N > 1$), the exposed pattern on the wafer is reduced laterally to $1/N$ of the mask pattern size on the reticle, and often only part of the wafer is illuminated at any one time. After one field is exposed, the stage then travels in the horizontal plane to step the wafer to the next field position with high precision, repeating the exposure in another part of the wafer. In today's typical reduction stepper systems, the stage travels in a Cartesian grid of the horizontal plane underneath a fixed, vertically mounted lens [84, 85].

One main advantage of the steppers is the high-accuracy step-and-scan exposure mode which significantly increases the production throughput. The exposure time per pattern is relatively independent of the pattern size. Hence we can increase the size of the meta-optics to be printed without increasing the exposure time required. Compared to electron beam lithography, the stepper is capable of fast large-scale printing. The resolution limit of a stepper is highly dependent on the exposure wavelength and projection optics. Today's stepper utilizes extreme ultraviolet (EUV) lithography to achieve patterning resolution down to tens of nanometers. For example, ASML's latest generation lithography system, TWINSCAN NXE:3600D, employs a 13.5 nm light source and is capable of achieving a pattern resolution down to 13 nm while still maintaining a wafer throughput of 160 wafers per hour [86]. Another advantage of steppers is the reduction power between the reticle print and wafer pattern, with a typical reduction factor N with a value between 1 and 10. A N value larger than 1 has the benefits of reducing the adverse effects of linewidth variations and misregistration on the reticle, giving higher tolerance for defects and more lenience for critical dimension definition during reticle fabrication. In addition, many steppers can be linked to automatic spin-coating and development systems for fully automatic production lines, utilizing their high-throughput potential for mass-production in an industrial environment.

However, the requirement of a physical photomask post restrictions on fast prototyping and increase the turnaround time for design adjustments to some extent. The reticle can easily cost more than a thousand dollars based on the critical dimension and equipment compatibility requirements. For example, while a typical reticle for an i-line stepper often costs around a thousand dollars, a typical reticle for EUV stepper can cost at least a hundred times more. Moreover, to ensure stable chamber condition and reliable performance, extensive care and resources are required for tool installation and maintenance, making the stepper one of the most expensive pieces of capital equipment in the nanofabrication facilities.

7.1.3 *Laser Direct-Write*

Laser direct-write is a fast, versatile maskless photolithography technique designed for research and development. In a direct-write system, a spatial light modulator (SLM) serves as a programmable mask and exposes the pattern directly onto a photoresist-coated substrate, skipping the time and resources needed to fabricate the photomasks required for regular contact and projection lithography. This also allows frequent design adjustment and immediate re-exposure for fast prototyping. The printing size of the design is technically only limited by the moving range of the wafer stage. For example, the Heidelberg DWL66+ direct-write system can be customized for writing over a substrate with a size up to 9-inch by 9-inch [87], giving high potential for large-area pattern direct writing. Since the exposure time and resolution are inversely related, most direct-write systems offer multiple write modes with different speeds and resolutions to fill the lithography requirements of various applications with different specifications and emphasis.

The resolution limit of a direct-write system is highly dependent on the wavelength of the source laser and optics used in various write modes. The typical diode lasers used for direct-write systems are at 405 nm or 375 nm, limiting the minimum feature size to 300 nm [87]. The

maintenance of direct-write systems is often less tedious than electron beam lithography and stepper lithography, giving higher robustness in fabrication processes with some sacrifice in pattern resolution.

7.1.4 *Exposure Method Comparison*

Table 7.9 compares the tool resolutions and exposure times of one meta-optic pattern with a circular diameter of 1 cm designed for the visible spectrum, using electron beam lithography, stepper lithography (speculated based on other similar projects) and laser direct-write lithography with the equipment available in the Washington Nanofabrication Facility (WNF). Johannes Fröch from the NOISE Lab supplied the electron beam lithography information. The laser direct-write part of this project is discussed in more detail in Chapter 10.

Table 7.9. Tool resolution and exposure time for a circular meta-optic with a diameter of 1 cm, using the tools available at the Washington Nanofabrication Facility.

Method	Tool	Tool Resolution	Exposure Time
Electron beam lithography	JEOL JBX6300FS	50 nm	5 hours
i-line stepper	Canon FP4-3000 i4	350 nm	1 minute
Laser direct-write	Heidelberg DWL66+ (HiRes)	300 nm	1 hour
Laser direct-write	Heidelberg DWL66+ (4 mm)	800 nm	10 minutes

Since this meta-optic is designed for operation in the visible spectrum, the ideal scatterer geometries should be sub-wavelength compared to the visible light. Therefore, electron beam lithography is the conventional method for fulfilling the patterning resolution requirements. However, the high resolution inevitably increases the writing time to several hours. Together with high tool operation and maintenance costs, such long exposure time and relatively large pattern

size will quickly drive EBL patterning to be one of the most expensive steps in the fabrication of large-area meta-optics.

The i-line stepper sacrifices some patterning resolution while enabling high-throughput with fastest exposure among all the options listed here. However, the requirement of a reticle designed for each iteration in process development increases the overall cost and time, making this technique less desirable for frequent prototyping. Moreover, though not a limitation in this example, the stepper still has a maximum patterning area limitation based on the reticle size and lens reduction factor. For example, the Canon FP4-3000 i4 stepper at WNF has a lens reduction factor of 5 and uses a 6-inch reticle. Subtracting the area on the reticle required for printing tool calibration and alignment features, the maximum pattern size that can be transferred onto the substrate without stitching is only 26 cm wide per exposure, limiting the possibility of printing meta-optics with larger areas unless involving the more complicated process of stitching patterns exposed from multiple reticles.

The laser direct-write system has an exposure speed between the electron beam lithography and stepper lithography. Being maskless, direct-write has the advantages over stepper lithography for fast iterative prototyping and no additional cost for photomasks. Using the newly installed HiRes write head, we are able to achieve resolution similar to i-line stepper lithography, with some sacrifice in printing sub-wavelength features for visible meta-optics. For other projects with larger critical dimensions, such as in the long-wave infrared meta-optics, the 4 mm write head can be used for faster patterning with little sacrifice in the required resolution when utilizing proper design compensation. Moreover, beyond this particular example, we have also used laser direct-write to pattern meta-optics up to 75 mm in diameter (Section 8.4), which would have been either extremely expensive or infeasible by electron beam lithography or stepper lithography.

Technically, the ultimate maximum patternable size of the direct-write system is the stage motion range of 9-inch by 9-inch in our case, which is not achievable in either electron beam lithography or stepper lithography systems.

7.2 Optical Proximity Effects

Though we design CAD layouts based on rigorous performance simulations, the lithographically printed features always differ from mask or layout specifications. As shown by the example in Figure 7.1, both the overall size and shape of the fabricated features are different from the design layout, and the extent of deviation varies from feature to feature. Often, the deviations in size and shape of the printed features are dependent on their proximity to other structures.

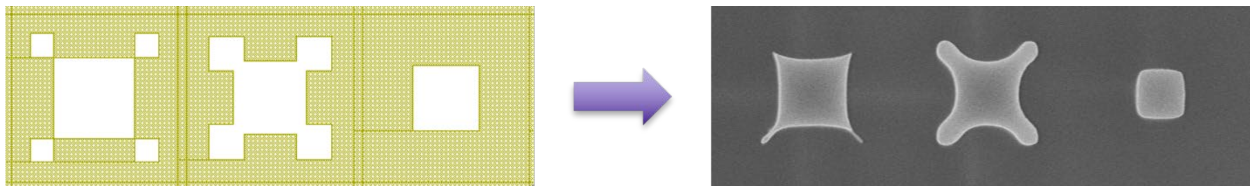

Figure 7.1. Optical proximity effect resulting in the pattern size and shape differences between the design layout (left) and the actually patterned scatterers (right).

With the same exposure conditions, the same feature exposed as an isolated item and in a densely packed group will end up with different lithographic dimensions. This iso-dense bias is a result of the proximity of features to other geometries and is known as the optical proximity effect (OPE) [85]. For lithography processes with pattern critical dimensions much larger than the resolution limit, such an effect is often negligible. However, when the printed feature sizes approach the resolution limit, the optical proximity effect becomes more significant and causes undesirable deviation in device fabrication and the resultant performance. The magnitude of such an effect can be affected by lens parameters, illuminator settings, and resist processes.

Print bias, also known as linearity, describes the phenomenon in which the extent of deviation between the input design and the printed dimension varies as a function of feature size [84]. Given that the meta-optics we fabricate usually consist of optical scatterers of various dimensions arranged in a fixed periodic square array, the print bias, and the proximity effects together contribute to the dimension deviation of the meta-optic scatterers using non-EBL techniques in our facility.

The optical system used in projection lithography systems practically acts as a low-pass filter. The lens collects the diffracted beams from the low-spatial-frequency parts of the photomask pattern, while the aperture cuts off the beams from the high-spatial-frequency parts [85]. Many meta-optic scatter designs involve sharp corners, which represent high-spatial-frequency parts of geometries, and are effectively filtered out by the optical system during projection imaging, causing corner rounding and a drop in spatial resolution.

In a laser direct-write system, the optical proximity effect is also highly dependent on the intensity spread in the laser beam with finite spot size. When the laser beam exposes a spot on the photoresist-coated wafer, the absorbed energy density follows Gaussian functions describing the primary laser beam spread and forward light scattering in the photoresist [88]. The resultant effects include line shortening and corner rounding, as illustrated in Figure 7.2.

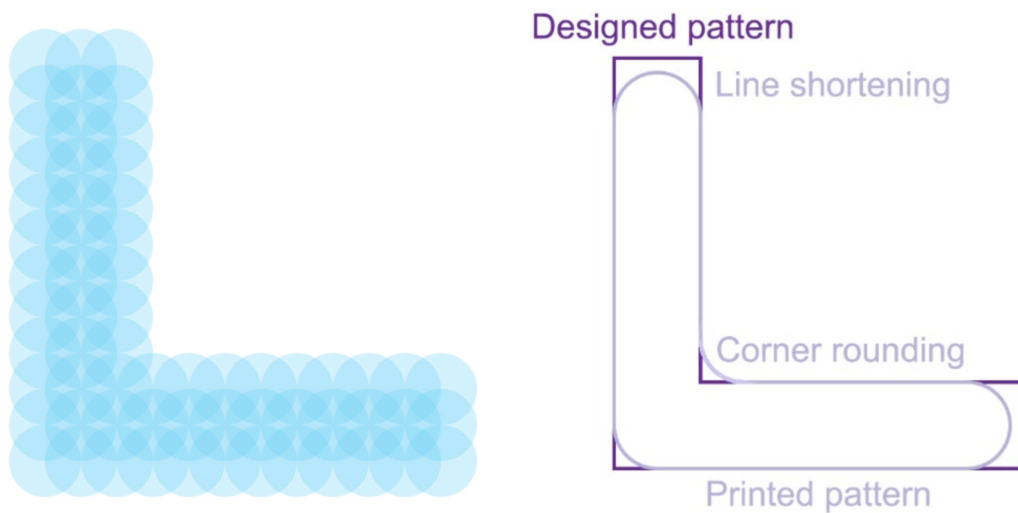

Figure 7.2. Illustration of (left) laser beam intensity spreading and (right) the resultant line shortening and corner rounding in laser direct-write lithography.

Local dose compensation and optical proximity correction are two common approaches to improving the quality of fabricated features. Rigorous simulation based on chosen lithography conditions and photoresist choices can be performed to determine the optimal exposure dose over the pattern to ensure a consistent amount of absorbed energy density in all parts of the designed pattern. Then the required exposure dose as a function of coordinates is programmed into the lithography tool to produce varying laser intensity accordingly. However, this is only realizable on laser direct-write systems with associated capabilities and often not feasible with stepper lithography systems.

The adjustments of features on the photomask or in the direct-write layout pattern to compensate for the printing deviation are known as optical proximity corrections (OPC). The implementation of optical proximity corrections is an essential task for advanced semiconductor lithography, but it is seldom trivial, especially in complicated patterns printing various feature geometries over a wide range of sizes. The modification of feature sizes in the input layout can

help reduce the effect of iso-dense bias and print linearity for various dimensions and pitches. The introduction of serifs and hammerheads can help address the issue of line shortening and corner rounding of abrupt corners, while the addition of notches can reduce the occurrence of necking between closely positioned features. Because our stepper lithography and laser direct-write lithography system are not properly equipped for local dose compensation, the optical proximity corrections are primarily performed to compensate for printing deviation in dimensions for large-area meta-optics.

7.2.1 *Size Compensation*

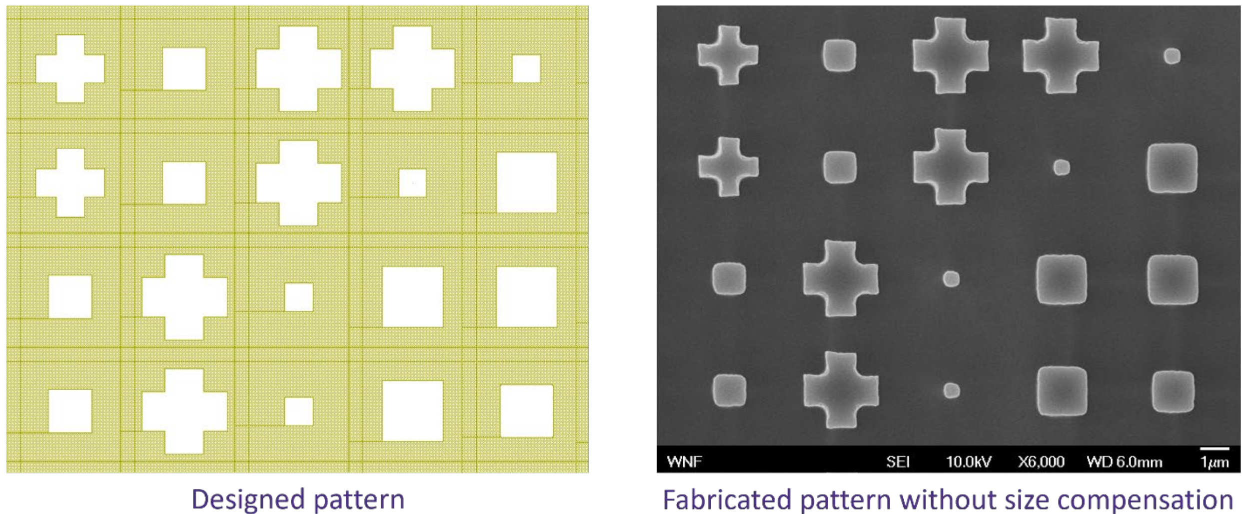

Figure 7.3. Size deviation between a designed pattern (left) and the corresponding fabricated pattern (right) for a meta-optic exposed with laser direct-write lithography.

Our meta-optics usually consist of optical scatterers with varying dimensions arranged in a square grid with a fixed pitch to map the designed phase profiles created for various imaging applications. When using stepper lithography and laser direct-write lithography in our facility, often we are printing features with dimensions approaching the tool resolution limit, which results in size deviation between the design and printed pattern, as shown in Figure 7.3 (LWIR device from

Section 8.5). The optical proximity effects, such as iso-dense bias and linearity, cause the overall printed feature size deviations dependent on their proximity to other structures as well as their designed dimensions.

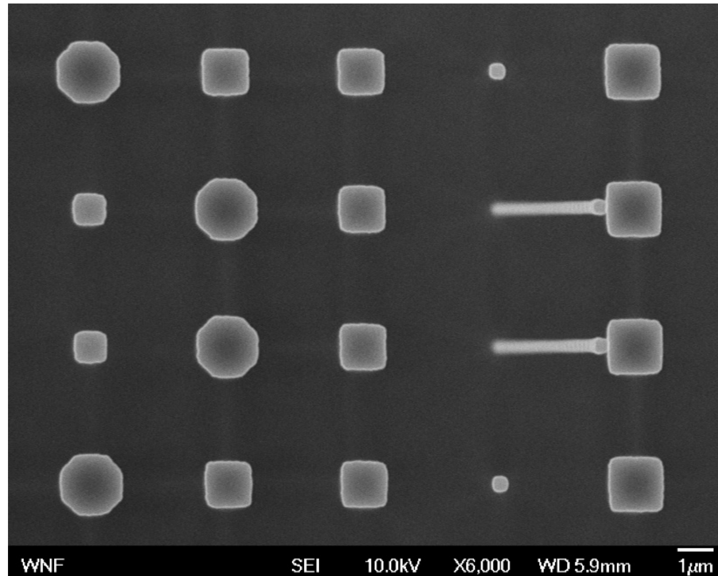

Figure 7.4. Top-view SEM image of fabricated silicon scatterer array for an LWIR meta-optic without size compensation. The smallest pillars shrink in size due to optical proximity and linearity effect, making them too thin to be stable after DRIE, hence eventually falling down.

In the square grid with fixed periodicity, a scatterer with a smaller area can be considered further away from its neighbors than its larger counterparts. With a smaller designed dimension and a larger surrounding empty space, the printed smaller feature is typically not only shrunk in dimension but also with a dimension deviation more significant than that of a larger feature. As a result, there is more size distortion in the smaller structures than in large structures when patterned with the same exposure conditions. For meta-optic designs with a wide range of feature dimensions, too much shrinkage in patterning may even lead to the complete loss of the smaller features or to shrinking them down so much that the etched pillars would eventually fall down after dry etching, as illustrated by the example in Figure 7.4.

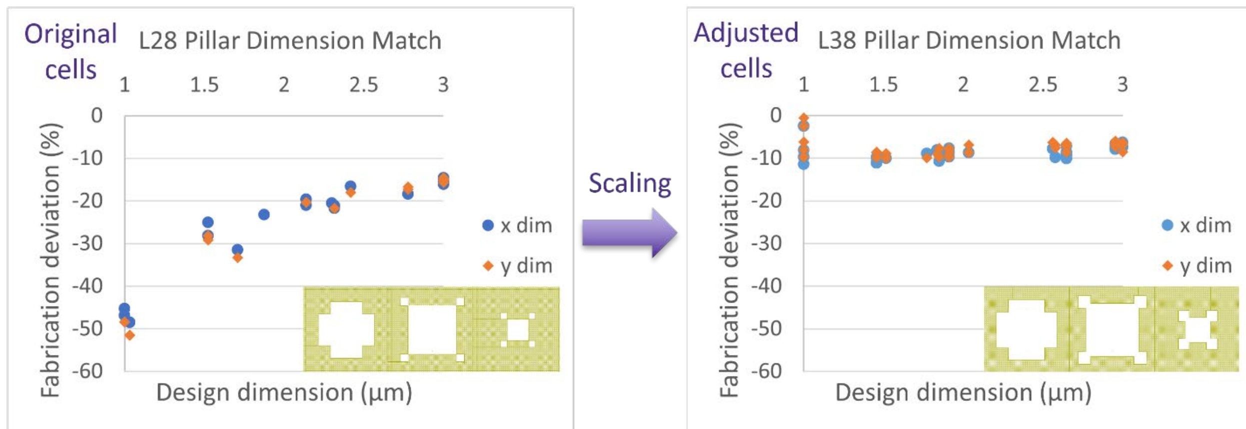

Figure 7.5. Fabricated scatterer sizes with original CAD designs (left) and compensated CAD designs (right) for laser direct-write lithography. The insets show portions of the pattern layouts.

Figure 7.5 plots the comparison of fabricated feature dimensions before and after size compensation in the direct-write input layout. The data is from the long-wave infrared (LWIR) projects presented in Section 8.5. As shown in the left plot, the printed feature dimensions are not only smaller than the design but also with a deviation extent dependent on the feature size. While the largest 3 μm features are exposed 15% smaller than the design, the smallest 1 μm features are exposed 50% smaller than the design, making them fragile structures that have a high risk of breakage after dry etch.

Appropriate size compensation is estimated based on the deviation data. For the device represented by the right plot, a size adjustment of 100 nm has been added to all edges of all scatter features, as shown by the difference between the two layout insets. Although the absolute compensation value is the same for all features with different sizes, the smaller features experience larger percentage changes in dimension, which is sufficient to compensate for the linearity effect. With such size compensation in the input layout for direct-write, the dimension deviation of patterned features is around 10% smaller than the design, which is much smaller and more uniform than before compensation, much independent of feature size. This verifies that appropriate size

compensation in the input layout can significantly mitigate the effects of optical proximity and linearity. Another approach for size compensation is by applying a scaling function dependent on the feature size, which will scale up smaller features to a further extent than a larger feature. An example is executed in Chapter 10, in which a scaling function is applied to scale the smallest features up by 20% while keeping the largest feature the same. The approaches for optical proximity effects are never universal or exclusive; rather they are often complicated and highly dependent on design factors such as the scatterer geometries and layout. Frequently, we need to evaluate and determine the details of optical proximity corrections on a case-by-case basis to achieve satisfactory lithography results.

7.2.2 *Shape Compensation*

Corner rounding is a common form of shape distortion in pattern writing close to the resolution limit of lithography tools. Figure 7.6 shows the example of writing generic crosses with 1-µm wide arms using our Heidelberg DWL66+ system's 4 mm write head, which has a patterning resolution limit of 800 nm. No optical proximity corrections are applied. The left column of Figure 7.6 shows the input layout design details at the central junction (top row) and the end tip (bottom row) of a cross, while the right column shows the corresponding SEM images at those locations. As seen in the SEM images, the concave corners at the central junction and the convex corners at the tip end are all visibly rounded, distorting the patterned shape relative to the input designs. The layering edges of the pattern are due to the generation of standing waves inside the photoresist.

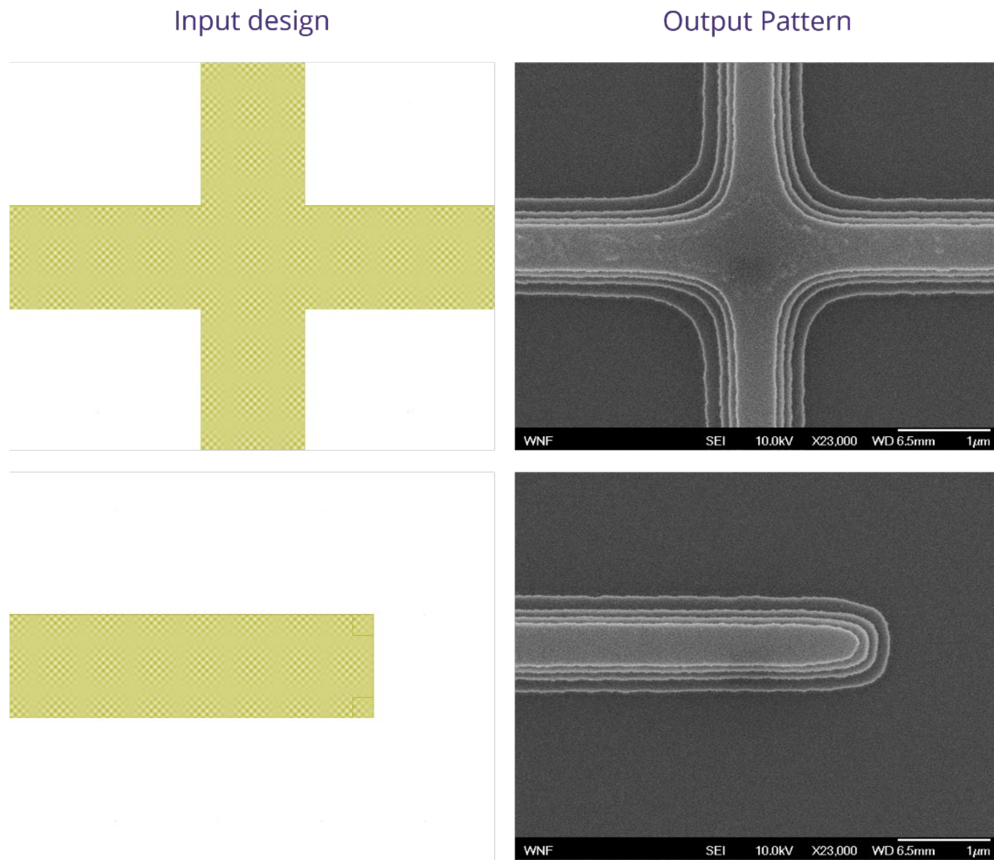

Figure 7.6. Comparisons between input layout designs (left columns) and SEM images of the laser direct-write output patterns (right columns) at concave (top row) and convex (bottom row) corners without any shape compensation.

In the IC industry, where closely packed gates and interconnects need to be patterned with high integrity, the loss of sharp corners can have adverse effects when the physical masks and reticles in the optical systems act as low-pass filters removing high-spatial-frequency geometries in the designed pattern during exposure. To resolve this issue, the IC engineers add structures like serifs and hammerheads to their lithography mask designs to preserve the patterning integrity of the fine features [85].

Here we adapt the introduction of serifs to our direct-write pattern designs to compensate for the potential loss of sharp corners in the pattern due to the laser beam dispersing in the photoresist. Figure 7.7 shows a similar comparison between the input designs and output patterns of the same

cross writing process. This time, square notches (empty serifs) are added to the concave corners at the central joints, whereas square serifs are added to the convex corners of the tip ends. Properly sized serifs are sub-resolution structures, which do not print with fidelity, but rather modify the patterned image locally to preserve more discernible corners and fine structures. As shown in the left column of Figure 7.7, we test and adjust both the serif size and the overlapping distance between the serif and the original conner until we achieve satisfactory compensation effects to create written patterns (right column) with higher resemblance to the target design patterns presented in the left column of Figure 7.6.

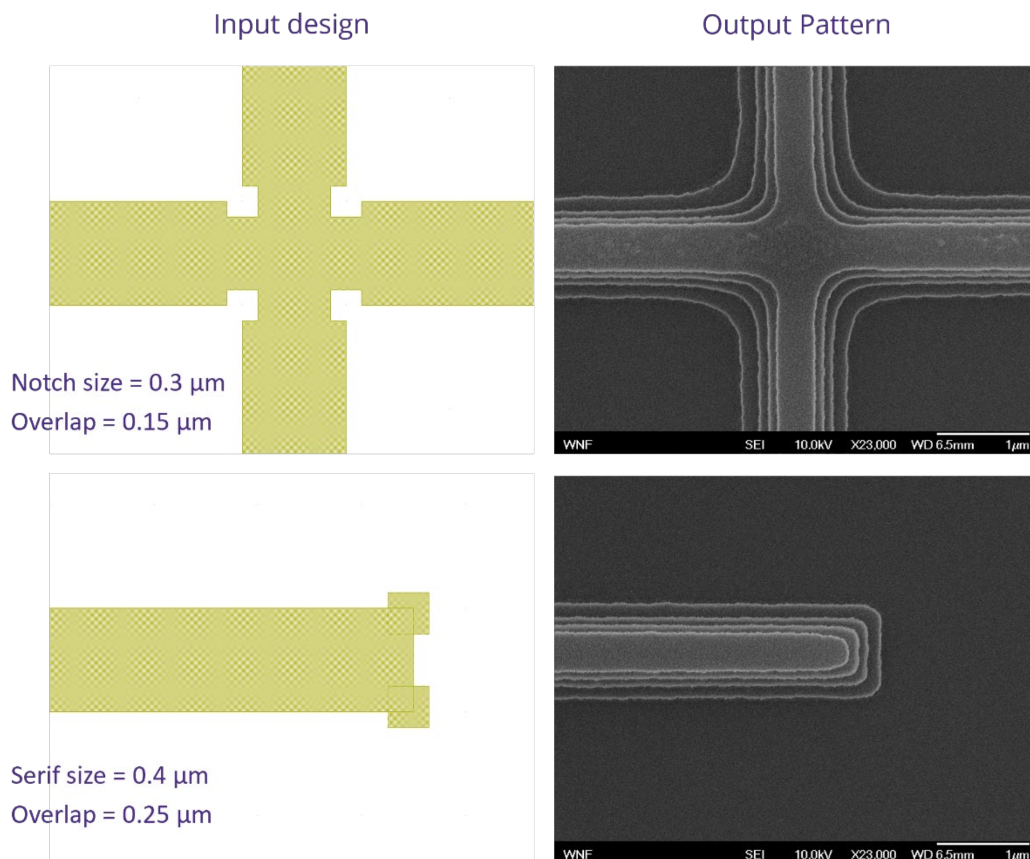

Figure 7.7. Comparisons between input layout designs (left columns) and SEM images of the laser direct-write output patterns (right columns) at concave (top row) and convex (bottom row) corners with the shape compensation using square notches and serifs.

The majority of our meta-optics consists of either simple scatterers with square cross-sections or complex scatterers with additional sharp protrusions or joints. We are writing the features with critical dimensions at the same scale as the write head resolution limit. Therefore, without proper compensation, the written patterns tend to suffer from corner rounding and, eventually, loss of some fine definitions. The left image of Figure 7.8 captures a patterned sample without any shape compensation. The layout inset on the top-left corner corresponds to the middle column of printed crosses. We can see that both the convex and concave corners of the cross-shaped scatterers have been consistently rounded, distorting the scatterer shape and affecting the resultant optical performance.

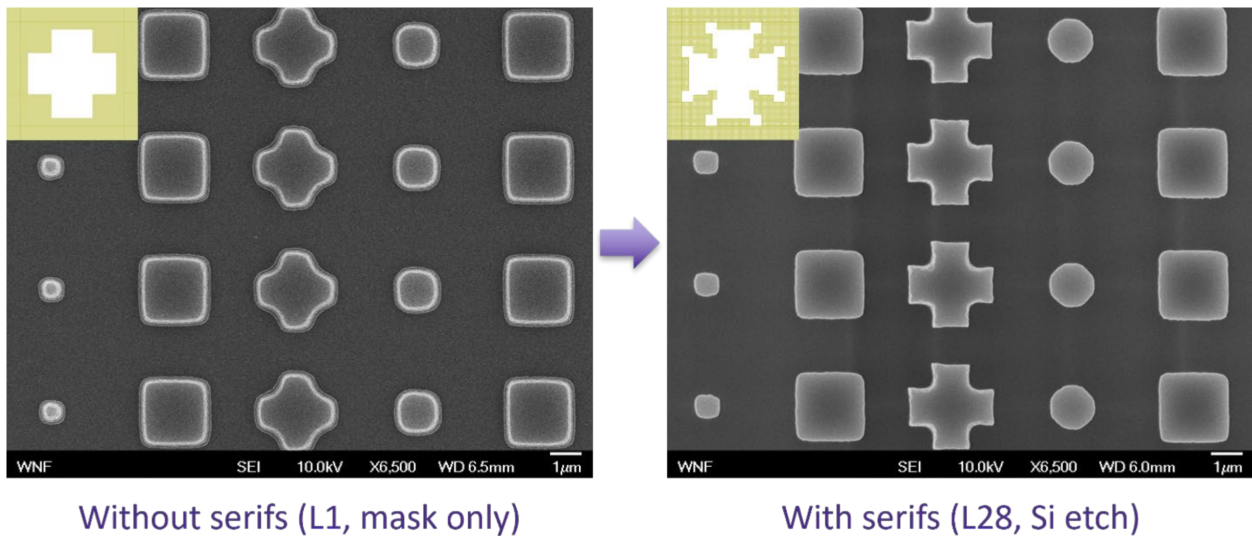

Figure 7.8. SEM images of meta-optic scatterer patterning outcomes by laser direct-write without serifs (left) and with serifs (right).

To preserve the sharp corners, we have introduced square serifs to the convex corners and square notches to the concave corners, as illustrated in the layout inset of the right image of Figure 7.8. The sizes of the serifs and notches are determined by patterning tests with a wide range of sweeping serif dimensions. As shown in the right image of Figure 7.8, the same column of crosses, now printed with serifs, have significantly more crisp and discernible conners at both convex and

concave sites. This is an even more crucial step to ensure the accurate patterning of customized scatterers with complex geometric designs (Section 8.6).

7.3 DEFECTS FROM LITHOGRAPHY AND DRY ETCHING

After lithography, all the meta-optics are etched with reactive-ion etching to transfer the lithography pattern to the corresponding structural layer to construct the scatterer nanopost arrays. Therefore, the quality and accuracy of the dry etch processes are crucial for the final device performance as well. The mid-wave infrared (Chapter 9) and visible (Chapter 10) meta-optics fabricated have relatively low aspect ratios (nanopost height and width are no more than 4:1), and the nanopost heights are less than 1.5 μm. Hence inductively coupled plasma (ICP) etching is used in these meta-optics. The long-wave infrared meta-optics (Chapter 8) have high aspect ratios up to 10:1 and large etch depths of 10 μm. Therefore, we utilize deep reactive ion etching (DRIE) to create these relatively tall meta-optic scatterers.

The various dry etch choices have their own advantages and issues, which are further dependent on the meta-optic designs, aperture sizes, and lithographic processes.

7.3.1 *Lithography Defects Near Wafer Edge*

The large-area meta-optics are designed with various aperture sizes, ranging from 0.5 cm up to 75 cm in diameter. Initially, to conform to the commercial lens holder dimension, we have chosen to fabricate any meta-optics with a diameter smaller than 50 cm on a 2-inch wafer. Here, we use long-wave infrared (LWIR) meta-optics fabricated for the foveated imaging project (Section 8.4) as demonstrating examples. These are full-silicon meta-optics on silicon substrates. The meta-optic patterns are exposed with laser direct-write in the photoresist and transferred to the surface of the silicon wafer via DRIE.

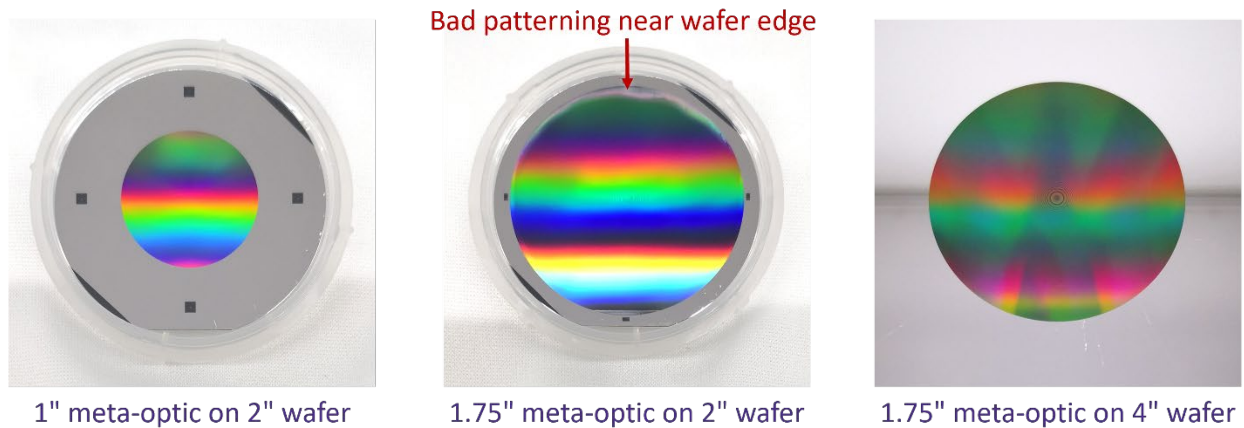

Figure 7.9. LWIR Meta-optics with various dimensions patterned on silicon substrates with different diameters. When the meta-optic diameter is too close to the substrate size (middle), lithographic defects arise near the wafer edge, transferring patterning imperfections to the scatterer layer after dry etch.

Figure 7.9 shows various full-silicon meta-optics fabricated on silicon wafers with different diameters. As shown in the left case, a meta-optic with a 1-inch diameter is patterned on a 2-inch wafer without any visible defects to the naked eye. However, the middle case has a meta-optic with a 1.75-inch diameter patterned on a 2-inch wafer, and the lithographic defects near the top arch of the pattern are apparent even to the naked eye. Such defects occur repeatedly with 1.75-inch meta-optics patterned on 2-inch wafers, though at various locations along the pattern arch. This is primarily due to the proximity of the pattern boundary and the wafer edge. Upon close inspection, the backsides of the 2-inch wafers are not flat all the way to the edge; rather, they have a slightly tapered thickness near the edge, causing poor contact between the wafer and the hotplate in the corresponding regions during the essential baking steps for lithography. Therefore, the exposure and development of meta-optic patterns are defective near the edge of the 2-inch wafer, which is transferred to the silicon scatterer nanoposts after DRIE, causing those edges to be optically useless. After some discussion, we have updated the fabrication process and switched to patterning the 1.75-inch meta-optic on a 4-inch silicon wafer instead. As shown in the right case

of Figure 7.9, thanks to the uniform baking across the exposure region on the larger substrate, the fabricated meta-optic looks decent to the naked eye without any edge lithographic defects.

7.3.2 *Excessive Heating with the Use of a Carrier Wafer*

As shown in the same fabrication examples from the previous section, the initial batch of meta-optics is fabricated on 2-inch silicon wafers. However, the dry etch tools at WNF are not compatible with 2-inch wafers as they are currently configured. In order to perform dry etching for pattern transfer from the photoresist to the structural layer, a 2-inch wafer needs to be affixed on a 4-inch carrier wafer, which can be properly loaded onto the etching stage. Usually, we apply Santovac oil between the 2-inch meta-optic wafer and the 4-inch carrier wafer to promote adhesion and heat conduction.

Both ICP etching and DRIE processes involve polymerization and etching, either simultaneously or in alternative steps. To achieve straight etch sidewalls for the closely packed meta-optic scatterers, the precise balance between the etching and polymerization is crucial. Both etching systems are equipped with stage cooling to aid such balance. However, if a process wafer experiences a gradual temperature increase due to prolonged plasma etching or reduced heat conduction to the stage (such as using a carrier wafer), the polymerization process will be inhibited to some extent as the etching proceeds, causing the etch profiles to deviate from the ideal vertical sidewalls.

For example, when we affix the 2-inch silicon wafer carrying a 1.75-inch meta-optic onto a 4-inch carrier substrate for the DRIE process to etch 10 μm of silicon, the use of the carrier layer adds another barrier for heat conduction between the 2-inch processing silicon wafer and the cooling chuck. Over the period of plasma etching, the temperature of the 2-inch wafer rises gradually and leads to the reduction of polymerization on the sidewalls. As a result, as the etch

depth increases, the sidewalls are less and less protected and hence more etched laterally by the plasma, causing the negative sidewall profiles to taper towards the bottom, as shown in the left image of Figure 7.10.

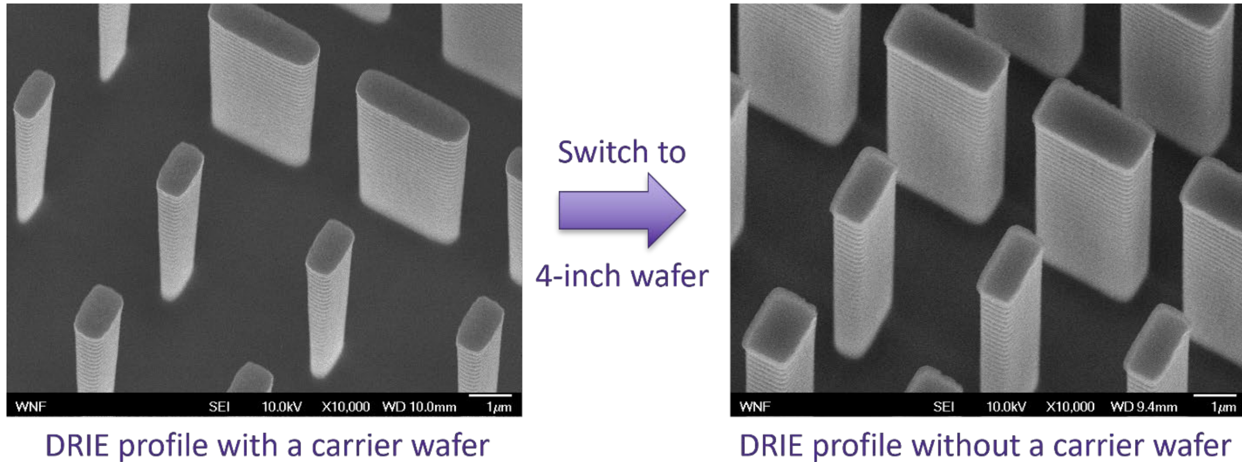

Figure 7.10. SEM images of scatterer etch profiles with and without the carrier wafer.

After we switch the fabrication process to 4-inch silicon substrates, there is no longer the need to use a carrier wafer for the dry etching process. Therefore, better wafer cooling and balance between the etching and polymerization processes are restored. As shown in the right image of Figure 7.10, the resultant DRIE profile patterned with the same meta-optic design has much more vertical sidewalls with little variation in dimension between the nanopost top and bottom, preserving pattern size and discernible corners as well. Such improvement is another reason to support the switch of all static meta-optic processes to 4-inch wafers regardless of meta-optic dimensions. By eliminating the need for a carrier wafer, we ensure better wafer cooling and vertical etch profile for the meta-optic scatterers.

7.3.3 *Scatterer Sidewall Profiles*

In the ideal case, to produce good optical performance, the etch sidewalls of the scatterer pillars should be as smooth as possible. This is a challenging requirement as the etch chemistry and sidewall profiles are often dependent on many factors, such as the etching mechanisms, structural materials, lithography processes, and the current chamber conditions. Some processes may be improved to produce smoother sidewalls, but the process development may be time-consuming. Some processes will have inevitable sidewall structures tied with the operating principles of the etching process, which may be mitigated to some extent but may not be fully eliminated. Hence, it is important that the fabrication engineer and the optical designer communicate well regarding the possible effects on final performance and include tolerance in the initial design if possible.

Our dielectric meta-optics for the MWIR (Chapter 9) and visible (Chapter 10) spectra are mostly etched in the inductively coupled plasma (ICP) etchers for their high compatibility with many semiconductor materials and etching masks. ICP etching can pattern meta-optics with low to intermediate aspect ratios. Rigorous process development has the potential to achieve relatively smooth etch sidewalls. Figure 7.11 shows the SEM image of silicon nitride scatterers on silicon substrate for the MWIR meta-optics discussed in Chapter 9, patterned with fluorine-based ICP etching. This process has utilized an aluminum hard mask for the meta-optic pattern to reach an etch depth of 2 μm. Though not entirely straight, the etch sidewall is relatively vertical with mild textures. Figure 7.12 shows the SEM image of silicon nitride scatterers on fused silica substrate patterned with fluorine-based ICP etching. This design is a preliminary etch test for the later direct-write visible meta-optics presented in 9.4; hence instead of going to the full extent of using a hard mask, we use a photoresist mask to produce a shallow etch of 750 nm because of the relatively low selectivity between silicon nitride and photoresist in the ICP process. As observed in the SEM

image, the sidewalls are vertical but with rough textures, especially close to the nitride-silica interface at the bottom.

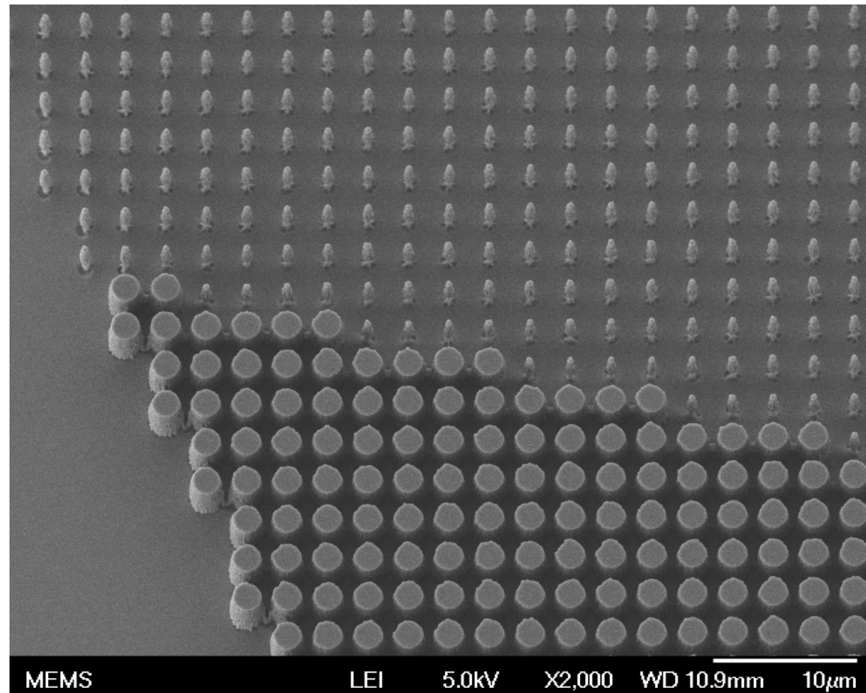

Figure 7.11. SEM image of MWIR silicon nitride meta-optic scatterers on silicon substrate patterned with fluorine-based ICP etching.

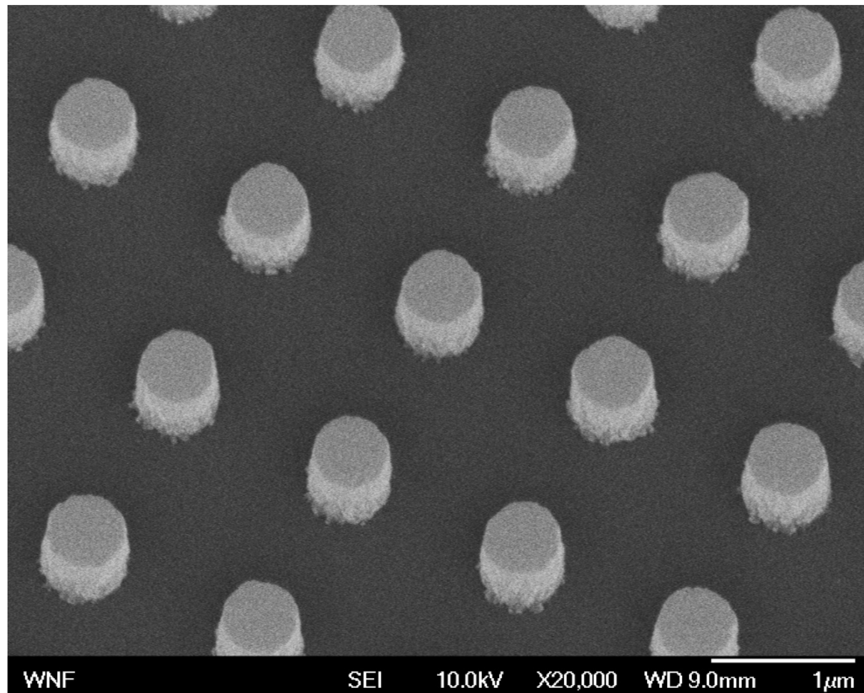

Figure 7.12. SEM image of visible silicon nitride meta-optic scatterers on fused silica substrate patterned with fluorine-based ICP etching.

Deep reactive ion etching (DRIE), as the name states, is built for etching deep features with high aspect ratios. Since our DRIE system is restricted to silicon etching only, we utilize its advantages to create all-silicon meta-optics for the LWIR spectrum as presented in Chapter 8. DRIE operates based on a high-density inductively coupled plasma source and an alternating process of silicon etching and polymer passivation (Bosch process). During the passivation step, an inhibiting polymer film is deposited on all the exposed surfaces, including cavities. The etching step of the next cycle preferentially removed the polymer from the trench bottoms by ion bombardment while preserving the protection on the sidewalls [89]. “Scallop” sidewall profiles are produced as the result of the alternating etching and passivation steps. Figure 7.13 shows the complex scatterers patterned for LWIT MTF-engineered meta-optics in Section 8.5. Luckily, the sidewall scallops, in this case, do not affect the optical performance of the fabricated meta-optics

too much, and it is more important to produce 10 μm tall silicon scatterers with vertical sidewalls utilizing the DRIE process.

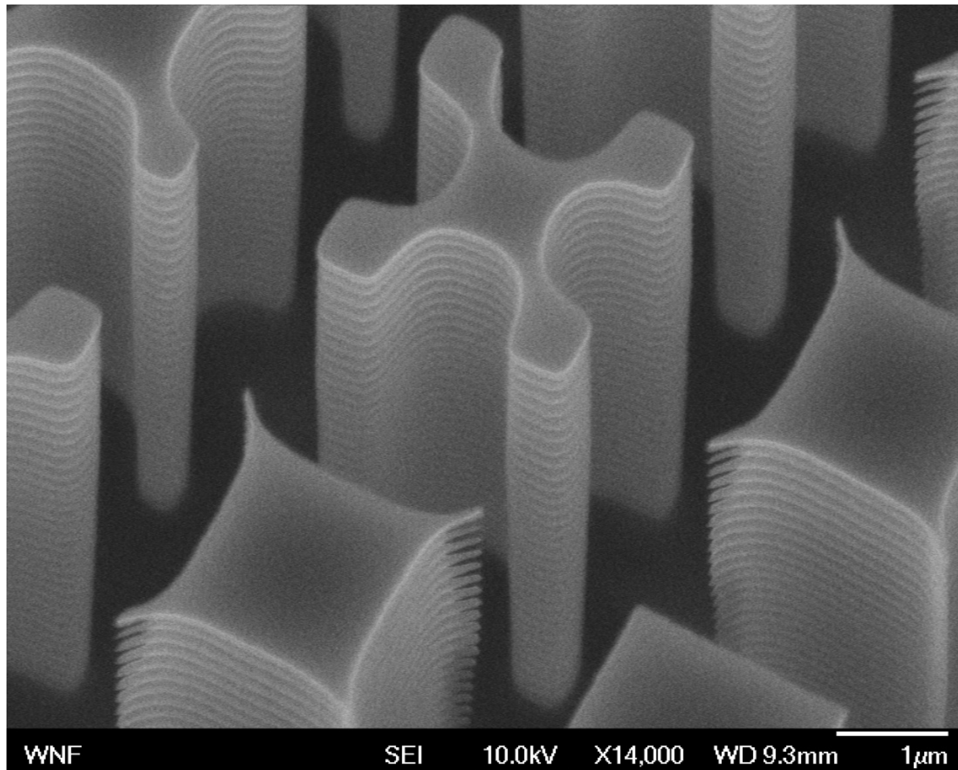

Figure 7.13. SEM image of LWIR silicon meta-optic scatterers on silicon substrate patterned with DRIE. The scalloping from the Bosch process is apparent.

As an intrinsic property of the Bosch process, the elimination of scalloping is almost impossible in DRIE. However, for applications that require both high feature aspect ratios and relatively smooth sidewall profiles, the magnitude of scalloping may be reduced by various approaches. Since the scallops are produced during the isotropic etching step and their size is dependent on the etching time per cycle, shortening the cycle and etch time can produce scallops with both smaller pitch and smaller magnitude. Time-multiplexed alternating processes can also be applied to utilize the gas residence time in the etch chamber and allow a continuous flow of the reagent gases while switching between the etching step and the passivation step. With an accurate

balance between the etch and passivation, such time-multiplexing can achieve both an anisotropic etch profile and mild scalloping with high process stability [90].

Chapter 8. FABRICATION OF LARGE-AREA LONG-WAVE INFRARED (LWIR) META-OPTICS

8.1 INTRODUCTION

Imaging in the long-wave infrared (LWIR) regime generates quantitative radiometric digital images of object scenes in the wavelength range of 8-14 μm. In this regime, the thermal sensors often require less complex components or maintenance than thermal imaging in shorter wavelength regimes. LWIR imaging is a vital technology widely employed in defense, surveillance, environmental monitoring, biomedical imaging, and non-contact thermography. In this chapter, we explore the possibility of utilizing diffractive ultra-thin meta-optics to replace the bulky conventional refractive optics in a wide range of LWIR applications and try to push the aperture limit to fabricate large-aperture LWIR meta-optics with laser direct-write lithography, which has several advantages such as large patterning area, relatively fast writing speed and high design flexibility for fast prototyping.

8.2 GENERAL FABRICATION FLOW FOR SINGLE-SIDED LWIR META-OPTICS

Most of the LWIR meta-optics are fabricated with silicon scatterers on silicon substrates. Since LWIR devices typically operate in the spectral range of 8-14 μm, the required minimum feature size in the LWIR meta-optics is often no less than 1 μm, which is large enough to utilize the fast-prototyping capabilities of laser direct-write systems. Lightly doped silicon has low absorption in this wavelength range as well. Therefore, in order to improve the signal-to-noise ratio in the final operating meta-optical system, a metal aperture layer is often necessary to be patterned around the meta-optics to block the background noise from stray light rays. The LWIR meta-optics require a scatterer post height up to 10 μm with ideally vertical sidewall profiles. Therefore, the scatterer

pattern transfer to the silicon structures is executed with deep reactive ion etching (DRIE), which technique is known for its high-aspect-ratio etching capability and high selectivity relative to a thin photoresist mask.

With reference to Figure 8.1, we can summarize the general fabrication process flow for large-area LWIR meta-optics patterned with laser direct-write lithography. We start with a lightly doped, double-side polished silicon wafer and coat it with a negative photoresist. With direct-write lithography, we define the area of the meta-optic aperture and alignment marks in the photoresist layer. Then we deposit the metal of choice onto the developed negative photoresist. After the metal lift-off, the wafer is now covered with a metal aperture layer except for the region reserved for the meta-optic layer. Then we apply another photoresist layer, on which we expose the meta-optic pattern using direct-write lithography, with alignment to the metal aperture with the aid of previously patterned alignment marks. After development, the meta-optic pattern is defined inside the aperture, while the extent of the photoresist should cover the entire metal layer to prevent metal loss and chamber contamination during dry etching. Then we transfer the meta-optic pattern from the photoresist layer to the bulk silicon inside the aperture by deep reactive ion etching. Once the desired scatterer depth is achieved, we can unload the wafer and strip any residual photoresist on the wafer surface. The detailed dimensions for aperture and meta-optics vary across projects.

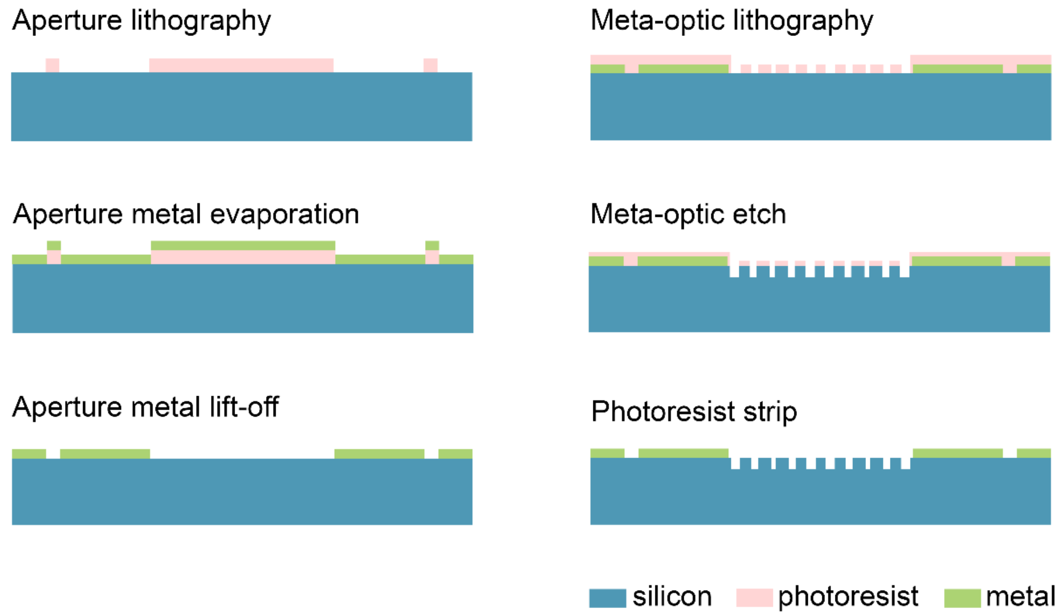

Figure 8.1. General fabrication flow for silicon LWIR meta-optics.

8.3 Infrared Imaging under Ambient Thermal Radiation

This project aims to design, fabricate, and characterize an all-silicon LWIR meta-optic for broadband imaging. The imaging experiments are carried out in a mixed-temperature environment to emulate different wavelengths to verify that the proposed system can maintain good imaging quality across various environments [91].

This work has been published in the journal Optical Materials Express with the title "Long wavelength infrared imaging under ambient thermal radiation via an all-silicon metalens" [91].

8.3.1 *Device Parameters*

Table 8.10 summarizes the design parameters of the broadband LWIR meta-optic. As an early attempt to patterning large-area meta-optics with laser direct-write lithography, this set of exposure does not have size or shape compensations incorporated.

Table 8.10. LWIR meta-optic parameters for broadband thermal imaging.

Scatterer Array		
Aperture Shape	Circular	
Aperture Size	1 inch	
Lattice Grid	Square	
Lattice Constant	4 μm	
Nanopost Design		
Post Material	Silicon	
Substrate Material	Silicon	
Post Cross-section	Square	
Post Height	10 μm	
Dimension Levels	10	
Individual Elements	**Duty Cycle**	**Edge length (μm)**
Minimum Nanopost	0.4535	1.814
Maximum Nanopost	0.6920	2.768

8.3.2 *Device Fabrication*

We start with a double side polished Si wafer with a thickness of 300 μm and p-type doping with boron giving a sheet resistivity of 1 W·cm to 100 W·cm. We first fabricate the metal aperture stop. A negative photoresist is spin-coated onto the substrate before being exposed to laser direct write lithography using Heidelberg DWL 66+ and development. Next, 193 nm of aluminum is evaporated via e-beam evaporator CHA SEC-600, following lift-off, creating the aluminum aperture stop. Then, a positive photoresist is spin-coated on the substrate. We then again use laser direct writing with Heidelberg DWL 66+ to create the metalens pattern inside the previously defined aperture. We develop the pattern and deep reactive-ion etch 10 μm of the silicon using SPTS Rapier. We note that the pillar height is controlled by the etch time, which is calibrated beforehand to approximately achieve the desired thickness of the silicon scatterer. The residual photoresist is subsequently stripped by oxygen plasma in YES CV200 RFS Downstream Asher.

The left image of Figure 8.2 captures a fabricated 4-inch wafer carrying four 1-inch meta-optics. The right image of Figure 8.2 shows an optical image of the meta-optic pattern near the aperture center. The different shades of colors are the optical effects dependent on the local scatterer coverage density. The periodic light-color vertical lines in the optical image correspond to the location of the laser stripe edges, which are visible in the patterned designs if the adjacent laser stripe paths are not precisely aligned and matched. This is one of the intrinsic tool artifacts associated with laser direct-write lithography. For designs with high sensitivity to pattern deviation, careful calibrations of the laser direct-write tool need to be executed to produce a smoother and more continuous exposure profile across stripes. Scanning electron microscopy images in Figure 8.3 show the square-based nanopost arrays arranged in a fixed periodicity with varying edge lengths to map the desired meta-optic phase profiles.

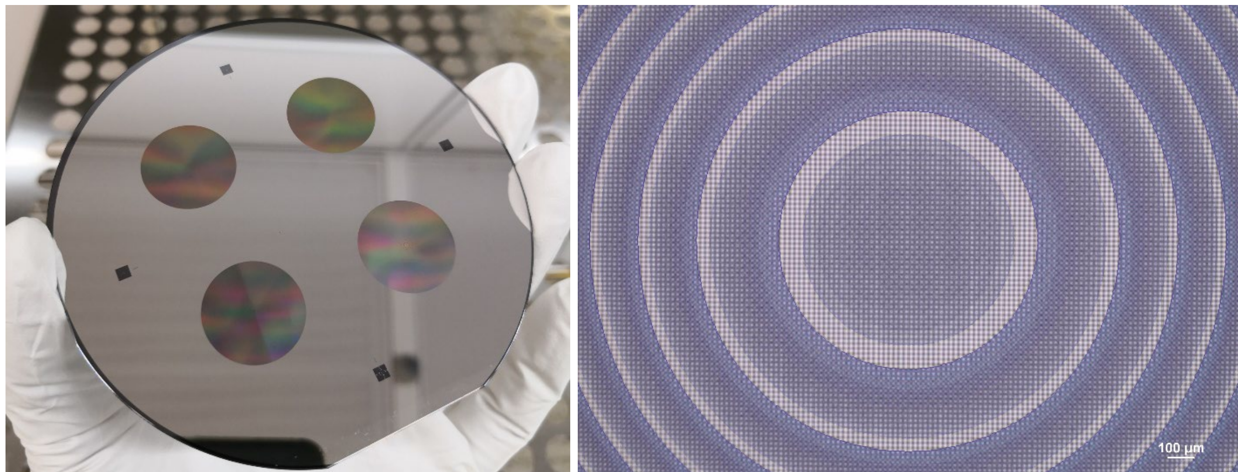

Figure 8.2. Fabricated LWIR meta-optic. (Left) Photograph of four 1-inch meta-optics fabricated on a 4-inch wafer. (Right) optical image of a meta-optic pattern near the aperture center.

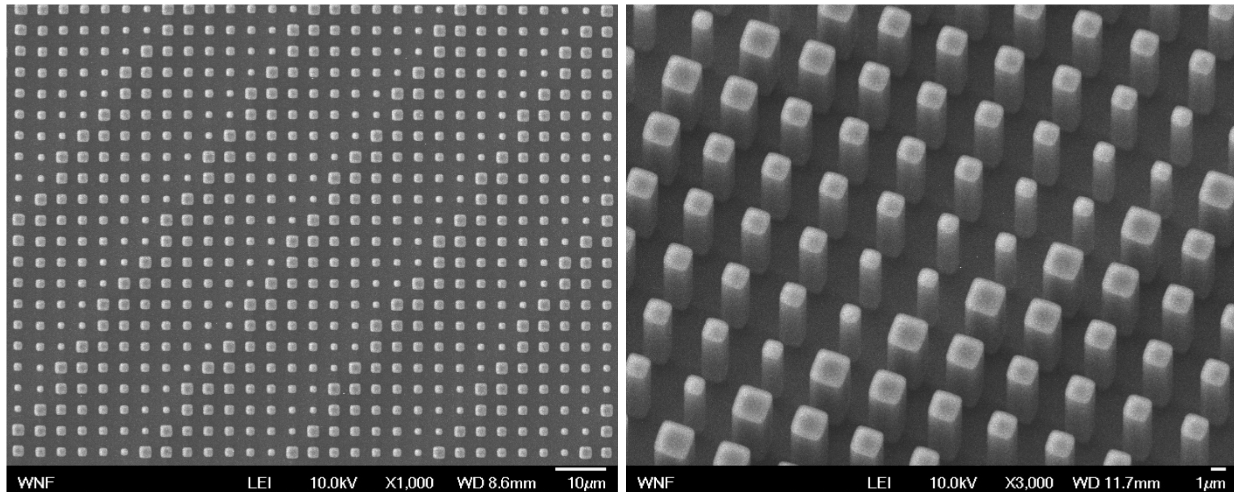

Figure 8.3. SEM images of the fabricated LWIR meta-optic. (a) Top view. (b) Oblique view.

8.3.3 *Optical Performance*

We are the first to demonstrate "in the wild" LWIR imaging in a real-life environment using the simple meta-optic. Since the black-body radiation spectrum differs at different temperatures, real-life objects with different temperatures are used to evaluate the imaging performance of this meta-optic under various extreme temperatures, such as the hot soldering iron in Figure 8.4a and Figure 8.4b, and the ice pack in Figure 8.4c. The imaging of a person holding both the ice pack and blowtorch in Figure 8.4c also demonstrates the good contrast in meta-optic imaging for daily objects at different temperatures. With a simple setup, our meta-optic has shown strong potential for LWIR imaging for real-world ambient thermal emission applications [91].

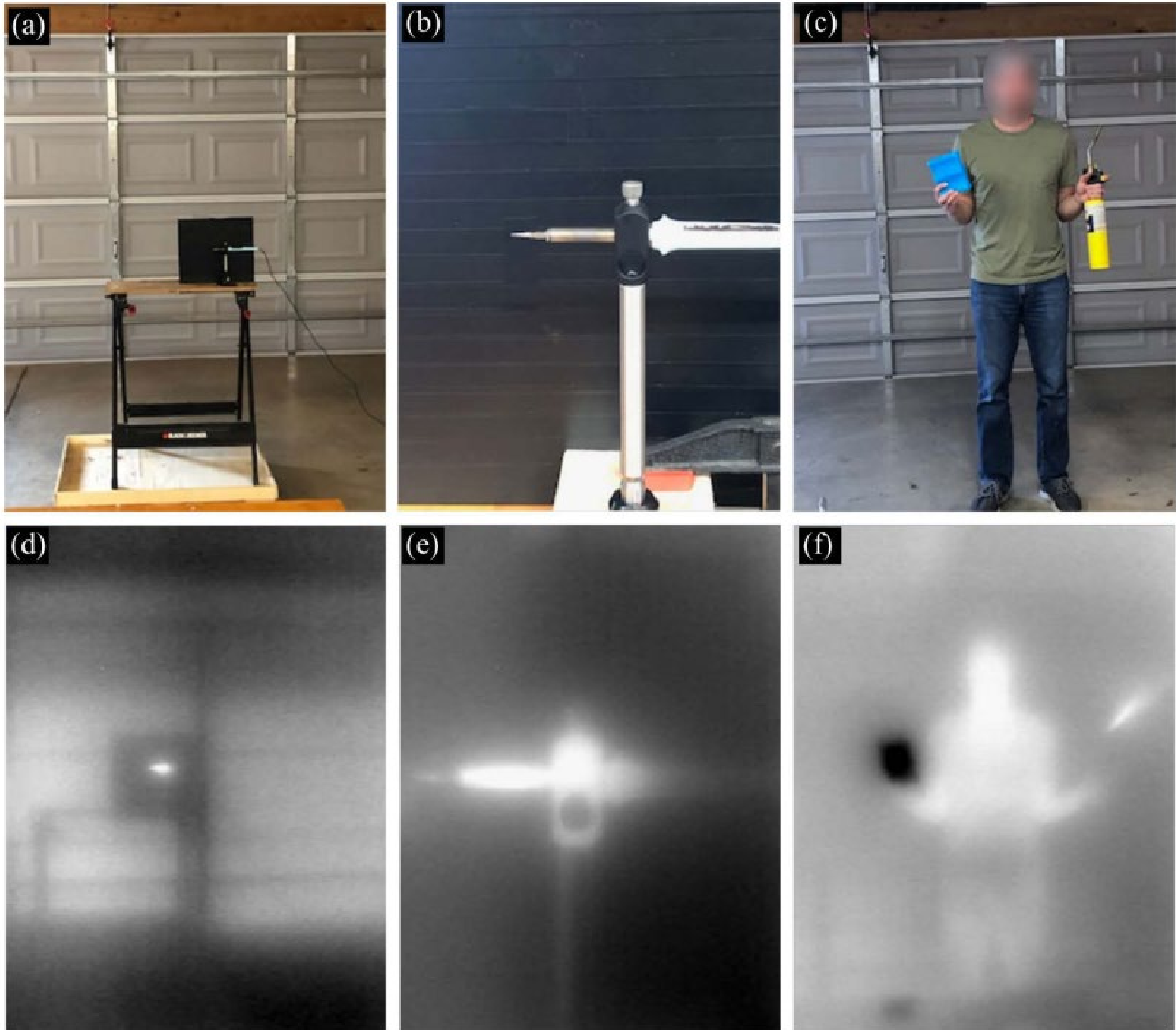

Figure 8.4. “In the wild” imaging using the LWIR meta-optic. (a) A hot soldering iron is seen in front of a steel plate covered with black tape with an emissivity of 0.95. (b) A close-up image of the hot soldering iron on a metal holder. (c) A person is holding an ice pack (left) and a blowtorch (right). (d), (e) and (f) display the corresponding images captures by the LWIR meta-optic, respectively [91].

8.4 FOVEATED THERMAL COMPUTATIONAL IMAGING

In this project, collaborated with Rice University, we demonstrate computational foveated imaging by exploiting the ability of a meta-optical frontend to differentiate orthogonal polarization states

and a computational backend to reconstruct the captured image or video, simultaneously enabling high resolution and large field of view. The frontend consists of two large-area LWIR meta-optics, respectively converging s-polarized light and p-polarized light at two different focal lengths without interfering with each other. A computational backend then utilizes Deep Image Prior (a convolutional neural network that enhances a given image with no prior training data) [92] to separate the resultant multiplexed image or video captured into a foveated image consisting of both high-resolution center and lower-resolution large field of view context [93].

This work is currently under review by the journal Nature Communications with the title "Foveated Thermal Computational Imaging in the Wild using All-silicon Meta-optics."

8.4.1 *Meta-optic Parameters*

Table 8.11 summarizes the design scatterer parameters for the foveated imaging meta-optics. Though with different diameters and designed focal lengths, all the foveated meta-optics consist of the same set of basic rectangular-base scatterer designs arranged in different patterns. When converting the layouts for laser direct-write, a 700 nm critical dimension bias has been added to compensate for feature size shrinkage due to optical proximity and linearity effects.

Table 8.11. LWIR meta-optic parameters for foveated thermal computational imaging.

Scatterer Array		
Aperture Shape	Circular	
Lattice Grid	Square	
Lattice Constant	4 μm	
Aperture diameter (mm)	Focal length (mm)	
12.7	25	
25	25	
45	75	
75	150	
Nanopost Design		
Post Material	Silicon	
Substrate Material	Silicon	
Post Cross-section	Rectangular	
Post Height	10 μm	
Dimension Levels	>100	
Individual Elements	Duty Cycle	Edge length (μm)
Nanopost x minimum	0.25	1
Nanopost x maximum	0.745	2.98
Nanopost y minimum	0.2905	1.162
Nanopost y maximum	0.75	1.768

8.4.2 *Device Fabrication*

Each meta-optic was fabricated on a 500-μm thick double-side polished silicon wafer, lightly doped with boron, giving a sheet resistivity of 10-20 Ω-cm. We used direct-write lithography (Heidelberg DWL 66+) to define the location of the metalens aperture in a negative photoresist layer. A 240-nm thick aluminum layer was deposited via electron beam evaporation (CHA Solution) and lifted off to form the metal mask surrounding the designated aperture of the metalens, reducing the noise in the experiments. The metalens scatterer layout was aligned and patterned into the open circular aperture using direct-write lithography with a positive photoresist. We

utilized deep reactive-ion etching (SPTS DRIE) to transfer the metalens pattern into the silicon layer with a scatterer depth of 10 μm and highly vertical sidewalls.

As shown in Figure 8.5, we have fabricated four different meta-optic designs with the same set of basic optical scatterers. All designs are fabricated on a 4-inch substrate for better control of lithography and etching conditions. Thanks to the large exposure range of the laser direct-write system, we have successfully fabricated LWIR foveated meta-optics with a wide range of diameters from 25 mm all the way to 75 mm. The corresponding focal lengths vary from 25 mm to 150 mm. The switching between imaging for s-polarization and p-polarization is achieved by rotating the meta-optic by 90°. A foveated imaging pair of meta-optics consists of two such meta-optics with a 90° rotation offset so that the system can capture both s-polarized light and p-polarized light without interference with each other. After some tests on the meta-optic combination, the top two meta-optics present in Figure 8.5 ($\emptyset = 25\ mm, f = 25\ mm$ and $\emptyset = 75\ mm, f = 150\ mm$) are selected as a pair for the main foveated imaging experiments.

Figure 8.6 shows the optical images of the fabricated meta-optics, partially capturing the mapped convex phase function (left) of the meta-optics and the local variation of scatterer designs for phase mapping. Figure 8.7 shows the SEM images of the fabricated scatterers for the foveated meta-optics. The pillar sidewalls are very vertical without dimension variation through the entire depth. The scalloping from the DRIE process is visible, but fortunately, it does not have significant effects on the imaging results. The corners of the rectangular bases are slightly rounded. If future work requires a sharper definition of the scatterer patterns, corner serifs may be introduced to enhance the sharp features.

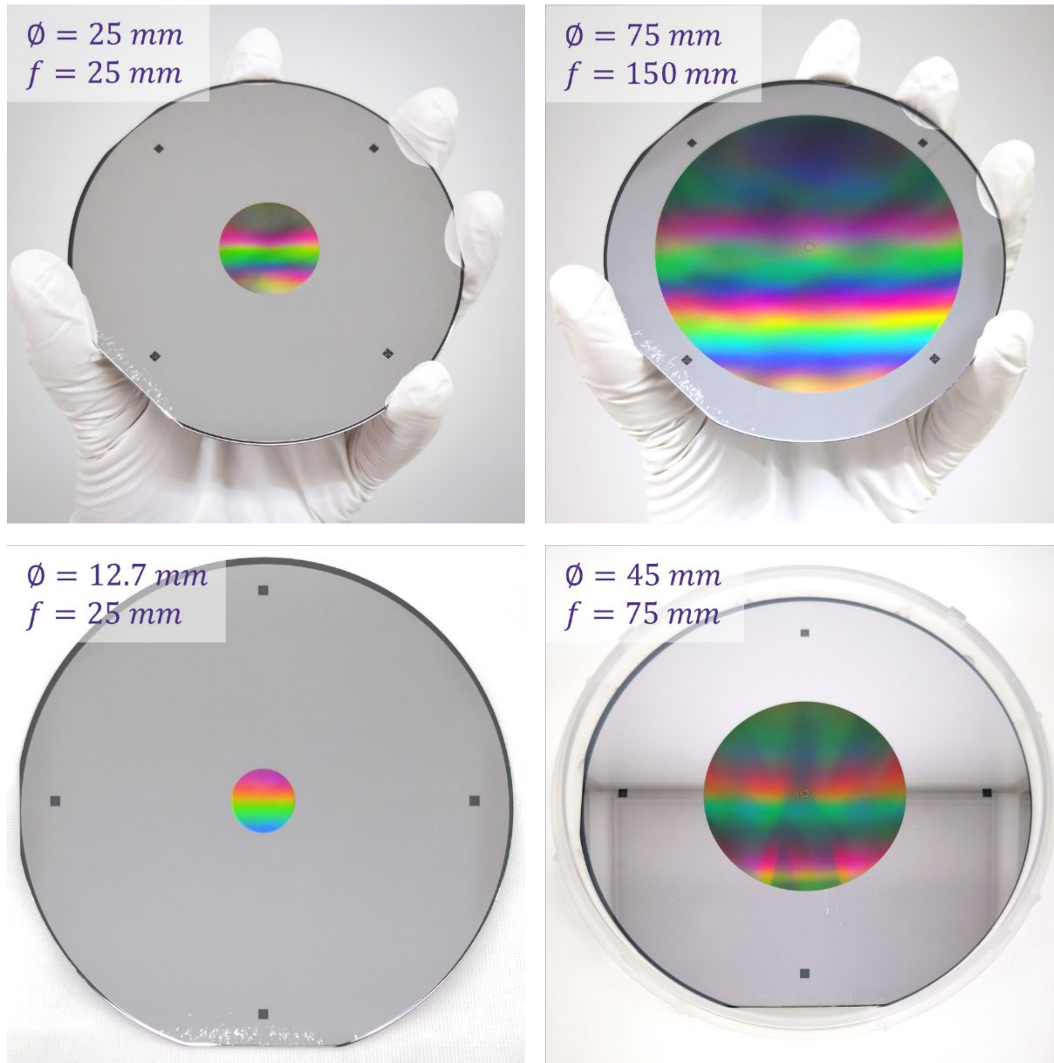

Figure 8.5. Four designs of silicon-based LWIR meta-optics fabricated on 4-in wafers for foveating imaging. The diameter spans from 12.7 mm to 75 mm, while the single-optic focal length varies from 25 mm to 150 mm. The top two (with 25 mm and 75 mm diameters) are eventually selected as a pair to perform the imaging experiments.

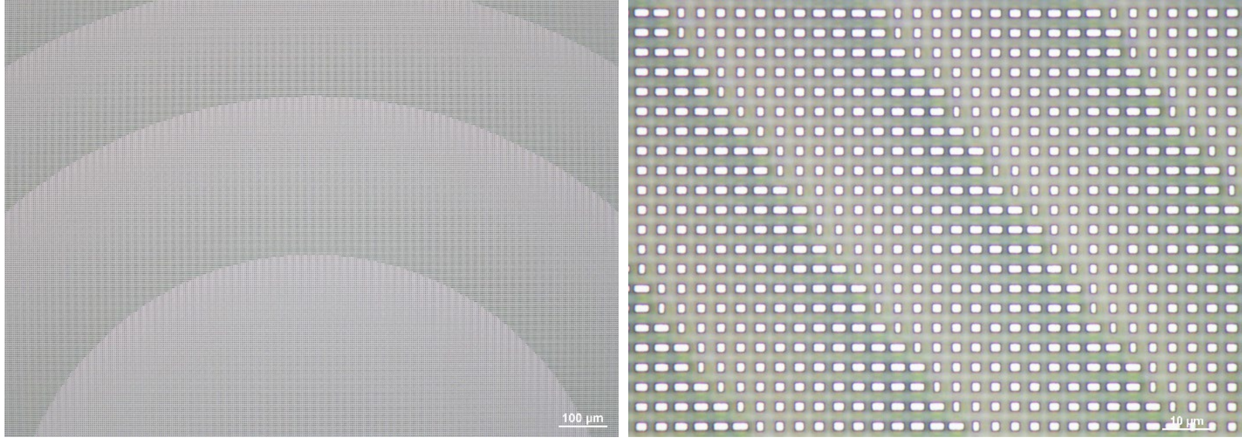

Figure 8.6. Optical images of the foveated meta-optics showing the mapped convex phase profile (left) and zoomed-in view of the varying scatterers (right).

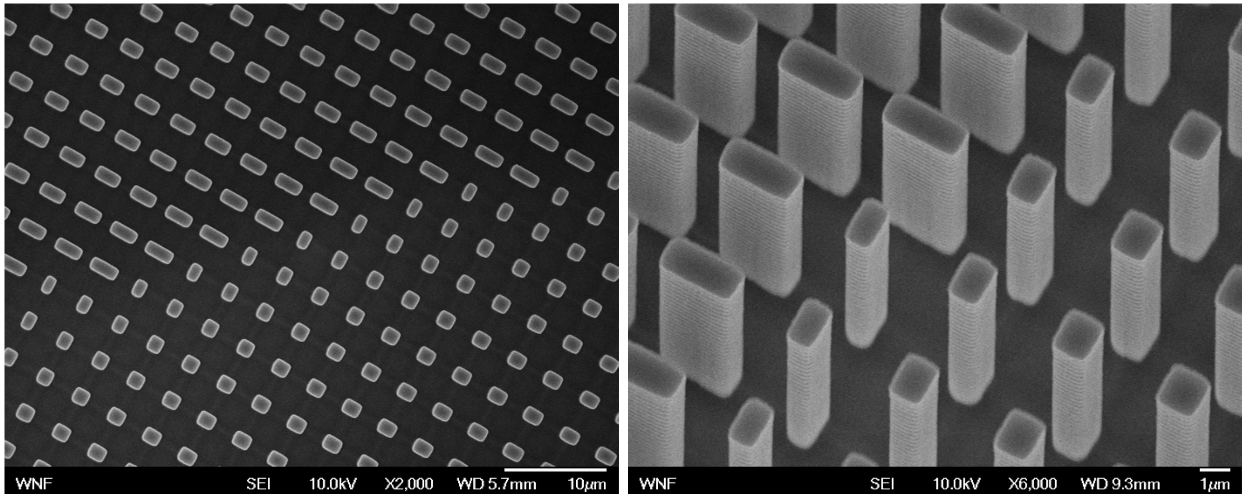

Figure 8.7. SEM images of the meta-optic scatterers for foveated imaging viewed from the top (left) and at an oblique angle (right).

8.4.3 *Optical Performance*

Utilizing the two large-aperture (25 mm and 75 mm diameter), polarization-sensitive LWIR meta-optics with primary focal lengths of 25 mm and 150 mm, respectively, we have constructed a first-of-its-kind prototype system to demonstrate real-time, foveated capture of image and video in the wild for the LWIR spectrum. Figure 8.8 illustrates the fundamental setup of the foveated imaging system. The two frontend polarization-sensitive meta-optics with different focal lengths capture

the image with different fields of view and resolutions, which can be separated by a computational backend to construct a foveated image containing both high-resolution information and a large field of view. The meta-optic at surface 1 is called the foveal element, which only modulates the s-polarized light, while the other meta-optic at surface 2 is called the perifoveal element, which only modulates the p-polarized light [93].

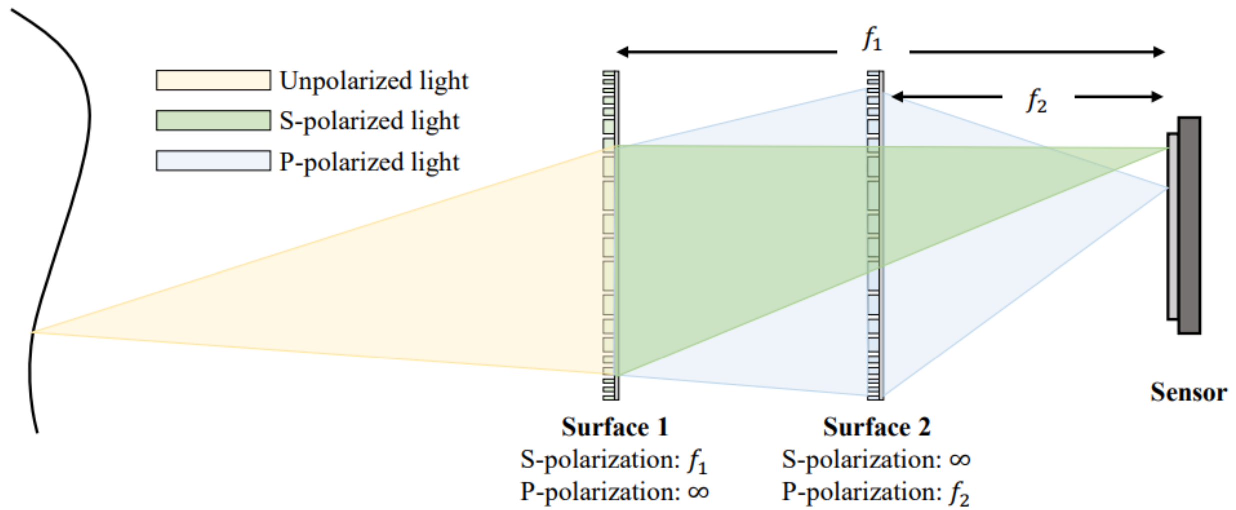

Figure 8.8. Experimental setup of foveated imaging. (Image credit to Vishwanath Saragadam at Rice University)

The optical setup utilizing the meta-optic pair coupled with a powerful computational backend for image detail reconstructions has produced high-resolution foveated images in diverse indoor and outdoor settings. Figure 8.9 shows an example of static imaging of a rooftop scene. The perifoveal meta-optic captures an image with a large field of view, providing a context of the surrounding areas, whereas the foveal meta-optic captures an image with finer details, giving high-resolution information about the central region of interest. With the computational backend, we can recover many fine features, such as the windows and eaves of the faraway tower. The paper includes more imaging examples at various temperatures, indoor and outdoor [93].

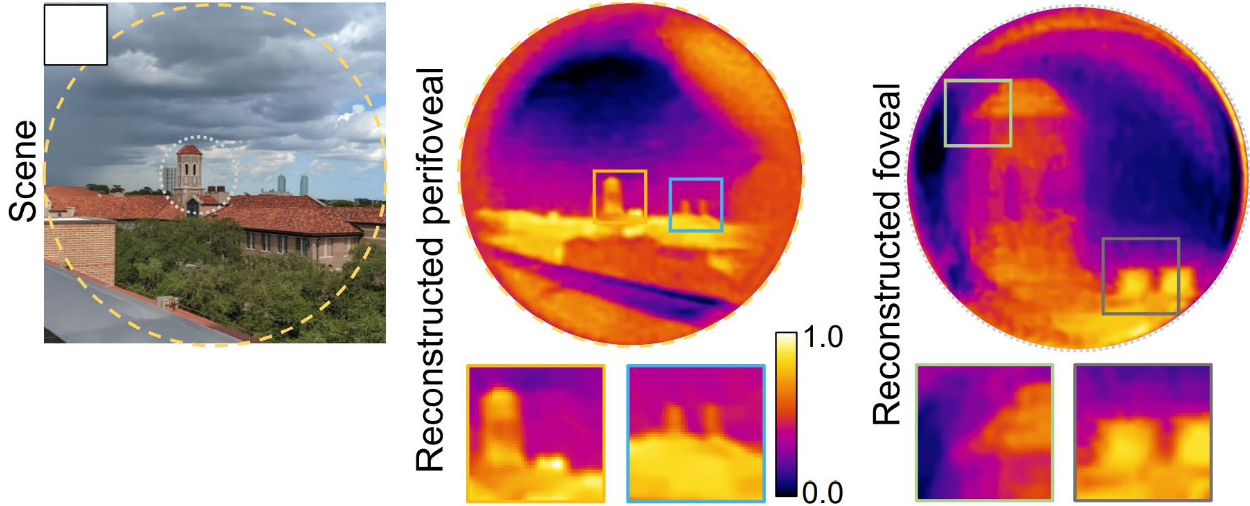

Figure 8.9. Static imaging in the wild captures an outdoor rooftop scene (left), where the perifoveal meta-optic generates an image with a large field of view (left) while the foveal meta-optics generates an image with finer details [93].

8.5 MTF-ENGINEERED META-OPTICS

In this project, we explore the possibility of creating novel scatter designs to fabricate meta-optics with a specially engineered modulation transfer function (MTF) to achieve better imaging quality in the wild and explore additional functionalities.

This work is currently being prepared for publication.

8.5.1 *Meta-optic Parameters*

Table 8.12 summaries the meta-optic parameters with MTF-engineered scatterers. Both MTF-engineered meta-optics with aperture diameters of 1 cm and 2 cm have been fabricated with similar process flows. However, due to some optical design errors, only the 1-cm MTF-engineered meta-optics produce imaging results aligned with the designs. Hence the device fabrication and experiment results presented later mainly focus on the 1-cm meta-optics.

Table 8.12. LWIR meta-optic parameters for MTF-engineered meta-optics.

Scatterer Array		
Aperture Shape	Circular	
Aperture Diameter	1, 2 cm	
Lattice Grid	Square	
Lattice Constant	4 μm	
Nanopost Design		
Post Material	Silicon	
Substrate Material	Silicon	
Post Cross-section	Square, complex	
Post Height	10 μm	
Dimension Level	>100	
Individual Elements	Duty Cycle	Edge length (μm)
Minimum Nanopost	0.25	1
Maximum Nanopost	0.75	4

Figure 8.14 displays some examples of MTF-engineered scatterer designs tested. The basic shapes of scatterers contain squares (left column), crosses (middle column), and x-shapes (right column). The "simple" MTF-engineered meta-optics and the basic hyperboloid metalenses for controlled samples only contain squares with varying sizes. The "complex" MTF-engineered meta-optics consists of all three basic scatterer structures with changing dimensions (including arm length and width for crosses, central and corner square size for x-shapes, etc.) arranged to map various phase profiles. As shown in Figure 8.14, optical proximity corrections such as dimension scaling (size compensation) and corner serifs (shape compensation) for the simple square scatterer designs can be applied readily, matching the printed pattern to the target design.

However, for more complex scatterer designs, optical proximity corrections become more complicated. The middle column of the cross scatterer example is from a preliminary sample for the shape compensation test with no size compensation. In the SEM image, all the patterned scatterers have shrunk in size, especially the smaller squares, indicating the importance of feature

size compensation when patterning with direct-write lithography. Nevertheless, the corners of the crosses are preserved by shape compensation using proper serifs and notches (details presented in Section 7.2.2).

The x-shape scatterer designs require more complicated calculations for their shape compensation. As shown in the right column of Figure 8.14, the basic design of an x-shape scatterer involves many infinitely small joints connecting the central square and the corner squares, which suffer more optical proximity and linearity effects because of their small sizes and standalone nature. As shown in the corresponding SEM image, the corner squares shrink significantly in size relative to the design. Moreover, any infinitely small joints are almost impossible to print with lithography, especially when the wavelength of our direct-write system is relatively large at 405 nm, limiting the achievable printing resolution. Hence as expected, the SEM image also shows necking effects replacing those joints. Common sub-wavelength correction features such as serifs and notches cannot be added around the small corner squares and infinite joints easily. Also, due to the relatively large aperture size, dense pitch, and a large number of scatterer dimension levels (distinctive individual scatterer designs with different dimensions) in the MTF-engineered meta-optic design, applying complicated shape compensation structures can require heavy computation. Therefore, we test complex meta-optics fabricated with only size compensation. Fortunately, the complex MTF-engineered designs are robust enough to tolerate the necking effects and shrinkage of corner squares. Therefore, for the purpose of demonstrating the concept of MTF-engineered meta-optics in this project, complex meta-optic designs involving x-shape scatterers only receive appropriate size compensation without shape adjustment.

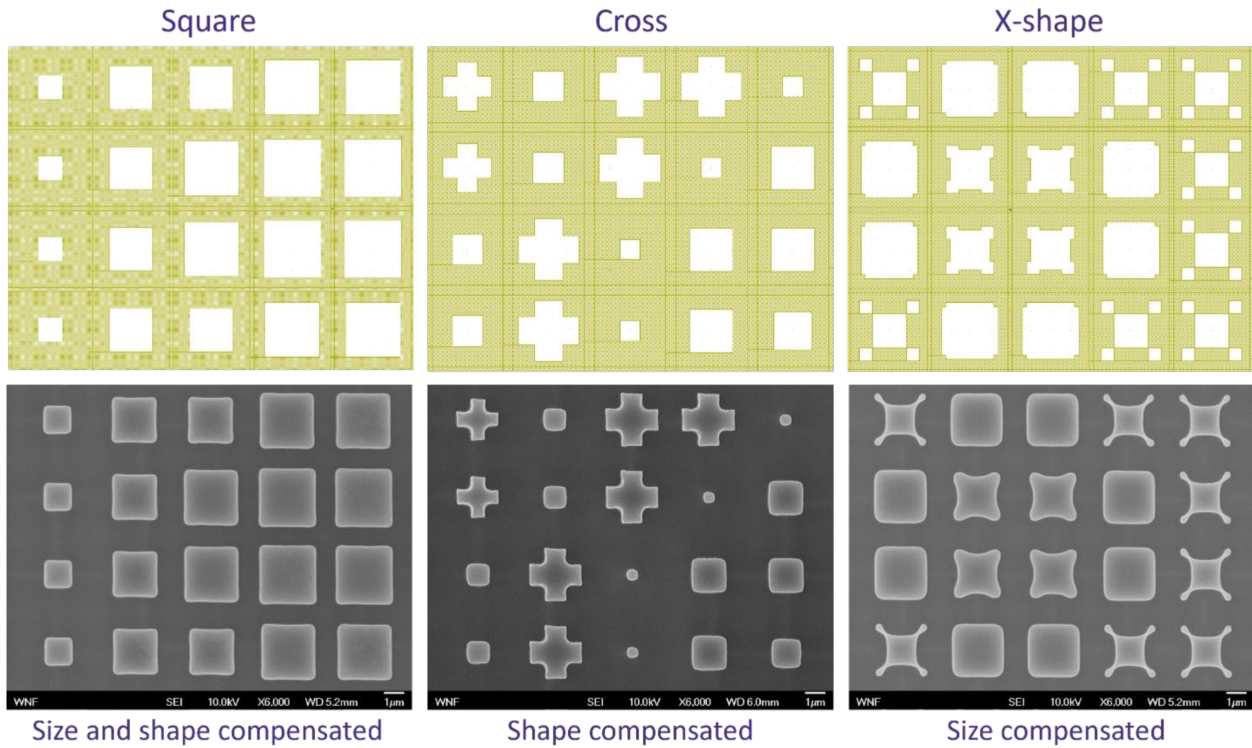

Figure 8.10. Categories of scatterer designs used to construct MTF-engineered meta-optics, showing both the target layout designs (top row) and the corresponding SEM images of the fabricated structures (bottom row) with optical proximity corrections. Hyperboloid metalens for reference only consists of square scatterers.

In the case of a 1-cm aperture, we have constructed and fabricated four designs of MTF-engineered meta-optics; one of them consists of only simple square scatterers with varying dimensions, while the other three are constructed with complex combinations of all scatterer designs with different dimensions. One design of hyperboloid metalens is mapped with the same set of square scatterers as the controlled group.

The simple MTF-engineered meta-optics and the hyperboloid metalenses containing only squares have both their size and shape compensated. We first apply 300-nm wide square serifs to the corners of all square scatterers with an overlap length of 200 nm (i.e., the protrusion length is

100 nm). Then when converting to the direct-write job, a critical dimension bias of 200 nm is added to combat feature shrinkage due to proximity and linearity effects.

The complex MTF-engineered meta-optics only receive a critical dimension bias of 200 nm on all features during job conversion for direct write.

8.5.2 *Device Fabrication*

The 1-cm meta-optics are fabricated on a 500-µm thick double-side polished silicon wafer, lightly doped with boron, giving a sheet resistivity of 1-10 Ω-cm. Direct-write lithography (Heidelberg DWL 66+) is used to define the aperture locations in the photoresist covering the wafer surface. A 220-nm thick aluminum layer is deposited via electron beam evaporation (CHA Solution) and lifted-off to construct the metal mask around the aperture, reducing ambient noise in the experiments. The wafer is coated with another thinner photoresist and then patterned with the meta-optic patterns via direct-write lithography, aligned inside the defined apertures. The photoresist pattern is transferred to the bulk silicon by 10-µm deep reactive ion etching (SPTS DRIE), utilizing its capability to etch with high aspect ratios and vertical sidewalls.

The fabrication of the 2-cm meta-optics is similar, except that the aluminum in the metal layer is replaced by a 100-nm gold with chrome as the adhesion material.

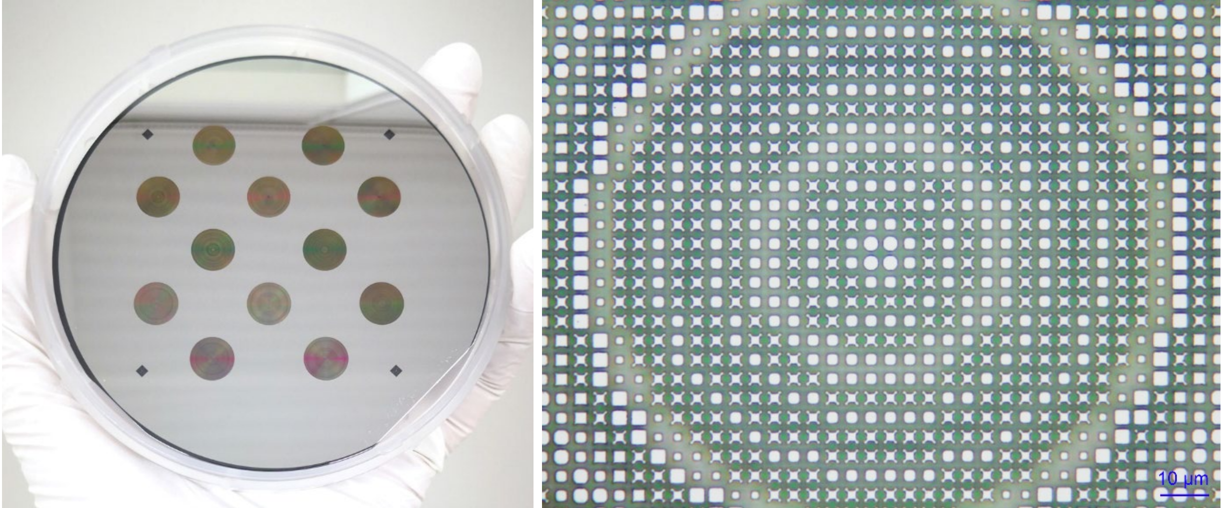

Figure 8.11. Fabricated MTF-engineered meta-optics and hyperboloid metalenses with 1-cm diameters. (Left) 12 meta-optics fabricated on a 4-inch wafer. (Right) Optical image around the center of a complex MTF-engineered meta-optic.

Figure 8.11 shows a 4-in wafer carrying 12 fabricated meta-optics and a top-view optical image showing the silicon scatterers at the center of a complex MTF-engineered meta-optic, in which we can observe scatterers with various shapes and dimensions arranged in a square lattice.

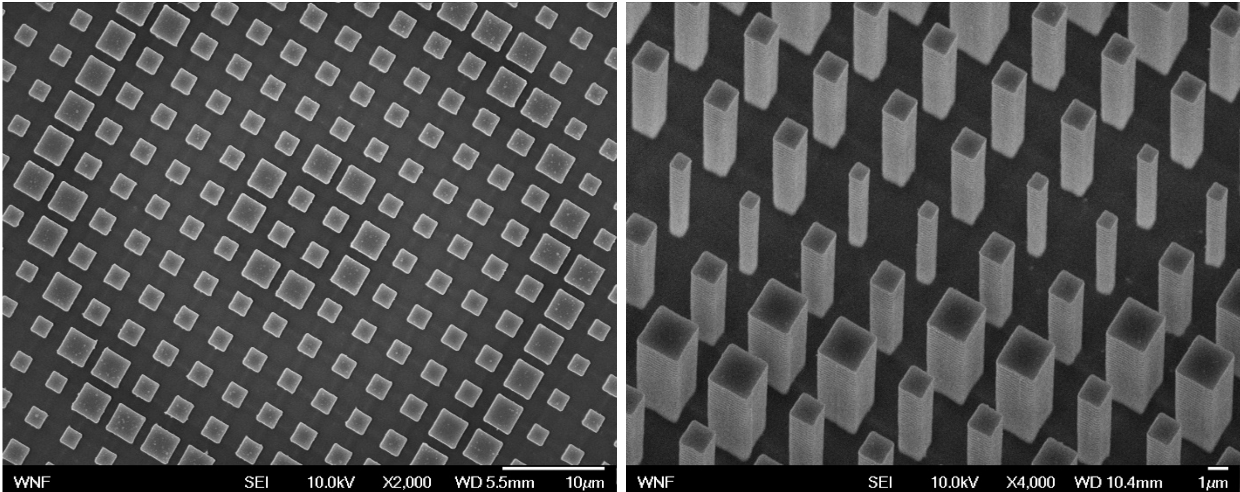

Figure 8.12. SEM images of “simple” MTF-engineered meta-optics fabricated solely with square-based scatterers viewed from the top (left) and at an oblique angle (right).

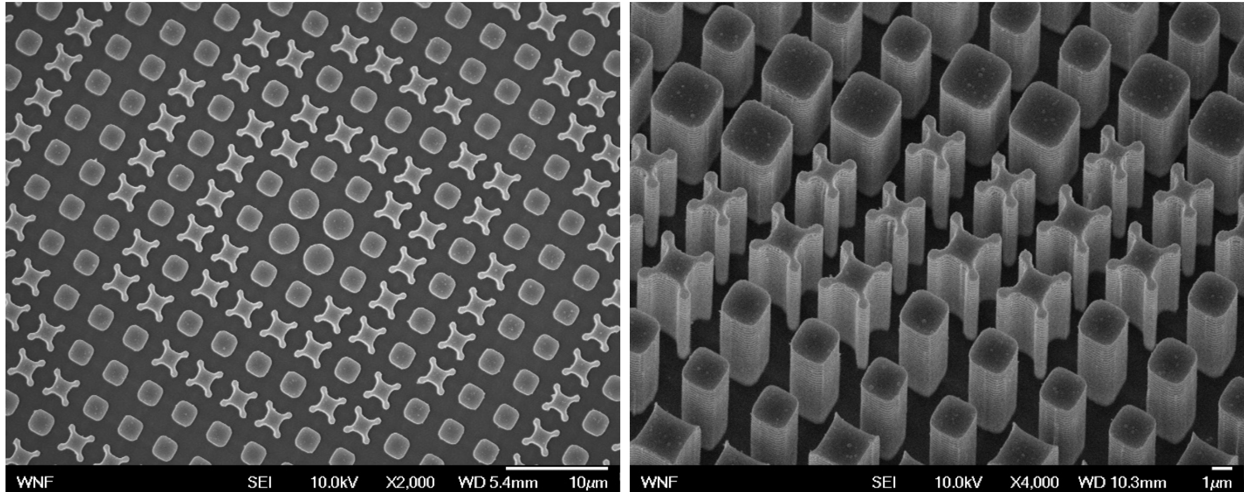

Figure 8.13. SEM images of "complex" MTF-engineered meta-optics fabricated with multiple scatterer designs, viewed from the top (left) and at an oblique angle (right).

Figure 8.12 and Figure 8.13 show the SEM images of the "simple" and "complex" MTF-engineered meta-optics, respectively. The "simple" meta-optics have square-based scatterers with consistent volumes and straight sidewalls throughout the depth. The "complex" meta-optics have the same DRIE sidewall quality and etch stability across scatterers with a wide range of complex base designs. As mentioned before, the x-shape scatterers cannot be realized with high precision due to the existence of infinitely small joints in the design patterns. Instead, necking and shrinkage of corner squares have occurred, which turn out to have negligible effects because of the high robustness of the MTF-engineered meta-optics with the novel scatterer designs.

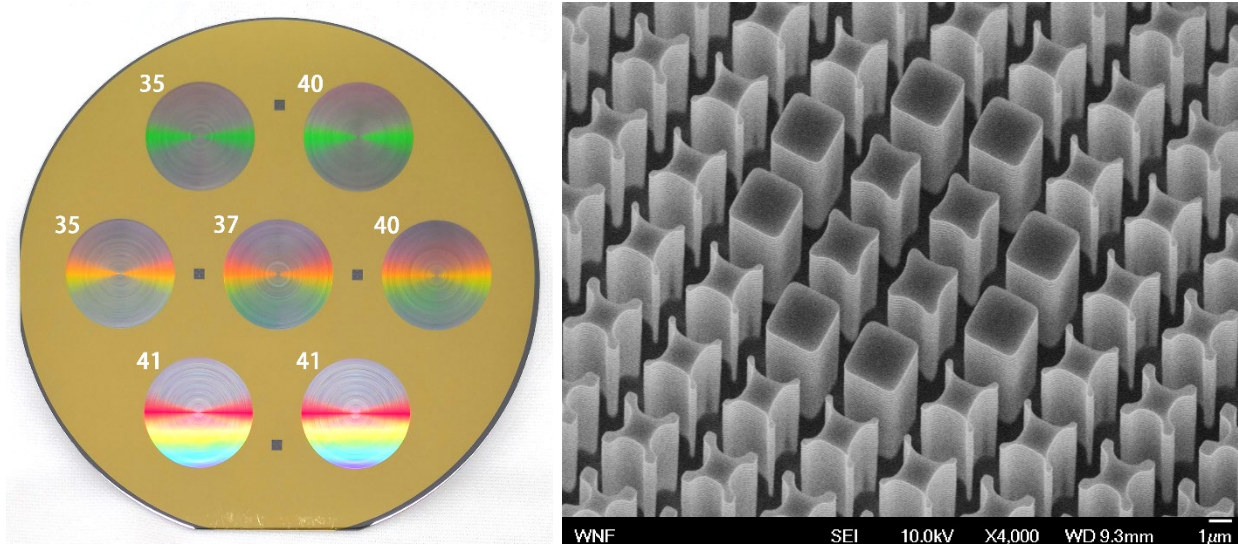

Figure 8.14. Fabricated MTF-engineered meta-optics and hyperboloid metalenses with 2-cm diameters. (Left) 7 meta-optics on a 4-inch wafer. (Right) Zoomed-in SEM image near the center of a complex MTF-engineered meta-optics.

The same fabrication process can be easily adapted to make MTF-engineered meta-optics with different aperture sizes. For example, Figure 8.14 shows a group of 2-cm MTF-engineered meta-optics on a 4-inch wafer using the same fabrication flow except for changing the aperture metal layer to gold (which does not create much difference in performance). The SEM image displays similarly decent patterning and etching qualities as the 1-cm meta-optics presented earlier. Although due to some optical design errors, this particular batch of 2-cm meta-optics did not work as predicted by simulations, this sub-project proves the robustness of the designed fabrication flow and its readiness to be quickly adapted for meta-optics with other aperture dimensions.

8.5.3 *Optical Performance*

The fabricated 1-cm MTF-engineered meta-optics and hyperboloid metalens are tested in a lab environment using a hotplate at 140 °C as the source, illuminating a black-painted metal stencil with a laser-cut pattern. We use computational algorithms to deconvolute the raw images and

compare them with the captured image from a refractive lens. As displayed in Figure 8.15, the imaging results from both the hyperboloid metalens (controlled group) and the “simple” MTF-engineered meta-optic have relatively strong haze even after post-processing, with the “simple” MTF-engineered meta-optic behaving poorer. The “complex” MTF-engineered meta-optic imaging results are significantly better than the other two, with crisper edges and higher contrast, showing more potential for the MTF-engineered meta-optics constructed with a wide range of complex scatterer designs.

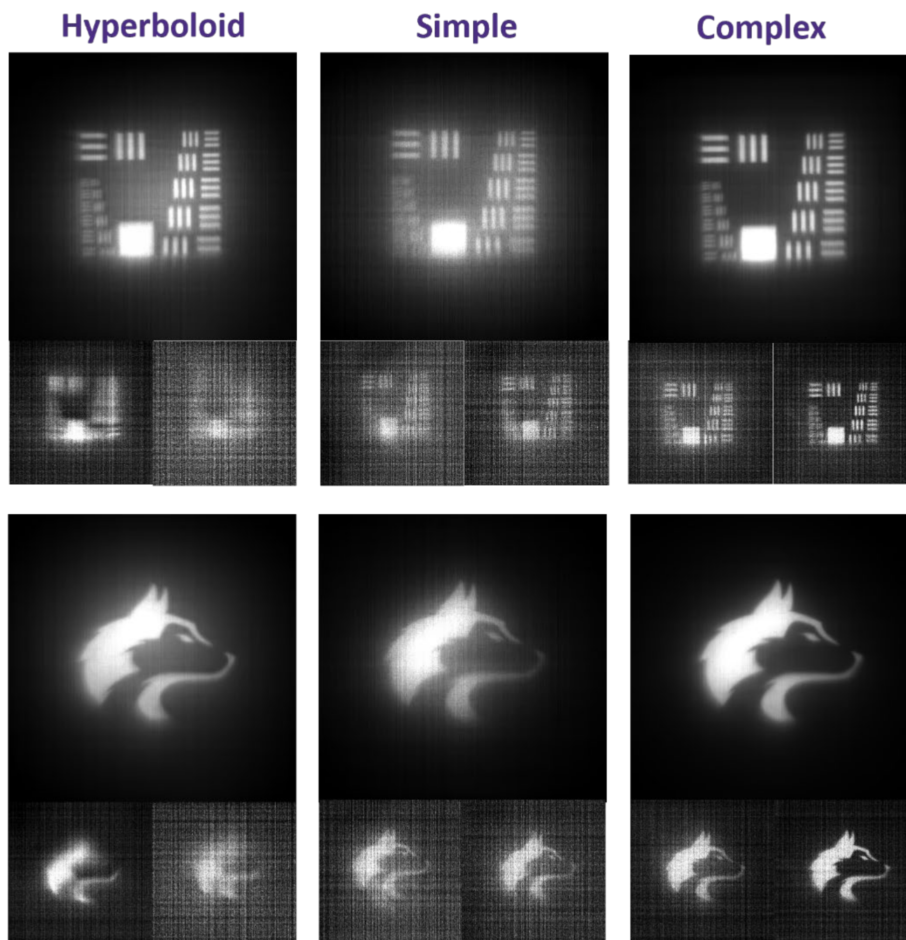

Figure 8.15. Deconvoluted infrared images from black-painted metal stencils set before a hotplate, captured via a hyperboloid metalens (left column), a “simple” MTF-engineered meta-optic (middle column), and a “complex” MTF-engineered meta-optic. (Image credits to Anna Wirth-Singh and Saswata Mukherjee)

Then we build a portable optics station and conduct “in the wild” imaging of real-life scenes outside the lab. We use the hyperboloid metalens (control group) and two different designs of “complex” MTF-engineered meta-optics from the same wafer to capture the same scenes and compare the deconvoluted imaging results with the photos through a commercial refractive lens. Figure 8.16 shows two groups of imaging results. The top row captures a dark grey car parking under the sun, with both the car and the concrete floor emitting large amounts of heat. The bottom row captures me sitting on the floor outside the glass doors of an air-conditioned library. Compared to the chilled glass in the background, the human body is evidently emitting more heat. When comparing across the columns, we can see that, though still inferior to the refractive lens, the two complex MTF-engineered meta-optics perform notably better than the hyperboloid metalens, showing better contrast between objects, well-defined outlines and more detailed features such as my glasses. All the results have verified that MTF engineering is a promising approach to producing ultra-thin meta-optics with superior performance than regular metalenses. Moreover, coupled with large-aperture design and fabrication, such MTF-engineered lenses show large potential to be utilized in many “in the wild” imaging applications calling for compact optics.

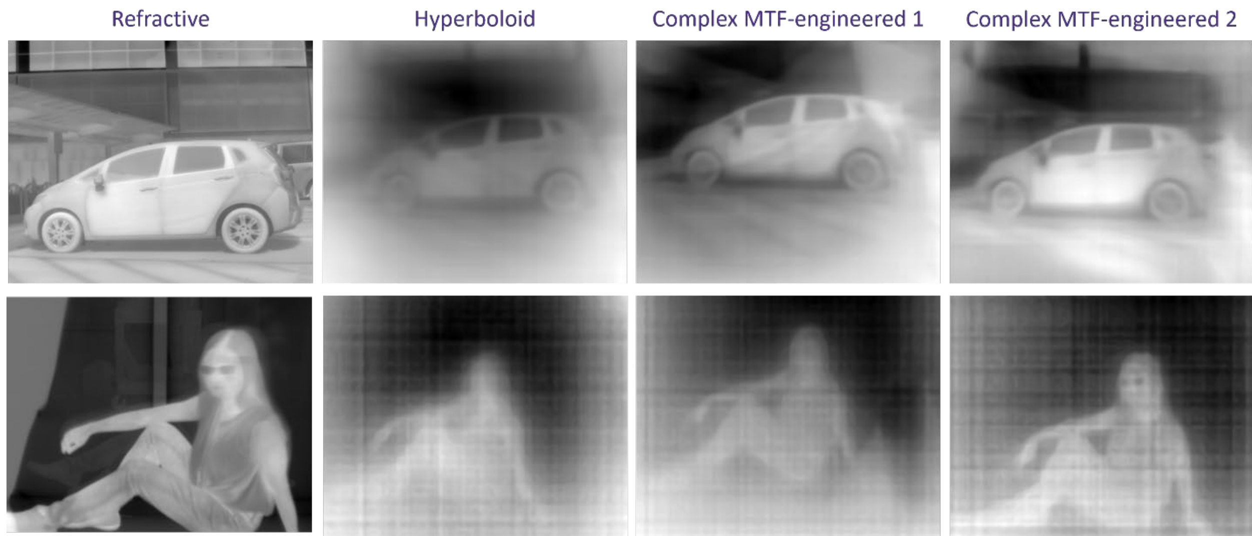

Figure 8.16. Deconvoluted infrared images of "in the wild" scenes, captured via a commercial refractive lens, a hyperboloid metalens, a "simple" MTF-engineered meta-optic, and a "complex" MTF-engineered meta-optic. The top row captures a grey car parking under the sun, and the bottom row captures me sitting against the glass doors of an air-conditioned library. (Image post-processed by Anna Wirth-Singh)

8.6 Double-sided MTF-engineered Meta-optics

This sub-project is an experimental extension of the previous section. Here we explore the possibility of fabricating double-sided meta-optics for MTF engineering. We have designed and executed a fabrication process flow to fabricate a group of double-sided meta-optics on one single wafer without the necessity for manual alignment and bonding using regular nanofabrication tools readily available on site of WNF.

Although due to some miscalculations in the original meta-optics designs, the optical performance of this batch of meta-optics does not comply with the design specifications, the full fabrication flow developed for this project will be beneficial for future double-sided meta-optics projects with improved optical designs.

8.6.1 *Meta-optic Parameters*

Table 8.13 lists the target parameters for the double-sided meta-optics. Both the entry and exit meta-optics consist of the same fundamental sets of simple and complex scatterers, similar to what has been displayed in the previous section. The metal aperture layer is deposited on the exit side of the wafer.

Table 8.13. LWIR meta-optic parameters for double-sided MTF-engineered meta-optics.

Scatterer Array		
Aperture Shape	Circular	
Aperture Diameter	1 cm	
Lattice Grid	Square	
Lattice Constant	4 μm	
Nanopost Design		
Post Cross-section	Silicon	
Substrate Material	Silicon	
Post Cross-section	Square, complex	
Post Height	10 μm	
Individual Elements	**Duty Cycle**	**Edge length (μm)**
Minimum Nanopost	0.25	1
Maximum Nanopost	0.75	4

8.6.2 *Device Fabrication*

Figure 8.18 shows the full process flow to fabricate the double-sided MTF-engineered meta-optics. We start with a 500-μm thick double-side polished silicon wafer, lightly doped with boron, giving a sheet resistivity of 1-10 Ω-cm. We spin-coat both sides of the wafer with the photoresist. The front side will be patterned with the entry meta-optics, while the back is protected from scratching during contact with processing equipment. We use laser direct-write lithography (Heidelberg DWL 66+) to define the entry meta-optics and wafer alignment marks in the front side photoresist.

After development, the pattern is transferred to the front side bulk silicon via deep reactive ion etching (SPTS DRIE) to create the entry meta-optics with a 10-μm depth. The residual photoresist is stripped from both sides. Then we spin-coat the wafer front side (with entry meta-optics patterned) with photoresist first as protection, then flipping the wafer and followed by spin-coating the back side with photoresist. We use a backside contact aligner (EVG Aligner 620) to define the back side aperture regions aligned to the patterned alignment marks on the front (entry) side of the wafer. We deposit a 100-nm thick gold layer with chrome as adhesion on to the wafer's backside with electron beam evaporation (CHA Solution) and lift off with the patterned photoresist, defining the back side apertures surrounded by the metal mask. The lift-off process removes the photoresists on both sides of the wafer. Therefore, we spin-coat the wafer with photoresist again, starting with the front side patterned with the entry wafer and then the back side with a metal aperture. We use laser direct-write to pattern the exit meta-optics on the back side of the wafer, positioned inside the defined apertures utilizing alignment marks patterned inside the metal mask layer. Similar to the front side, we transfer the exit meta-optic patterns to the bulk silicon via DRIE with an etch depth of 10 μm. At last, we strip the photoresist from both sides without direct physical contact with meta-optics.

DSP silicon

Photoresist spin-coat

Cover backside when processing frontside for integrity

Front meta-optic lithography - direct-write

Include marks for backside alignment

Front meta-optic etching - DRIE

Residual photoresist strip

Photoresist spin-coat

Coat front first for contact protection (dissolve during lift-off)

Back aperture lithography

Back aperture deposition and lift-off

Photoresist spin-coat

Coat front side first for contact protection

Back meta-optic lithography - direct-write

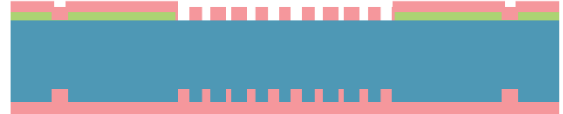

Back meta-optic etchiing - DRIE

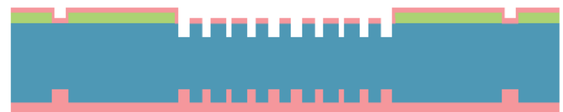

Residual photoresist strip

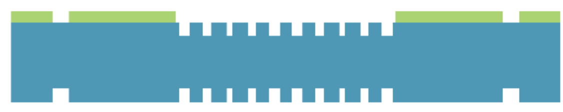

Use stripping methods without direct back contact

silicon metal photoresist

Figure 8.17. Fabrication process flow of double-sided MTF-engineered meta-optics.

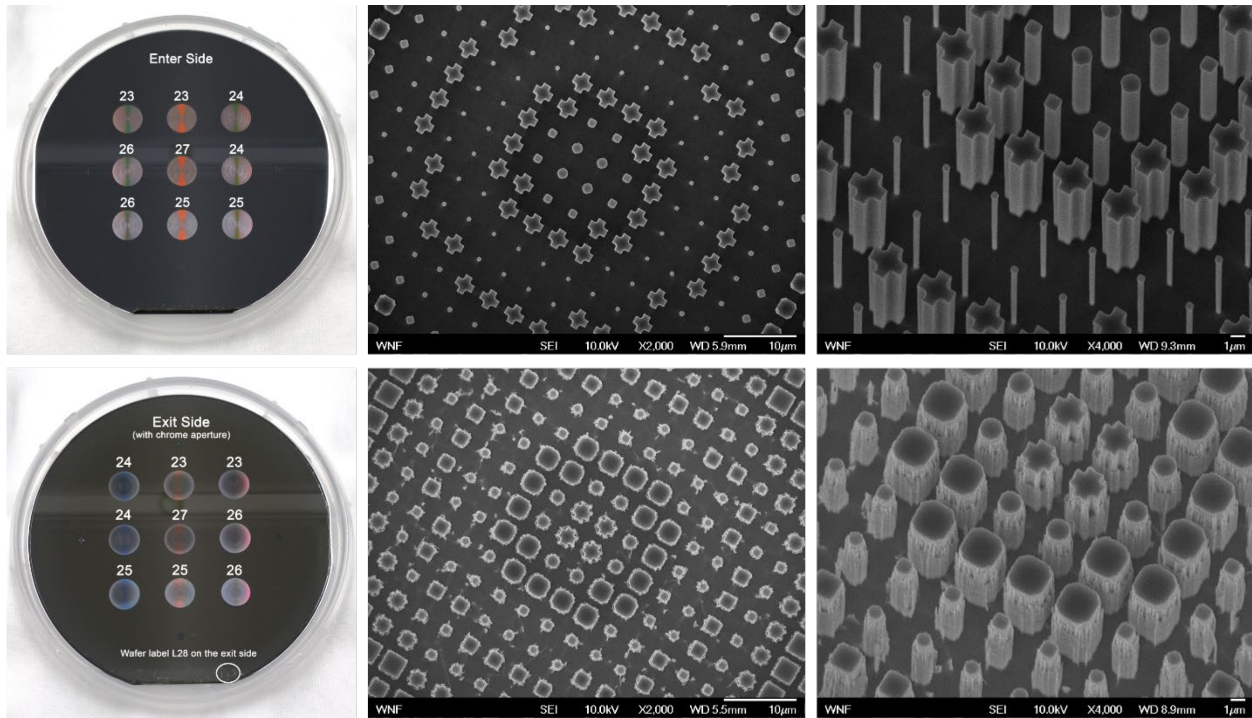

Figure 8.18. Photographs and SEM images of the fabricated double-sided MTF-engineered meta-optics. (Top row) Entry meta-optics. (Bottom row) Exit meta-optics.

Figure 8.18 shows the photographs and zoomed-in SEM images of the entry meta-optics on the front of the wafer and exit meta-optics on the back of the wafer. As shown in the SEM images, the etch quality of the front meta-optics is decent, but the same etch process has generated rough sidewall profiles on the back meta-optics. We attribute this to excessive local heating while etching the back meta-optics. Because of the existence of entry meta-optics on the other side, during DRIE, the regions of the back meta-optics cannot dissipate heat to the cooling chuck effectively, leading to overheating and redeposition of photoresist mask in the proximity of the features, which is then transferred to the rough etch sidewalls. Though we have determined that the main cause for the device malfunctioning is due to some optical design error, the fabrication process for future double-sided meta-optics can be further improved to promote more uniform wafer cooling during the dry etch processes.

Chapter 9. FABRICATION OF LARGE-AREA MIDDLE-WAVE INFRARED (MWIR) META-OPTICS

9.1 DUAL BAND COMPUTATIONAL INFRARED SPECTROSCOPY VIA LARGE APERTURE META-OPTICS

This project aims to demonstrate the concept of a computational spectrometer in the MWIR spectrum (3-5 μm) consisting of a meta-optical frontend and a computational backend. The frontend utilizes the strongly chromatic rotating point spread functions of a high-efficiency double helix meta-optic to encode the spectral distribution of a light source. The captured signal is subsequently decoded by the computational backend to accurately reconstruct optical spectra [94].

9.2 META-OPTIC PARAMETERS

Table 9.14 summarizes the design parameters of the dual-helix MWIR meta-optic. This pattern consisting of cylindrical scatterers is printed by 5:1 stepper lithography without any size or shape compensation in layout.

Table 9.14. Design parameters for dual-helix MWIR meta-optic.

Scatterer Array		
Aperture Shape	Circular	
Aperture Size	5 mm	
Lattice Grid	Square	
Lattice Constant	1.3 µm	
Nanopost Design		
Post Material	Silicon nitride	
Substrate Material	Silicon	
Post Cross-section	Circular	
Post Height	2 µm	
Dimension Level	6	
Individual Elements	**Duty Cycle**	**Diameter (nm)**
Nanopost 1	0.3948	513.3
Nanopost 2	0.4316	561.1
Nanopost 3	0.4991	648.8
Nanopost 4	0.5932	771.1
Nanopost 5	0.7404	962.5
Nanopost 6	0.9019	1172

9.3 FABRICATION FLOW

Figure 9.1 summarizes the device fabrication flow with stepper lithography. The silicon nitride meta-optics were fabricated on a 525-µm thick double-side polished silicon wafer, lightly doped with boron, giving a sheet resistivity of 8-15 Ω-cm. We deposited a 2-µm thick silicon nitride layer with plasma-enhanced chemical vapor deposition (PECVD) at 350 °C (SPTS SPM). We utilized stepper lithography (Canon FPA-3000 i4) to pattern the meta-optics in the photoresist layer. A 170-nm thick aluminum layer was evaporated (CHA Solution) and lifted off to create a hard etching mask for the meta-optics. Then we transferred the pattern to the 2-µm silicon nitride layer via fluorine-based inductively coupled plasma (ICP) etching (Oxford PlasmaLab 100). The

residual aluminum hard mask is stripped in an aqueous solution containing 2.38% tetramethylammonium hydroxide (TMAH). The cleaned wafer is then diced (Disco DAD321) into individual chips carrying one meta-optic each for optical experiments.

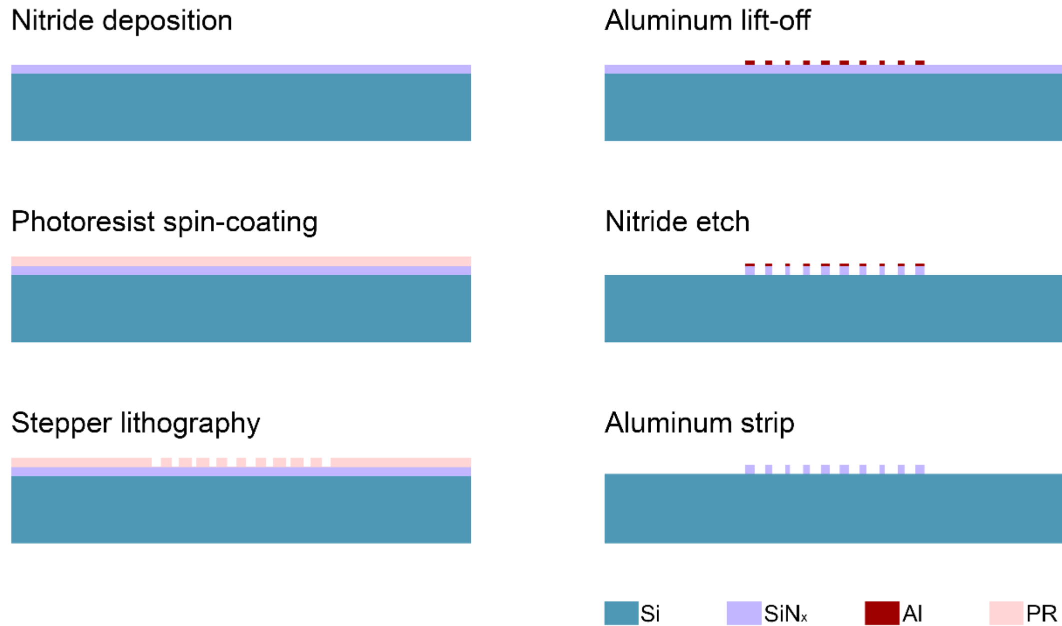

Figure 9.1. Fabrication flow of the MWIR dual-helix meta-optic with stepper lithography.

Figure 9.2 shows the fabricated MWIR dual-helix meta-optic with the apparent spiral pattern. The SEM image of Figure 9.2c shows the sidewall profiles of the etched meta-optic pillars, which are tapered towards the bottom, probably due to wafer heating over the prolonged etch time or different transport rates of reagent gases near the scatterer-substrate interface. Given that the minimum circular pattern dimension of 513 nm is larger than the stepper resolution limit of 350 nm, for this pattern, we have not included any size or shape compensation. However, the group of larger pillars is connected to each other in Figure 9.2c, which deviates from the discrete design circles in the photomask layout. Such printed dimension deviation and necking effect indicate that the lithography of this pattern has suffered from the optical proximity effect because even though not breaking, the feature sizes to be printed are very close to the resolution limit of the stepper,

resulting in nonlinear printing outcomes. Therefore, for future MWIR patterns with a similar range of dimensions, proper optical proximity corrections may still be necessary to achieve optimal fabrication quality and optical performance.

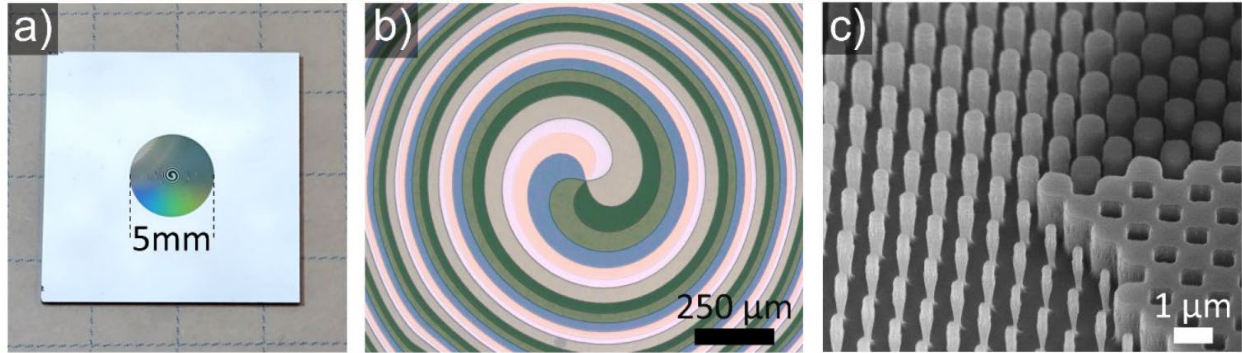

Figure 9.2. The fabricated MWIR dual-helix meta-optic. (a) Photography of the chip carrying an MWIR dual-helix meta-optic with an aperture size of 5 mm. (b) Optical image of the meta-optic spiral pattern near the center. (c) SEM image of the meta-optic scatterers near the center, taken at an oblique angle of 45° [94].

9.4 Optical Performance

The concept of a computational spectrometer utilizing a high-efficiency rotating double-helix point spread function (PSF) has been demonstrated with the fabricated meta-optic for two MWIR spectral ranges, 1260−1360 nm, and 1480−1640 nm. Figure 9.3d displays the basis set of captured PSFs for discrete wavelengths over the spectral range of 1480-1640 nm. The same PSF acquisition is also conducted for the spectral range of 1260-1360 nm with adjusted focal distance. Figure 9.3e and f plot the wavelength dependence of the PSFs for the two spectral ranges, respectively. With backend computational decoding, accurate reconstruction of various spectra is achieved with a spectral resolution of approximately 3.5 nm. As an outlook, by combining the dual-helix meta-optic with a second metalens in a dual aperture arrangement, the potential of the meta-optic may be fully employed to realize image reconstruction [94].

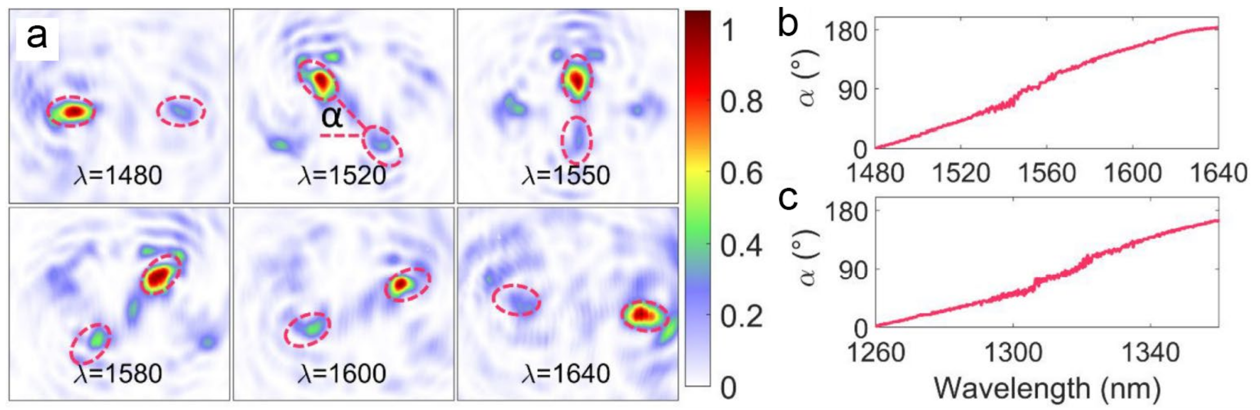

Figure 9.3. Characterization of the dual-helix meta-optic. (a) Experimental point spread functions for various wavelengths in the 1560 nm calibration range, with the main intensity lobes indicated by red dashed circles. The rotation angle of the lobe orientation as a function of wavelength for the 1560 and 1310 nm ranges are plotted in (b) and (c), respectively [94].

Chapter 10. FABRICATION OF LARGE-AREA VISIBLE META-OPTICS

10.1 Large Aperture Meta-optic for Full-Color Camera

In this project, we explore the possibility of fabricating a 1-cm visible meta-optic with extended-depth-of-focus (EDOF). The meta-optic consists of silicon nitride scatterers on a fused silica substrate patterned with direct-write lithography using the HiRes write head with a tool resolution limit of 300 nm. Based on preliminary exposure and etching tests, smaller features can be achieved with direct-write patterning, with reliability harder to control and requiring rigorous process fine-tuning.

The NOISE Lab has fabricated similar visible EDOF meta-optics with the same aperture size using electron beam lithography. As listed in Table 7.9 of Section 7.1.4, the EBL exposure time of the same meta-optic area is five times the corresponding direct-write time. Considering the high operating and maintenance cost of EBL, switching the exposure process to direct-write will reduce capital costs per device. However, as shown in the same table, even with the HiRes direct-write mode, there is a significant sacrifice in the printing resolution of the visible meta-optic, which inevitably affects the optical performance. Still, it is worthwhile to develop a fabrication process for direct-write visible meta-optics and compare the device performance with the EBL counterpart, not only to assess the possibility of using a more economical fabrication technique but also to explore the feasibility of writing even larger visible meta-optics (such as with a diameter up to 5 cm or 10 cm). The full work is under preparation for publication now.

10.2 META-OPTIC PARAMETERS

Table 10.15 summarizes the scatterer parameters of the visible EDOF meta-optics to be patterned with direct-write lithography. Since the resolution limit of the Heidelberg HiRes mode is 300 nm, feature size deviation and shape distortion are expected when the visible meta-optics with a minimum feature size of 278 nm is used.

Table 10.15. Scatterer parameters for visible EDOF meta-optics.

Scatterer Array		
Aperture Shape	Circular	
Aperture Size	1 cm	
Lattice Grid	Square	
Lattice Constant	1 μm	
Nanopost Design		
Post Material	Silicon nitride	
Substrate Material	Fused silica	
Post Cross-section	square	
Post Height	1.5 μm	
Dimension Level	6	
Individual Elements	**Duty Cycle**	**Edge length (nm)**
Nanopost 1	0.278	278
Nanopost 2	0.364	364
Nanopost 3	0.424	424
Nanopost 4	0.45	450
Nanopost 5	0.474	474
Nanopost 6	0.5	500

As the compensation for potential size deviation in the printed pattern, the square scatterers in the design layout are first scaled by the factor

$$x' = x \cdot \left(\frac{x_{max} - x}{x_{max} - x_{min}} \times 0.2 + 1\right)$$

where x is the original edge length of any scatterer, x' is the scaled edge length of the same scatterer, x_{max} and x_{min} are the maximum and minimum scatterer edge lengths in the array. This function scales the minimum features up by 20% in width while keeping the maximum features the same size. Square serifs with 100-nm edge length are added to the corners of the square scatterers with a 50-nm overlay. Then a critical dimension bias of 150 nm is introduced (expanding all scatterer feature edges by 75 nm) when converting the layout for a direct-write lithography job.

10.3 DEVICE FABRICATION

Figure 10.1 summarizes the fabrication process flow of the visible EDOF meta-optic. A 1.5-µm thick layer of silicon nitride is deposited by PECVD onto a fused silica substrate as the material layer for the meta-optic scatterers. Then a layer of 98-nm thick alumina is deposited on top as the hard etch mask layer. An anti-reflective (AR) coating BARLiII-90 is spin-coated on the wafer surface, followed by a photoresist (PR) AZ 1505. Then the meta-optic pattern is exposed onto the resist-coated wafer using Heidelberg DWL+ direct-write system with the HiRes write head. After resist development, the exposed AR coating is etched by fluorine-based ICP etching. The pattern is then transferred to the alumina layer underneath via chlorine-based ICP etching, forming the hard mask for the scatterer etching. The meta-optic scatterers are etched into the silicon nitride layer by fluorine-based ICP etching until hitting the fused silica substrate. After wafer dicing, cleaning, and inspection, the individual chips containing one visible meta-optic each are passed to Johannes Fröch for calibration and testing. Figure 10.2 shows one of the chips.

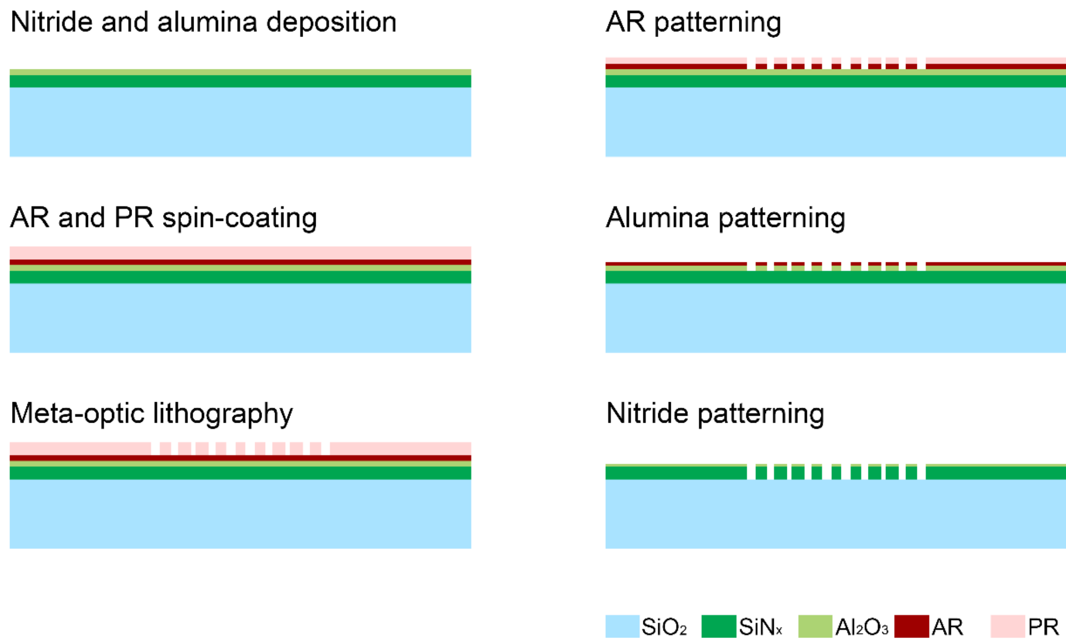

Figure 10.1. Fabrication flow of the visible EDOF meta-optic with laser direct-write.

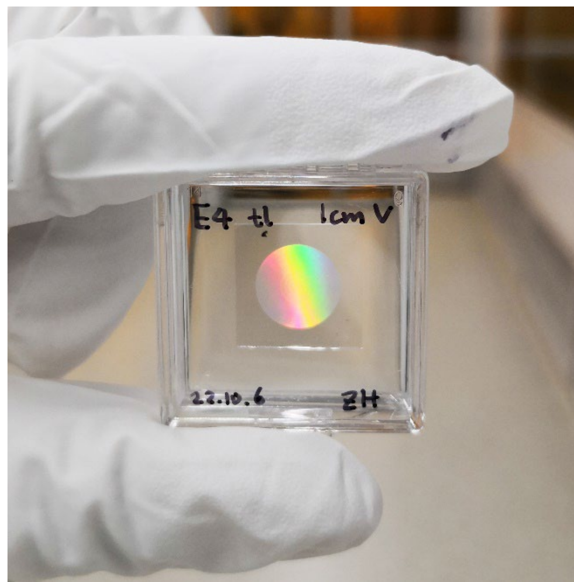

Figure 10.2. Phone photo of the visible EDOF meta-optics with a 1-cm diameter.

Figure 10.3 shows the optical images, and Figure 10.4 shows the SEM images of the visible meta-optics fabricated. Though both were fabricated with silicon nitride meta-optic scatterers on a fused silica substrate, the preliminary test wafer presented in Figure 7.12 and this sample have a very distinctive appearance of the scatterer nanoposts. An additional shell-like structure is created

surrounding the defined square scatterers at the centers, making the individual scatterer units effectively more cone-shaped with circular bases instead of designed pillar-shaped with square bases. The main difference between this sample and the case presented in Figure 7.12 is the usage of an alumina hard mask with AR coating to realize the total etch depth of 1.5 μm. The “shells” appear to be some structures redeposited around the lithography-patterned square scatterers and chemically resistant enough to stand through the etching process. Hence the primary hypothesis now involves heating of the fused silica wafer with prolonged exposure to high-energy plasma during the ICP etching process, causing the redeposition of the alumina mask in the surrounding area, blocking further etch of the silicon nitride layer in the “shell” region. Other graduate students in the group are going to explore the possibility of repeating this fabrication on a sapphire substrate, which has much better thermal conductivity than fused silica and may mitigate the issue of alumina hard mask redeposition if it is proven to be the cause of this unexpected scatterer profile.

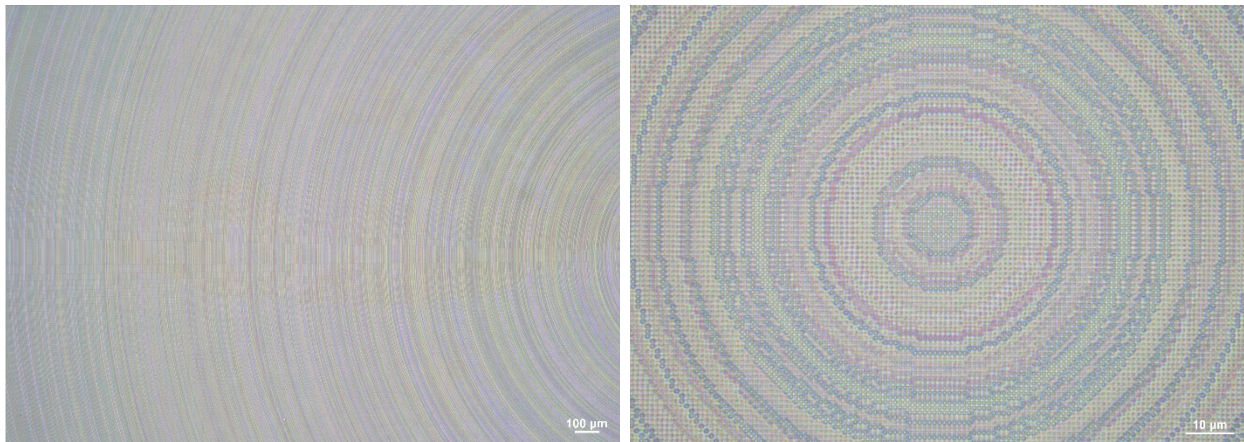

Figure 10.3. Optical images of the fabricated visible meta-optic with laser direct-write.

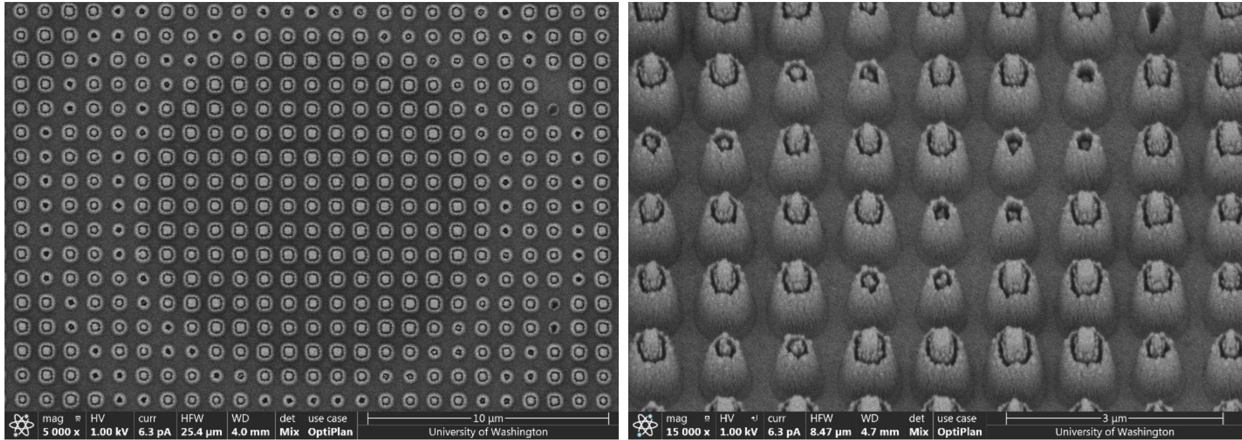

Figure 10.4. SEM images of the fabricated meta-optic scatterers. Unexpected shell-like structures are also patterned surrounding the designed scatterer pillars.

10.4 Optical Performance

Johannes Fröch from the NOISE Lab performed the optical characterization and imaging experiments on this sample. The measured point spread function (PSF) and the modulation transfer function (MTF) of the laser direct-write visible meta-optic are shown in Figure 10.5. Various imaging tests have been performed with the direct-write meta-optics and results have been compated with the meta-optic patterned with electron beam lithography. During the experiments, slightly longer acquisition times are required to achieve the same brightness as the tests for the EBL meta-optics, and the direct-write images have slightly more haze than the EBL images, as visible in the comparison of Figure 10.6. Computational backend algorithms are applied to denoise the images captured by the direct-write meta-optics.

Though with slightly inferior imaging quality, the results from the direct-write meta-optics are still promising to produce comparable quality with the aid of computational post-processing. This opens up many potentials to utilize direct-write lithography to fabricate meta-optics with much larger apertures (such as 5 cm or 10 cm in diameter), which would be very expensive if feasible with electron beam lithography.

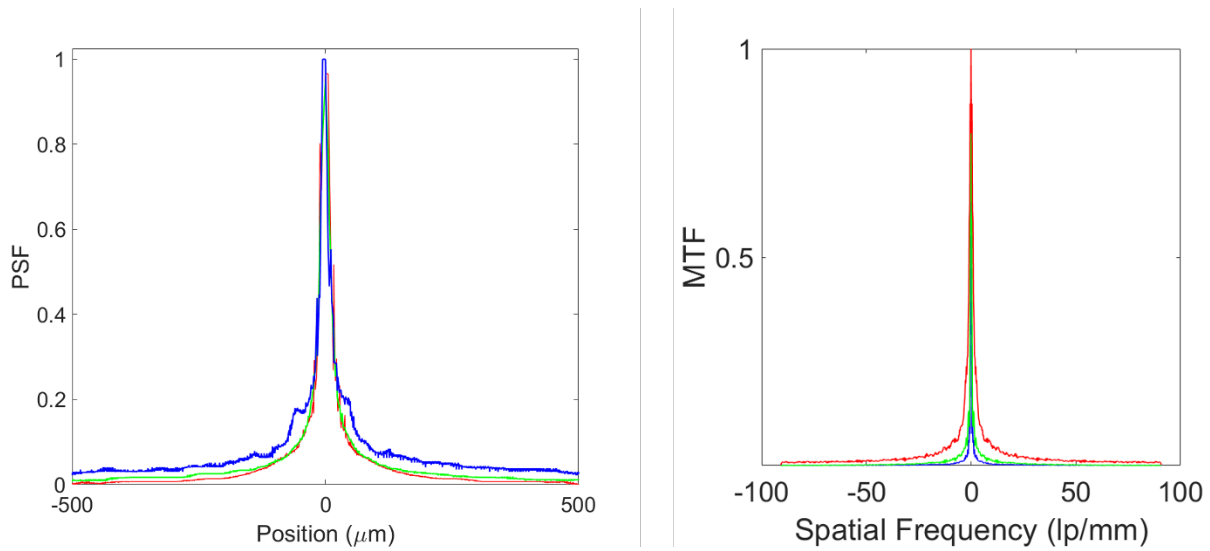

Figure 10.5. Point spread function (left) and modulation transfer function (right) of the laser direct-write visible EDOF meta-optic. (Image credits to Johannes Fröch.)

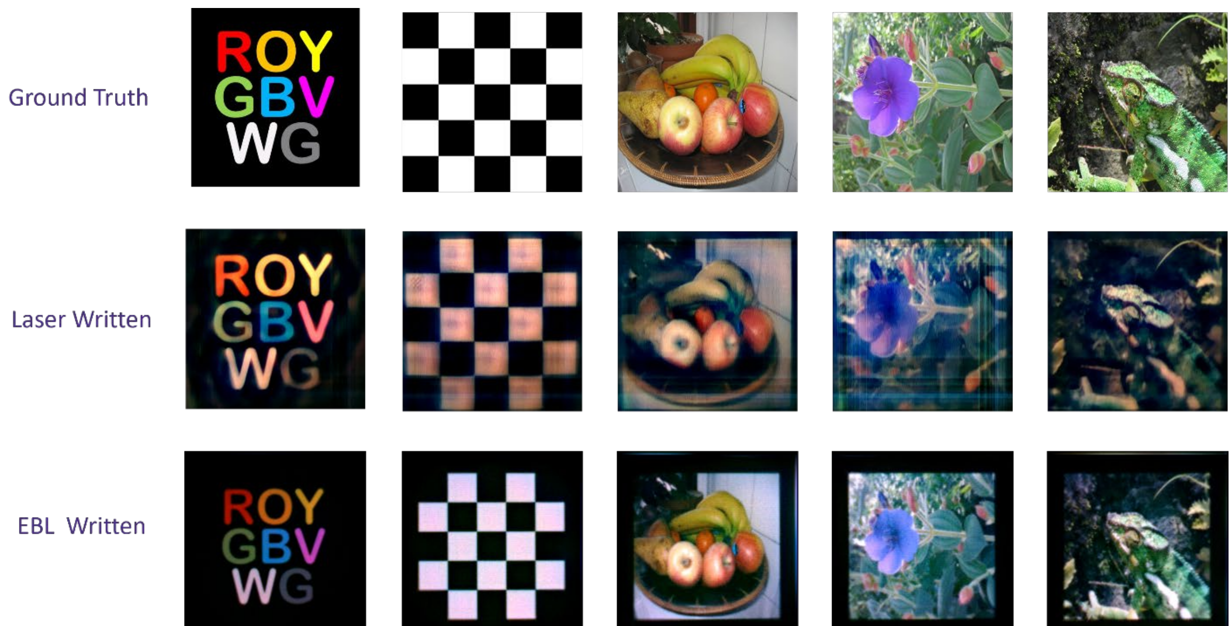

Figure 10.6. Comparison between the ground truth (top row), imaging results with the laser direct-write meta-optic (middle row), and the imaging results from the meta-optic written with electron beam lithography (bottom row). (Credits to Johannes Fröch.)

Chapter 11. OUTLOOK

In this thesis, we have presented various meta-optical devices for applications calling for compact optical systems. Future works will include both fabrication process improvement and exploring advanced applications with more complex systems.

11.1 3D Imaging by an Alvarez Grid

We have presented the performance of individual Alvarez meta-optic lenses in this thesis, but once the focus tuning performance is fully understood and calibrated, it may be possible to fabricate a 2D array of Alvarez lenses individually controlled by an electrical signal. When such an array is laid over a regular 2D display, and the desired depth information corresponding to the image content is converted to electrical signals by some means, a map of depth can be added to the image by the Alvarez grid with focus tuning in individual pixels controlled by the electrical signals corresponding to different locations of the 2D image. Moreover, if the individual Alvarez lens can be proven to work at frequencies higher than common video frame rates – say hundreds of Hertz – instead of a still image, a video can be played on the display with the depth information constantly being updated and added via the overlaying Alvarez grid, realizing a 3D monochromatic display system.

11.2 3D Imaging by Alvarez Scanning Lens

An alternative to the Alvarez lens grid mentioned above to create 3D images is to scan the focus of a single Alvarez meta-optic lens at high enough frequencies to cover the whole range of focal depths required by the image to be projected. For example, given a 2D image and its pixel-specified depth information to be associated, the range of depth can be divided into 10 levels. When

illuminated, the individual pixels of the 2D image will all project towards one single Alvarez lens, which is stationary in its overall location and actuated to scan across a range of focus continuously – covering all the 10 focus levels required by the image. When the Alvarez lens is scanning across a certain depth level, the image pixels with required depth information falling into that range turn on and project light through the Alvarez lens, acquiring the appropriate depth information along the way. When the Alvarez lens scans to the next level of focal depth, another set of 2D image pixels turns on, and so on and so forth. If the full range focus scan by the Alvarez lens can be fast enough to deceive the human eye, say 10 milliseconds per depth level, then with the light beams passing through the lens at different levels of tuning, a 3D image can be created with the 2D source and the introduced depth information.

This technique can be extended to create 3D videos given the required depth information as well. For example, if given a video with a frame rate of 50 fps and depth information again categorized into 10 levels, then there will be 2 milliseconds for the Alvarez lens to tune from one level to another. As long as the lens has an actuation frequency of at least 500 Hz in this case, designated depth information can be added to the pixels corresponding to the 10 depth levels in this video at every frame as described above to create a 3D video always appearing continuous to the viewer.

Both as means to add depth information to a given image or video, the Alvarez lens grid and the single scanning Alvarez lens have different advantages and challenges. The Alvarez grid requires lower tuning speed as it does not need to scan across multiple focal depth levels within a single frame, but the fabrication and independent tuning of an array of Alvarez lenses have challenges in terms of yield efficiency ("dead pixels") and the integration of control units for individual lenses. The single scanning Alvarez lens is favorable since only one lens is necessary

and no frame-specified control is needed; hence relatively simple circuitry can be used, but it also faces the challenge of reaching its operation frequency limits if the video frame rate and the number of depth levels keep increasing for videos with higher definition. These will be exciting topics to investigate in longer-term research of the Alvarez meta-optic lens.

11.3 Fabrication Improvement for Large-area Meta-optics

We have developed and demonstrated the fabrication for several large-area meta-optics. Many of them are successful, while some of them still have pending issues which should be investigated and improved in the future. The primary concern is about the heating and dry etching qualities of the large-area meta-optics, especially when fabricated on a dielectric substrate. As we move the designed operation spectrum to higher frequencies, such as the visible spectrum, we need to switch our substrate to a transparent wafer as the typical silicon substrate is getting more absorbent as the wavelength decreases. The plasma dry etching is a crucial step in creating functioning meta-optics, and its qualities are highly dependent on the substrate temperature during the etch process. As shown in the example presented in Chapter 10, as we switch to a dielectric substrate such as a fused silica wafer, the heat inside the substrate accumulates quickly with prolonged exposure to high-energy plasma. When the chuck cooling struggles to dissipate the substrate heat in time, it can cause unexpected predominance during etching, such as the sputtering of etch masks, and cause subsequent deviation in device fabrication.

Moreover, as the aperture size of the meta-optics gets larger, the etching uniformity across the entire meta-optics is crucial, which again is dependent on the uniform substrate temperature. This is usually not an issue with silicon substrates, which have decent thermal conductivities. However, when we switch to a dielectric substrate, the significant drop in thermal conductivity amplifies and non-uniformity in wafer temperature due to multiple causes, such as the locations of

the wafer lifting pins in the dry etch system. We have observed large deviations across the same meta-optics on a fused silica wafer corresponding to their relative positions to the stage pins, where the temperature is slightly cooler than the surroundings.

To mitigate these issues linked to the poor thermal conductivity of the common dielectric substrate, we are currently trying out the same fabrication on a sapphire substrate instead, which has a higher thermal conductivity than fused silica and is much closer to that of silicon. Some other adjustments for lithography and etching will be implemented to accommodate for the substrate materials change, but if sapphire is proven to be sufficiently conductive, we may resolve the various issues associated with excessive or non-uniform substrate heating simultaneously.

BIBLIOGRAPHY

[1] R. D. G. Daweke, M. Kelp, H. Lehr, O. Monnich, and P. Osiak, "Electromagnetic direct linear drives for medical endoscopes," in *Optimization of Electrical and Electronic Equipment (OPTIM), 2014 International Conference on*, 2014: IEEE, pp. 245-251.

[2] S. W. Seo *et al.*, "Microelectromechanical-system-based variable-focus liquid lens for capsule endoscopes," vol. 48, no. 5R, p. 052404, 2009.

[3] M.-S. Chen, P.-J. Chen, M. Chen, and Y.-H. Lin, "An electrically tunable imaging system with separable focus and zoom functions using composite liquid crystal lenses," *Optics express,* vol. 22, no. 10, pp. 11427-11435, 2014.

[4] L. W. Alvarez, "Two-element variable-power spherical lens," 1967.

[5] A. W. Lohmann, "A new class of varifocal lenses," *Applied Optics,* vol. 9, no. 7, pp. 1669-1671, 1970.

[6] L. W. Alvarez, "Development of variable-focus lenses and a new refractor," *Journal of the American Optometric Association,* vol. 49, no. 1, pp. 24-29, 1978.

[7] Y. Zou, W. Zhang, F. S. Chau, and G. J. O. e. Zhou, "Miniature adjustable-focus endoscope with a solid electrically tunable lens," vol. 23, no. 16, pp. 20582-20592, 2015.

[8] G. Zhou, H. Yu, and F. S. Chau, "Microelectromechanically-driven miniature adaptive Alvarez lens," *Optics Express,* vol. 21, no. 1, pp. 1226-1233, 2013.

[9] Y. Zou, W. Zhang, F. S. Chau, and G. Zhou, "Miniature adjustable-focus endoscope with a solid electrically tunable lens," *Optics Express,* vol. 23, no. 16, pp. 20582-20592, 2015.

[10] C. R. Johnson. "IBM Harnesses MEMS Cantilever for Patterning Nanostructures." https://www.memsjournal.com/2010/05/ibm-harnesses-mems-cantilever-for-patterning-nanostructures.html (accessed.

[11] H. Wang, X. Zhang, D. Zhang, L. Zhou, and H. Xie, "Characterization and reliability study of a MEMS mirror based on electrothermal bimorph actuation," in *2017 International Conference on Optical MEMS and Nanophotonics (OMN)*, 2017: IEEE, pp. 1-2.

[12] C. Burroughs. "New Five-Level Layering Process Pioneered by Sandia Promises More Reliable, Complex Micromachines." Sandia National Laboratories. https://www.sandia.gov/media/NewsRel/NR1999/layer.htm (accessed 2022).

[13] Torsional Ratcheting Actuator [Online] Available: https://www.sandia.gov/mesa/mems-video-image-gallery/

[14] M. Kandler. "Next generation of MEMS gyroscopes and inertial combo sensors from SensorDynamics." (accessed 2022).

[15] Q. T. Aten, B. D. Jensen, S. H. Burnett, and L. L. Howell, "A self-reconfiguring metamorphic nanoinjector for injection into mouse zygotes," *Review of Scientific Instruments,* vol. 85, no. 5, p. 055005, 2014.

[16] H. M. Soemers, "Design principles for precision mechanisms," 2010.

[17] D. M. Brouwer, A. Otten, J. Engelen, B. Krijnen, and H. Soemers, "Long-range elastic guidance mechanisms for electrostatic comb-drive actuators," in *International Conference of the European Society for Precision Engineering and Nanotechnology (EUSPEN)*, Delft, Netherlands, S. P., B. T., S. H., and V. B. H., Eds., 2010, Cranfield, United Kingdom: euspen, pp. 41-50.

[18] M. Khorasaninejad, W. T. Chen, R. C. Devlin, J. Oh, A. Y. Zhu, and F. Capasso, "Metalenses at visible wavelengths: Diffraction-limited focusing and subwavelength resolution imaging," *Science,* vol. 352, no. 6290, pp. 1190-1194, 2016.

[19] S. M. Kamali, E. Arbabi, A. Arbabi, and A. Faraon, "A review of dielectric optical metasurfaces for wavefront control," *Nanophotonics,* vol. 7, no. 6, pp. 1041-1068, 2018.

[20] N. Yu *et al.*, "Light propagation with phase discontinuities: generalized laws of reflection and refraction," *Science,* vol. 334, no. 6054, pp. 333-337, 2011.

[21] A. V. Kildishev, A. Boltasseva, and V. M. Shalaev, "Planar photonics with metasurfaces," *Science,* vol. 339, no. 6125, p. 1232009, 2013.

[22] F. Monticone, N. M. Estakhri, and A. Alù, "Full control of nanoscale optical transmission with a composite metascreen," *Physical review letters,* vol. 110, no. 20, p. 203903, 2013.

[23] N. Yu and F. Capasso, "Flat optics with designer metasurfaces," *Nature Materials,* vol. 13, no. 2, pp. 139-150, 2014.

[24] S. Jahani and Z. Jacob, "All-dielectric metamaterials," *Nature nanotechnology,* vol. 11, no. 1, p. 23, 2016.

[25] A. Zhan, S. Colburn, C. M. Dodson, and A. Majumdar, "Metasurface freeform nanophotonics," *Scientific Reports,* vol. 7, no. 1, p. 1673, 2017/05/10 2017, doi: 10.1038/s41598-017-01908-9.

[26] A. Arbabi, R. M. Briggs, Y. Horie, M. Bagheri, and A. Faraon, "Efficient dielectric metasurface collimating lenses for mid-infrared quantum cascade lasers," *Optics express,* vol. 23, no. 26, pp. 33310-33317, 2015.

[27] A. Arbabi, Y. Horie, A. J. Ball, M. Bagheri, and A. Faraon, "Subwavelength-thick lenses with high numerical apertures and large efficiency based on high-contrast transmitarrays," *Nature communications,* vol. 6, no. 1, pp. 1-6, 2015.

[28] S. Vo *et al.*, "Sub-wavelength grating lenses with a twist," *IEEE Photonics Technology Letters,* vol. 26, no. 13, pp. 1375-1378, 2014.

[29] P. R. West *et al.*, "All-dielectric subwavelength metasurface focusing lens," *Optics express,* vol. 22, no. 21, pp. 26212-26221, 2014.

[30] F. Lu, F. G. Sedgwick, V. Karagodsky, C. Chase, and C. J. Chang-Hasnain, "Planar high-numerical-aperture low-loss focusing reflectors and lenses using subwavelength high contrast gratings," *Optics express,* vol. 18, no. 12, pp. 12606-12614, 2010.

[31] D. Lin, P. Fan, E. Hasman, and M. L. Brongersma, "Dielectric gradient metasurface optical elements," *science,* vol. 345, no. 6194, pp. 298-302, 2014.

[32] F. Aieta *et al.*, "Aberration-free ultrathin flat lenses and axicons at telecom wavelengths based on plasmonic metasurfaces," *Nano letters,* vol. 12, no. 9, pp. 4932-4936, 2012.

[33] A. Arbabi, E. Arbabi, Y. Horie, S. M. Kamali, and A. Faraon, "Planar metasurface retroreflector," *Nature Photonics,* vol. 11, no. 7, pp. 415-420, 2017.

[34] D. Fattal, J. Li, Z. Peng, M. Fiorentino, and R. G. Beausoleil, "Flat dielectric grating reflectors with focusing abilities," *Nature Photonics,* vol. 4, no. 7, pp. 466-470, 2010.

[35] Q. Fan, P. Huo, D. Wang, Y. Liang, F. Yan, and T. Xu, "Visible light focusing flat lenses based on hybrid dielectric-metal metasurface reflector-arrays," *Scientific reports,* vol. 7, no. 1, pp. 1-9, 2017.

[36] Y. Yang, W. Wang, P. Moitra, I. I. Kravchenko, D. P. Briggs, and J. Valentine, "Dielectric meta-reflectarray for broadband linear polarization conversion and optical vortex generation," *Nano letters,* vol. 14, no. 3, pp. 1394-1399, 2014.

[37] X. Ma *et al.*, "A planar chiral meta-surface for optical vortex generation and focusing," *Scientific reports,* vol. 5, no. 1, pp. 1-7, 2015.

[38] F. Yue, D. Wen, J. Xin, B. D. Gerardot, J. Li, and X. Chen, "Vector vortex beam generation with a single plasmonic metasurface," *ACS photonics,* vol. 3, no. 9, pp. 1558-1563, 2016.

[39] Y. Ran, J. Liang, T. Cai, and H. Li, "High-performance broadband vortex beam generator using reflective Pancharatnam–Berry metasurface," *Optics Communications,* vol. 427, pp. 101-106, 2018.

[40] G. Zheng, H. Mühlenbernd, M. Kenney, G. Li, T. Zentgraf, and S. Zhang, "Metasurface holograms reaching 80% efficiency," *Nature nanotechnology,* vol. 10, no. 4, pp. 308-312, 2015.

[41] Y. Hu *et al.*, "Trichromatic and tripolarization-channel holography with noninterleaved dielectric metasurface," *Nano letters,* vol. 20, no. 2, pp. 994-1002, 2019.

[42] H. Ren, X. Fang, J. Jang, J. Bürger, J. Rho, and S. A. Maier, "Complex-amplitude metasurface-based orbital angular momentum holography in momentum space," *Nature Nanotechnology,* vol. 15, no. 11, pp. 948-955, 2020.

[43] P. Lalanne, S. Astilean, P. Chavel, E. Cambril, and H. Launois, "Blazed binary subwavelength gratings with efficiencies larger than those of conventional échelette gratings," *Optics letters,* vol. 23, no. 14, pp. 1081-1083, 1998.

[44] A. Arbabi *et al.*, "Increasing efficiency of high numerical aperture metasurfaces using the grating averaging technique," *Scientific reports,* vol. 10, no. 1, pp. 1-10, 2020.

[45] A. H. Dorrah, N. A. Rubin, A. Zaidi, M. Tamagnone, and F. Capasso, "Metasurface optics for on-demand polarization transformations along the optical path," *Nature Photonics,* vol. 15, no. 4, pp. 287-296, 2021.

[46] A. Arbabi, Y. Horie, M. Bagheri, and A. Faraon, "Dielectric metasurfaces for complete control of phase and polarization with subwavelength spatial resolution and high transmission," *Nature nanotechnology,* vol. 10, no. 11, pp. 937-943, 2015.

[47] A. Zhan, S. Colburn, C. M. Dodson, and A. J. S. r. Majumdar, "Metasurface freeform nanophotonics," vol. 7, no. 1, p. 1673, 2017.

[48] G. Kafaie Shirmanesh, R. Sokhoyan, R. A. Pala, and H. A. Atwater, "Dual-gated active metasurface at 1550 nm with wide (> 300) phase tunability," *Nano letters,* vol. 18, no. 5, pp. 2957-2963, 2018.

[49] H.-S. Ee and R. Agarwal, "Tunable metasurface and flat optical zoom lens on a stretchable substrate," *Nano Letters,* vol. 16, no. 4, pp. 2818-2823, 2016.

[50] S. M. Kamali, E. Arbabi, A. Arbabi, Y. Horie, and A. Faraon, "Highly tunable elastic dielectric metasurface lenses," *Laser & Photonics Reviews,* vol. 10, no. 6, pp. 1002-1008, 2016.

[51] A. Afridi, J. Canet-Ferrer, L. Philippet, J. Osmond, P. Berto, and R. Quidant, "Electrically driven varifocal silicon metalens," *ACS Photonics,* vol. 5, no. 11, pp. 4497-4503, 2018.

[52] W. J. Padilla, A. J. Taylor, C. Highstrete, M. Lee, and R. D. Averitt, "Dynamical electric and magnetic metamaterial response at terahertz frequencies," *Physical review letters,* vol. 96, no. 10, p. 107401, 2006.

[53] J. Valente, J.-Y. Ou, E. Plum, I. J. Youngs, and N. I. Zheludev, "A magneto-electro-optical effect in a plasmonic nanowire material," *Nature communications,* vol. 6, no. 1, pp. 1-7, 2015.

[54] A. She, S. Zhang, S. Shian, D. R. Clarke, and F. J. S. A. Capasso, "Adaptive metalenses with simultaneous electrical control of focal length, astigmatism, and shift," vol. 4, no. 2, p. eaap9957, 2018.

[55] T. Roy, S. Zhang, I. W. Jung, M. Troccoli, F. Capasso, and D. Lopez, "Dynamic metasurface lens based on MEMS technology," *APL Photonics,* vol. 3, no. 2, p. 021302, 2018.

[56] E. Arbabi, A. Arbabi, S. M. Kamali, Y. Horie, M. Faraji-Dana, and A. J. N. c. Faraon, "MEMS-tunable dielectric metasurface lens," vol. 9, no. 1, p. 812, 2018.

[57] J.-Y. Ou, E. Plum, J. Zhang, and N. I. Zheludev, "An electromechanically reconfigurable plasmonic metamaterial operating in the near-infrared," *Nature nanotechnology,* vol. 8, no. 4, pp. 252-255, 2013.

[58] A. She, S. Zhang, S. Shian, D. R. Clarke, and F. Capasso, "Adaptive metalenses with simultaneous electrical control of focal length, astigmatism, and shift," *Science Advances,* vol. 4, no. 2, p. eaap9957, 2018.

[59] E. Arbabi, A. Arbabi, S. M. Kamali, Y. Horie, M. Faraji-Dana, and A. Faraon, "MEMS-tunable dielectric metasurface lens," *Nature communications,* vol. 9, no. 1, pp. 1-9, 2018.

[60] A. L. Holsteen, A. F. Cihan, and M. L. Brongersma, "Temporal color mixing and dynamic beam shaping with silicon metasurfaces," *Science,* vol. 365, no. 6450, pp. 257-260, 2019.

[61] H.-S. Ee and R. Agarwal, "Tunable metasurface and flat optical zoom lens on a stretchable substrate," *J Nano letters,* vol. 16, no. 4, pp. 2818-2823, 2016.

[62] T. Roy, S. Zhang, I. W. Jung, M. Troccoli, F. Capasso, and D. J. A. P. Lopez, "Dynamic metasurface lens based on MEMS technology," vol. 3, no. 2, p. 021302, 2018.

[63] S. Colburn, A. Zhan, and A. Majumdar, "Varifocal zoom imaging with large area focal length adjustable metalenses," *Optica,* vol. 5, no. 7, pp. 825-831, 2018/07/20 2018, doi: 10.1364/OPTICA.5.000825.

[64] S. Colburn, A. Zhan, and A. J. a. p. a. Majumdar, "Varifocal zoom imaging with large area focal length adjustable metalenses," 2018.

[65] A. Zhan, S. Colburn, R. Trivedi, T. K. Fryett, C. M. Dodson, and A. Majumdar, "Low-contrast dielectric metasurface optics," *ACS Photonics,* vol. 3, no. 2, pp. 209-214, 2016.

[66] V. Liu and S. Fan, "S4: A free electromagnetic solver for layered periodic structures," *Computer Physics Communications,* vol. 183, no. 10, pp. 2233-2244, 2012.

[67] C. Liu, *Foundations of MEMS*. Pearson Education India, 2012.

[68] R. Legtenberg, A. Groeneveld, M. J. J. o. M. Elwenspoek, and microengineering, "Comb-drive actuators for large displacements," vol. 6, no. 3, p. 320, 1996.

[69] R. Legtenberg, A. Groeneveld, and M. Elwenspoek, "Comb-drive actuators for large displacements," *Journal of Micromechanics and Microengineering,* vol. 6, no. 3, p. 320, 1996.

[70] D. Hah, S.-Y. Huang, J.-C. Tsai, H. Toshiyoshi, and M. C. J. J. o. M. S. Wu, "Low-voltage, large-scan angle MEMS analog micromirror arrays with hidden vertical comb-drive actuators," vol. 13, no. 2, pp. 279-289, 2004.

[71] L. Zhang, R. Barrett, P. Cloetens, C. Detlefs, and M. Sanchez del Rio, "Anisotropic elasticity of silicon and its application to the modelling of X-ray optics," *Journal of synchrotron radiation,* vol. 21, no. 3, pp. 507-517, 2014.

[72] J. Taylor, *Introduction to error analysis, the study of uncertainties in physical measurements*. 1997.

[73] C. Hong, S. Colburn, and A. Majumdar, "Flat metaform near-eye visor," *Applied Optics,* vol. 56, no. 31, pp. 8822-8827, 2017.

[74] D. Lin *et al.*, "Optical metasurfaces for high angle steering at visible wavelengths," *Scientific Reports,* vol. 7, no. 1, p. 2286, 2017.

[75] E. Bayati, S. Colburn, and A. Majumdar, "Metasurface Optics for Ultra-Compact Augmented Reality (AR) Visors," in *CLEO: QELS_Fundamental Science*, San Jose, United States, 5–10 May 2019, Washington, DC, United States: Optical Society of America, p. FTh3M. 4.

[76] S. S. Rege, T. S. Tkaczyk, and M. R. Descour, "Application of the Alvarez-Humphrey concept to the design of a miniaturized scanning microscope," *Optics Express,* vol. 12, no. 12, pp. 2574-2588, 2004.

[77] Y. Zou, W. Zhang, F. S. Chau, and G. Zhou, "Miniature adjustable-focus endoscope with a solid electrically tunable lens," vol. 23, no. 16, pp. 20582-20592, 2015.

[78] S. Colburn and A. Majumdar, "Simultaneous Achromatic and Varifocal Imaging with Quartic Metasurfaces in the Visible," *ACS Photonics,* 2019.

[79] E. Arbabi, A. Arbabi, S. M. Kamali, Y. Horie, M. Faraji-Dana, and A. Faraon, "MEMS-tunable dielectric metasurface lens," *Nature Communications,* vol. 9, no. 1, p. 812, 2018.

[80] Z. Han, S. Colburn, A. Majumdar, and K. F. Böhringer, "MEMS-actuated metasurface Alvarez lens," *Microsystems & Nanoengineering,* vol. 6, no. 1, pp. 1-11, 2020.

[81] S. Colburn and A. Majumdar, "Simultaneous achromatic and varifocal imaging with quartic metasurfaces in the visible," *ACS Photonics,* vol. 7, no. 1, pp. 120-127, 2019.

[82] G. Yoon, T. Tanaka, T. Zentgraf, and J. Rho, "Recent progress on metasurfaces: applications and fabrication," *Journal of Physics D: Applied Physics,* 2021.

[83] R. M. J. McCord Mark A, "Electron Beam Lithography," in *Handbook of microlithography, micromachining, and microfabrication: microlithography*, vol. 1, P. Rai-Choudhury Ed.: SPIE press, 1997, ch. 2.

[84] A. W. H. Levinson Harry J, "Optical Lithography," in *Handbook of microlithography, micromachining, and microfabrication: microlithography*, vol. 1, P. Rai-Choudhury Ed.: SPIE press, 1997, ch. 1.

[85] H. J. Levinson, *Principles of lithography*, 4 ed. SPIE press, 2019.

[86] "TWINSCAN NXE:3600D." ASML. https://www.asml.com/en/products/euv-lithography-systems/twinscan-nxe-3600d (accessed 2022).

[87] "DWL 66+." Heidelberg Instruments. https://heidelberg-instruments.com/product/dwl-66-laser-lithography-system (accessed 2022).

[88] S. V. Babin, "Measuring the proximity effects in laser pattern generation," *Optical Engineering,* vol. 36, no. 9, pp. 2508-2512, 1997.

[89] G. T. Kovacs, "Micromachined transducers sourcebook," p. 278, 1998.

[90] B. Wu, A. Kumar, and S. Pamarthy, "High aspect ratio silicon etch: A review," *Journal of applied physics,* vol. 108, no. 5, p. 9, 2010.

[91] L. Huang *et al.*, "Long wavelength infrared imaging under ambient thermal radiation via an all-silicon metalens," *Optical Materials Express,* vol. 11, no. 9, pp. 2907-2914, 2021.

[92] D. Ulyanov, A. Vedaldi, and V. Lempitsky, "Deep image prior," in *Proceedings of the IEEE conference on computer vision and pattern recognition*, 2018, pp. 9446-9454.

[93] V. Saragadam *et al.*, "Foveated Thermal Computational Imaging in the Wild Using All-Silicon Meta-Optics," *arXiv preprint arXiv:2212.06345,* 2022.

[94] J. E. Fröch *et al.*, "Dual Band Computational Infrared Spectroscopy via Large Aperture Meta-Optics," *ACS Photonics,* 2022.

VITA

Zheyi is pursuing a Ph.D. degree in Electrical and Computer Engineering at the University of Washington, with a research concentration on optical MEMS design and microfabrication. She has earned her Bachelor's degree in Materials Science and Engineering at Cornell University and her Master's degree in the same major at the University of Washington.